Constraining the UV background with the proximity effect

Aldo Dall'Aglio
Astrophysikalisches Institut Potsdam

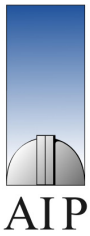

Dissertation zur Erlangung des akademischen Grades
doctor rerum naturalium (Dr. rer. nat.)
in der Wissenschaftsdisziplin Astrophysik
Eingereicht an der Mathematisch-Naturwissenschaftlichen Fakultät
der Universität Potsdam

Mai 2009

Published online at the
Institutional Repository of the University of Potsdam:
URL http://opus.kobv.de/ubp/volltexte/2009/3871/
URN urn:nbn:de:kobv:517-opus-38713
http://nbn-resolving.org/urn:nbn:de:kobv:517-opus-38713

Dedica

Questo lavoro e' dedicato alle Scelte,
a quell'invisibile disequilibrio
che ci porta ad intraprendere
sentieri sconosciuti per farci diventare
quello che siamo oggi.

Aldo

Contents

Abstract

After the epoch of reionisation the intergalactic medium (IGM) is kept at a high photoionisation level by the cosmic UV background radiation field. Primarily composed of the integrated contribution of quasars and young star forming galaxies, its intensity is subject to spatial and temporal fluctuations. In particular in the vicinity of luminous quasars, the UV radiation intensity grows by several orders of magnitude. Due to an enhanced UV radiation up to a few Mpc from the quasar, the ionised hydrogen fraction significantly increases and becomes visible as a reduced level of absorption in the H I Lyman alpha (Lyα) forest. This phenomenon is known as the *proximity effect* and it is the main focus of this thesis. Modelling the influence on the IGM of the quasar radiation, one is able to determine the UV background intensity at a specific frequency (J_{ν_0}), or equivalently, its photoionisation rate ($\Gamma_{\rm b}$). This is of crucial importance for both theoretical and observational cosmology. Thus far, the proximity effect has been investigated primarily by combining the signal of large samples of quasars, as it has been regarded as a statistical phenomenon. Only a handful of studies tried to measure its signature on individual lines of sight, albeit focusing on one sight line only. Our aim is to perform a systematic investigation of large samples of quasars searching for the signature of the proximity effect, with a particular emphasis on its detection on individual lines of sight.

We begin this survey with a sample of 40 high resolution ($R \sim 45\,000$), high signal to noise ratio ($S/N \sim 70$) quasar spectra at redshift $2.1 < z < 4.7$, publicly available in the European Southern Observatory (ESO) archive. The extraordinary quality of this data set enables us to detect the proximity effect signature not only in the combined quasar sample, but also along each individual sight line. This allows us to determine not only the UV background intensity at the mean redshift of this sample, but also to estimate its intensity in small ($\Delta z \sim 0.2$) redshift intervals in the range $2 \lesssim z \lesssim 4$. Our estimates ($J_{\nu_0} \sim 3 \times 10^{-22}$ erg s^{-1} cm^{-2} Hz^{-1} sr^{-1}) are for the first time in very good agreement with different constraints of its evolution obtained from theoretical predictions and numerical simulations.

We continue this systematic analysis of the proximity effect with the largest search to date invoking the Sloan Digital Sky Survey (SDSS) data set. The sample consists of 1733 quasars at redshifts $z > 2.3$. In spite of the low resolution and limited S/N we detect the proximity effect on about 98% of the quasars at a high significance level. Thereby we are able to determine the evolution of the UV background photoionisation rate within the redshift range $2 \lesssim z \lesssim 5$ finding $\Gamma_{\rm b} \sim 1.6 \times 10^{-12}$ s^{-1}. With these new measurements we explore literature estimates of the quasar luminosity function and predict the stellar luminosity density up to redshift of about $z \sim 5$. Our results are globally in good agreement with recent determinations inferred from deep surveys of high redshift galaxies.

We then compare our measurements on the UV background photoionisation rate inferred from the two samples at high and low resolution. While these data sets show extreme differences, our determinations are in considerable agreement at $z \lesssim 3.3$, even though they show less agreement at higher redshifts. We suspect that this may be caused by either the small number of high resolution quasar spectra at the highest redshifts considered or by some systematic effect due to the limited data quality of SDSS.

Complementary to the observational investigation of the proximity effect on high redshift quasars, we exploit some theoretical aspects linked to and based on the results on this phenomenon. We employ complex numerical simulations of structure formation to achieve a better representation of the Lyα forest. Modelling the signature of the proximity effect on randomly selected sight lines, we prove the advantages of dealing with individual lines of sight instead of combining their signal to investigate this phenomenon. Furthermore, we develop and test novel techniques aimed at a more precise determination of the proximity effect signal. With this investigation we demonstrate that the technique developed and employed in this thesis is the most accurate adopted thus far.

Tighter determinations of the UV background are certainly based on suitable methods to detect its signature, but also on a deeper understanding of the environments in which quasars form and evolve. We initiate an investigation of complex numerical simulations including the radiative transport of energy to model in a more detailed way the proximity effect. Such a simulation may lead to the characterisation of the quasar environment based on the comparison between the observed and simulated statistical properties of the proximity effect signature.

Zusammenfassung

Nach dem kosmologischen Zeitalter der Reionisation wird der hohe Photoionisationsgrad des intergalaktische Mediums (IGM) durch die kosmische UV-Hintergrundstrahlung aufrecht erhalten. Zur Intensität der Hintergrundstrahlung tragen hauptsächlich Quasare und jungen Galaxien bei. Daher entstehen sowohl räumliche als auch zeitliche Fluktuationen, wobei die Intensistät insbesondere in der Nähe von leuchtkräftigen Quasaren um mehrere Größenordnungen ansteigt. Aufgrund der erhöhten UV-Strahlung in einer Entfernung von bis zu einigen Mpc von einem Quasar wird ein größerer Anteil des intergalaktischen Wasserstoffs ionisiert, was als reduzierte Absorption im Lyman alpha (Lyα) Wald sichtbar wird. Dieses Phänomen wird *proximity effect* genannt und ist das Hauptthema dieser Arbeit. Durch Modellierung des Einflusses des Quasars auf das IGM kann die Intensität des UV-Hintergrunds bei einer bestimmten Frequenz (J_{ν_0}) bzw. die entsprechende Photoionisationrate (Γ_b) bestimmt werden. Dies ist sowohl für die theoretische als auch für die beobachtende Kosmologie eine wichtige Größe. Bisher wurde der Proximity-Effekt als ein statistisches Phänomen untersucht, wobei die Signale vieler einzelner Quasare kombiniert wurden. Nur in wenigen Analysen wurde versucht, den Effekt in einzelnen Sehlinien zu detektieren. Das Ziel dieser Arbeit ist eine systematische Untersuchung des Proximity-Effekts in einer großen Anzahl von Quasaren, wobei der besonderen Schwerpunkt auf seiner Detektion in einzelnen Sehlinien liegt.

Zunächst werden 40 Quasare im Rotverschiebungsbereich $2.1 < z < 4.7$ untersucht, deren Spektren mit hoher Auflösung ($R = 45\,000$) und hohem Signal-zu-Rausch-Verhältnis ($S/N \sim 70$) im Archiv des European Southern Observatory (ESO) vorliegen. Die außerordentlich gute Qualität dieser Daten ermöglicht die Detektion des Proximity-Effekts nicht nur als kombiniertes Signal aller Quasare sondern auch in jeder einzelnen Sehlinie. Daher konnten wir nicht nur die Intensität des UV-Hintergrunds bei der mittleren Rotverschiebung ermitteln sondern auch in kleineren Rotverschiebungsintervallen ($\Delta z \sim 0.2$) im Bereich $2 \lesssim z \lesssim 4$. Unsere Ergebnisse ($J_{\nu_0} \sim 3 \times 10^{-22}$ erg s^{-1} cm^{-2} Hz^{-1} sr^{-1}) stimmen zum ersten Mal gut anderen Bestimmungen überein, die auf theoretischen Voraussagen und auf numerischen Simulationen beruhen.

Unsere systematische Analyse des Proximity-Effekts wird mit dem bisher größten Datensatz bestehend aus 1733 Quasaren mit Rotverschiebungen $z > 2.3$ aus dem Sloan Digital Sky Survey (SDSS) fortgeführt. Trotz der niedrigen Auflösung und dem begrenzten S/N detektieren wir den Proximity-Effekt mit einer hohen Signifikanz in etwa 98% der Sehlinen. Dabei kann die Entwicklung der Photoionisationsrate $\Gamma_\mathrm{b} \sim 1.6 \times 10^{-12}$ s^{-1} im Rotverschiebungsbereich $2 \lesssim z \lesssim 5$ bestimmt werden. Mit diesen neuen Messungen diskutieren wir verschiedene Quasar-Leuchtkraftfunktionen aus der Literatur und berechnen die stellare Emissivität bis $z \sim 5$. Unsere Ergebnisse stimmen im Allgemeinen gut mit denen von neueren Himmelsdurchmusterungen nach hochrotverschobenen Galaxien überein.

Dann vergleichen wir die auf den hoch bzw. niedrig aufgelösten Spektren basierenden Photoionisationsraten miteinander. Obwohl die Datensätze sehr unterschiedlich sind, führen sie bei $z \lesssim 3.3$ zu den selben Ergebnissen, während die Resultate bei höheren Rotverschiebungen weniger gut übereinstimmen. Wir vermuten, dass dies entweder durch die kleine Anzahl von hochaufgelösten Quasarspektren bei den höchsten Rotverschiebungen, oder durch systematische Effekte der geringen SDSS Datenqualität hervorgerufen wird.

Ergänzend zu der Auswertung der Beobachtungsdaten führen wir basierend auf unseren Ergebnissen einige theoretische Untersuchugen durch. Wir benutzen komplexe Strukturbildungssimulationen, um eine bessere Beschreibung des Lyα-Walds zu gewinnen. Mit Hilfe der Modellierung des Proximity-Effekts in zufällig ausgesuchten Sehlinien zeigen wir den Vorteil auf, den die Analyse einzelner Sehlinien im Vergleich zur kombinierten Auswertung mehrerer Spektren hat. Außerdem entwickeln und testen wir neue Ansätze zur genaueren Bestimmung des Proxmity-Effekts. Dabei zeigen wir, dass die im Rahmen dieser Arbeit entwickelte und angewendete Methode bisher zu den genauesten Ergebnissen führt.

Für eine noch bessere Bestimmung des UV-Hintergurnds brauchen wir neben der optimalen Detektionsmethode auch ein tieferes Verständnis der Umgebung, in der Quasare entstehen und sich entwickeln. Wir beginnen eine Analyse komplexer numerischer Simulationen, die auch Strahlungstransportrechungen beinhalten, um weitere Details des Proximity-Effekts zu verstehen. Der Vergleich der statistischen Eigenschaften des Proximity-Effekts in solchen Simulationen mit Beobachtungen könnte in Zukunft zu einer genaueren Beschreibung der Umgebung von Quasaren führen.

Chapter 1

Introduction

ABSTRACT

We present a broad introduction to the principal topics in this work. The purpose of this Chapter is to provide the non-expert reader with the necessary background knowledge and tools of understanding, crucial in the following. We will focus on a concise overview of the reionisation of the Universe, the intergalactic medium and the proximity effect as they represent the prime areas of investigation in this thesis.

1.1. The concordance model

Over the last two decades an impressive step forward has been achieved in describing the fundamental parameters of the Universe which are starting to be estimated at a high level of precision. Those parameters enter in what we call the concordance model of standard cosmology and it has been built on a large number of experiments and observations ranging from the cosmic microwave background (CMB) temperature anisotropy by the Wilkinson Microwave Anisotropy Probe (WMAP, Spergel et al. 2003; Spergel 2006) to the Sloan Digital Sky Survey (SDSS, Tegmark et al. 2004; Eisenstein et al. 2005). Moreover, also the 2dF Galaxy Redshift Survey (Cole et al. 2005) and the Lyα forest (Croft et al. 2002; Viel et al. 2004; Kim et al. 2007) have provided crucial constraints allowing us to agree on a picture of the Universe which is expanding, spatially flat and, homogeneous and isotropic on scales above a few hundred Mpc (Wu et al. 1999). The energy density of the present-day Universe is dominated by dark energy and cold dark matter (CDM), while only a few percent are baryons. Also known as a Λ-CDM model, it predicts that structure originated as tiny density fluctuations in the hot, dense primordial Universe, grown under the influence of gravity in a sudden exponential expansion also known as inflation (Guth 1981; Linde 1984). In this scenario, state-of-the-art numerical simulations have been an indispensable tool to explore different models of structure growth, leading to the current understanding of hierarchical structure formation driven by gravitational instabilities.

1.2. Structure growth in the high redshift Universe

It is within the hierarchical structure formation paradigm that the main evolutionary stages of the Universe can be characterised. The baryonic content of the Universe evolves in a few distinct phases. At high redshift ($z > 1100$) the baryons are predominately hot, ionised, and optically thick to Thomson scattering, which implies that they are coupled to the photon field. As the Universe expands, this hot plasma of primordial baryonic particles cools and at some point recombines leading to the formation of the first neutral atoms (the so-called *epoch of recombination*). At completion, this process leaves a surface of last scattering, known as the cosmic microwave background (CMB), which is the best proof of a homogeneous and isotropic Universe. The CMB photons are then redshifted and thus observed at the present day at a lower temperature of $T_{\rm CMB} = 2.726 \pm 0.010$ K (Mather et al. 1994). The tiny density fluctuations inferred from the WMAP results grew through gravitational instability which accurately describe the behaviour of the dark matter component of the Universe. However, the baryonic component is as well subject to other dissipative and radiative forces allowing it to marginally depart from the evolutionary behaviour of the dark matter. After the epoch of recombination, both the dark and baryonic matter continue to collapse giving rise to the first clumps of gas dense enough to lead to the formation of the first generation of stars. Under the further influence of gravity, the matter in the Universe tends to form a net of overdense filaments and web-like structures the intersection of which are suitable for the formation of luminous objects like stars, proto-galaxies and quasars.

1.2.1. The first structures

As the dense collapsing regions begin to grow, the first generations of stars are expected to form in unique environmental conditions, i.e. out of metal[1] free gas. These so-called Population III stars (or Pop III) originate from the collapse of protostellar clouds where cooling by radiative processes is efficient enough to ensure the collapse and thus the formation of the star. Numerical simulations suggest that these Pop III stars might form already at redshift $z \simeq 30$, having much larger masses than today's stellar populations (100 $M_\odot$, Abel et al. 2002; Bromm et al. 2002; Schneider et al. 2004; Ciardi & Ferrara 2005), but are also capable of emitting strong UV flux

[1] With metals we typically identify all chemical species other than hydrogen or helium

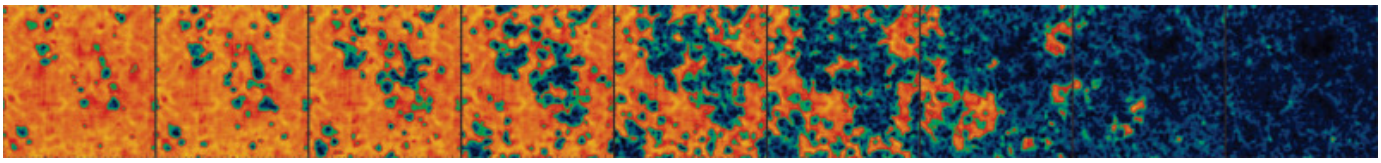

Fig. 1.1. The process of reionisation as predicted by numerical simulations of structure formation. Nine snapshots from Ciardi & Madau (2003, priv. comm.) show the 21 cm emission (orange regions) coming from the neutral hydrogen component in the Universe around the first structures. As the medium becomes ionised, the 21 cm signal drops (blue-black regions).

(Bromm et al. 2001). Such ionising radiation becomes crucial in the triggering of the *re*-ionisation of the Universe.

1.2.2. Reionisation

The massive injection of UV photons into the surrounding space characterised the end of the cosmic *dark ages*. These photons hold enough energy to ionise the hydrogen atoms (H I $\rightarrow$ H II Potential: 13.6 eV $\equiv$ 1 Ryd) around the first stars and galaxies. The change of state, from neutral to ionised, of the intergalactic medium (IGM) is known as the *epoch of reionisation* and due to the inhomogeneous distribution of the ionising sources, this process is expected to be extremely patchy. Numerical simulations seem to agree in predicting a three-phase reionisation process as presented in Fig. 1.1. The first phase is the pre-overlap phase where individual sources begin to ionise just the space surrounding them and thus create isolated H II regions. These ionised bubbles begin to grow in size and number and eventually overlap. The second phase is the overlap phase, also associated with the origin of a UV background radiation field, still highly inhomogeneous and spatially fluctuating (Gnedin 2004). The last, or post-overlap phase characterises the stage where only high density and self shielded regions are further ionised by the rapidly increasing intensity of the UV background (UVB) radiation field.

The epoch of reionisation is likely to have occurred over an extended period of time. Observational constraints from WMAP and by the so-called Gunn-Peterson effect, provide different insights concerning the end of the reionisation process, thus yielding upper and lower limits, respectively. The polarisation data obtained by WMAP (Page et al. 2006) lead to an estimate of the electron scattering optical depth which is consistent with an end of the reionisation process around $z \simeq 10$. Only in the last years, the deployment of extremely large arrays of low-frequency radio telescopes has become capable of probing the Universe in its neutral-to-ionised transition phase, for example using the hydrogen 21cm transition signal (see Fig. 1.1). Most of the observations performed thus far to probe the Universe beyond redshifts of four have been made possible due to the extremely luminous objects known as quasi stellar objects or quasars (QSOs). The direct observations of point-like sources such as bright quasars at redshift $z \lesssim 6$ demonstrate that the process of reionisation is completed at these redshifts. It is in fact the lack of a significant continuum absorption blueward of Lyα emission line (the so called Gunn-Peterson trough, Gunn & Peterson (1965)) that proves the existence of highly ionised hydrogen at redshift $z \lesssim 6$ (Becker et al. 2001; Fan et al. 2002; Songaila 2004).

Even if quasars are capable of emitting an extreme amount of UV radiation, their number density rapidly declines beyond $z = 3$ (Warren et al. 1994; Wolf et al. 2003), leading to the notion that QSOs only mildly contribute to the fraction of ionising photons and thus are not capable of reionising the Universe alone (Meiksin 2005). Other UV sources are needed to complete the process of the reionisation of the Universe. A dominant fraction of the UV radiation field originates from young star-forming galaxies. Observations of high redshift galaxies suggest a luminosity density of ionising photons which is smaller than predicted by theoretical models and thus insufficient to reionise the Universe (Madau et al. 1999). However, the detection of such galaxies is extremely challenging even with modern instrumentations and only a very limited fraction of fields have been investigated via deep survey (Ouchi et al. 2004; Tresse et al. 2007). Furthermore, the unknown escape fraction of ionising photons from high redshift galaxies makes the predictions of the stellar contribution even more uncertain. Recent results from both observations (Steidel et al. 2001; Fernández-Soto et al. 2003; Inoue et al. 2005) and simulations (Ricotti et al. 2000; Fujita et al. 2003; Gnedin 2008) are highly discrepant showing an escape fraction ranging from a few percent to up to 25%.

Also, the first generation of stars, formed out of metal-free gas, are a non-negligible source of UV photons in particular in their final evolutionary stage. Theoretical calculations show that due to their large masses (up to hundreds of solar masses), they are likely to collapse after their nuclear-burning phase and form a black hole which via merging and accretion could form a mini quasar (Haiman & Loeb 1998; Ricotti & Ostriker 2004).

The process of reionisation is therefore quite complex, inhomogeneous and closely connected to the properties of the triggering sources. Studying the formation and evolution of the UV background radiation field provides an important key to interpret this process and understand in detail the sources most likely behind it. Once the reionisation process is complete, the low density baryonic component of the intergalactic medium mainly consists of hydrogen, mostly ionised, singly ionised helium and various species of metals. The observation of the IGM via quasar absorption lines, upon which this thesis is based, offers one of the few possibilities to probe the Universe up to the epoch of reionisation. In the next section we will review most of the observed properties of the IGM (as we understand them).

1.3. The intergalactic medium

1.3.1. Quasar absorption lines

Quasars are among the most luminous class of objects in the Universe. Their high energetic output is thought to be powered

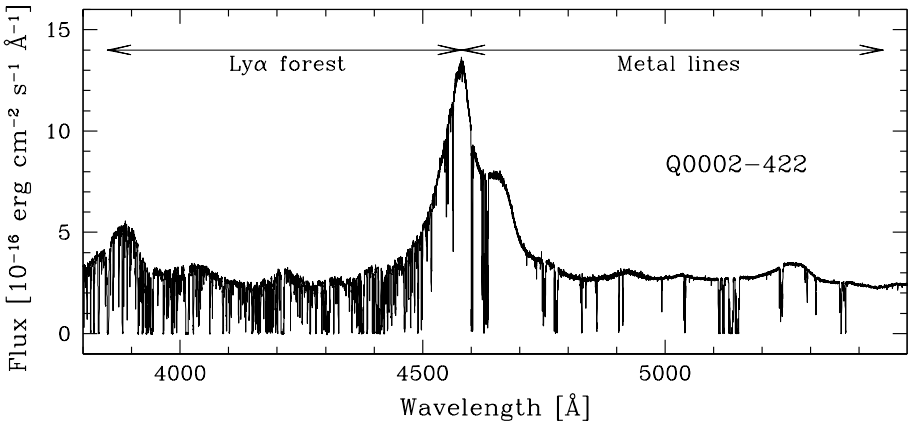

Fig. 1.2. An example of a high redshift quasar spectrum (Q 0002−422 at $z_{\rm em} = 2.767$) as observed by UV-Visual Echelle Spectrograph (UVES, Dekker et al. 2000) at VLT. The large number of absorption lines blueward of the redshifted Lyα emission peak is known by the name of the Lyman forest and it is the manifestation of the intervening lower redshift, low density hydrogen component of the IGM. All the transitions observed redward of the Lyα emission line belong to metal species typically associated with denser Lyα systems.

by accretion onto a supermassive black hole and is characterised by a power law continuum spectrum superimposed by broad emission lines originating from hot gas in the vicinity of the black hole within the host galaxy.

The IGM becomes *observable* as it leaves an imprint on the spectra of such objects. The light of high redshift quasars undergoes a systematic change as it travels through the intergalactic space towards us. Any emitted photon is observed at a longer wavelength proportional to its emitted value (the proportionality constant is $1+z_{\rm em}$, with $z_{\rm em}$ being the redshift of the emitting source). As soon as a high-frequency photon is redshifted to the Lyα transition, any neutral hydrogen atom is capable of absorbing that particular photon. Thus, any smooth distribution of hydrogen in the IGM would be detectable as a trough blueward of the Lyα wavelength of a source that is emitting at shorter wavelengths. The lack of this trough in spectra of high redshift sources like quasars up to redshift $z \sim 6$ demonstrates that the hydrogen is not uniformly distributed and it is highly ionised by the UVB (Gunn & Peterson 1965; Fan et al. 2006).

The observational imprint of a clumpy hydrogen distribution in the IGM is the plethora of absorption lines in the spectra of quasars at redshifts $z_{\rm em} < 6$, usually called the Lyman forest. Figure 1.2 presents a typical quasar spectrum at a redshift $z_{\rm em} \sim 2.7$ as observed by a high resolution ground based spectrograph. The broad emission line at about 4600 Å corresponds to the Lyα emission associated with the quasar. The Lyα forest is thereby mostly composed of Lyα absorption lines at different redshifts $z_{\rm abs} < z_{\rm em}$ where

$$\lambda_{\rm obs} = \lambda_{\rm rest}\,(1 + z_{\rm abs}) \tag{1.1}$$

with $\lambda_{\rm rest} = 1215.67$ Å for the Lyα transition. The absorption lines observed redward of the Lyα emission line are metal transitions associated with denser hydrogen systems along the line of sight.

The different absorbers in the Lyα forest have been classified into three major categories according to their column density, i.e. the projected density along the line of sight:

1. Lyα absorbers, typically with column densities between $\sim 10^{12}$ and $\sim 10^{17}$ cm^{-2}, are the weak line component of the Lyman forest.
2. Lyman limit systems (LLSs), typically with column densities between $\sim 10^{17}$ and $\sim 10^{20}$ cm^{-2}, are saturated absorbers which generate a cutoff of flux for rest frame wavelengths smaller than the Lyman limit transition (912Å).
3. Damped Lyα absorbers (DLAs), typically with column densities larger than $\sim 10^{20}$, are saturated absorbers with damping wings.

The last two classes of absorbers are optically thick to ionising radiation and are a reservoir of metals in the IGM.

Understanding the properties of these absorbers and the nature of the Lyα forest has been the focus of a multitude of works done by several groups both observationally (e.g. Hu et al. 1995; Lu et al. 1996; Kim et al. 1997) and theoretically (e.g. Cen et al. 1994; Hernquist et al. 1996) for more than a decade.

Up to now, several surveys have been carried out aimed at investigating QSO intervening absorption systems, providing a large statistical sample which has been (and still is) explored to derive the statistical properties of such systems. Those concentrating on the Lyα forest were conducted by Bechtold (1994); Storrie-Lombardi et al. (1996); Bechtold et al. (2002); Kim et al. (2002); Tytler et al. (2004); Kim et al. (2007). Lyman Limit Systems were investigated by Sargent et al. (1989); Lanzetta et al. (1995); O'Meara et al. (2007) while Damped Lyα absorbers were in the focus of Wolfe et al. (1986); Lanzetta (1991); Lu & Wolfe (1994); Lanzetta et al. (1995); Storrie-Lombardi & Wolfe (2000); Ellison et al. (2002); Chen & Lanzetta (2003); Srianand et al. (2005).

In our current understanding, the Lyα forest is well represented by a combination of four main distributions which we address separately in the following sections.

1.3.2. Column density distribution

The neutral hydrogen column densities of the absorbers have been observed ranging from about $N_{\rm H\,I} \sim 10^{12}$ cm^{-2} up to $N_{\rm H\,I} \sim 10^{22}$ cm^{-2}. The detection of smaller column density systems is extremely challenging and the completeness significantly drops (Hu et al. 1995) below 10^{12} cm^{-2}. It was Tytler (1987) who for the first time discovered that the column densities in the forest are distributed as a power law in the form

$$\frac{{\rm d}n}{{\rm d}N_{\rm H\,I}} \propto N_{\rm H\,I}^{-\beta} \tag{1.2}$$

with $\beta \sim 1.5 - 1.7$ (Tytler 1987; Hu et al. 1995; Kim et al. 2002). Although there have been claims of a broken power law

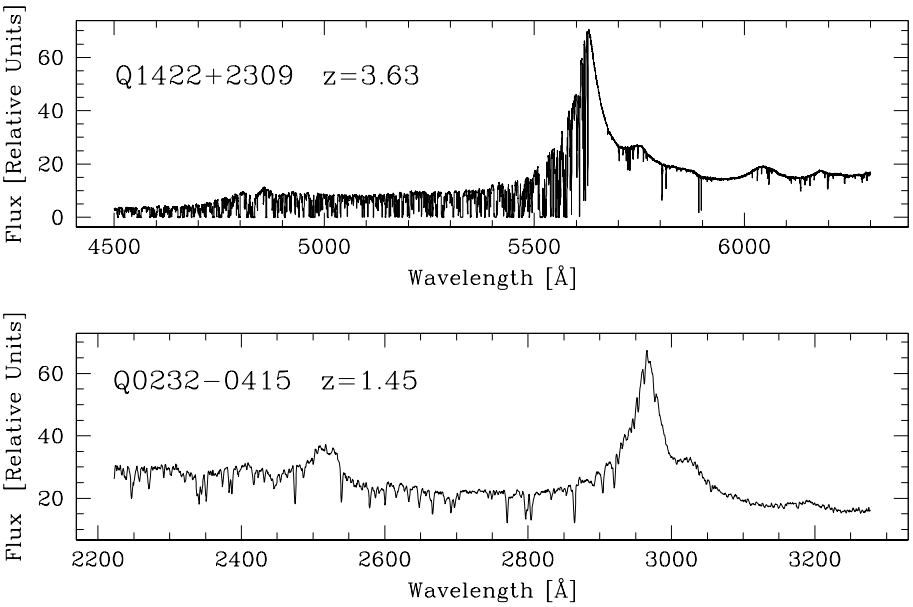

Fig. 1.3. The dramatic change in the absorption as observed via the Lyα forest of two quasars at redshift of $z_{\rm em}$ = 3.63 (Songaila 1998) and $z_{\rm em}$ = 1.45 (Bechtold et al. 2002). As the Universe evolves and larger structure are formed, the imprints on the Lyα forest evolve resulting in emptier voids between denser collapsing structures.

(Giallongo et al. 1993; Petitjean et al. 1993), the almost perfect single power law over such an enormous dynamic range motivates us to assume in the following work a single power law representation. Note that any deviation from this will have a negligible impact on both the observational and the theoretical results presented here.

1.3.3. Doppler parameter distribution

At spectral resolutions large enough to resolve and fit single absorption line profiles ($R \gtrsim 10\,000$), the Doppler velocity b of the system can be estimated adopting a Gaussian or a Voigt profile as a theoretical model for an absorption line. The measured Doppler velocities b are in the range $10 < b < 100$ km s^{-1}, showing a concentration between 15−60 km s^{-1} (Hu et al. 1995; Kim et al. 1997; Kirkman & Tytler 1997; Lu et al. 1996). This distribution is well approximated by

$$\frac{{\rm d}n}{{\rm d}b} \propto b^{-5} \exp\left[-b_\sigma^4/b^4\right] \tag{1.3}$$

where $b_\sigma \simeq 24$ km/s (Kim et al. 2001) is a parameter dependent on the average amplitude of the fluctuations in the velocity space of the absorbers (Hui & Rutledge 1999).

1.3.4. Evolution of the Lyα forest

As the Universe evolves and larger structures are successively formed, so do the imprints of the IGM onto the Lyα forest change. A clear observational example of this evolution is presented in Fig. 1.3. Characterising the change of the Lyα forest has been a key research driver over several decades and one approach widely adopted to achieve this goal has been and still is the line fitting procedure (applied to individual absorbers). This method allows not only to analyse the line number density, but also to derive column densities and Doppler parameters as presented earlier. Already in the early 1980s it has been recognised that the line density per unit redshift is well approximated by a power law dependence on $(1 + z)$ of the form

$$\frac{{\rm d}n}{{\rm d}z} = n_0(1+z)^\gamma \tag{1.4}$$

yielding accurate fits to the line counts (Sargent et al. 1980; Young et al. 1982; Murdoch et al. 1986). The exponent γ, which can have values within the range $1.5 < \gamma < 3$, embodies the redshift dependence of the line density.

This technique, however, requires high resolution spectra which are not easy to obtain as it is expensive in terms of observing time and resources. Therefore, another observable has been employed already by Gunn & Peterson (1965), enabling the investigation of the Lyα forest at low to medium resolutions: the flux decrement, or equivalently, the effective optical depth. Both quantities are a measure of the average transmission within a certain redshift interval and are closely connected to the evolution of the line density with redshift. The details about this connection are out of the scope of this introduction, however a detailed calculation is presented in Appendix A.2.

The effective optical depth can be derived when rectifying the observed flux of a quasar spectrum $F_{\rm q}$ with its continuum emission F_0 before it is affected by the IGM along the line of sight. Thus we can write that

$$< T >= \left\langle \frac{F_{\rm q}}{F_0} \right\rangle \equiv < {\rm e}^{-\tau} >= {\rm e}^{-\tau_{\rm eff}} \tag{1.5}$$

where T is the transmitted flux, or simply transmission, τ is the optical depth of the Ly forest and $\tau_{\rm eff}$ the effective optical depth.

Studying absorption lines and their properties requires a large number of QSO sight lines to obtain a *statistically significant* sample (e.g. Bechtold 1994; Lu et al. 1996; Kirkman & Tytler 1997; Scott et al. 2000). Adopting instead the transmission or the effective optical depth as prime investigation tool, one achieves higher accuracy in estimating the statistical properties of the Lyman forest such as the flux probability distribution, the effective optical depth evolution or the flux power spectrum (e.g. McDonald et al. 2000; Miralda-Escudé et al. 2000; Kim et al. 2001, 2002; Becker et al. 2007).

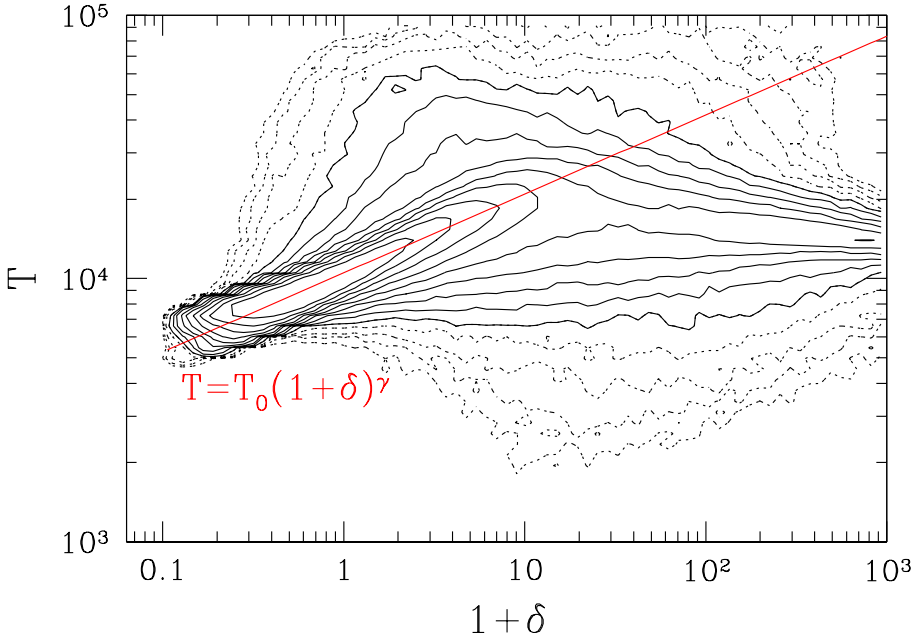

Fig. 1.4. The baryonic temperature as a function of overdensity in the intergalactic medium at redshift $z = 4$ as predicted in a numerical simulations by Gnedin & Fan (2006, priv. comm.). At the low densities characteristic for the Ly forest, the gas follows a tight power law relation (solid red line, Eq. 1.7). At higher densities, shock heating and eventually radiative cooling become important and begin to dominate, yielding a departure from a pure power law. Thick contours shows above average and dotted contours below average probability density to find a fluid element with these T and δ; contour stepping is set to 0.25 dex.

The change of opacity in the Lyα forest is well represented by a power law evolution of $\tau_{\rm eff}$ as

$$\tau_{\rm eff} = \tau_0(1+z)^{\gamma+1} \tag{1.6}$$

where the exponent γ has been shown to change with redshift as well (Weymann et al. 1998; Kim et al. 2001; Becker et al. 2007). Towards low redshift ($z \lesssim 1.7$) the evolution of $\tau_{\rm eff}$ becomes much shallower than within the range $1.7 \lesssim z \lesssim 4$, primarily because of (i) a decrease in the intensity of the UV background radiation as the QSO number density drops and (ii) the further collapse of dense structures. At high redshift ($z \gtrsim 4$), investigation of the Lyα and Lyβ forest seems to suggest an acceleration in the increase of opacity which ultimately leads to the appearance of the Gunn-Peterson trough (Fan et al. 2002; Fan et al. 2006).

1.3.5. Temperature of the intergalactic medium

The analysis of the thermal state of the IGM is a highly challenging research area which requires, observationally, very high resolution quasar spectroscopy and theoretically a great amount of computational resources as hydrodynamical effects need to be taken into account.

The temperature of the IGM is the outcome of a balance between photo-heating by the UV background radiation field and cooling due to the adiabatic expansion of the Universe. In the low density regime (where the IGM originates) this balance results in a power law temperature-density relation as

$$T = T_0\,(1+\delta)^{\tilde{\gamma}-1}, \tag{1.7}$$

where T_0 is the temperature at the mean density, δ is the baryonic density contrast and $\tilde{\gamma}$ is the slope of the equation of state for low densities. An example of the thermal state of the IGM as obtained by numerical simulations is presented in Fig. 1.4. Note that T here is the temperature and has no connection to the transmission described earlier (Hui et al. 1997). This relation is usually referred to as the effective equation of state (EOS) of the IGM. For the typical overdensities encountered in the IGM, $\delta \lesssim 10$, T_0 and $\tilde{\gamma}$ have been constrained to be of the order of $10^{3.6} < T_0 < 10^{4.5}$ K and $1 < \tilde{\gamma} < 1.6$ (Bolton et al. 2004; Schaye et al. 2000; McDonald et al. 2001). Their actual values depend on the ionisation history of the Universe and are tightly connected to the evolution of the UV background radiation field.

The effective EOS has been constrained using high resolution quasar spectroscopy albeit yielding large uncertainties (Schaye et al. 1999; Ricotti et al. 2000; McDonald et al. 2001).

1.4. The ionisation state of the intergalactic medium

Thus far we have introduced the most important properties of the IGM as we observe them through the analysis of quasar spectra and the Lyα forest. In itself, the existence of the Lyα forest is the best indication of the ionisation state of the IGM which is kept at a high photoionisation level by the overall amount of UV photons generated by the global population of star-forming galaxies and quasars at redshift $z < 6$.

The multitude of absorption lines observed blueward of the Lyα emission line arise from a tiny amount of neutral hydrogen along the line of sight towards a quasar: about 1 part in 100 000. As a result, the intensity of the UVB can be estimated from the analysis of the Lyα forest and this will be the main goal of this thesis.

An accurate estimate of the UVB is not only of great importance for understanding the sources contributing to it, but also since this radiation field is a crucial ingredient when modelling and studying the physical state and evolution of the IGM via numerical simulations.

1.4.1. Estimating the UV background radiation field

Theoretically, two methods have been developed to predict the UV background.

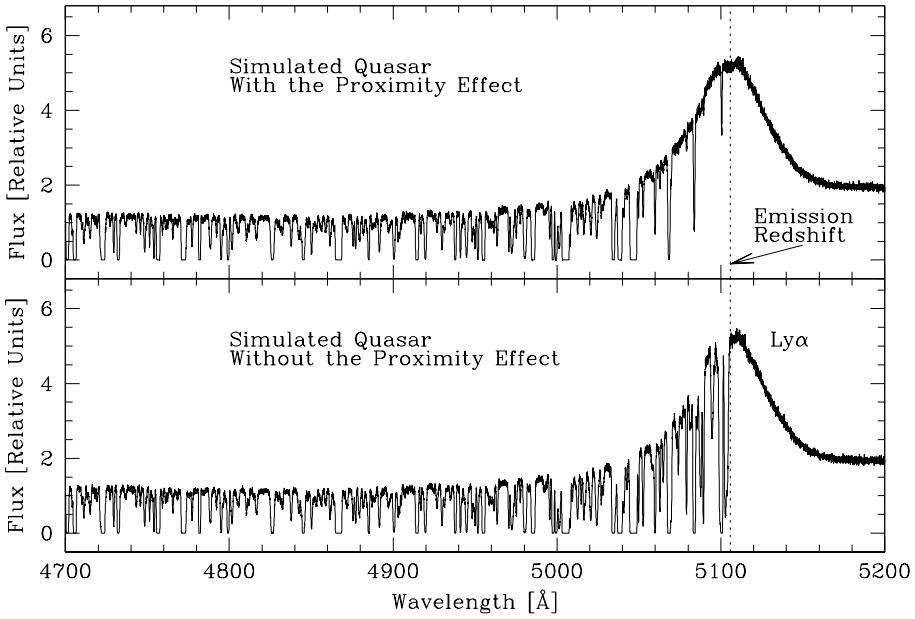

Fig. 1.5. A simulated quasar spectrum illustrating the effect of the quasar radiation on the neutral hydrogen distribution close to its emission, i.e. the *proximity effect*. The strong UV radiation field emitted by the QSO is capable of ionising almost all the hydrogen in its proximity leading to the large lack of absorption lines in the blue wing of the Lyα emission line. The dotted vertical line marks the emission redshift, also identified by the strong Lyα emission.

Firstly, the UVB can be modeled by integrating the contribution of all the observed sources thought to be active building blocks of the UV background. Once the luminosity functions and the spectral energy distributions (SEDs) of these sources are known, one can numerically derive the amplitude and spectral shape of the UV background radiation field (Bechtold et al. 1987). The main strength of these calculations consists in predicting the relative contributions of quasars (Haardt & Madau 1996; Fardal et al. 1998) and star-forming galaxies (Madau et al. 1999; Haardt & Madau 2001) to the UV background intensity as a function of redshift, albeit based on some poorly constrained quantities. The luminosity function, in particular of galaxies, is extremely difficult to determine, particularly at high redshift where deep surveys like the Vimos VLT Deep Survey (VVDS, Tresse et al. 2007) might be significantly affected by cosmic variance due to their small field of view. Moreover, the galaxy contribution also depends on the poorly estimated escape fraction of ionising photons. Even though quasars are extremely bright sources and their luminosity function is well estimated at different redshifts (Wolf et al. 2003; Bongiorno et al. 2007), the shape of their SEDs is under debate. The quasar continuum below the Lyman limit frequency is well approximated by a power law $f_\nu \propto \nu^{-\alpha}$ with $\alpha \simeq 1.7$ (Telfer et al. 2002). However, recently Scott et al. (2004) presented new evidence for a change in the spectral shape of low-redshift low-luminosity AGN which may influence the outcome of these calculations. This radiation field is subsequently filtered by the matter distribution in the IGM which imprints a particular frequency dependence. The intensity of the UVB at a given frequency, $J_\mathrm{b}(\nu)$ is then governed by (i) the cosmological expansion, (ii) the evolution of the different UV sources and (iii) the baryonic content of the IGM (e.g. Davé et al. 1999). Due to the rapid rise of the UV background intensity after the epoch of reionisation, most of the IGM is optically thin to ionising photons and thus has a relatively large mean free path for H I ionising photons (up to one hundred proper Mpc, Madau et al. 1999; Miralda-Escudé et al. 2000; Meiksin & White 2004).

Secondly, the H I UVB photoionisation rate has been inferred employing 3D numerical simulations of structure formation. As already mentioned, one of the key ingredients in these simulations is the intensity of the UV background or equivalently its ionisation rate. With an accurate match of the statistical properties of the simulated transmission spectra with high resolution observation of quasars at different redshift, the UVB can be constrained (e.g. Rauch et al. 1997; McDonald et al. 2000; Meiksin & White 2004; Tytler et al. 2004; Bolton et al. 2005; Kirkman et al. 2005; Jena et al. 2005; Faucher-Giguere et al. 2008). The main obstacle of this approach is the large number of free parameters entering the computation which in the end leads in some cases to contradicting results (e.g. Bolton et al. 2009; Faucher-Giguère et al. 2008).

Observationally, only one method of estimating the UVB exists and it is based on the so-called *proximity effect*, illustrated in Fig 1.5.

As quasars are very powerful sources of UV photons, the relative impact of their radiation compared to the background drastically changes in their vicinity (Carswell et al. 1987; Bajtlik et al. 1988), reaching in some cases up to four orders of magnitude enhancement. Typically the UVB estimates inferred from the proximity effect have been obtained from large samples of quasars (Bajtlik et al. 1988; Lu et al. 1991; Espey 1993; Giallongo et al. 1993; Kulkarni & Fall 1993; Bechtold 1994; Fernández-Soto et al. 1995; Giallongo et al. 1996; Srianand & Khare 1996; Cooke et al. 1997; Scott et al. 2000; Liske & Williger 2001; Scott et al. 2002), but also investigating individual sight lines (Williger et al. 1994; Cristiani et al. 1995; Lu et al. 1996; Savaglio et al. 1997), and yielded an estimate of the UVB intensity at the Lymann limit (J_{ν_0}).

In spite of the large statistical and systematic errors present in most measurements (both of which will be characterised in the course of this thesis), there are indications for a change in the UV intensity at low redshifts $z \lesssim 2$ (Dobrzycki et al. 2002) and high redshifts $z \gtrsim 4$ (Fan et al. 2006), somehow connected to the decline in the QSO contribution to the background field.

However, most of these measurements yielded systematically higher values than the predictions of theoretical calculations (e.g. Madau et al. 1999; Haardt & Madau 2001; Sokasian et al. 2003; Schirber & Bullock 2003). We list in the following some of the effects that might help to explain this discrepancy.

(i) An enhancement in the density field near the quasars: If quasars reside in overdense regions and the resulting higher hydrogen fraction is neglected, this will cause J_{ν_0} to be overestimated by a factor ~ 3 (Loeb & Eisenstein 1995; Rollinde et al. 2005; Faucher-Giguère et al. 2008).

(ii) A poorly constrained emission redshift: It is well known that quasars show broad emission lines coming from low and high ionisation transitions. Typically, redshift measurements from the Lyα or high ionisation lines such as C IV are systematically lower than those from low-ionisation lines (Gaskell 1982), leading to a value of J_{ν_0} to be overestimated by a factor ~ 3 (Espey 1993).

(iii) Quasar variability: Quasars are variable sources, thus a change in the radiative output on timescales of several Myrs will also tend to an overestimate of J_{ν_0} due to a Malmquist bias in the selected quasar sample (Schirber et al. 2004).

1.5. The proximity effect

The prime astrophysical tool of investigation in this thesis is the proximity effect. It refers to the enhanced UV radiation field the hydrogen is exposed to in the vicinity of bright quasars and as we already mentioned, it can outshine the background radiation by several orders of magnitude. Consequently, the ionised hydrogen fraction significantly increases within a few Mpc from the source. This leads to a systematic decrease in the Lyα absorption near the quasar compared to an "average" location along the line of sight only affected by the UV background radiation.

This effect was discovered in the early 1980's when the first large sample of medium resolution quasar spectra was investigated. Weymann et al. (1981) first suggested that the line density of Lyα absorbers in the vicinity of a quasar was systematically lower than in the remaining Ly forest, implying a high degree of ionisation. Later, Murdoch et al. (1986) explained the countervailing trend of a decreasing line density near the quasar against the already well established increase in the Lyα forest as a locally enhanced UV radiation field. Only with the first ionisation model presented by Bajtlik et al. (1988) did it became possible to connect the UV background to the signature of the proximity effect in the quasar spectra. The principal disadvantage was the large number of sight lines required for this investigation since the statistics on individual absorption lines was the only tool of analysis. Their ionisation model has been used ever since to infer the UV background intensity via the proximity effect, albeit with some minor modifications (e.g. Williger et al. 1994; Lu et al. 1996; Scott et al. 2000).

The original computation is based on a few assumptions: (i) the quasar and UV background do have equivalent SEDs, (ii) the quasar radiation field is attenuated only due to geometrical dilution, meaning that the IGM is totally optically thin to ionising radiation and (iii) the UV background is constant within the redshift range probed by the observations. The model predicts the decrease in the number of lines approaching the emission of the quasar based on a comparison between the ionisation equilibrium with only the UVB as an ionising source and, alternatively, with the UVB *and* quasar.

Therefore an absorber with column density $N_{\mathrm{H\,I},\infty}$ will experience a reduction in the neutral hydrogen fraction when located close to a quasar according to

$$N_{\mathrm{H\,I}}(z) = \frac{N_{\mathrm{H\,I},\infty}(z)}{1+\omega(z)}, \tag{1.8}$$

where $N_{\mathrm{H\,I}}$ is the observed column density in the presence of a quasar while $N_{\mathrm{H\,I},\infty}$ defines the column density that would be measured if the quasar would be located at infinite distance from the same absorber. The attenuation factor $1+\omega(z)$ describes how strongly the radiation of the quasar overcomes the intensity of the UVB such that

$$\omega(z) = \frac{\Gamma_{\mathrm{q}}(z)}{\Gamma_{\mathrm{b}}(z)}. \tag{1.9}$$

The value of $\omega(z)$ at a given redshift is defined as the ratio between the H I photoionisation rate of the quasar (Γ_{q}) and the UV background (Γ_{b}). Since the quasar contribution decreases with increasing distance to the absorber, $\omega(z)$ defines a distance indicator, meaning that, towards the quasar emission redshift the value of $\omega(z)$ increases.

By estimating the quasar luminosity at the Lyman limit, a value for the average UV background at the same wavelength can be inferred. A detailed derivation is out of the scope of this introduction, but it will be presented in Appendix A.1..

If the proximity effect influence on the line number density distribution is then taken into account, we can write the expected departure of the number of H I clouds in the Lyα forest and obtain

$$\frac{\mathrm{d}n}{\mathrm{d}z} = n_0\,(1+z)^{\gamma}\,(1+\omega(z))^{1-\beta} \tag{1.10}$$

where β is the slope of the column density distribution (Bajtlik et al. 1988).

Similarly, we can express the behaviour of the effective optical depth as presented by Liske & Williger (2001).

$$\tau_{\mathrm{eff}}(z) = \tau_{\mathrm{eff},\infty}\,(1+\omega(z))^{1-\beta} = \tau_0\,(1+z)^{\gamma+1}\,(1+\omega(z))^{1-\beta}\,. \tag{1.11}$$

This indicator is very well suited for high- and low-resolution spectra as it does not require any fit of individual absorbers. Applying both techniques on the same set of quasars, we will demonstrate in Chapter 2 the advantages of the flux statistics, leading to much tighter constraints on the UV background intensity. However, when estimating the proximity effect with the effective optical depth, one has to assume a slope for the column density distribution, which can be determined only with line fitting and on high resolution quasar spectra.

1.6. Outline and structure of the work

The aim of this thesis is to exploit the proximity effect as an astrophysical tool from both an observational point of view as well as theoretical. We will present a comprehensive investigation of this phenomenon on a variety of different quasar spectra pursuing the prime goal of characterising the evolution of the cosmic UV background radiation field.

This thesis is divided into Chapters meant to be stand-alone articles, accepted, submitted or to be submitted to major Journals such as *Astronomy & Astrophysics* and *The Astrophysical Journal*. Within each, the reader will find an additional introduction focussing on a more detailed description of the topics closely related to the analysis presented in the Chapter.

We begin our analysis in Chapter 2, with a sample of 40 high resolution quasar spectra obtained from the European Southern Observatory archive. Chapter 3 focusses on the largest data set thus far explored to determine the signature of the proximity effect (thank to the Sloan Digital Sky Survey). With high resolution numerical simulations of structure formation, we begin in Chapter 4 to compare different theoretical methods aimed at the detection of the proximity effect on individual lines of sight. Chapter 5 presents the first radiative transfer simulation concentrating on the proximity effect at high redshift. Our conclusions and future perspectives are discussed in Chapter 6 and at the end of each of the mentioned Chapters.

References

Abel, T., Bryan, G. L., & Norman, M. L. 2002, Science, 295, 93
Bajtlik, S., Duncan, R. C., & Ostriker, J. P. 1988, ApJ, 327, 570
Bechtold, J. 1994, ApJS, 91, 1
Bechtold, J., Dobrzycki, A., Wilden, B., et al. 2002, ApJS, 140, 143
Bechtold, J., Weymann, R. J., Lin, Z., & Malkan, M. A. 1987, ApJ, 315, 180
Becker, G. D., Rauch, M., & Sargent, W. L. W. 2007, ApJ, 662, 72
Becker, R. H., Fan, X., White, R. L., et al. 2001, AJ, 122, 2850
Bolton, J., Meiksin, A., & White, M. 2004, MNRAS, 348, L43
Bolton, J. S., Haehnelt, M. G., Viel, M., & Springel, V. 2005, MNRAS, 357, 1178
Bolton, J. S., Oh, S. P., & Furlanetto, S. R. 2009, ArXiv e-prints
Bongiorno, A., Zamorani, G., Gavignaud, I., et al. 2007, A&A, 472, 443
Bromm, V., Coppi, P. S., & Larson, R. B. 2002, ApJ, 564, 23
Bromm, V., Ferrara, A., Coppi, P. S., & Larson, R. B. 2001, MNRAS, 328, 969
Carswell, R. F., Webb, J. K., Baldwin, J. A., & Atwood, B. 1987, ApJ, 319, 709
Cen, R., Miralda-Escudé, J., Ostriker, J. P., & Rauch, M. 1994, ApJ, 437, L9
Chen, H.-W. & Lanzetta, K. M. 2003, ApJ, 597, 706
Ciardi, B. & Ferrara, A. 2005, Space Science Reviews, 116, 625
Ciardi, B. & Madau, P. 2003, ApJ, 596, 1
Cole, S., Percival, W. J., Peacock, J. A., et al. 2005, MNRAS, 362, 505
Cooke, A. J., Espey, B., & Carswell, R. F. 1997, MNRAS, 284, 552
Cristiani, S., D'Odorico, S., Fontana, A., Giallongo, E., & Savaglio, S. 1995, MNRAS, 273, 1016
Croft, R. A. C., Weinberg, D. H., Bolte, M., et al. 2002, ApJ, 581, 20
Davé, R., Hernquist, L., Katz, N., & Weinberg, D. H. 1999, ApJ, 511, 521
Dekker, H., D'Odorico, S., Kaufer, A., Delabre, B., & Kotzlowski, H. 2000, in Presented at the Society of Photo-Optical Instrumentation Engineers (SPIE) Conference, Vol. 4008, Proc. SPIE Vol. 4008, p. 534-545, Optical and IR Telescope Instrumentation and Detectors, Masanori Iye; Alan F. Moorwood; Eds., ed. M. Iye & A. F. Moorwood, 534–545
Dobrzycki, A., Bechtold, J., Scott, J., & Morita, M. 2002, ApJ, 571, 654
Eisenstein, D. J., Zehavi, I., Hogg, D. W., et al. 2005, ApJ, 633, 560
Ellison, S. L., Yan, L., Hook, I. M., et al. 2002, A&A, 383, 91
Espey, B. R. 1993, ApJ, 411, L59
Fan, X., Carilli, C. L., & Keating, B. 2006, ARA&A, 44, 415
Fan, X., Narayanan, V. K., Strauss, M. A., et al. 2002, AJ, 123, 1247
Fardal, M. A., Giroux, M. L., & Shull, J. M. 1998, AJ, 115, 2206
Faucher-Giguère, C.-A., Lidz, A., Hernquist, L., & Zaldarriaga, M. 2008, ApJ, 682, L9
Faucher-Giguere, C.-A., Lidz, A., Zaldarriaga, M., & Hernquist, L. 2008, ApJ, 673, 39
Faucher-Giguère, C.-A., Prochaska, J. X., Lidz, A., Hernquist, L., & Zaldarriaga, M. 2008, ApJ, 681, 831
Fernández-Soto, A., Barcons, X., Carballo, R., & Webb, J. K. 1995, MNRAS, 277, 235
Fernández-Soto, A., Lanzetta, K. M., & Chen, H.-W. 2003, MNRAS, 342, 1215
Fujita, A., Martin, C. L., Mac Low, M.-M., & Abel, T. 2003, ApJ, 599, 50
Gaskell, C. M. 1982, ApJ, 263, 79
Giallongo, E., Christiani, S., D'Odorico, S., Fontana, A., & Savaglio, S. 1996, ApJ, 466, 46
Giallongo, E., Christiani, S., Fontana, A., & Trèvese, D. 1993, ApJ, 416, 137
Gnedin, N. Y. 2004, ApJ, 610, 9
Gnedin, N. Y. 2008, ApJ, 673, L1
Gnedin, N. Y. & Fan, X. 2006, ApJ, 648, 1
Gunn, J. E. & Peterson, B. A. 1965, ApJ, 142, 1633
Guth, A. H. 1981, Phys. Rev. D, 23, 347
Haardt, F. & Madau, P. 1996, ApJ, 461, 20
Haardt, F. & Madau, P. 2001, in Clusters of Galaxies and the High Redshift Universe Observed in X-rays, ed. D. M. Neumann & J. T. V. Tran
Haiman, Z. & Loeb, A. 1998, ApJ, 503, 505
Hernquist, L., Katz, N., Weinberg, D. H., & Miralda-Escudé, J. 1996, ApJ, 457, L51+
Hu, E. M., Kim, T.-S., Cowie, L. L., Songaila, A., & Rauch, M. 1995, AJ, 110, 1526
Hui, L., Gnedin, N. Y., & Zhang, Y. 1997, ApJ, 486, 599
Hui, L. & Rutledge, R. E. 1999, ApJ, 517, 541
Inoue, A. K., Iwata, I., Deharveng, J.-M., Buat, V., & Burgarella, D. 2005, A&A, 435, 471
Jena, T., Norman, M. L., Tytler, D., et al. 2005, MNRAS, 361, 70
Kim, T.-S., Bolton, J. S., Viel, M., Haehnelt, M. G., & Carswell, R. F. 2007, MNRAS, 382, 1657
Kim, T.-S., Carswell, R. F., Cristiani, S., D'Odorico, S., & Giallongo, E. 2002, MNRAS, 335, 555
Kim, T.-S., Cristiani, S., & D'Odorico, S. 2001, A&A, 373, 757
Kim, T.-S., Hu, E. M., Cowie, L. L., & Songaila, A. 1997, AJ, 114, 1
Kirkman, D. & Tytler, D. 1997, ApJ, 484, 672
Kirkman, D., Tytler, D., Suzuki, N., et al. 2005, MNRAS, 360, 1373
Kulkarni, V. P. & Fall, S. M. 1993, ApJ, 413, L63
Lanzetta, K. M. 1991, ApJ, 375, 1
Lanzetta, K. M., Bowen, D. V., Tytler, D., & Webb, J. K. 1995, ApJ, 442, 538
Linde, A. D. 1984, Reports on Progress in Physics, 47, 925
Liske, J. & Williger, G. M. 2001, MNRAS, 328, 653
Loeb, A. & Eisenstein, D. J. 1995, ApJ, 448, 17
Lu, L., Sargent, W. L. W., Womble, D. S., & Takada-Hidai, M. 1996, ApJ, 472, 509
Lu, L. & Wolfe, A. M. 1994, AJ, 108, 44
Lu, L., Wolfe, A. M., & Turnshek, D. A. 1991, ApJ, 367, 19
Madau, P., Haardt, F., & Rees, M. J. 1999, ApJ, 514, 648
Mather, J. C., Cheng, E. S., Cottingham, D. A., et al. 1994, ApJ, 420, 439
McDonald, P., Miralda-Escudé, J., Rauch, M., et al. 2001, ApJ, 562, 52
McDonald, P., Miralda-Escudé, J., Rauch, M., et al. 2000, ApJ, 543, 1
Meiksin, A. 2005, MNRAS, 356, 596
Meiksin, A. & White, M. 2004, MNRAS, 350, 1107
Miralda-Escudé, J., Haehnelt, M., & Rees, M. J. 2000, ApJ, 530, 1
Murdoch, H. S., Hunstead, R. W., Pettini, M., & Blades, J. C. 1986, ApJ, 309, 19
O'Meara, J. M., Prochaska, J. X., Burles, S., et al. 2007, ApJ, 656, 666
Ouchi, M., Shimasaku, K., Okamura, S., et al. 2004, ApJ, 611, 660
Page, K. L., King, A. R., Levan, A. J., et al. 2006, ApJ, 637, L13
Petitjean, P., Webb, J. K., Rauch, M., Carswell, R. F., & Lanzetta, K. 1993, MNRAS, 262, 499
Rauch, M., Miralda-Escude, J., Sargent, W. L. W., et al. 1997, ApJ, 489, 7
Ricotti, M., Gnedin, N. Y., & Shull, J. M. 2000, ApJ, 534, 41
Ricotti, M. & Ostriker, J. P. 2004, MNRAS, 350, 539
Rollinde, E., Srianand, R., Theuns, T., Petitjean, P., & Chand, H. 2005, MNRAS, 361, 1015
Sargent, W. L. W., Steidel, C. C., & Boksenberg, A. 1989, ApJS, 69, 703
Sargent, W. L. W., Young, P. J., Boksenberg, A., & Tytler, D. 1980, ApJS, 42, 41
Savaglio, S., Christiani, S., D'Odorico, S., et al. 1997, A&A, 318, 347
Schaye, J., Theuns, T., Leonard, A., & Efstathiou, G. 1999, MNRAS, 310, 57
Schaye, J., Theuns, T., Rauch, M., Efstathiou, G., & Sargent, W. L. W. 2000, MNRAS, 318, 817
Schirber, M. & Bullock, J. S. 2003, ApJ, 584, 110

Schirber, M., Miralda-Escudé, J., & McDonald, P. 2004, ApJ, 610, 105
Schneider, R., Ferrara, A., & Salvaterra, R. 2004, MNRAS, 351, 1379
Scott, J., Bechtold, J., Dobrzycki, A., & Kulkarni, V. P. 2000, ApJ, 130, 67
Scott, J., Bechtold, J., Morita, M., Dobrzycki, A., & Kulkarni, V. P. 2002, ApJ, 571, 665
Scott, J. E., Kriss, G. A., Brotherton, M., et al. 2004, ApJ, 615, 135
Sokasian, A., Abel, T., & Hernquist, L. 2003, MNRAS, 340, 473
Songaila, A. 1998, AJ, 115, 2184
Songaila, A. 2004, AJ, 127, 2598
Spergel, D. N. 2006, The Universe at z ¿ 6, 26th meeting of the IAU, Joint Discussion 7, 17-18 August 2006, Prague, Czech Republic, JD07, #6, 7
Spergel, D. N., Verde, L., Peiris, H. V., et al. 2003, ApJS, 148, 175
Srianand, R. & Khare, P. 1996, MNRAS, 280, 767
Srianand, R., Petitjean, P., Ledoux, C., Ferland, G., & Shaw, G. 2005, MNRAS, 362, 549
Steidel, C. C., Pettini, M., & Adelberger, K. L. 2001, ApJ, 546, 665
Storrie-Lombardi, L. J., McMahon, R. G., Irwinand, M. J., & Hazard, C. 1996, ApJ, 468, 121
Storrie-Lombardi, L. J. & Wolfe, A. M. 2000, ApJ, 543, 552
Tegmark, M., Blanton, M. R., Strauss, M. A., et al. 2004, ApJ, 606, 702
Telfer, R. C., Zheng, W., Kriss, G. A., & Davidsen, A. F. 2002, ApJ, 565, 773
Tresse, L., Ilbert, O., Zucca, E., et al. 2007, A&A, 472, 403
Tytler, D. 1987, ApJ, 321, 49
Tytler, D., Kirkman, D., O'Meara, J. M., et al. 2004, ApJ, 617, 1
Viel, M., Haehnelt, M. G., Carswell, R. F., & Kim, T.-S. 2004, MNRAS, 349, L33
Warren, S. J., Hewett, P. C., & Osmer, P. S. 1994, ApJ, 421, 412
Weymann, R. J., Carswell, R. F., & Smith, M. G. 1981, ARA&A, 19, 41
Weymann, R. J., Jannuzi, B. T., Lu, L., Bahcall, J. N., et al. 1998, ApJ, 506, 1
Williger, G. M., Baldwin, J. A., Carswell, R. F., et al. 1994, ApJ, 428, 574
Wolf, C., Wisotzki, L., Borch, A., et al. 2003, A&A, 408, 499
Wolfe, A. M., Turnshek, D. A., Smith, H. E., & Cohen, R. D. 1986, ApJS, 61, 249
Wu, K., Lahav, O., & Rees, M. 1999, Nature, 397, 225
Young, P., Sargent, W. L. W., & Boksenberg, A. 1982, ApJ, 252, 10

Chapter 2

An unbiased measurement of the UV background and its evolution via the proximity effect in quasar spectra⋆

Aldo Dall'Aglio, Lutz Wisotzki, and Gábor Worseck

Astrophysikalisches Institut Potsdam, An der Sternwarte 16, D-14482 Potsdam, Germany

ABSTRACT

We investigated a set of high-resolution ($R \sim 45\,000$), high signal-to-noise ($S/N \sim 70$) quasar spectra to search for the signature of the so-called proximity effect in the H I Lyα forest. The sample consists of 40 bright quasars with redshifts in the range $2.1 < z < 4.7$. Using the flux transmission statistic, we determined the redshift evolution of the H I effective optical depth in the Lyman forest between $2 \lesssim z \lesssim 4.5$, finding good agreement with previous measurements based on smaller samples. We also see the previously reported dip in $\tau_{\rm eff}(z)$ around redshift $z \sim 3.3$, but as the significance of that feature is only 2.6σ, we consider this detection tentative. Comparing the flux transmission near each quasar with what was expected from the overall trend of $\tau_{\rm eff}(z)$, we clearly detect the proximity effect not only in the combined quasar sample, but also towards each individual line of sight at high significance, albeit with varying strength. We quantify this strength using a simple prescription based on a fiducial value for the intensity of the metagalactic UV background (UVB) radiation field at 1 Ryd, multiplied by a free parameter that varies from QSO to QSO. The observed proximity effect strength distribution (PESD) is asymmetric, with an extended tail towards values corresponding to a weak effect. We demonstrate that this is not simply an effect of gravitational clustering around quasars, as the same asymmetry is already present in the PESD predicted for purely Poissonian variance in the absorption lines. We present the results of running the same analysis on simulated quasar spectra generated by a simple Monte Carlo code. Comparing the simulated PESD with observations, we argue that the standard method of determining the UVB intensity J_{ν_0} by averaging over several lines of sight is heavily biased towards high values of J_{ν_0} because of the PESD asymmetry. Using instead the *mode* of the PESD provides an estimate of J_{ν_0} that is unbiased with respect to his effect. For our sample we get a modal value for the UVB intensity of $\log J_{\nu_0} = -21.51 \pm 0.15$ (in units of erg cm^{-2} s^{-1} Hz^{-1} sr^{-1}) for a median quasar redshift of 2.73. With J_{ν_0} fixed we then corrected $\tau_{\rm eff}$ near each quasar for local ionisation and estimated the amount of excess H I absorption attributed to gravitational clustering. On scales of ~ 3 Mpc, only a small minority of quasars show substantial overdensities of up to a factor of a few in $\tau_{\rm eff}$; these are exactly the objects with the weakest proximity effect signatures. After removing those quasars residing in overdense regions, we redetermined the UVB intensity using a hybrid approach of sample averaging and statistical correction for the PESD asymmetry bias, arriving at $\log J_{\nu_0} = -21.46^{+0.14}_{-0.21}$. This is the most accurate measurement of J_{ν_0} to date. We present a new diagnostic based on the shape and width of the PESD that strongly supports our conclusion that there is no systematic overdensity bias for the proximity effect. This additional diagnostic breaks the otherwise unavoidable degeneracy of the proximity effect between UVB and overdensity. We then applied our hybrid approach to estimate the redshift evolution of the UVB intensity and found tentative evidence of a mild decrease in $\log J_{\nu_0}$ with increasing redshift, by a factor of ~ 0.4 from $z = 2$ to $z = 4$. Our results are in excellent agreement with earlier predictions for the evolving UVB intensity, and they also agree well with other methods of estimating the UVB intensity. In particular, our measured UVB evolution is much slower than the change in quasar space densities between $z = 4$ and $z = 2$, supporting the notion of a substantial contribution of star-forming galaxies to the UVB at high redshift.

2.1. Introduction

High-resolution spectra of high-redshift, quasi-stellar objects (QSOs) show a plethora of narrow absorption lines from various species along their lines of sight through the intergalactic medium (IGM). Most absorption lines blueward of an Lyα emission line stem from the Lyα transition of intervening neutral hydrogen, giving rise to the Lyα forest (Sargent et al. 1980; Weymann et al. 1981; Rauch 1998). High-resolution spectra of the Lyα forest enabled a statistical analysis of the absorbers, as

⋆ This Chapter is published in *Astronomy & Astrophysics*, Volume 491, Issue 2, 2008, pp.465-481

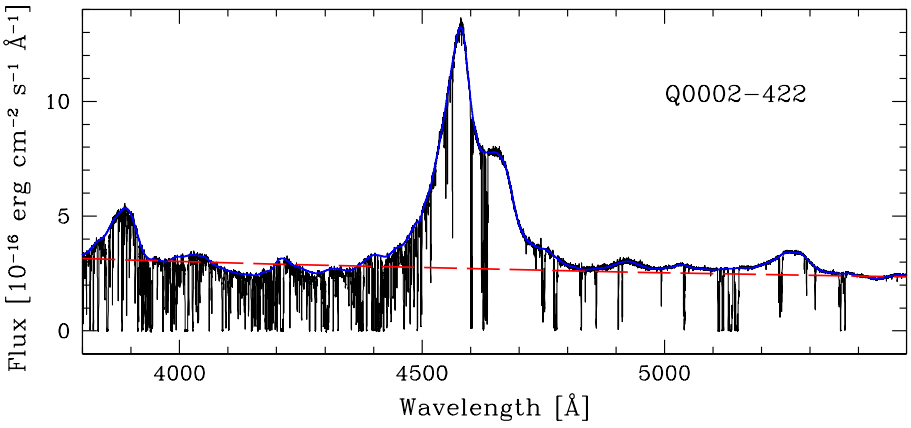

Fig. 2.1. A typical quasar spectrum from our sample (Q 0002−422 $z = 2.768$) together with the power law continuum fit (dashed red line) and the local continuum fit (blue line).

well as their physical properties (e.g. Kim et al. 2001; Schaye et al. 2003; Kim et al. 2004).

The vast majority of H I Lyα absorbers are optically thin to ionising photons and are thus kept highly photoionised by the metagalactic UV background (UVB) generated by the overall population of quasars and star-forming galaxies (Haardt & Madau 1996; Fardal et al. 1998; Haardt & Madau 2001). The UVB intensity at a given frequency is determined by the evolving population of UV sources, modified by cosmological expansion and absorption (e.g. Davé et al. 1999). It is important to determine the amplitude of the UVB and its spectral shape as a function of redshift in order to constrain the relative contributions of quasars and star-forming galaxies to the UVB, as well as to provide a key ingredient to numerical simulations of structure formation.

There are different ways to constrain the H I UVB photoionisation rate in the IGM. Assuming its spectral energy distribution it is possible to infer the UVB intensity at the Lyman limit J_{ν_0}. First, the UVB can be predicted by integrating the contributions of the observed source population. Given the luminosity functions of the sources, a characteristic intrinsic spectral energy distribution and the observed absorber distribution functions in the IGM, the amplitude and spectral shape of the UVB can be calculated numerically as the radiation is filtered by the IGM (Bechtold et al. 1987). In particular, comparing these models to observations provides constraints on the relative contributions of quasars (Haardt & Madau 1996; Fardal et al. 1998) and star-forming galaxies (Haardt & Madau 2001).

Furthermore, the H I photoionisation rate at $2 < z < 4$ has been constrained by matching the Lyα forest absorption and the IGM temperature evolution from numerical simulations of structure formation to observations (Rauch et al. 1997; Theuns et al. 1998; McDonald et al. 2000; Meiksin & White 2004; Tytler et al. 2004; Bolton et al. 2005; Kirkman et al. 2005; Jena et al. 2005).

A more direct approach to estimate the UVB photoionisation rate is based on the so-called proximity effect. In the vicinity of a luminous quasar the UV radiation field is expected to be enhanced, resulting in a statistical deficit of Lyα absorbers near the quasar compared to far away from it along the line of sight (Weymann et al. 1981; Carswell et al. 1982; Murdoch et al. 1986). Knowing the UV luminosity of the quasar, the deficit of lines (or generally Lyα opacity) yields an estimate of the UVB intensity at the H I Lyman limit (Carswell et al. 1987; Bajtlik et al. 1988). Traditionally, the proximity effect has been considered as a statistical effect and large samples of up to $\sim$ 100 quasars have been compiled to measure the mean UVB at $2 \lesssim z \lesssim 4$ (e.g. Bajtlik et al. 1988; Lu et al. 1991; Giallongo et al. 1996; Cooke et al. 1997; Scott et al. 2000; Liske & Williger 2001). Nevertheless, the proximity effect can also be detected towards individual quasars (e.g. Williger et al. 1994; Cristiani et al. 1995; Lu et al. 1996; Savaglio et al. 1997; Dall'Aglio et al. 2008).

Proximity effect analyses at different redshifts can constrain the redshift evolution of the UVB, showing that it broadly peaks at $z \sim 3$. The decrease in the UVB at $z < 2$ (Kulkarni & Fall 1993; Scott et al. 2002) and $z \gtrsim 4$ (Williger et al. 1994; Lu et al. 1996; Savaglio et al. 1997) is likely due to the declining space density of quasars (Haardt & Madau 1996; Fardal et al. 1998). Whereas the UVB evolution at low redshifts is sufficiently fast to be detectable within a single sample (Scott et al. 2002), there is presently little direct evidence of evolution within the redshift range $2 \lesssim z \lesssim 4$.

It is currently an open issue whether the measured UVB at $z \lesssim 3$ is consistent with the integrated emission of quasars, or whether a significant share of ionising photons has to be provided by star-forming galaxies (e.g. Madau et al. 1999; Sokasian et al. 2003; Schirber & Bullock 2003; Hunt et al. 2004). One difficulty lies in the fact that the UVB estimates via the proximity effect are subject to several systematic uncertainties, all of which can lead to an overestimate of the inferred UV background:

1. *Quasar variability:* The size of the proximity effect zone scales as the average quasar luminosity over the photoionisation equilibrium timescale in the IGM ($\sim 10^4$ yr). Quasar variability on shorter timescales will tend to overestimate the UVB due to Malmquist bias in the selected quasar samples (Schirber et al. 2004). It is not known how important this effect is in practice.
2. *Underestimated quasar redshifts:* Quasar emission redshifts determined from broad high-ionisation lines are likely underestimated (e.g. Gaskell 1982; Richards et al. 2002), causing the UVB to be overestimated by a factor $\sim$ 3 (Espey 1993). However, this effect can be largely avoided by using low-ionisation lines to determine systemic redshifts.

3. *Overdense environment:* In the standard ionisation model of the proximity effect (Bajtlik et al. 1988), the Lyα forest line density is extrapolated into the quasar vicinity, assuming that the matter distribution is not altered by the presence of the QSO. If quasars typically reside in high intrinsic overdensities instead, the UVB will be overestimated by a factor of up to ~ 3 (Loeb & Eisenstein 1995). Conversely, the disagreement between the UVB estimates from the proximity effect and those obtained by matching simulations to the mean Lyα forest absorption has recently been used as an argument that quasars are surrounded by substantial overdensities (Rollinde et al. 2005; Guimarães et al. 2007; Faucher-Giguere et al. 2008).

In the present Chapter we pursue a new approach to employ the proximity effect as a tool to investigate the UVB, based on measuring its signature towards individual QSO sight lines. We demonstrated recently (Dall'Aglio et al. 2008, hereafter Paper I) that indeed essentially all quasars show this signature, even at relatively low spectral resolution. Here we follow up on this finding, now based exclusively on high resolution, high S/N quasar spectra. The plan of the Chapter is as follows. We begin with a brief description of our spectroscopic data (Sect. 2.2). In Sect. 2.3 we explain the Monte Carlo simulations used to assess uncertainties and to interpret the observed proximity effect strength distribution. We then determine the redshift evolution of the effective optical depth in the Lyα forest in Sect. 2.4, followed by a comparison between the two most commonly adopted methods of revealing the proximity effect in Sect. 2.5. We very briefly report on the analysis of the combined QSO sample in Sect. 2.6. In Sect. 2.7 we investigate the proximity effect in individual sight lines, showing that the traditional sample-combining method is biased. We then estimate the excess Lyα absorption near quasars (Sect. 2.8), and use this to constrain the redshift evolution of the UVB (Sect. 2.9). We present our conclusions in Sect. 2.10.

Throughout this Chapter we assume a flat Universe with Hubble constant $H_0 = 70\,\mathrm{km\,s^{-1}\,Mpc^{-1}}$ and density parameters $(\Omega_\mathrm{m}, \Omega_\Lambda) = (0.3, 0.7)$. All distances are expressed in physical units.

2.2. Data

2.2.1. Sample description and data reduction

The sample consists of 40 quasar sight lines observed with the UV-Visual Echelle Spectrograph (UVES, Dekker et al. 2000) at VLT/UT2 on Cerro Paranal, Chile. All 40 spectra were taken from the ESO archive and are publicly available. We selected the QSO sample based on the following criteria: (i) a minimum of 10 exposures and (ii) a complete or nearly complete coverage of the Lyα forest region especially close to the quasar. Table 2.1 lists the complete sample of quasars with adopted redshifts (Sect. 2.2.4) and quasar luminosities at the Lyman limit (Sect. 2.2.3).

The data were reduced within the ECHELLE/UVES environment (version 2.2) of the software package MIDAS and following the procedures described in Kim et al. (2004). After the bias and inter-order background subtraction from each science frame, an optimal extraction of the spectrum was performed, order by order, assuming a Gaussian distribution along the spatial direction. The sky was estimated and subtracted together with the Gaussian fit, maximising the quality of the extracted spectrum (e.g. Kim et al. 2001). Cosmic rays were identified and removed using a median filter. The wavelength calibration was performed with the available ThAr lamp frames. Relative flux calibration was performed using the master-response functions publicly available on the ESO website and accounting for different airmasses. This allowed us to place our spectra onto a relative flux scale reasonably well, while the absolute scale

Table 2.1. List of analysed QSOs, ordered by redshift.

QSO	Mag	Filter	S/N	$f^{\ddagger}_{\nu_0}$	$\log L^{\star}_{\nu_0}$	$z_\mathrm{em}{}^{\dagger}$
HE 1341−1020	17.1	*B*	70	139	31.17	2.137
Q 0122−380	16.7	*B*	60	291	31.51	2.192
PKS 1448−232	17.0	*V*	70	282	31.50	2.222
PKS 0237−233	16.6	*V*	100	750	31.93	2.224
HE 0001−2340	16.7	*V*	60	403	31.68	2.278
HE 1122−1648 [a]	16.5	*V*	120	866	32.05	2.407
Q 0109−3518	16.4	*B*	70	404	31.72	2.406
HE 2217−2818	16.0	*V*	80	796	32.02	2.414
Q 0329−385	17.0	*V*	50	226	31.48	2.437 [b]
HE 1158−1843	16.9	*V*	60	268	31.56	2.459
Q 2206−1958	17.3	*V*	70	255	31.57	2.567
Q 1232+0815	18.4	*r*	50	055	30.91	2.575
HE 1347−2457	16.8	*B*	60	772	32.06	2.615
HS 1140+2711 [a]	16.7	*r*	80	581	31.94	2.628
Q 0453−423	17.1	*V*	70	168	31.41	2.664
PKS 0329−255	17.1	*V*	50	243	31.58	2.706
Q 1151+0651	18.1	*r*	50	100	31.21	2.758
Q 0002−422	17.2	*V*	60	346	31.76	2.769
Q 0913+0715	17.8	*r*	60	181	31.48	2.788
HE 0151−4326	17.2	*B*	70	499	31.92	2.787
Q 1409+095	18.6	*r*	40	067	31.06	2.843
HE 2347−4342	16.7	*V*	100	630	32.05	2.886
Q 1223+1753	18.1	*r*	40	794	31.16	2.955
Q 0216+080 [a]	18.1	*V*	40	084	31.20	2.996
HE 2243−6031	16.4	*V*	100	776	32.17	3.012
CTQ 0247	17.4	*V*	70	239	31.66	3.025
HE 0940−1050	16.4	*V*	50	691	32.13	3.089
Q 0420−388	16.9	*V*	100	426	31.93	3.120
CTQ 0460	17.5	*V*	60	281	31.76	3.141
Q 2139−4434	17.7	*V*	40	117	31.39	3.207
Q 0347−3819	17.7	*V*	60	213	31.66	3.229
PKS 2126−158	17.0	*V*	60	380	31.92	3.285 [c]
Q 1209+0919	18.6	*r*	40	120	31.42	3.291 [c]
Q 0055−2659	17.5	*V*	60	245	31.81	3.665 [c]
Q 1249−0159 [a]	18.6	*g*	60	071	31.27	3.668
Q 1621−0042	17.3	*r*	70	307	31.91	3.709
Q 1317−0507	17.7	*R*	50	084	31.35	3.719
PKS 2000−330 [a]	17.0	*V*	60	178	31.69	3.786
BR 1202−0725	17.8	*R*	100	460	32.24	4.697
Q 1451−1512	17.3	*I*	60	332	32.12	4.766

‡: Lyman limit flux in units of μJy with uncertainties around 7%.
⋆: Lyman limit luminosities in units of $\mathrm{erg\,s^{-1}\,Hz^{-1}}$ with uncertainties of the order of $\sigma_{\log L_{\nu_0}} \simeq^{+0.05}_{-0.1}$ dex.
†: Systemic redshift estimated from Si II+O I at $\lambda_\mathrm{rest} = 1305.77$Å (Morton 2003). Redshift uncertainty is $\sigma_z = 0.003$.
a: Gaps in the spectral range of the Lyα forest.
b: Redshift measured from C IV emission line and corrected according to Richards et al. (2002).
c: Redshift taken from Paper I.

had to be tied to external photometry (Sect. 2.2.2). In each final coadded spectrum the individual extractions were weighed corresponding to their S/N and re-sampled on 0.05 Å bins. The resolving power is $\sim$ 45 000 in the regions of interest, corresponding to a velocity resolution of $\sim$ 6 km s^{-1} (FWHM). The wavelengths in the final spectra are vacuum heliocentric, and the fluxes are corrected for galactic reddening. An example of a final spectrum as well as our continuum definitions (Sect. 2.2.3) is shown in Fig. 2.1.

2.2.2. Quasar magnitudes

Table 2.1 provides our adopted apparent magnitudes and Lyman limit fluxes. The photometric data were collected from various sources, in particular SDSS, Véron-Cetty & Véron (2006), Rollinde et al. (2005), Cooke et al. (1997), Ellison et al. (2005), and Paper I. Where more than one measurement was available, the data were consistent to within $\sigma_m < 0.1$ mag. Note that while knowledge of the Lyman limit luminosity is indispensable for the quantitative interpretation of the proximity effect, even perfectly simultaneous high-S/N photometry would not account for the effects of quasar variability averaged over the photoionisation time scale. By randomly changing the flux scale of some objects by up to 20% we confirmed that our conclusions concerning the proximity effect are not affected by photometric uncertainties.

2.2.3. Continuum definition

In order to search for the proximity effect, we needed to convert the quasar spectra into continuum-rectified transmission spectra. We also needed to know the quasar flux at the Lyman limit. To achieve this we determined two types of continua: (i) a global power law ($f_\nu \propto \nu^\alpha$), excluding emission and absorption regions, used to estimate the quasar flux at the Lyman limit and (ii) a more local estimate that also includes the broad emission lines as a quasi-continuum, used to compute the transmission spectrum. We constrained the Lyman limit flux via a power law continuum fit since in most cases this wavelength is either not covered by the observations or is located in the far blue range of the spectrum where the S/N significantly drops.

We developed an algorithm to automatically fit the local continuum, building on the work by Young et al. (1979) and Carswell et al. (1982). A cubic spline was interpolated on adaptive intervals along the spectrum. The fixpoints for the spline interpolation were chosen starting from a regular sampling of the spectrum with a binning that becomes finer whenever the slope of the computed continuum exceeds a given threshold. This was done in order to better reproduce the wings of emission lines.

To assess the continuum uncertainties we proceeded in the same way as described in Paper I. With the help of Monte Carlo simulations we computed the average ratio between the recovered and the input continua at different redshifts. The results are presented in Fig. 2.2. The top panel shows the mean systematic error of the fitted continuum with respect to the input continuum for five different redshifts. The bottom panel presents the intrinsic uncertainties of the continuum. Due to the high resolution and the high S/N of the spectra, the statistical error associated

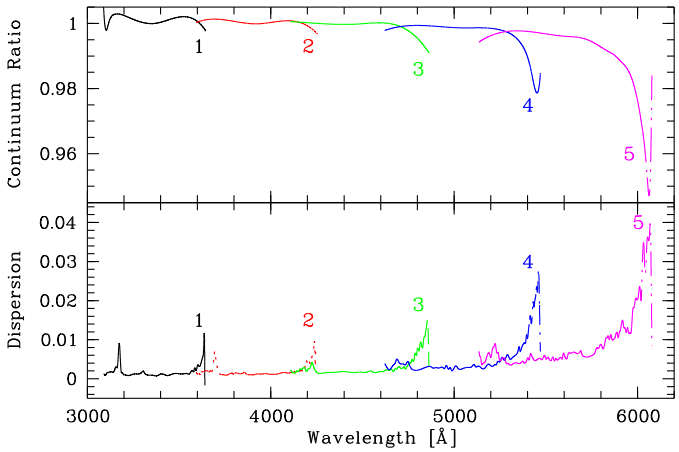

Fig. 2.2. Top panel: Average ratio between the fitted and input continuum for the five sets of 500 simulated QSOs at z = 2.0, 2.5, 3.0, 3.5, 4.0 with S/N = 70, denoted with numbers 1, 2, 3, 4 and 5 respectively. Bottom panel: Standard deviation profiles relative to the above systematic bias.

with continuum placement is limited to a few percent at most in the Lyα line wing. The automatically fitted continuum was corrected for the systematic bias and used to compute the transmission $T = F_{\rm qso}/F_{\rm cont}$.

Regarding the Lyman limit fluxes, the uncertainties are of the order of 7%, dominated by the somewhat subjective choice of the continuum wavelength ranges redward of the Lyα emission used to fit the power laws.

2.2.4. Systemic quasar redshift

The spectral range covered by the UVES observations can maximally extend from ~3 000 to ~10 000 Å. However, not all QSOs have such wide wavelength coverage. Most of them extend far enough to the red of Lyα to allow the detection of several emission lines (Si II+O I, C II, Si IV+O IV], C IV) from which a redshift can be measured. Several authors (e.g. Gaskell 1982; Tytler & Fan 1992; Richards et al. 2002) pointed out the existence of a systematic shift between high and low ionisation lines attributed to the relative motion of gas near the AGN. In order to measure a redshift as close as possible to the systemic one, we used low-ionisation lines if these were available. In almost all cases we adopted Si II+O I measurements for the final emission redshift, as listed in Table 2.1. For four objects (PKS 2126−158, Q 0329−385, Q 1209+0919 and Q 0055−2659) this was not possible due to either a non-detection of these lines or lack of wavelength coverage. For PKS 2126−158, Q 1209+0919 and Q 0055−2659 we adopted the redshifts based on Si II+O I from the low-resolution spectra in Paper I, while for Q 0329−385 we could only take the C IV based redshift and corrected it for the mean systematic shift determined by Richards et al. (2002).

2.3. Monte Carlo simulations of artificial spectra

A deeper understanding of statistical and systematic effects contributing to the proximity effect signature is made possible by

comparing observations with simulated spectra. Typically, numerical 3D simulations are successful in reproducing the properties of the Lyα forest at any redshift. However, such computations are very time consuming and their major shortcoming is the limited redshift coverage of the simulated sight lines, especially at high resolution.

We developed a straightforward Monte Carlo code to generate synthetic spectra and employed the simulations for three main purposes. First, to estimate the influence of the quasar continuum placement in the spectra (Sect. 2.2.3); then to compute the line-of-sight variations in the evolution of the optical depth in the Lyα forest (Sect. 2.4); and finally to study the influence of the fact that only a finite number of absorbers contributes to the measured optical depth (Sect. 2.5.3).

The procedure used to generate synthetic spectra is based on the assumption that the Lyα forest is well represented by three observed distributions:

1. The line number density distribution, approximated by a power law of the form $\mathrm{d}n/\mathrm{d}z \propto (1+z)^{\gamma}$ where γ will be measured in Sect. 2.4.
2. The column density distribution, given by $f(N_{\mathrm{H\,I}}) \propto N_{\mathrm{H\,I}}^{-\beta}$ where the slope is $\beta \simeq 1.5$ (Kim et al. 2001).
3. The Doppler parameter distribution, given by $\mathrm{d}n/\mathrm{d}b \propto b^{-5}\exp\left[-b_{\sigma}^{4}/b^{4}\right]$ where $b_{\sigma} \simeq 24$ km/s (Kim et al. 2001).

The simulated absorbers have column densities within the range $10^{12} < N_{\mathrm{H\,I}} < 10^{18}$ cm^{-2} and Doppler parameters between $10 < b < 100$ km/s. The slope of the column density distribution was fixed to $\beta = 1.5$.

For our purposes these approximations are sufficient to yield the accuracy we need in the following analysis. Every simulated sight line was populated with absorption features drawn from the above distributions until the computed effective optical depth was consistent with its evolution presented in Sect. 2.4. Once the simulated transmission was computed, an artificial quasar spectral energy distribution, including emission lines of varying strengths and widths, was generated via the principal components method described by Suzuki (2006) and already employed in Paper I. Gaussian noise was added to the final quasar spectrum, in order to match the S/N level of our observed objects.

2.4. Evolution of the Lyα effective optical depth

The H I effective optical depth is related to the mean transmission as $\tau_{\mathrm{eff}} \equiv -\ln\langle T\rangle \equiv -\ln\langle e^{-\tau_{\mathrm{H\,I}}}\rangle$, where $\langle\ \rangle$ indicates the average over predefined redshift intervals. Note that the effective optical depth is defined as the negative logarithm of the average pixel by pixel transmission, and not as the average value of the pixel by pixel optical depth in a given redshift interval. Its redshift evolution (Zuo 1993) is usually well represented by a power law

$$\tau_{\mathrm{eff}} = \tau_0(1+z)^{\gamma+1}. \quad (2.1)$$

We explored two methods of determining the evolution of τ_{eff} with redshift.

In the first approach each Lyα forest spectrum was divided into two redshift intervals, each covering the same redshift path length to sample the increasing opacity along single sight lines. The upper panel of Fig. 2.3 shows the results obtained using all those pixels in the Lyα forest range decontaminated from damped Lyα or Lyman limit systems (DLAs and LLSs respectively) and the proximity effect region ($\Delta v < 5000$km s^{-1} were excluded).

Table 2.2. Effective optical depth in the Lyα forest of our combined QSO sample.

$< z >$	Δz	τ_{eff}	$\sigma_{\tau_{\mathrm{eff}}}$
1.874	0.15	0.166	0.021
2.024	0.15	0.180	0.026
2.174	0.15	0.185	0.028
2.324	0.15	0.217	0.031
2.474	0.15	0.270	0.035
2.624	0.15	0.327	0.040
2.774	0.15	0.349	0.042
2.924	0.15	0.378	0.046
3.074	0.15	0.420	0.051
3.224	0.15	0.388	0.054
3.374	0.15	0.439	0.061
3.524	0.15	0.569	0.068
3.749	0.30	0.726	0.054
3.974	0.15	0.807	0.084
4.124	0.15	0.861	0.093
4.274	0.15	0.967	0.095
4.483	0.27	1.093	0.099

The second approach consists of measuring the mean τ_{eff} in the forest of all quasars intersecting a particular redshift slice ($\Delta z = 0.15$). The results are shown in Table 2.2 and in the lower panel of Fig. 2.3, yielding best-fit values of $(\log\tau_0, \gamma) = (-2.21 \pm 0.09, 2.04 \pm 0.17)$.

For both approaches the uncertainties in the effective optical depth, $\sigma_{\tau_{\mathrm{eff}}}$, quantify the amount of variance between the individual lines of sight for the considered redshift range and the continuum uncertainties.

In Figure 2.3 we present the results from the two approaches in comparison to the evolution of the Lyα optical depth as measured by Schaye et al. (2003), using a similar technique on 19 QSO spectra taken with UVES and HIRES and the fit by Kim et al. (2007) combining 18 UVES spectra. Our results agree well with both Schaye et al. (2003) and Kim et al. (2007) fits. There is less agreement at high redshift, probably due to the limited number of QSOs at $z > 3.6$, but our results are formally consistent within the errors.

Although both panels use the same data, these were combined in different ways and thus return slightly different results. It is clear from the top panel that the first method suffers from a lack of data points in the range $3.6 < z < 4$, leading us to slightly underestimate the effective optical depth at high redshift. The second approach significantly reduces the scatter caused by cosmic variance as already pointed out by Kim et al. (2002). It is also in good agreement with literature estimates. Therefore we adopt the best-fit parameters from the second method to describe the redshift dependence of the normalised effective optical depth in our quasar spectra.

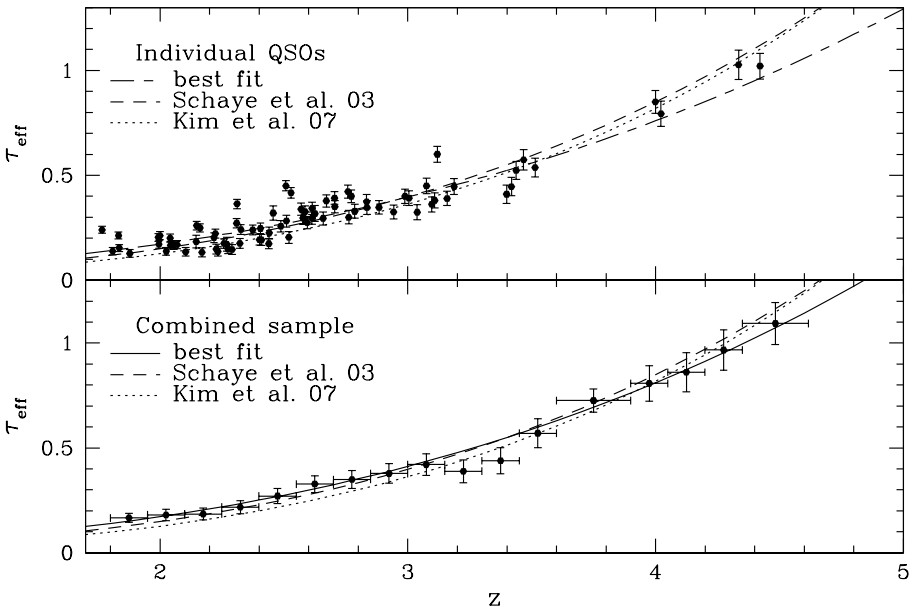

Fig. 2.3. Observed effective optical depth as a function of redshift after removal of pixels contaminated by Lyα absorption lines with damping wings, Ly limit systems and the proximity effect. Measurements from each individual quasar are shown in the upper panel, while those from the combined sample of QSOs are shown in the lower panel. The solid curve shows the power law least-squares fit to the data while the dashed curve indicates the evolution of the Lyα optical depth fitted by Schaye et al. (2003) and the dotted line that by Kim et al. (2007).

In the bottom panel of Fig. 2.3 we identify a marginally significant departure of $\tau_{\rm eff}$ from the power law evolution in the redshift range $3.2 \lesssim z \lesssim 3.4$. This feature, first discovered by Bernardi et al. (2003) using SDSS quasar spectra (but see McDonald et al. 2005), has been been interpreted to be a result of one or more of the following effects: (i) a change in the IGM temperature; (ii) a change in the free electron number density; or (iii) an enhancement in the UV background possibly connected to He II reionisation. Recently, Faucher-Giguère et al. (2008) found the same dip in $\tau_{\rm eff}(z)$ using a sample of ESI and HIRES spectra. In the light of this debate and using a completely independent data sample, we confirm the detection of this feature. We note, however, that its significance is only 2.6σ (two pixels with each 1.8σ), so the detection can be called no more than tentative.

2.5. Methods of quantifying the proximity effect

The direct signature of an enhanced ionisation field near bright quasars is a reduction of the neutral hydrogen fraction on a physical scale of several Mpc. Two principal techniques to detect it have been developed in the last two decades, which we briefly review in the following subsections.

2.5.1. Flux transmission statistics

The method used in this work to reveal the proximity effect along single lines of sight is based on the comparison between the observed effective optical depth and the expected one in the Lyα forest (Liske & Williger 2001). Approaching the quasar systemic redshift, the photoionisation rate of the source starts to dominate over the UVB. This effect leads to an enhancement in H^+ relative to H^0, reducing the opacity of absorbers close to the QSOs. This influence modifies the effective optical depth, which becomes

$$\tau_{\rm eff} = \tau_0 (1+z)^{\gamma+1} (1+\omega)^{1-\beta} \qquad (2.2)$$

(Liske & Williger 2001) where β is the slope in the column density distribution and ω is the ratio between the quasar and background photoionisation rates.

Following the assumptions outlined in Bajtlik et al. (1988) to compute ω, we get

$$\omega(z) = \frac{f_\nu(\lambda_0(1+z))}{4\pi J_{\nu_0}} \frac{1}{(1+z)} \left(\frac{d_L(z_{\rm q},0)}{d_L(z_{\rm q},z)} \right)^2 \qquad (2.3)$$

with z as the redshift along the LOS such that $z < z_{\rm q}$, $d_L(z_{\rm q},0)$ the luminosity distance of the QSO to the observer, and $d_L(z_{\rm q},z)$ as seen at any foreground redshift in the LOS.

Equation 2.3 implies that the spectral shape of the QSO and the background are approximately the same around 1 Ryd, which might not be exactly true. Assuming a quasar spectral shape $f_\nu \propto \nu^\alpha$, with $\alpha_{\rm q} \simeq -0.5$ (Vanden Berk et al. 2001) and taking a background spectral index of $\alpha_{\rm b} \simeq -1.4$ (Agafonova et al. 2005), the resulting scale of ω is shifted by ~ 0.1 dex. However, there may be an indication of a break in the spectral slope of quasars around the Lyman limit (Telfer et al. 2002). Such a break would make the quasar spectrum more similar again to that of the background, reducing the effect on ω.

We adopt the following notation: The ratio of the observed optical depth to the one expected in the Lyα forest, or the *normalised effective optical depth* ξ, is given by

$$\xi = \frac{\tau_{\rm eff}}{\tau_0 (1+z)^{\gamma+1}} = (1+\omega)^{1-\beta}. \qquad (2.4)$$

with the parameters $(\log \tau_0, \gamma)$ measured in Sect. 2.4.

The proximity effect is apparent as a decrease in the normalised optical depth below unity as $\omega \to \infty$, i.e. towards the quasar. We make use of this technique, first to detect the proximity effect on our combined sample of quasars (Sect. 2.6), then towards single lines of sight (Sect. 2.7) and finally to assess the dependence of the measured UV background on redshift and overdensities (Sect. 2.9).

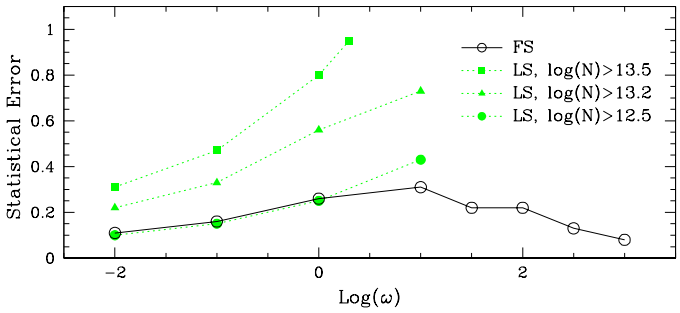

Fig. 2.4. Statistical errors associated with individual lines of sight using the line statistic (LS) and the flux statistic (FS) method. The different column density thresholds represent the completeness limits from Scott et al. (2000) and Hu et al. (1995) (solid squares and triangles, respectively). The filled circles show the level of uncertainty if the line list were complete up to the minimum column density at our resolution and S/N.

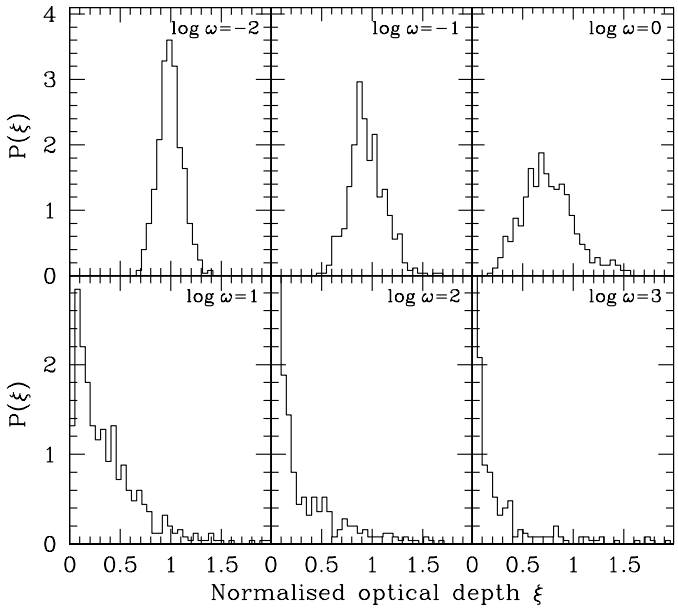

Fig. 2.5. Distribution of the normalised optical depth ξ under the influence of increasing ω values. The histograms represent the ξ distribution of 500 simulated spectra with $z_{\rm QSO} = 3$.

2.5.2. Line counting

Counting absorption lines stronger than a given threshold is historically the first technique used to measure the deficit of absorption near high redshift quasars. Typically represented by a Voigt profile, each absorption line has to be fitted and associated with a set of parameters $(N_{\rm H\,I}, z, b)$ describing its column density, redshift, and Doppler parameter, respectively. At medium resolution only the equivalent width can be measured. Several authors (e.g., Giallongo et al. 1996; Scott et al. 2000) used this approach to detect the proximity effect and to measure the UV background on combined samples of QSOs with the formalism introduced by Bajtlik et al. (1988). It is clear that at low spectral resolution, line counting is vastly inferior to the flux transmission statistic because of line blending. On the other hand, at the high resolution of UVES and similar instruments, line counting could still be a reasonable approach. We therefore conducted a performance comparison of the two techniques, following the prescription in Sect. 2.3. We simulated the Lyα forest of a quasar at redshift $z = 3$, obtaining not only the spectrum but also keeping the *complete* line list. We repeated this step to create 500 independent simulated spectra.

The principal limitation of the absorption line fitting approach is line blending, leading to incompleteness of weak lines at low column densities. Even at high resolution where lines with $\log N_{\rm H\,I} \simeq 12.5$ are detectable, the completeness is $< 25\%$ for column densities $\log N_{\rm H\,I} < 13.2$ (Hu et al. 1995). Another problem in fitting absorption lines is that there is no unique solution, and much is left to the experience and ability of the scientist/software code in finding a *good* fit. For our simulation study we employed the code AUTOVP[1] to fully automatically fit an array of absorption lines to each spectrum. The proximity effect signature is then a decrease in the number density of lines N relative to that expected for the redshift. Thus we can define an alternative quantity

$$\xi' = \frac{N}{N_0} = (1+\omega)^{1-\beta}, \qquad (2.5)$$

which again is expected to decrease from unity to zero as ω increases. We measured ξ (using the flux transmission statistic) and ξ' (from the automated line counts, adopting different column density thresholds) for all 500 simulated spectra, and computed mean and dispersion values for several bins of $\log\omega$.

Figure 2.4 presents the results of this study, showing the standard deviation of ξ or ξ', i.e. the statistical error of the measurement for a single line of sight, as a function of ω (approaching the quasar). For a realistic completeness limit in column density $\log N_{\rm H\,I} > 13$, the flux transmission approach is always more sensitive than line counting. In the unrealistic ideal case where we used the true input line lists, the two methods are equivalent at low ω, but even then the line counting approach fails in probing ξ' very close to the emission redshift of the quasar. This can easily be understood as the quasar radiation reduces the column densities by a factor $1 + \omega$; thus, close to the quasar, where $\omega \gtrsim 100$, original column densities of $\log N_{\rm H\,I} \gtrsim 15$ are needed to produce a detectable absorption line. Such absorbers are very rare, which leads to increased uncertainties.

We conclude that line counting is less sensitive to the expected proximity effect signature than the flux transmission method, even at high spectral resolution, and all our results will be based exclusively on the flux transmission technique.

2.5.3. Poissonian variance between lines of sight

At the spectral resolution in our sample, the major source of uncertainty is due to the variation in the number of absorption features along individual lines of sight. The probability of finding or not finding an absorption line at a given redshift is to first approximation a Poissonian process which can be easily modelled by our Monte Carlo simulations. While a full accounting of the expected effects of cosmic variance due to the large-scale struc-

[1] Developed by R. Davé: http://ursa.as.arizona.edu/~rad

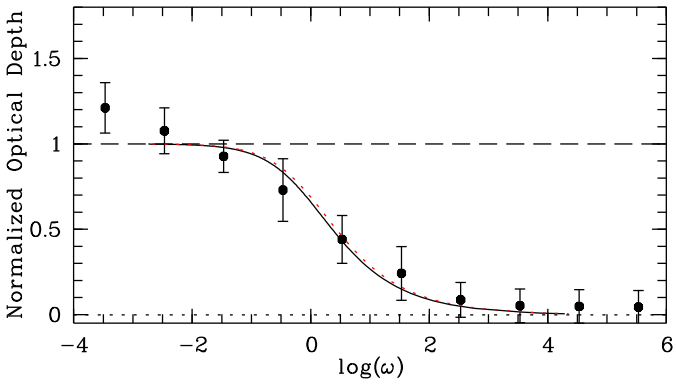

Fig. 2.6. Normalised effective optical depth versus ω for the combined sample of 40 quasars, binned in steps of $\Delta \log \omega = 1$. The curved lines are the best fit of the simple photoionisation model to the data, corresponding to a UV background of $\log(J_{\nu_0}) = -21.10$ (solid line) in units of erg cm^{-2} s^{-1} Hz^{-1} sr^{-1}, while the dotted curve denotes to the fiducial UVB ($J^\star$) for the computation of ω. The horizontal dashed line illustrates the case of no proximity effect.

ture of the IGM would require cosmological 3D simulations, it is actually useful to start with the Poissonian approximation, as it allows us to appreciate to what extent the observed level of variance is consistent with pure Poisson noise.

Equation 2.3 shows that ω depends on the redshift and luminosity of the quasar, implying that each QSO will have its own particular $\log \omega$ scale. Consequently, in a fixed $\log \omega$ interval the influence of Poisson noise will vary from line of sight to line of sight, since the corresponding redshift range in the Lyα forest is determined by the quasar emission redshift and its Lyman limit luminosity. Therefore, the distribution of the normalised optical depth ξ as a function of $\log \omega$ will depend on (i) Poisson noise, (ii) quasar redshift, and (iii) quasar luminosity.

We studied how the distribution of ξ is affected by different UV radiation fields (i.e. in different $\log \omega$ bins) at a given redshift. We computed the standard deviation σ given by

$$\sigma^2 = \int (\xi - \mu)^2 \, P(\xi) \, \mathrm{d}\xi \tag{2.6}$$

where $P(\xi)$ describes the probability density function of ξ estimated using our mock catalogue of sight lines as displayed in Fig. 2.5, and μ is its mean value. For illustration purposes, we assumed a quasar at redshift $z = 3$ and luminosity $\log L_{\nu_0} = 31.5$ with a binning of $\Delta \log \omega = 1$. Each panel displays how Poisson noise affects a different portion of the Lyα forest according to the quasar properties, i.e. for different values of ω. The final error bars in the proximity effect analysis are a composition of the following three effects, ordered by descending relative importance: (i) the standard deviation computed above, (ii) the continuum uncertainties (Sect. 2.2.3) and (iii) the intrinsic noise present in the spectrum. The Poisson noise in the placement of lines dominates the total error. Continuum uncertainties and the intrinsic noise are almost negligible.

2.6. The proximity effect in the combined sample of quasars

We first present briefly the evidence of the proximity effect in the traditional way, as a signal in the combined full sample of QSOs. The result is displayed in Fig. 2.6. As expected, the normalised effective optical depth ξ starts at unity for $\omega \ll 1$ and then goes down to zero for $\omega \gg 1$. In the definition of ω (Eq. 2.3) we had to assume a fiducial value of the UVB intensity, $J^\star = 10^{-21}$ erg cm^{-2} s^{-1} Hz^{-1} sr^{-1}. This uniquely converts the redshift scale into an ω scale. We defined a regularly spaced grid along the $\log \omega$ axis and in each bin we determined the average transmission and effective optical depth values, and using Eq. 2.4 the corresponding values of ξ. We then modelled the decrease in ξ with $\log(\omega)$ according to the formula

$$F(\omega) = \left(1 + \frac{\omega}{a}\right)^{1-\beta} \tag{2.7}$$

where a is the single free parameter which expresses the *observed* turnover of ξ and thereby provides the best-fit value of J_{ν_0}, since obviously $J_{\nu_0} = a \times J^\star$. The slope of the column density distribution was fixed to $\beta = 1.5$ (see Sect. 2.3 for details).

For the median redshift of our sample of $z = 2.73$ we thus obtain $J_{\nu_0} = (7.9 \pm 3.1) \times 10^{-22}$ erg cm^{-2} s^{-1} Hz^{-1} sr^{-1}, or in logarithmic units $\log J_{\nu_0} = -21.10^{+0.14}_{-0.22}$. This number is very close to the value of $\log J_{\nu_0} = -21.03$ reported by us in Paper I and is also consistent with several other literature estimates. A detailed comparison with the literature is hampered by the fact that the vast majority of previous UVB measurements were derived adopting the almost obsolete Einstein-de Sitter model. Typically, values for J_{ν_0} are then about a factor of 1.4 (0.15 dex) higher than in a Λ−Universe. Cooke et al. (1997) measured $\log J_{\nu_0} = -21.00^{+0.18}_{-0.15}$ on 11 high resolution quasar spectra using line statistics. Scott et al. (2000) obtained $\log J_{\nu_0} = -21.15^{+0.17}_{-0.43}$, applying the same method on more than a hundred spectra at ~ 1 Å resolution. Liske & Williger (2001) used the flux statistic on 10 QSO spectra with ~ 2 Å resolution and a S/N of ~ 40, obtaining $\log J_{\nu_0} = -21.45^{+0.30}_{-0.20}$.

While the formal errors of this measurement are small, there are reasons to believe that the proximity effect exploited this way delivers systematically too high values of J_{ν_0}. Overdense environments around quasars have been suggested as the prime reason; we shall demonstrate in the next section that in fact the averaging process inherent in the sample combination is responsible for a major bias in the UVB determination.

2.7. The proximity effect in individual lines of sight

2.7.1. The distribution of the proximity effect strengths

For our investigation of the proximity effect towards single lines of sight, the approach was essentially identical to that of the combined analysis: We computed the normalised effective optical depths for individual sight lines within a given range $\Delta \log \omega$ and checked whether ξ systematically decreases for high values of ω. For presentation purposes, the results of a subsample of 9 objects are displayed in Fig. 2.7, one panel per quasar (see Appendix B for the complete sample). The error bars are dominated by Poissonian shot noise, estimated from the simulations

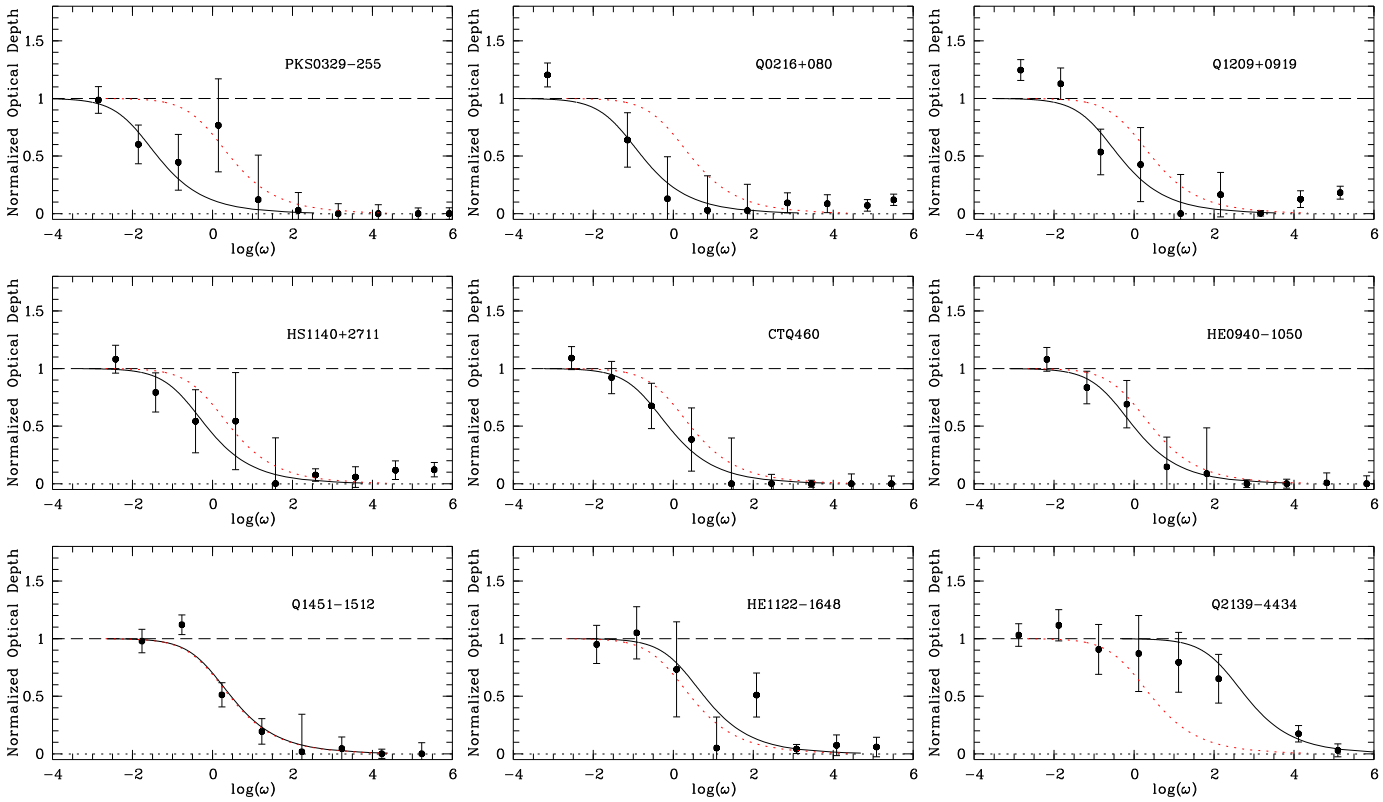

Fig. 2.7. The proximity effect signatures in individual lines of sight, for a subsample of 9 QSOs. Each panel shows the normalised effective optical depth ξ versus ω, binned in steps of $\Delta \log \omega = 1$, with the best-fit model of the combined analysis superimposed as the dotted red line (see Sect. 2.6). The solid lines delineate the best fit to each individual QSO as described in the text. This subsample was chosen for presentation purposes to show the variable strength of the proximity effect, going from *strong* (top-left panel) to *weak* (bottom-right panel).

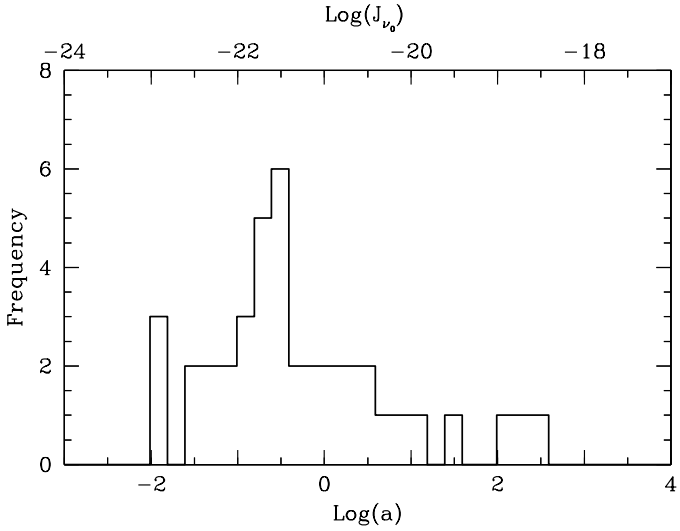

Fig. 2.8. Observed distribution of the proximity effect strength (given by $\log a$) for our sample of objects. The distribution is characterised by a prominent peak and a skewed profile which extends over several orders of magnitude in strength.

as described in Sect. 2.5.3. In each panel, $\xi(\omega)$ is shown for the fiducial reference value $J_{\nu_0} = J^\star$. Figures 2.7 and B.1 illustrate that in all cases, ξ decreases substantially as ω increases. Thus we conclude that the proximity effect is detected in all of our quasar spectra. This is in excellent agreement with our finding in Paper I, where in only 1 out of 17 low-resolution quasar spectra we failed to detect the proximity effect (and for that object, HE 2347−4342, we now detect a weak effect in the high-resolution UVES spectrum; see Appendix B).

We then applied the above fitting procedure (Eq.2.7) to each spectrum separately. The results are shown as the solid curves in Fig. 2.7, while Table 2.3 summarises the fit results. The value of the fitting parameter a, which describes the horizontal offset of the solid curve relative to the dotted one, will be regarded in the following as a measure of the strength of the proximity effect signal. It shows significant scatter between the different quasars. Note that the zeropoint of $\log a$ is arbitrary and depends only on our assumed fiducial UVB value $J^\star$. Figure 2.8 presents the measured proximity effect strength distribution (PESD), i.e. the distribution of $\log a$ for our sample.

Three major characteristics emerge:
(i) the distribution covers almost five orders of magnitude in a, ranging from a very weak proximity effect ($a \gg 1$) to a very strong one ($a \ll 1$),
(ii) it shows a well-defined peak, and
(iii) it is significantly skewed.
In the following we will investigate the effects behind these properties.

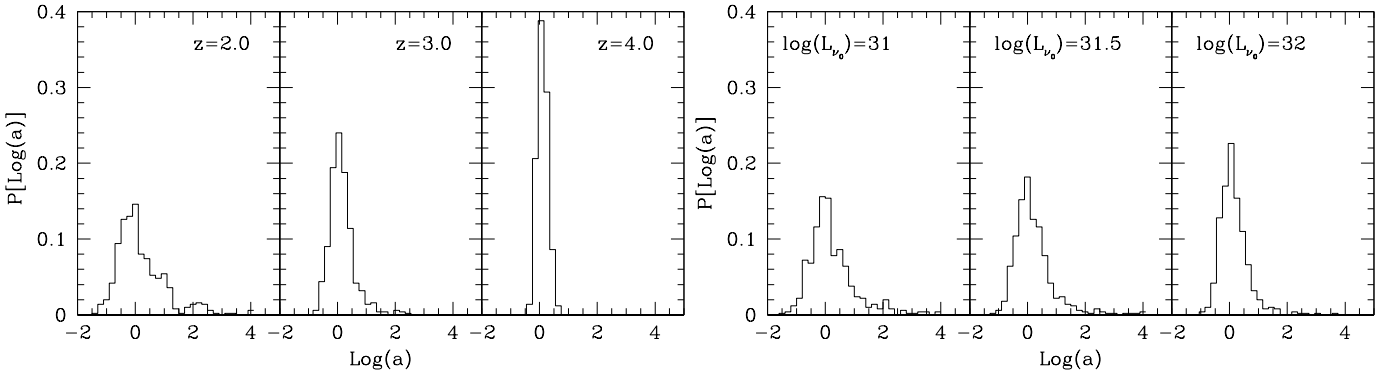

Fig. 2.9. Proximity effect strength distributions in our synthetic spectra for different quasar redshifts (left-hand panel) and luminosities (right-hand panel). The distributions are computed from 500 artificial sight lines generated by our Monte Carlo code as described in Sect. 2.3 and are affected only by Poissonian shot noise.

2.7.2. The effects of variance between sight lines

The most obvious contributor to a spread in proximity effect strengths is the variance in the absorber distribution between different lines of sight. To investigate this effect we employed our Monte Carlo simulated spectra, for which by design this variance can be accurately described as a pure Poissonian process.

The proximity effect was introduced in the synthetic spectra as a reduction in the optical depth by a factor $1 + \omega$, with ω given by Eq. 2.3. We first fixed the luminosity of the quasar to a value of $\log(L_{\nu_0}/\mathrm{erg\ s^{-1}\ Hz^{-1}}) = 31.5$ and considered three different redshifts: $z = 2.0$, 3.0, and 4.0, in order to see how the distribution of a changes with z. Then we took a constant redshift of $z = 3.0$ and considered three quasar luminosities: $\log(L_{\nu_0}/\mathrm{erg\ s^{-1}\ Hz^{-1}}) = 31$, 31.5, and 32. The UV background was fixed to $J_{\nu_0} = J^\star$ in both cases. Our results are presented in Fig. 2.9; recall that high a values imply a weak proximity effect.

Two main characteristics become apparent in Fig. 2.9: The distributions are significantly skewed, and the skewness decreases towards higher redshifts and higher luminosities. This asymmetry is a direct result of the non-linear dependence of ω on redshift as expressed in eq. 2.3. Towards the quasar redshift equal $\Delta \log \omega$ bins correspond to progressively smaller Δz intervals. Very close to the QSO, the (Poissonian) distribution of the number of absorbers per $\Delta \log \omega$ bin deviates significantly from a Gaussian. Similarly the distribution of effective optical depth becomes skewed at $z \to z_{\mathrm{em}}$, resulting in high τ_{eff} values being more likely than expected for a normal distribution. The asymmetry of the PESD directly reflects this statistical effect.

The dependence with redshift can be explained by the fact that on the one hand, Poisson noise has a weaker impact at high redshifts and on the other hand, an increasing luminosity is capable of a substantial reduction in the optical depth further away from the quasar emission, overionising even strong systems in the quasar vicinity.

Because of the asymmetric nature of the PESD at any given redshift and luminosity, one tends to overestimate the best fit values of Eq. 2.7 when combining multiple sight lines together in an averaging process. By comparing how the distribution widths evolve with redshift and luminosity, we conclude that luminosity has a weaker effect than redshift in changing the shape of the PESD.

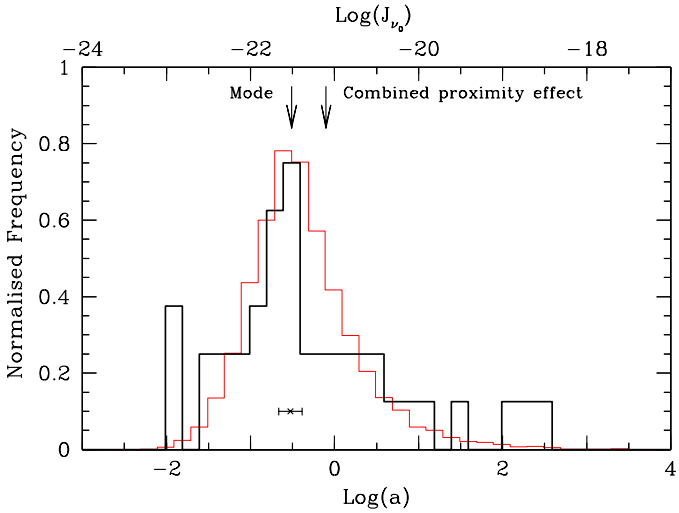

Fig. 2.10. Comparison between observed (thick) and simulated (thin) distribution of the proximity effect strength (given by $\log(a)$) for our sample of quasars. We mark the position of the mode of the observed distribution and the relative error associated to it. The error bars are computed from the dispersion of the mode in the 500 realisations of the simulated sample. We also display the value of the UVB computed in the combined analysis of the proximity effect.

A remarkable feature of Fig. 2.9 is the fact that the mode of the distribution always stays at the input value corresponding to $\log a = 0$. We exploit this property in the next section.

2.7.3. An unbiased measurement of the UV background

Unfortunately, we do not have 500 observed quasar spectra at one particular redshift or luminosity, but rather a quasar sample distributed in redshift and luminosity. We created another set of simulated spectra to predict the 'PESD as observed', assuming that only Poissonian variance contributes to the spread of $\log a$, in the following way: We constructed 40 simulated QSO spectra with the condition that their redshifts and luminosities were

Table 2.3. The proximity effect strength $\log a$ along single lines of sight.

QSO	$z_{\rm em}$	$\log L^{\dagger}_{\nu_0}$	$\log a$
Q 1232+0815	2.575	30.91	-1.89 ± 0.37
Q 0329−385	2.438	31.48	-1.86 ± 0.29
PKS 0329−255	2.706	31.58	-1.86 ± 0.25
HE 0001−2340	2.278	31.68	-1.46 ± 0.36
HE 1347−2457	2.615	32.06	-1.43 ± 0.25
Q 0216+080	2.996	31.20	-1.26 ± 0.36
HE 2217−2818	2.414	32.02	-1.21 ± 0.31
Q 0109−3518	2.406	31.72	-1.10 ± 0.38
Q 1249−0159	3.668	31.27	-1.08 ± 0.22
PKS 2126−158	3.285	31.92	-0.99 ± 0.22
Q 1209+0919	3.291	31.42	-0.85 ± 0.29
Q 0913+0715	2.788	31.48	-0.84 ± 0.34
Q 0002−422	2.769	31.76	-0.78 ± 0.32
PKS 1448−232	2.222	31.50	-0.75 ± 0.47
Q 0055−2659	3.665	31.81	-0.67 ± 0.20
HS 1140+2711	2.628	31.94	-0.63 ± 0.35
HE 2243−6031	3.012	32.17	-0.61 ± 0.24
CTQ 0460	3.141	31.76	-0.61 ± 0.27
HE 0940−1050	3.089	32.13	-0.49 ± 0.26
Q 1621−0042	3.709	31.91	-0.49 ± 0.20
Q 1151+0651	2.758	31.21	-0.45 ± 0.46
PKS 2000−330	3.786	31.69	-0.45 ± 0.23
Q 0122−380	2.192	31.51	-0.42 ± 0.44
Q 1409+095	2.843	31.06	-0.33 ± 0.54
Q 0347−3819	3.229	31.66	-0.23 ± 0.30
Q 0420−388	3.120	31.93	-0.18 ± 0.32
Q 1451−1512	4.766	32.12	-0.01 ± 0.14
Q 1317−0507	3.719	31.35	$+0.13 \pm 0.31$
Q 0453−423	2.664	31.41	$+0.18 \pm 0.45$
HE 1122−1648	2.407	32.05	$+0.30 \pm 0.33$
HE 1158−1843	2.459	31.56	$+0.35 \pm 0.38$
BR 1202−0725	4.697	32.24	$+0.51 \pm 0.14$
Q 1223+1753	2.955	31.16	$+0.58 \pm 0.36$
CTQ 0247	3.025	31.66	$+0.76 \pm 0.25$
HE 2347−4342	2.886	32.05	$+0.87 \pm 0.17$
Q 2206−1958	2.567	31.57	$+1.15 \pm 0.21$
HE 1341−1020	2.137	31.17	$+1.51 \pm 0.14$
PKS 0237−233	2.224	31.93	$+2.07 \pm 0.12$
Q 2139−4434	3.207	31.39	$+2.32 \pm 0.26$
HE 0151−4326	2.787	31.92	$+2.57 \pm 0.15$

†: Lyman limit luminosities and uncertainties $\left(\sigma_{\log L_{\nu_0}} \simeq ^{+0.05}_{-0.1}\right)$ in units of erg s^{-1} Hz^{-1}

exactly the same as the observed ones, and we constructed the PESD for this 'sample'. We repeated the process 500 times and averaged the PESD. The result is shown in Fig. 2.10 as a thin histogram, superimposed on the observed data of our quasar sample.

The predicted distribution of the proximity effect strength parameter $\log a$ looks amazingly similar to the observed one. In particular, the degree of asymmetry is very nearly the same. The observed PESD seems to show a slightly narrower core, and it certainly has some outliers on both sides, at $\log a \simeq -2$ and $\log a > 2$. We interpret this excellent agreement as an indication

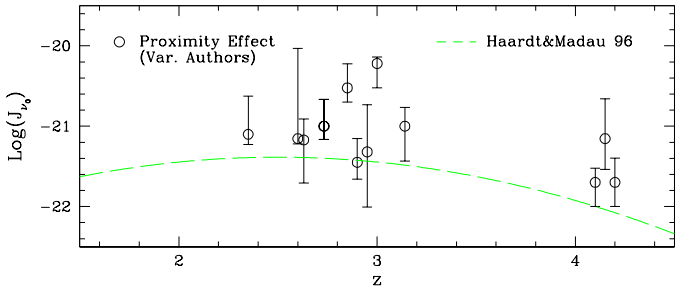

Fig. 2.11. Redshift evolution of the UVB modelled by Haardt & Madau (1996) in comparison to previous measurements of the UVB via the proximity effect (Bajtlik et al. 1988; Lu et al. 1991; Giallongo et al. 1993; Williger et al. 1994; Bechtold 1994; Fernández-Soto et al. 1995; Srianand & Khare 1996; Giallongo et al. 1996; Lu et al. 1996; Savaglio et al. 1997; Cooke et al. 1997; Scott et al. 2000; Liske & Williger 2001), all for an Einstein-de Sitter Universe.

that the statistical fluctuations of the distribution of absorption features between individual sight lines is responsible for most of the spread and in fact for most of the asymmetry in the PESD.

What does this imply for the UV background? We again find that the modal value of the 'as observed' distribution recovers the input UVB intensity, whereas the combined analysis heavily overestimates it. From the 500 realisations we derive that the mode of the PESD of 40 quasars is consistent with the value of input model to within ±0.15 dex. Similarly we can quantify the bias introduced by the combined analysis. For this purpose, we computed the best-fit $\log a$ as in Sect. 2.6 and averaged it over the 500 realisations. Typically, the averaged value of J_{ν_0} is overestimated by $\Delta \log a = 0.3$ dex, or a factor of 2.

From Fig. 2.10 we estimated the position of the mode of the observed PESD to be located at $\log a = -0.51$ and converted it into a measurement of the UVB, yielding a value of $\log J_{\nu_0} = -21.51 \pm 0.15$. The uncertainty was derived from the dispersion of the mode in the simulated PESDs. This value of the UVB is 0.4 dex lower than the best-fit of the combined proximity effect analysis given in Sect. 2.6.

For completeness we also considered what happens when one computes the average of the best-fit $\log a$ values for individual quasars (as listed in Table 2.3), instead of fitting the average ξ-ω profile. This results in a UVB value of $\log J_{\nu_0} = -21.24 \pm 0.17$, lower than the outcome of the combined proximity effect analysis as well, but still much higher than the modal value (and also systematically offset in the simulations).

We compiled several literature results in measuring the UVB by the proximity effect together with our new our results in Figs. 2.11 and 2.12. As said above, the cosmological model employed does have an effect on the UVB result. Figure 2.11 collects literature measurements that were performed for an Einstein-de Sitter model. Most of them agree poorly with the UVB model by Haardt & Madau (1996) (which was computed for the same cosmological model), in the sense that the measurements are systematically higher.

Figure 2.12 puts our new determination of J_{ν_0} into context. It is remarkable that our modal value is almost exactly on the

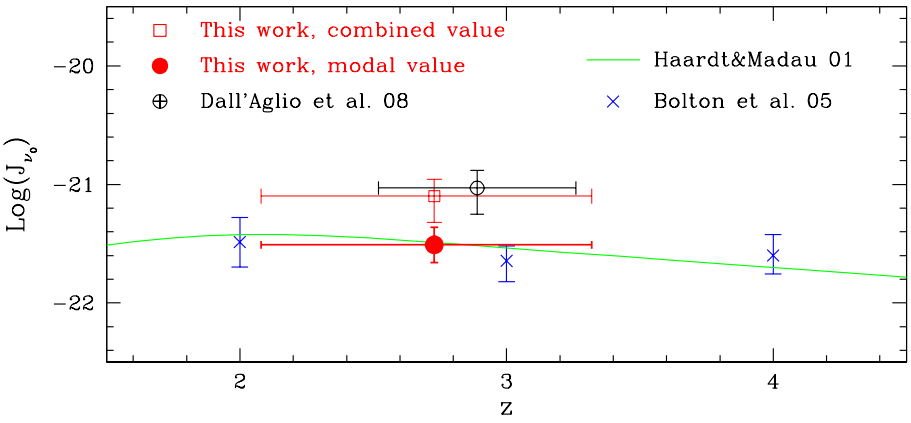

Fig. 2.12. Measured intensity of the UVB for a Λ Universe. Our best estimate is the modal value of J_{ν_0} (filled red circle); the biased 'combined value' (open square) as well as the similarly obtained value from Paper I (open circle) are shown for comparison. Also shown are the most recent evolving UVB model by Haardt & Madau (2001) (continuous green line) and the determination by Bolton et al. (2005). The horizontal bars indicate the lower and upper quartile of the quasar redshifts.

predicted curve based on the newer UVB model by Haardt & Madau (2001). Their computation was based on assuming a combined contribution of QSOs and star-forming galaxies to the UV background, now performed for a Λ Universe. It is also fully consistent with the determination of the UVB photoionisation rate by Bolton et al. (2005) obtained by matching the observed Ly forest transmission to cosmological simulations. It is equally evident that our 'combined value' is too high, as is our similarly obtained best-fit value in Paper I.

We summarise this section by stating that the distribution of proximity effect strengths as determined in individual quasar spectra is largely consistent with a purely Poissonian random process. We thus understand why the PESD is asymmetric, and why previous measurements based on averaging sample properties were bound to overestimate the UVB background. So far we have identified the modal value of the PESD as a largely unbiased estimator of the UVB. In the next section we will improve on this estimator by proposing a hybrid approach that also takes physical overdensities into account.

2.8. The role of overdensities around quasars

2.8.1. Quantifying overdensities

We have demonstrated above that much of the disagreement between proximity effect and other measurements of the UVB is due to the asymmetric shape of the PESD, even for the idealised case of purely Poissonian variance between sight lines. However, this does not imply that other effects can be neglected altogether. The most suspicious additional bias in this context is the degree of typical H^0 overdensity within a few Mpc around quasars. Obviously, if a quasar environment is overdense and thus more likely to show high column density absorption than the general Lyman forest, the proximity effect will appear to be weakened (Loeb & Eisenstein 1995).

This issue has been recently addressed by Rollinde et al. (2005) and Guimarães et al. (2007) using both observations and numerical simulations. Their basic approach consisted of a comparison of the cumulative optical depth probability distributions at difference distances to their quasars. Close to the quasars, that distribution deviates from the one for the general Lyman forest. Assuming that the UVB photoionisation rate is well constrained from the cosmic mean H^0 opacity and accounting for the expected proximity effect signature based on

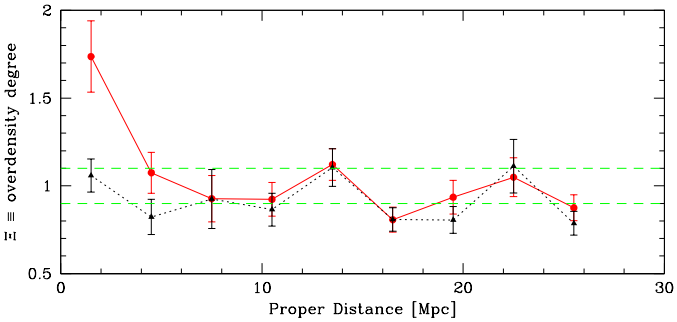

Fig. 2.13. Average overdensity degree Ξ as function of proper distance for the complete sample of quasars (solid line) and in a subsample with Ξ consistent with no sign of overdensities within 3 Mpc from the quasar (dotted line). The two horizontal lines mark the $\pm 1\sigma$ scatter expected from our simulation in the case of no overdense environment.

the known quasar luminosities, they concluded from the discrepancy between the measured and predicted distributions that quasars reside in physical overdensities of a factor of a few (averaged over $\sim 2.5h^{-1}$ proper Mpc). The amount of inferred overdensity depends, as one would expect, on the adopted value of the general UVB photoionisation rate.

Here we approach the same problem from a different angle. We also assume that the mean UVB photoionisation rate, or the mean intensity J_{ν_0}, can be measured. We adopt the modal value of the PESD estimated in Sect. 2.7.3, which we demonstrated above to be in excellent agreement with other methods of estimating the UVB. We then again consider each individual quasar in our sample in turn, aiming at measuring the *distribution* of (over)density properties. For the present work we are not interested in estimating physical overdensities, but only in identifying the quasars with strongly overdense environments. We therefore adopted a pragmatic definition of 'density' that simply involves the absorber optical depth within a certain filter length as a proxy. We computed this 'overdensity degree' Ξ in the following way:

1. We reconstructed the optical depth profile $\tau^*(z)$, *removing the radiative influence of the quasar* by multiplying the optical depth $\tau(z)$ in the Lyα forest by $1 + \omega(z)$. For the UVB intensity we used the modal value of the PESD, $\log J_{\nu_0} =$

−21.51. Despite the high S/N of our spectra, this procedure required particular attention for transmission points falling below zero and above unity due to noise and continuum uncertainties. The negative points belong to saturated lines which will become even more saturated after the inverse correction for the proximity effect; such points were left uncorrected. Pixels with transmission values $T > 1$ were also disregarded in the correction in order to prevent numerical problems or an artificially increased S/N level. Both cases apply only to a small number of pixels, and their in- or exclusion does not affect the results.

2. From the corrected $\tau^*(z)$ we computed the effective optical depth in bins along the line of sight and divided it by the expected values at the appropriate values of z (given by eq. 2.1). This procedure had to be carried out for each object separately. We define this ratio of effective optical depths as the *overdensity degree* Ξ. We performed this calculation for different bin sizes, corresponding to increments of 2, 3, 5 and 8 proper Mpc. Qualitatively, the results are the same, with a bin size of 3 Mpc showing the clearest trends. We only quote results for that bin size in the following.
3. We then merged all lines of sight, resulting in 40 estimates of Ξ per distance bin. In each bin we estimated the mean and the standard deviation of Ξ. We used our Monte Carlo simulated spectra to reproduce our QSO sample and thereby estimated the amount of variance in Ξ attributed to pure Poisson noise.

2.8.2. Overdensity distribution

The dependence of the average Ξ as a function of distance is presented in Fig. 2.13 (solid line). At large distances (> 5 Mpc), Ξ fluctuates around unity as predicted by perfect Poissonian noise. Only in the innermost bin for $\lesssim$ 3 Mpc does the mean value of Ξ increase towards an overdensity degree of a factor of 2 (in units of optical depth). So far this can be seen as supporting the notion of quasars *typically* residing in overdense regions (e.g. D'Odorico et al. 2008). However, in the same panel we also show the average Ξ if the 10 objects (25 % of the sample) with the highest individual overdensities are removed (see below for details of this deselection). For all bins beyond $\sim$ 5 Mpc, the run of Ξ with distance is statistically indistinguishable for the two samples. Only for the nearest two bins the two profiles deviate, in the sense that the dotted profile (based on 75 % of the sample) is fully consistent with no overdensities at all.

Figure 2.14 shows the individually measured 'overdensity degrees' within the innermost 3 Mpc bin as a function of quasar luminosity at the Lyman limit, quasar redshift, and proximity effect strength $\log a$ (cf. Sect. 2.7.1), respectively. This diagram reveals that the corrected effective optical depths for individual quasars range from close to zero to up to 6 times larger than in the mean Lyα forest. The horizontal dashed lines again indicate the amount of scatter ($\pm 1\sigma$) expected for pure Poissonian variance within the same physical scale around each of the QSOs.

Panel [a] shows that there is no systematic tendency of Ξ to vary with the quasar Lyman limit luminosity. The spread appears to be somewhat larger at high luminosities, which may reflect the expected trend of luminous quasars to reside in more massive environments. But there are also several high-L objects with Ξ values around unity.

Regarding the redshift dependence depicted in Panel [b] of Fig. 2.14, no significant trend can be seen here either. There may be a deficit of high overdensities for $z > 3$, but this could equally be an effect of small number statistics.

However, panel [c] of Fig. 2.14 reveals some dependence between Ξ and proximity effect strength $\log(a)$. The four QSOs with $\Xi > 3$ are among the six objects with the weakest proximity effect (highest values of $\log a$). A quantitative test using the standard linear correlation coefficient r shows that $\log \Xi$ is indeed correlated with $\log a$, $r = 0.6$ (with a probability of < 1 % of no correlation), but that this trend is strongly driven by the few points with $\Xi > 3$. Without these points, the correlation coefficient reduces to $r = 0.4$, and there is a 3 % probability of no intrinsic correlation.

2.8.3. Effects of overdensities on the proximity effect strength distribution

We now investigate how the presence of some fraction of the QSOs residing in dense environments changes the properties of the PESD. We generated a new sample of synthetic spectra at $z = 2$, 3 and 4, respectively, at a fixed luminosity of $\log(L_{\nu_0}/\mathrm{erg\ s^{-1}\ Hz^{-1}}) = 31.5$, with the difference that we now required that our sight lines show excess absorption near the emission redshift. We did not assume any particular radial distribution for the overdensity profile, but simply continued to populate the spectrum within 3 Mpc with lines until the effective optical depth reached a given threshold. We constructed two samples, for overdensities of $\Xi = 2$ and 4, respectively, to approximately mimic our observational results (500 spectra for every Ξ).

These simulations show that if all quasars had the same enhanced expectation value $\langle\Xi\rangle$, the *shape* of the PESD would not be greatly affected for all studied redshifts. The main effect would be a global shift of the PESD towards higher $\log a$ values, with the shift increasing as $\langle\Xi\rangle$ becomes larger. This is shown in the top panel of Fig. 2.15, where we plotted the PESD for three expectation values of $\langle\Xi\rangle = 1$, 2, and 4, respectively. Already for an average enhancement of $\langle\Xi\rangle = 2$, the peak of the PESD is shifted by $\sim$ 0.6 dex.

It follows that if quasar environments are systematically overdense by some uniform factor, we would be unable to tell this from our data alone: Our empirical determination of Ξ depends on assuming the correct global J_{ν_0}. If the mode of the PESD is biased by some factor, we would *underestimate* the Ξ values of the individual quasars by the same factor, effectively renormalising the *observed* Ξ scale to an expectation value of unity. Of course, this is nothing but yet another manifestation of the well-known degeneracy between the UVB and overdensities around quasars.

However, such a simple picture of all quasars having the same density enhancement factor would be highly unrealistic. If quasars reside in overdensities, the enhancement will have a distribution stretching over at least a factor of few. Because the shift of the PESD depends on $\langle\Xi\rangle$, this will lead to a broadening of the PESD by an amount depending on the physical spread

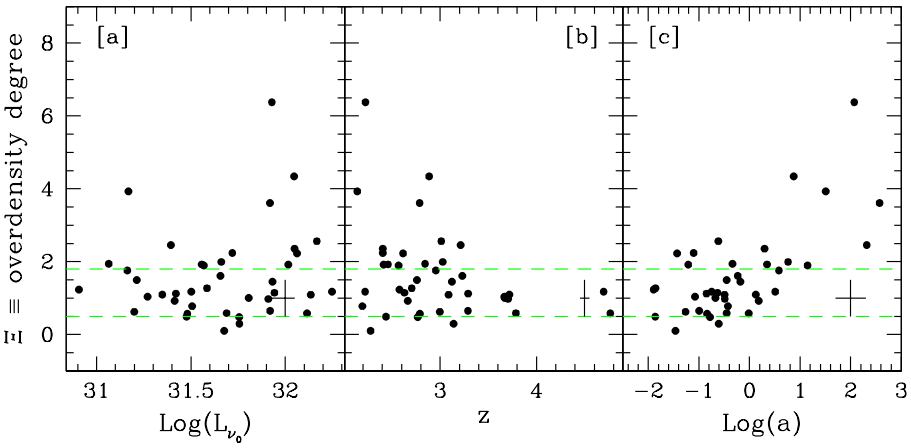

Fig. 2.14. Dependence of the overdensity degree on quasar luminosity (panel [a]), redshift (panel [b]), and on the proximity effect strength (panel [c]). The uncertainties relative to each measurements are represented by the solid cross in the respective panel. The solid line in the right-hand panels shows the least-square linear fit to the data. In each panel the dashed horizontal lines give an estimate of the amount of Poissonian shot noise in the simulations of the forest for $R_0 = 3$ Mpc from the emission redshift, as $\pm 1\sigma$ envelopes around the expected $\tau_{\rm eff}$ in the case of no overdensity ($\Xi = 1$).

of overdensities. Notice that this spread will come on top of the inevitable scatter due to Poissonian variance. As an example toy model, we show in the bottom panel of Fig. 2.15 the modified PESD for an assumed physical rms scatter in $\langle\Xi\rangle$ of 0.25 dex. The predicted distribution is considerably different; it is much broader and more box-shaped, and certainly much less in agreement with the observed PESD than the one for $\langle\Xi\rangle = 1$. While the assumption of a scatter of 0.25 dex is entirely ad-hoc, the example shows that the PESD reacts quite sensitively, and a very small physical dispersion around the expectation value of Ξ is required to make observed and predicted PESD consistent. This is naturally obtained only if the expectation value for most quasars is close to $\langle\Xi\rangle \approx 1$.

These considerations strongly support the notion that there is no strong *systematic* overdensity bias for the proximity effect. While the excellent agreement between our modal estimate and other ways of determining the UVB intensity (Fig. 2.12) is already highly suggestive, we cannot of course use this agreement both to justify our method *and* regard it as an independent measurement of the UVB. The comparison of expected and observed PESD shapes adds independent information from the distribution properties and breaks the UVB-overdensity degeneracy.

Clearly some fraction of objects sits in overdense regions. This, however, only produces a tail to the PESD by adding some high values of $\log a$. A comparison of Fig. 2.14c with Fig. 2.10 shows that the objects with strong overdensities are exactly those lying outside the prediction for the simple Poissonian model.

We note in passing that there is no reason to interpret the few quasars showing an extremely strong proximity effect as sitting in 'underdensities'. The three objects with the lowest $\log a$ values have a mean Ξ very close to unity (see Fig. 2.14c), and only one object is located outside of the $\pm 2\sigma$ envelope of Ξ expected for pure Poissonian fluctuations around the mean density.

2.8.4. A hybrid method of estimating the UV background

In the following we adopt the notion that only a relatively small fraction of at most ~ 25 % of our quasars is affected by significant overdensities. If this is true, then for a completely unbiased estimation of the UVB we need to: (i) remove the quasars with

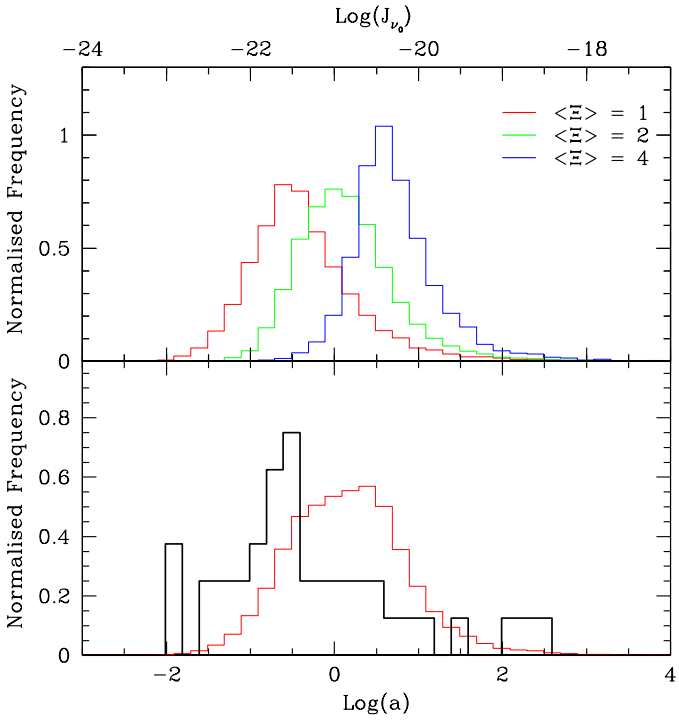

Fig. 2.15. Top panel: Expected PESD computed from Monte Carlo simulations for different expectation values of the overdensity degree ($\Xi = 1, 2, 4$, respectively). The main effect is a substantial shift towards an on average weaker proximity effect. Bottom panel: Comparison of the observed PESD and the expectation for an assumed Gaussian distribution of overdensities (see text for details).

biased environments; (ii) correct for the asymmetry bias in the proximity effect strength distribution.

In order to conduct the first step we had to identify outliers in the Ξ distribution. However, recall that Ξ is based on the assumption that we already know the UVB background. As an initial guess we adopted the modal value from the PESD, from which we then could compute Ξ for all quasars. There is no obvious cutoff, and many quasars have Ξ values that are consistent with weak overdensities. We decided to make a conservative cut in the sense that we would rather avoid too many even mildly overdense objects. We set the threshold at $+1\sigma$ (pre-

dicted scatter for Poissonian variance), implying that quasars with $\Xi > \Xi_0 = 1.8$ would be excluded from the analysis. This was the case for 10 objects, or 25 % of the sample.

We then constructed the PESD based on the remaining 30 objects. The modal value remains unchanged, but the uncertainty obviously increases (0.2 rather than 0.15 dex). The fact that the mode of the PESD is robust against the inclusion or exclusion of 25 % of the sample is certainly encouraging. It is also clear that it would not be possible to use a much smaller fraction of objects, as the uncertainties of estimating the mode would rapidly go up.

Next, we determined the systematic offset of the 'combined sample averaging' estimator (used in Sect. 2.6) due to the asymmetry of the PESD. We proceeded as follows: We generated mock quasar samples from the Monte Carlo simulated spectra, assuming no systematic overdensity bias, with the same redshift and luminosity distributions as the observed sample. We removed those objects showing apparent overdensities (occurring because of statistical noise) and determined the best-fit UVB value using the standard sample combination method as described in Sect. 2.6. Repeating this step 500 times, we averaged over the differences to the input UVB, obtaining a mean offset of $\Delta \log a = 0.27$ dex.

Finally, we conducted the same procedure for the observed sample with $\Xi < 1.8$, performing a least-squares fit of Eq. 2.7 to the data and correcting the resulting value by the above offset. The inferred value is $\log J_{\nu_0} = -21.46^{+0.14}_{-0.21}$, which we consider as the best and most robust estimate of the global UV background intensity for our sample.

In order to find out how much the method depends on the adopted criterion to eliminate outliers, we repeated the described procedure once more, but now setting the threshold at $+2\sigma$, corresponding to $\Xi_0 = 3.1$. This implies that only the four objects with the highest Ξ values were excluded from our sample. We redetermined the mean offset, which remained unchanged. The least-squares fit of Eq. 2.7 to the data, corrected for the relative offset, yields again a value of $\log J_{\nu_0} = -21.49^{+0.14}_{-0.21}$, demonstrating that our hybrid method is highly robust and quite insensitive to the outlier criterion.

Determining the UVB intensity using this hybrid method has one important advantage over the modal PESD estimator: It depends less critically on the sample size. The mode is a robust statistical quantity only if the histogram from which it is estimated is reasonably well defined. In the next section we will split the sample into subsets to investigate the redshift evolution of the UVB. It will be seen that the PESD of such subsamples can become rather broad, inhibiting any confident mode estimation. The hybrid technique, on the other hand, involves straightforward averaging and therefore also works for smaller samples.

Table 2.4 summarises all our different methods of estimating the UVB intensity and the resulting values.

Table 2.4. Summary of our UV background measurements and employed methods, for the sample median redshift $z = 2.73^{\dagger}$.

Method	$\log J_{\nu_0}$
fit to combined sample	$-21.10^{+0.14}_{-0.22}$
mode of PESD	$\mathbf{-21.51 \pm 0.15}$
mean of individual $\log a$	-21.24 ± 0.17
fit to combined subsample ($\Xi < 1.8$)	$-21.19^{+0.14}_{-0.21}$
fit to combined subsample ($\Xi < 1.8$,corrected)	$\mathbf{-21.46^{+0.14}_{-0.21}}$

†: The two boldfaced rows represent the unbiased estimates.

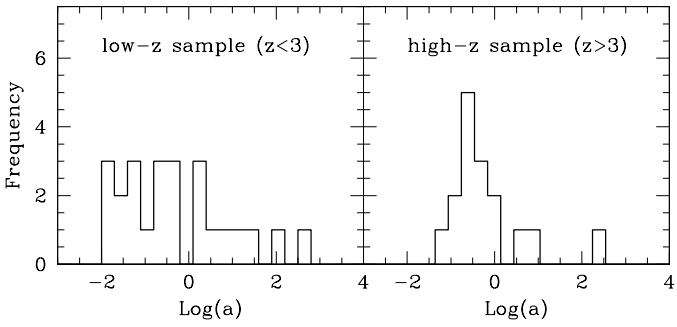

Fig. 2.16. Observed PESD for our sample of quasars divided into two redshift intervals. The shapes of the two PESDs differ substantially from each other as predicted in Sect. 2.7.2.

2.9. The redshift evolution of the UV background

The high S/N of our data and the size and redshift range of the sample prompted us to explore whether we could split the sample into subsets of different redshifts and still get meaningful constraints on the UVB.

As a first attempt we divided the sample into two subsets with $z < 3$ and $z > 3$. For each subset we constructed the PESD separately, shown in Fig. 2.16. The distributions look substantially different from each other. The PESD of the lower redshift subset is very broad, and no clear peak can be recognised. On the other hand, the high redshift PESD is significantly narrower and displays a well-defined maximum. The overall behaviour is qualitatively consistent with the predictions of Fig. 2.9 based on our Monte Carlo simulations, where we found that the widths of the PESD should decrease as redshift increases (Sect. 2.7.2). The modal value obtained from the high redshift sample is $\log J_{\nu_0} \simeq -21.6$, slightly lower than the overall best estimate. In the lower redshift subset, even a rough guess of the distribution mode is impossible.

A more powerful way of estimating the UVB intensity is the hybrid method described in the previous subsection. We now employed this method to investigate the redshift evolution of the UVB. After merging all quasar spectra in the same way as for measuring the evolution of the Lyα effective optical depth (Sect. 2.4) we sampled the Lyα forest in redshift bins of $\Delta z = 0.2$. We used only the forest in the redshift range $2 \lesssim z \lesssim 4$ in order not to be affected by small number statistics. For every bin we fitted Eq. 2.7 to the data and obtained a preliminary estimate of J_{ν_0}. These values are still systematically high, both as a result of the PESD asymmetry and because of the influence of overdense lines of sight. In particular, the redshift ranges at $z \sim 2.2$ and at $z \sim 2.9$ are heavily affected by the latter effect, as

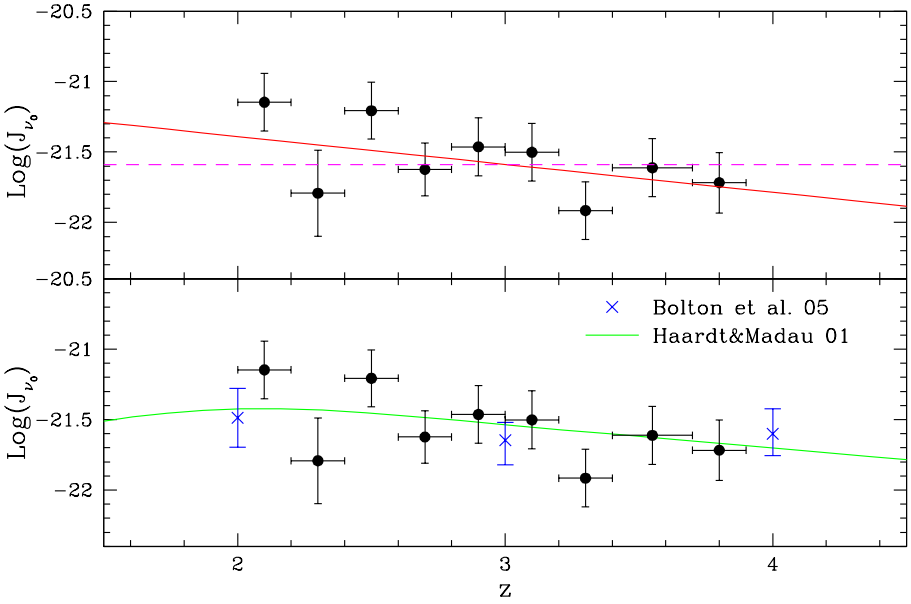

Fig. 2.17. Evolution of the mean intensity of the UV background with redshift from those quasars with overdensity degree $\Xi < 1.8$ (see text for details). We estimated the UVB using the combined analysis of the proximity effect in $\Delta z = 0.2$ intervals over the range $2 \lesssim z \lesssim 4$. *Top panel*: $\log J_{\nu_0}(z)$ in comparison to a constant evolutionary model (dashed) and a linear fit to the data (solid). *Bottom panel*: $\log J_{\nu_0}(z)$ in comparison to the model by Haardt & Madau (2001) and the more recent determination of the UVB evolution from Bolton et al. (2005). The errors in the z direction represent the range used to measure the average UVB.

Table 2.5. UV background intensity as function of redshift for the set of quasars that show overdensity degree $\Xi \leq 1.8$ as plotted in Fig. 2.17.

$< z >$	$\log J_{\nu_0}$	$\sigma_{\log J_{\nu_0}}$
2.10	-21.15	0.20
2.30	-21.89	0.20
2.50	-21.20	0.19
2.70	-21.62	0.19
2.90	-21.46	0.20
3.10	-21.50	0.20
3.30	-21.91	0.20
3.55	-21.61	0.20
3.80	-21.71	0.21

at these redshifts we find the majority of objects with a strongly overdense environment (cf. Fig. 2.14). In such narrow redshift bins, the values of the UVB are extremely sensitive to locally enhanced absorption, causing deviations of up to 1.3 dex.

We now followed the same recipe as in Sect. 2.8.4 above: We removed from the sample those objects with $\Xi > 1.8$ within the innermost 3 Mpc. We then applied the combined average estimator for each redshift interval and applied the PESD asymmetry bias determined from the simulations. We obtained in total eight values of J_{ν_0}, for eight different redshift bins as listed in Table 2.5. These result are presented as black points in Fig. 2.17, where the horizontal bars indicate the redshift interval and the vertical bars are the statistical errors.

The top panel of Fig. 2.17 shows that our measurements do suggest a certain evolution of the UVB intensity with redshift. Fitting a simple least-squares linear relation to the data points we get

$$\log J_{\nu_0}(z) = (-0.20 \pm 0.14)\, z + (-21.0 \pm 0.4)\,. \qquad (2.8)$$

This fit (depicted as the solid line in the top panel of Fig. 2.17) yields residuals fully consistent with random errors. However, the slope is not very steep, and in view of the size of the error bars it is appropriate to ask whether evolution is actually *demanded* by the data. For comparison we considered also the null hypothesis of no evolution, which is represented by the horizontal dashed line in Fig. 2.17). The quality of that model is somewhat poorer, but a KS test gives still 10 % acceptance probability, which is at best a marginal rejection. We can therefore only tentatively claim to detect the UVB evolution within this redshift interval. In a different take, we can confidently exclude a very steep redshift evolution, such as would be predicted from a UV background made predominantly of quasar light.

How do these results compare with other works aimed at estimating or predicting the UVB evolution at similar redshifts? We first consider the prediction by Haardt & Madau (2001). They constrained $J_{\nu_0}(z)$ by integrating the contributions of the observed quasar and young star-forming galaxy populations, accounting also for intergalactic absorption and re-emission. Their predicted redshift evolution of the UVB intensity is depicted as the solid green line in the lower panel of Fig. 2.17). The agreement with our data points could hardly be better; in particular, the shallow slope is almost exactly reproduced. We roughly estimate a slope of $\mathrm{d}J/\mathrm{d}z = -0.16$ for the Haardt & Madau model at $z \gtrsim 2.2$, which is extremely close to our best-fit value of -0.2. Nevertheless it should be emphasised that the galaxy contribution to the UVB crucially depends on the poorly constrained escape fraction of Lyman continuum photons from galaxies (e.g. Shapley et al. 2006; Gnedin et al. 2007).

Recently, several studies calibrated the outcome of hydrodynamical IGM simulations through the measured Lyα forest opacity to estimate the photoionisation history of intergalactic hydrogen (e.g., Bolton et al. 2005; Faucher-Giguère et al. 2008). These studies typically gave an approximately constant UVB intensity within the range $2 < z < 4$. As an example we show the results of Bolton et al. (2005) by the crosses in the lower panel of Fig. 2.17). As stated above, a no-evolution scenario as found by these studies is also consistent with the errors, and our results are also consistent with those of Bolton et al. (2005) and Faucher-Giguère et al. (2008).

At any rate, our measurements confirm the prevailing assumption that quasars alone are unable to keep the IGM at a highly ionised state at redshifts larger than three. The integrated UV emissivity of AGN has a maximum very close to $z = 2$ and drops by about an order of magnitude towards $z = 4$ (Wolf et al. 2003; Hopkins et al. 2007), whereas we find the UVB intensity to fall by only ~ 0.2 dex (2σ limit is 0.48 dex). This strengthens the notion for a non-negligible contribution by star-forming galaxies to the UV background radiation field; their fractional contribution increases when going to higher redshifts.

We can make a simple back-of-an-envelope estimate of the mixing ratio between quasars and stars by assuming that the absolute UV emissivity of star-forming galaxies is roughly constant with redshift between $z = 2$ and $z = 4$. Since the integrated quasar emissivity at $z = 4$ falls to ~ 10 % of its $z = 2$ value (Hopkins et al. 2007), and using our best-fit measurement of the overall UV background evolution (adopting a factor 0.4 between $z = 2$ and $z = 4$), we obtain that the H^0 photoionisation rate at $z = 2$ is dominated by quasars by a factor of ~ 2 over star forming galaxies. At $z = 4$, galaxies would then dominate by a factor of 5 over quasars. Any change towards making the total UVB evolution more constant with redshift would increase the fraction of starlight in the UVB.

2.10. Conclusions

We have analysed the largest sample of high-resolution quasar spectra presented in a single study to date. We demonstrated that the line-of-sight proximity effect is a universal phenomenon that can be found in the spectrum of essentially every individual high-redshift quasar. While in Paper I we arrived at the same conclusion using low-resolution spectra, we now can significantly reinforce this claim. In particular, continuum placing uncertainties, which were a bit of an issue in Paper I, play absolutely no role now, given the high spectral resolution and high S/N data exploited in this Chapter.

Our study rehabilitates the proximity effect as a tool to investigate the intensity at 1 Ryd (more accurately: the H^0 photoionisation rate) of the cosmic ultraviolet background. Previous investigations using the proximity effect nearly always produced UVB estimates that were suspiciously high and indeed at variance with other means to estimate or predict the UVB. It has been suggested in the literature that quasars typically reside in denser than average large-scale environments, and that therefore excess absorption biases the proximity effect to appear too weak, resulting in an overestimated UVB. We argue that this is not the main reason for the discrepancies between the proximity effect and other methods.

The actually measured strength of the proximity effect in a single quasar line of sight depends on the UVB, but also on the number of absorption lines present in the 'proximity effect zone'. That number is generally small, and to first approximation the presence or absence of a line at a given redshift can be described as a Poissonian random process. We have demonstrated that the distribution of the resulting 'proximity effect strength' parameter (which directly relates to the UVB) is significantly skewed, even without invoking any physical overdensities. Any direct averaging over a sample of sight lines will inevitably bias the resulting UVB. Only by looking at individual lines of sight separately can this effect be detected and removed.

We proposed and used two different methods of estimating the UVB intensity in the presence of this bias. In the first method, the UVB is taken directly from the mode of the proximity effect strength distribution (PESD). This method is simple and robust against a small number of outliers; on the other hand it is limited to large samples and depends on the condition that the mode is not affected by the outliers. Our second method involves Monte Carlo simulations to calibrate the asymmetry bias of the PESD and then uses straightforward sample averaging, possibly combined with a prior rejection of outliers, and the result is then corrected for the bias. This 'hybrid' method is quite stable and works also for smaller samples; it is, however, more complicated to use and depends on a successful removal of outliers.

Our best estimates of the UVB intensity using these two methods give very similar results. The modal estimate is $\log J_{\nu_0} = -21.51 \pm 0.15$, and the hybrid estimator gives $\log J_{\nu_0} = -21.46^{+0.14}_{-0.21}$, which is statistically indistinguishable. This value is in excellent agreement with other methods to estimate or predict the UVB.

If the UV background is known, the data used for the proximity effect can also be employed to reconstruct the absorption pattern without the radiative influence of the quasar. Doing this for our sample of 40 quasars we found that only 10 % of them showed very significant excess absorption (by more than a factor of ~ 3) while most are distributed in a way more or less consistent with Poissonian fluctuations around the cosmic mean absorption expected at these redshifts. Given the widespread notion of quasars residing in massive galaxies, which in turn should sit in massive haloes with significantly clustered environments, this sounds surprising. We have no intention of questioning that picture, and we stress that our measurements constrain exclusively the neutral hydrogen distribution averaged on scales of ~ 3 proper Mpc towards the quasar.

Nevertheless, our results may bear some relevance to the question of what are the typical halo masses for quasars. Most of the QSOs in our sample are optically selected and therefore presumably radio-quiet, which could mean that their haloes are not exceptionally massive. In a recent paper, Mandelbaum et al. (2008) estimated halo masses of AGN in the Sloan survey from clustering and galaxy-galaxy lensing, finding that optically selected AGN follow the same relation between stellar and halo mass as normal galaxies, whereas radio-loud AGN have much higher halo masses. (Incidentally, the outstanding object in our sample in terms of overdensity is the radio quasar PKS 0237−233; but the next-ranked objects are all optically selected.)

Our argument against significant overdensities of quasars and in favour of the applicability of the proximity effect to measure the UV background gains weight by the excellent agreement between our estimates of the UVB intensity and those obtained by completely different methods. This notion is supported independently by considering the *shape* of the PESD. The observed distribution width clearly favours average densities close to unity; if significant overdensities were involved, a much broader distribution would be expected than the one

observed. This additional constraint breaks the degeneracy between UV background and overdensities that has haunted the field for so long.

Finally, we also attempted to constrain the redshift evolution of the UVB intensity. Although the results are still quite uncertain, we could for the first time from a single quasar sample derive useful limits on the amount of evolution. We can rule out at high significance that quasar light dominates the UVB at redshifts $z \gtrsim 4$. Our best fit suggests a mild decrease in the UVB intensity towards higher redshifts, and the derived slope is in astonishingly good agreement with the predictions by Haardt & Madau (2001). Nevertheless, an approximately constant UVB as found by Bolton et al. (2005) and others is also formally consistent with our data.

We have shown that the proximity effect holds the potential to derive important cosmological quantities. While our sample is large in comparison to those of previous studies using high-resolution spectra, it still suffers in several aspects from small number statistics. As the public archives are growing, substantial progress can be expected from applying the proximity effect analysis to further spectra, in particular at higher redshift.

Acknowledgements. We would like to thank ESO for making the ESO data archive publicly available. We also thank Tae−Sun Kim for assisting us in the data reduction process. A.D. and G.W. were partly supported by a HWP grant from the International Helmholtz Institute for Supercomputational Physics. We finally acknowledge support by the Deutsche Forschungsgemeinschaft under Wi 1369/21-1.

References

Agafonova, I. I., Centurión, M., Levshakov, S. A., & Molaro, P. 2005, A&A, 441, 9
Bajtlik, S., Duncan, R. C., & Ostriker, J. P. 1988, ApJ, 327, 570
Bechtold, J. 1994, ApJS, 91, 1
Bechtold, J., Weymann, R. J., Lin, Z., & Malkan, M. A. 1987, ApJ, 315, 180
Bernardi, M., Sheth, R. K., SubbaRao, M., et al. 2003, AJ, 125, 32
Bolton, J. S., Haehnelt, M. G., Viel, M., & Springel, V. 2005, MNRAS, 357, 1178
Carswell, R. F., Webb, J. K., Baldwin, J. A., & Atwood, B. 1987, ApJ, 319, 709
Carswell, R. F., Whelan, J. A. J., Smith, M. G., Boksenberg, A., & Tytler, D. 1982, MNRAS, 198, 91
Cooke, A. J., Espey, B., & Carswell, R. F. 1997, MNRAS, 284, 552
Cristiani, S., D'Odorico, S., Fontana, A., Giallongo, E., & Savaglio, S. 1995, MNRAS, 273, 1016
Dall'Aglio, A., Wisotzki, L., & Worseck, G. 2008, A&A, 480, 359
Davé, R., Hernquist, L., Katz, N., & Weinberg, D. H. 1999, ApJ, 511, 521
Dekker, H., D'Odorico, S., Kaufer, A., Delabre, B., & Kotzlowski, H. 2000, in Presented at the Society of Photo-Optical Instrumentation Engineers (SPIE) Conference, Vol. 4008, Proc. SPIE Vol. 4008, p. 534-545, Optical and IR Telescope Instrumentation and Detectors, Masanori Iye; Alan F. Moorwood; Eds., ed. M. Iye & A. F. Moorwood, 534–545
D'Odorico, V., Bruscoli, M., Saitta, F., et al. 2008, MNRAS, 389, 1727
Ellison, S. L., Hall, P. B., & Lira, P. 2005, AJ, 130, 1345
Espey, B. R. 1993, ApJ, 411, L59
Fardal, M. A., Giroux, M. L., & Shull, J. M. 1998, AJ, 115, 2206
Faucher-Giguère, C.-A., Lidz, A., Hernquist, L., & Zaldarriaga, M. 2008, ApJ, 682, L9
Faucher-Giguere, C.-A., Lidz, A., Zaldarriaga, M., & Hernquist, L. 2008, ApJ, 673, 39
Faucher-Giguère, C.-A., Prochaska, J. X., Lidz, A., Hernquist, L., & Zaldarriaga, M. 2008, ApJ, 681, 831
Fernández-Soto, A., Barcons, X., Carballo, R., & Webb, J. K. 1995, MNRAS, 277, 235
Gaskell, C. M. 1982, ApJ, 263, 79
Giallongo, E., Christiani, S., D'Odorico, S., Fontana, A., & Savaglio, S. 1996, ApJ, 466, 46
Giallongo, E., Christiani, S., Fontana, A., & Trèvese, D. 1993, ApJ, 416, 137
Gnedin, N. Y., Kravtsov, A. V., & Chen, H.-W. 2007, ArXiv e-prints, 707
Guimarães, R., Petitjean, P., Rollinde, E., et al. 2007, MNRAS, 377, 657
Haardt, F. & Madau, P. 1996, ApJ, 461, 20
Haardt, F. & Madau, P. 2001, in Clusters of Galaxies and the High Redshift Universe Observed in X-rays, ed. D. M. Neumann & J. T. V. Tran
Hopkins, P. F., Richards, G. T., & Hernquist, L. 2007, ApJ, 654, 731
Hu, E. M., Kim, T.-S., Cowie, L. L., Songaila, A., & Rauch, M. 1995, AJ, 110, 1526
Hunt, M. P., Steidel, C. C., Adelberger, K. L., & Shapley, A. E. 2004, ApJ, 605, 625
Jena, T., Norman, M. L., Tytler, D., et al. 2005, MNRAS, 361, 70
Kim, T.-S., Bolton, J. S., Viel, M., Haehnelt, M. G., & Carswell, R. F. 2007, MNRAS, 382, 1657
Kim, T.-S., Carswell, R. F., Cristiani, S., D'Odorico, S., & Giallongo, E. 2002, MNRAS, 335, 555
Kim, T.-S., Cristiani, S., & D'Odorico, S. 2001, A&A, 373, 757
Kim, T.-S., Viel, M., Haehnelt, M. G., Carswell, R. F., & Cristiani, S. 2004, MNRAS, 347, 355
Kirkman, D., Tytler, D., Suzuki, N., et al. 2005, MNRAS, 360, 1373
Kulkarni, V. P. & Fall, S. M. 1993, ApJ, 413, L63
Liske, J. & Williger, G. M. 2001, MNRAS, 328, 653
Loeb, A. & Eisenstein, D. J. 1995, ApJ, 448, 17
Lu, L., Sargent, W. L. W., Womble, D. S., & Takada-Hidai, M. 1996, ApJ, 472, 509
Lu, L., Wolfe, A. M., & Turnshek, D. A. 1991, ApJ, 367, 19
Madau, P., Haardt, F., & Rees, M. J. 1999, ApJ, 514, 648
Mandelbaum, R., Li, C., Kauffmann, G., & White, S. D. M. 2008, ArXiv e-prints:astro-ph/0806.4089
McDonald, P., Miralda-Escudé, J., Rauch, M., et al. 2000, ApJ, 543, 1
McDonald, P., Seljak, U., Cen, R., et al. 2005, ApJ, 635, 761
Meiksin, A. & White, M. 2004, MNRAS, 350, 1107
Morton, D. C. 2003, ApJS, 149, 205
Murdoch, H. S., Hunstead, R. W., Pettini, M., & Blades, J. C. 1986, ApJ, 309, 19
Rauch, M. 1998, ARA&A, 36, 267
Rauch, M., Miralda-Escude, J., Sargent, W. L. W., et al. 1997, ApJ, 489, 7
Richards, G. T., Vanden Berk, D. E., Reichard, T. A., et al. 2002, AJ, 124, 1
Rollinde, E., Srianand, R., Theuns, T., Petitjean, P., & Chand, H. 2005, MNRAS, 361, 1015
Sargent, W. L. W., Young, P. J., Boksenberg, A., & Tytler, D. 1980, ApJS, 42, 41
Savaglio, S., Christiani, S., D'Odorico, S., et al. 1997, A&A, 318, 347
Schaye, J., Aguirre, A., Kim, T.-S., et al. 2003, ApJ, 596, 768
Schirber, M. & Bullock, J. S. 2003, ApJ, 584, 110
Schirber, M., Miralda-Escudé, J., & McDonald, P. 2004, ApJ, 610, 105
Scott, J., Bechtold, J., Dobrzycki, A., & Kulkarni, V. P. 2000, ApJ, 130, 67
Scott, J., Bechtold, J., Morita, M., Dobrzycki, A., & Kulkarni, V. P. 2002, ApJ, 571, 665
Shapley, A. E., Steidel, C. C., Pettini, M., Adelberger, K. L., & Erb, D. K. 2006, ApJ, 651, 688
Sokasian, A., Abel, T., & Hernquist, L. 2003, MNRAS, 340, 473
Srianand, R. & Khare, P. 1996, MNRAS, 280, 767
Suzuki, N. 2006, ApJS, 163, 110
Telfer, R. C., Zheng, W., Kriss, G. A., & Davidsen, A. F. 2002, ApJ, 565, 773
Theuns, T., Leonard, A., Efstathiou, G., Pearce, F. R., & Thomas, P. A. 1998, MNRAS, 301, 478
Tytler, D. & Fan, X.-M. 1992, ApJS, 79, 1
Tytler, D., Kirkman, D., O'Meara, J. M., et al. 2004, ApJ, 617, 1
Vanden Berk, D. E., Richards, G. T., Bauer, A., et al. 2001, AJ, 122, 549
Véron-Cetty, M.-P. & Véron, P. 2006, A&A, 455, 773
Weymann, R. J., Carswell, R. F., & Smith, M. G. 1981, ARA&A, 19, 41
Williger, G. M., Baldwin, J. A., Carswell, R. F., et al. 1994, ApJ, 428, 574
Wolf, C., Wisotzki, L., Borch, A., et al. 2003, A&A, 408, 499
Young, P. J., Sargent, W. L. W., Boksenberg, A., Carswell, R. F., & Whelan, J. A. J. 1979, ApJ, 229, 891
Zuo, L. 1993, A&A, 278, 343

Chapter 3

The UV background photoionisation rate at $2.3 \leq z \leq 4.6$ as measured from the Sloan Digital Sky Survey⋆

Aldo Dall'Aglio[1], Lutz Wisotzki[1], and Gábor Worseck[2]

[1] Astrophysikalisches Institut Potsdam, An der Sternwarte 16, D-14482 Potsdam, Germany
[2] UCO/Lick Observatory; University of California, Santa Cruz, Santa Cruz, CA 95064

ABSTRACT

We present the results from the largest investigation to date of the proximity effect in the H I Lyα forest, using the fifth Sloan Digital Sky Survey (SDSS) data release. The sample consists of 1733 quasars at redshifts $z \gtrsim 2.3$ showing a signal-to-noise of at least $S/N = 10$. We adopted the flux transmission statistic to infer the evolution of the H I effective optical depth in the Lyman forest between $2 \lesssim z \lesssim 4.5$, finding very good agreement with measurements from high-resolution quasar samples. By fitting a quasar continuum to each individual object we estimated a *continuum* composite spectrum in the rest frame wavelength range $1000 \lesssim \lambda \lesssim 3000$ Å. The flux in our composite spectrum closely follows a power law in the form $f_\nu \propto \nu^{\alpha_\nu}$ with $\alpha_\nu = -0.57$ in good agreement with similar estimates inferred from significantly smaller SDSS quasar samples. We compared the average opacity close to the quasar emission with its expected behaviour in the Lyα forest and estimated the signature of the proximity effect towards individual objects at high significance in about 98% of the quasars. Dividing the whole sample of objects in eight subsets according to their emission redshift, we quantify the strength of the proximity effect adopting a fiducial value of the cosmic UV background photoionisation rate, multiplied by a free parameter allowed to vary for different quasars. We inferred the proximity effect strength distribution (PESD) on each of the subsets finding in all cases a prominent peak and an extending tail towards values associated to a weak effect. We provide for the first time observational evidence for an evolution in the asymmetry of the PESD with redshift. Adopting the modal values of the PESDs as our best and unbiased estimates of the UV background photoionisation rate ($\Gamma_{\rm H\,I}$), we determine the evolution of $\Gamma_{\rm H\,I}$ within the redshift range $2.3 \leq z \leq 4.6$. Our measurements of UV background photoionisation rate do not show any significant decline towards high redshift as expected by theoretical model predictions. We employ these estimates and decompose the observed photoionisation rate into two major contributors: quasar and star-forming galaxies. By modelling the quasar contribution with different luminosity functions we estimated their contribution to the cosmic $\Gamma_{\rm H\,I}$, allowing us to put a constraint on the remaining amount of ionising photons necessary to obtain the observed photoionisation rate. We conclude that independently of the assumed luminosity function, stars are dominating the UV background $\Gamma_{\rm H\,I}$ at redshift $z > 3$.

3.1. Introduction

The intergalactic medium (IGM) is permeated by a quasi-continuous, spatially fluctuating density field, whose major constituents are hydrogen and helium. The distribution of these baryons gives rise to a multitude of narrow absorption features observed in the spectra of high redshift sources such as luminous quasars (QSOs), commonly known as the Lyα forest (Rauch 1998; Meiksin 2007). In the framework of hierarchical structure formation the IGM fills the low density regions between collapsed objects and it shows an extremely high ionisation state. The lack of Lyα absorption troughs indicates an inhomogeneous distribution of hydrogen and a high ionisation state of the IGM (Gunn & Peterson 1965), probed so far out to $z \sim 6$ (Fan et al. 2002). The cosmic UV background (UVB) maintaining this high ionisation state is generated by the overall population of quasars and star-forming galaxies (Haardt & Madau 1996; Fardal et al. 1998; Haardt & Madau 2001). The radiation emitted by the UV sources is filtered by the IGM and diluted by cosmological expansion, leading to a redshift and frequency dependence of the UVB intensity (e.g. Davé et al. 1999; Madau et al. 1999; Schirber & Bullock 2003).

Three methods are commonly employed to estimate the UVB intensity or the UVB hydrogen photoionisation rate at different epochs. In the first approach, the overall luminosity density is predicted from a given UV source luminosity func-

⋆ A version of this Chapter will be submitted to the *Astrophysical Journal*.

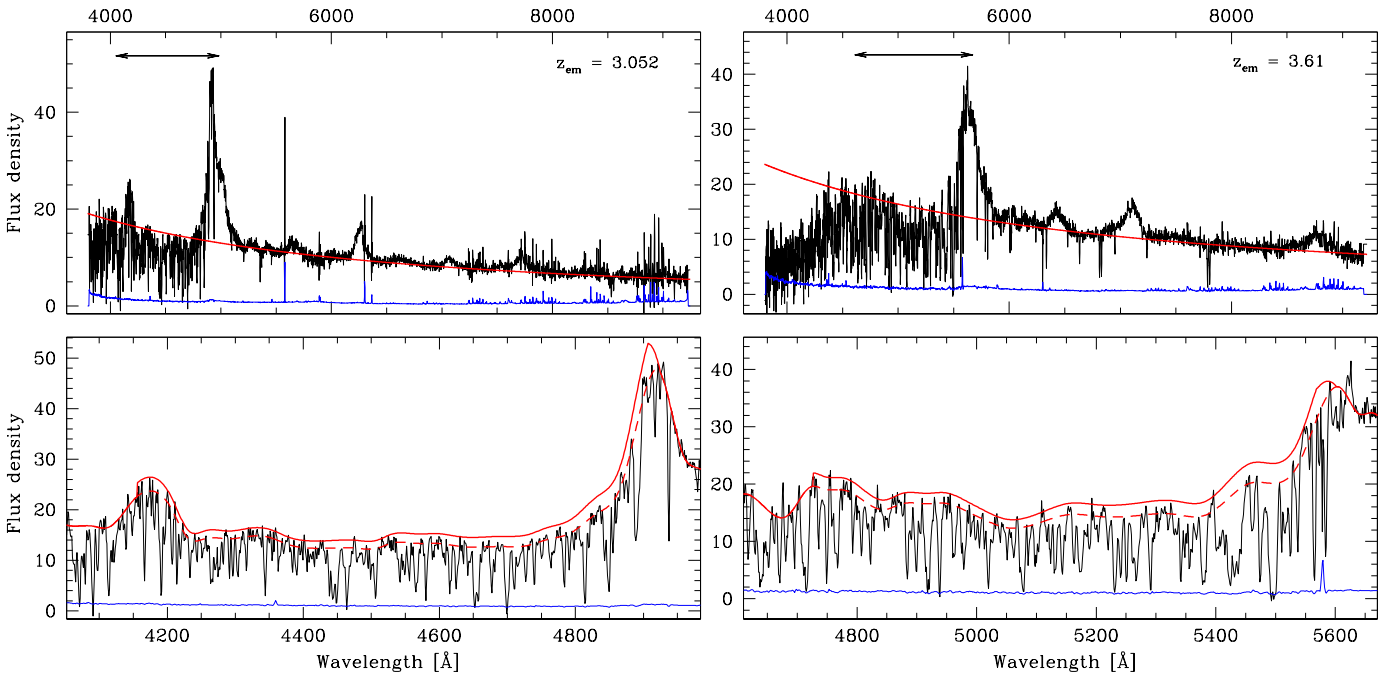

Fig. 3.1. Two examples of quasar spectra taken from the data set with $S/N \simeq 18$ (right-hand panels) and $S/N \simeq 10$ (left-hand panels). In the two upper panels the spectra are plotted along with the noise arrays and the power law fit continua. The horizontal arrows over the Lyα forest identify the wavelength range covered in the magnified lower panels where details about the local continua are presented. In all cases the flux density is expressed in units of 10^{-17} erg s^{-1} cm^{-2} Å^{-1}. The dashed lines indicate the fitted continua while the solid lines show the corrected shape as discussed in detail in Sect. 3.2.2.

tion, taking into account absorption and re-emission by the IGM (Madau et al. 1999; Haardt & Madau 2001; Schirber & Bullock 2003). While these computations rely on challenging observations such as the galaxy luminosity function at $z > 3$, they provide separate estimates on the relative contributions of quasars and star-forming galaxies to the UVB.

Secondly, the hydrogen photoionisation rate can be inferred by matching the level of Lyα forest absorption obtained in numerical simulations to observations (Rauch et al. 1997; Theuns et al. 1998; Bolton et al. 2005; Faucher-Giguère et al. 2008a). Although the physics of the IGM is well modelled in recent numerical simulations, the primary uncertainty in determining the UVB via this method is its degeneracy with respect to the observationally poorly constrained thermal state of the IGM.

The arguably most direct observational technique to infer the UVB photoionisation rate relies on the proximity effect of quasars. While fluctuations in the amplitude of the UVB in the general IGM are small (e.g. Meiksin & White 2004), the UV radiation field near luminous quasars is expected to be enhanced. The quasar is capable of over-ionising the gas in its vicinity, resulting in a systematic weakening if the Lyman alpha absorption within several Mpc from the quasar (Weymann et al. 1981; Carswell et al. 1982; Murdoch et al. 1986). The amplitude of this deficit depends on the relative contributions of ionising photons from the local source and the UVB. Knowing the QSO luminosity, the UV background photoionisation rate can be estimated (Carswell et al. 1987; Bajtlik et al. 1988).

Most previous analyses showed a large scatter in the inferred UVB level (e.g. Giallongo et al. 1996; Cooke et al. 1997; Scott et al. 2000; Liske & Williger 2001), owing to the relatively small sample sizes investigated. Although the proximity effect is detectable in individual QSO spectra (e.g. Williger et al. 1994; Cristiani et al. 1995; Lu et al. 1996; Savaglio et al. 1997; Dall'Aglio et al. 2008), the finite number of absorbers in each line of sight gives rise to a substantial random scatter that can only be compensated with sufficiently large samples (Chapter 2).

One of the key questions regarding the UV background is its evolution towards high redshift. Observations of the proximity effect of a few individual QSOs suggest a mild decline towards $z \gtrsim 4$ (Williger et al. 1994; Lu et al. 1996; Savaglio et al. 1997), in broad agreement with predictions from UVB synthesis (Haardt & Madau 2001). A similar result was obtained by us recently in an investigation of several high-resolution, high S/N quasar spectra (Chapter 2). On the other hand, two recent studies constraining the UVB from matching simulations to the observed Ly forest opacity gave a hydrogen photoionisation rate nearly constant within $2 \lesssim z \lesssim 4$, albeit on rather different levels (Bolton et al. 2005; Faucher-Giguère et al. 2008a). It is thus clear that the uncertainties are still substantial.

In the present study we build on our results obtained in Chapter 2 where we demonstrated the possibility to use the *distribution* of proximity effect strengths measured in individual quasar spectra for constraining the UV background. Our new sample of nearly 2000 QSOs from the Sloan Digital Sky Survey is by far the largest dataset ever submitted to an analysis of the proximity effect, including a significant number of QSOs at redshifts $z \gtrsim 4$.

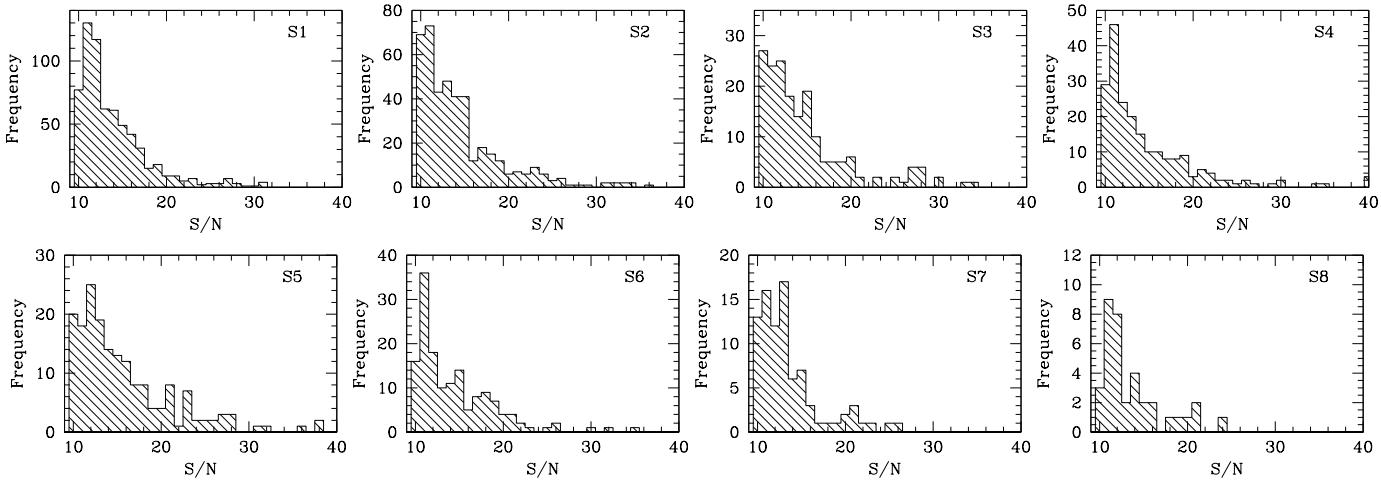

Fig. 3.2. Signal-to-noise distribution for each of the quasar subsets as defined in Table 3.1.

Table 3.1. Subset definitions of the SDSS quasars.

Subset	z_q	z_{mean}	Number of quasars
S1	2.30 – 2.50	2.40	604
S2	2.50 – 2.75	2.60	387
S3	2.75 – 3.00	2.88	153
S4	3.00 – 3.25	3.15	180
S5	3.25 – 3.50	3.36	160
S6	3.50 – 3.75	3.62	137
S7	3.75 – 4.00	3.86	78
S8	4.00 – 4.61†	4.21	34

†: The upper limit $z_q = 4.61$ identifies the highest redshift object in this subset

The plan of the Chapter is as follows. We begin with a description of the spectroscopic sample of quasars in Section. 3.2. We then briefly describe in Section 3.3 the code adopted to generate synthetic spectra. In Section. 3.4 and 3.5 we determine the quasar composite spectrum and the evolution of the Lyα effective optical depth, respectively. Section 3.6 introduces the theoretical background to measure the proximity effect and presents our results on the proximity effect signature towards individual objects. In Section 3.7 we determine the redshift evolution of the UVB, followed by a new estimation of the relative share of quasars and star-forming galaxies to the UVB. We end with our conclusions in Section 3.9.

Throughout this Chapter we assume a flat Universe with Hubble constant $H_0 = 70\ \mathrm{km\,s^{-1}\,Mpc^{-1}}$ and density parameters $(\Omega_m, \Omega_\Lambda) = (0.3, 0.7)$.

3.2. The Quasar Sample

3.2.1. Selection

The sample of quasar spectra was drawn from the fifth data release (DR5) of the Sloan Digital Sky Survey (SDSS) quasar catalogue (Schneider et al. 2007), with all data reprocessed by the DR6 reduction pipeline.

The two SDSS double channel spectrographs give a resolution of FWHM $\approx$ 2 Å ($R \sim 2000$) in the wavelength range from $\sim$ 3800 Å to $\sim$ 9200 Å. We required a coverage of the Lyman alpha forest of at least 200 Å, corresponding to a minimum emission redshift $z_q > 2.3$. Thereby we were left with $\sim$ 18 000 of the $\sim$ 77 400 visually classified quasars in the Schneider et al. (2007) catalogue. In order to be able to reliably measure the proximity effect in the SDSS spectra, we further imposed a minimum signal-to-noise ratio (S/N) of 10 in the quasar continuum near 1450 Å rest frame, reducing the number of QSOs to 1916. Among these there are 144 broad absorption line quasars (BAL QSOs) which cannot be used for the proximity effect analysis. Details about their identification are given in Sect. 3.2.3. Finally we inspected the remaining quasar spectra visually and removed 39 objects that were misclassified or were still suspected to be BAL QSOs. This procedure left us with a total of 1733 quasars.

The proximity effect analysis also requires accurate quasar redshifts and spectrophotometry. The redshifts in the Schneider et al. (2007) catalogue were measured from broad emission lines in the accessible wavelength range and statistically corrected for the systematic velocity shifts between low- and high-ionisation lines (e.g. Gaskell 1982). The statistical correction was determined by Shen et al. (2007) from a quasar sample at $1.8 < z_q < 2.2$, where the SDSS spectrograph covers the Si IV,C IV, C III], and Mg II emission lines. Adopting the Mg II emission redshift as systemic and applying their velocity correction, the redshift accuracy of higher redshift quasars is still $\sigma z_q \simeq 0.002$, sufficient for our purposes. Spectrophotometric accuracy is achieved by observing calibration stars together with the SDSS survey targets and tying the spectra to the accurate SDSS photometry ($\sigma_{mag} = 0.04$; York et al. 2000).

In the following we divide the sample into 8 subsets according to the quasar emission redshift as listed in Table 3.1. Each subset is characterised not only by the range in redshifts, but also its number-weighted mean z_{mean}. As an example of the average data quality, we show in Figure 3.1 two quasar spectra together with their 1σ noise arrays and the estimated continua which will be discussed in the next section. Additionally, Fig. 3.2 shows the S/N distribution for the subsets.

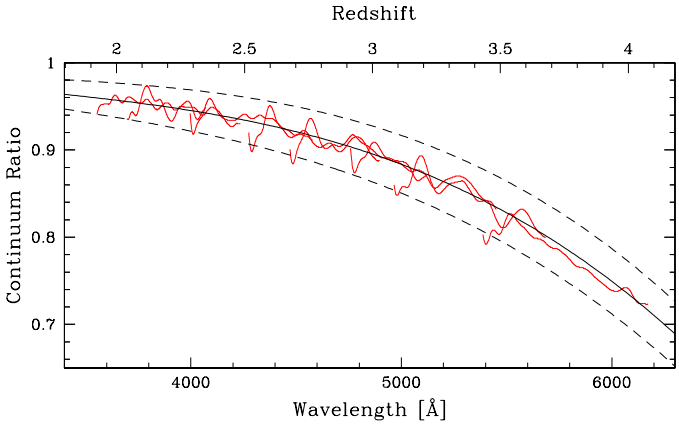

Fig. 3.3. Average ratios between the fitted and input continua in the Lyα forest of our simulations (red lines). The smooth profile with the dashed lines represents the least-square second order polynomial fit to the ratios and the $\pm 1\,\sigma$ errors.

3.2.2. Continuum estimation

In order to evaluate the proximity effect along each sight line, the quasar flux at the Lyman limit and the shape of its continuum emission are needed. Therefore two types of continua were estimated: (i) a global power law ($f_\nu(\nu) \propto \nu^\alpha$), excluding emission and absorption regions, used to estimate the quasar flux at the Lyman limit and (ii) a more local estimate that also includes the broad emission lines as a quasi-continuum, used to infer the continuum-normalised absorption-line spectrum.

The power law continuum was fitted though pre-defined continuum regions redward of the Lyα emission line free of any known emission lines (Sect. 3.4). Extrapolating the power law to the Lyman limit, we estimated the quasar Lyman limit flux. The necessity for this extrapolation is motivated by the difficulty to infer the Lyman limit flux due to the low S/N at short wavelengths or the lack of wavelength coverage at low redshifts.

The local continuum was automatically fitted using an algorithm based on the work by Young et al. (1979) and Carswell et al. (1982). A cubic spline was interpolated on adaptive intervals along the spectrum with respect to the continuum slope. The points for the spline interpolation were chosen starting from a regular sampling of the spectrum with a binning that becomes finer whenever the slope of the computed continuum exceeds a given threshold. This was done in order to better reproduce the wings of emission lines. To this continuum we additionally applied a systematic correction which accounts for the resolution effects and line blending, estimated from Monte Carlo simulated spectra (see Sect. 3.3 for details). We basically followed the procedure outlined in Chapter 2 and Dall'Aglio et al. (2008) hereafter Paper I. This approach consists of analysing the ratio between the input and fitted continuum in a set of 500 mock spectra. From this ratio we determined an average continuum ratio and a dispersion used as systematic and statistical uncertainties. Our results are presented in Fig. 3.3. The local, corrected continuum was finally used to estimate the quasar transmission $T = F_{\rm qso}/F_{\rm cont}$, defined as the ratio of the quasar flux ($F_{\rm qso}$) and the local continuum ($F_{\rm cont}$).

3.2.3. Broad absorption line quasars

The input sample of QSOs contains a significant fraction of BAL quasars which are not suitable to study the proximity effect and therefore need to be removed. To identify these objects we followed the procedure outlined by Weymann et al. (1991). The approach consists of computing the balnicity index defined as

$$BI = -\int_{v_1}^{v_2} [1 - T(v)/0.9]\, C\, {\rm d}v \qquad (3.1)$$

with $v_1 = 25000$ km s^{-1} and $v_2 = 3000$ km s^{-1}. $T(v)$ is the transmission as function of velocity and C is a constant initially set to zero. C becomes 1.0 whenever the term in the brackets remains positive for at least 2000 km s^{-1}, meaning that the first 2000 km s^{-1} of a BAL do not contribute to the balnicity index. C returns to zero whenever the quantity in brackets becomes negative. If a quasar shows a positive balnicity index, it was flagged and removed from our sample.

We note that in spite of the seemingly objective definition of the balnicity index, the identification of a BAL quasar still depends on the subjective choice of a number of factors such as the quasar continuum or the velocities v_1 and v_2. With this procedure we identified 144 BAL quasars not suitable for the analysis of the proximity effect. We noticed later that a few objects with BAL-like features survived this deselection and remained in the sample. We discuss their role in the proximity effect detection in Sect.3.6.3.

3.3. Monte Carlo simulations

Simulating quasar spectra provides a powerful tool of comparison which we employ to accurately control and calibrate a number of systematic effects present in real observations. We employed such simulations for three main purposes. (i) We estimated the systematic and statistical uncertainties of our continuum placement in the quasar spectra (Sect. 3.2.2). (ii) These uncertainties were used to obtain error bars on the effective optical depth in the forest, in addition to the variations in Lyα absorption among different lines of sight (Sect. 3.5). (iii) We used the simulated spectra to assess the bias arising from an asymmetric proximity effect strength distribution when combining the data to estimate the UVB photoionisation rate (Sect. 3.7).

The procedure used to generate synthetic spectra is identical to the one presented in Chapter 2. We generated a set of 500 synthetic spectra adopting a simple Monte Carlo prescription, assuming that the Lyα forest is well represented by three observed distributions:

1. The line number density distribution, approximated by a power law of the form ${\rm d}n/{\rm d}z \propto (1+z)^\gamma$ where $\gamma = 2.04$ (Chapter 2).
2. The column density distribution, given by $f(N_{\rm H\,I}) \propto N_{\rm H\,I}^{-\beta}$ where the slope is $\beta \simeq 1.5$ (Kim et al. 2001).
3. The Doppler parameter distribution, given by ${\rm d}n/{\rm d}b \propto b^{-5} \exp\left[-b_\sigma^4/b^4\right]$ where $b_\sigma \simeq 24$ km/s (Kim et al. 2001).

The algorithm populated the simulated sight lines with absorption features following the above distributions until the evolution of the effective optical depth matches the estimates made

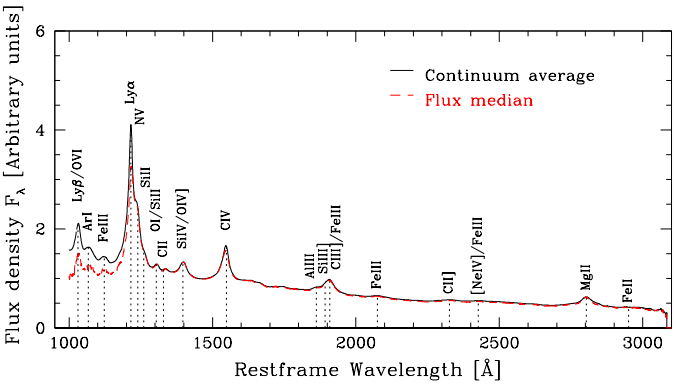

Fig. 3.4. The flux-median and continuum-mean SDSS composite spectra derived from our set of QSOs. The vertical dotted lines mark the positions of the most prominent emission lines known in quasar spectra. The difference between the two composites blueward of the Lyα emission line is due to the influence of the Lyα forest absorption.

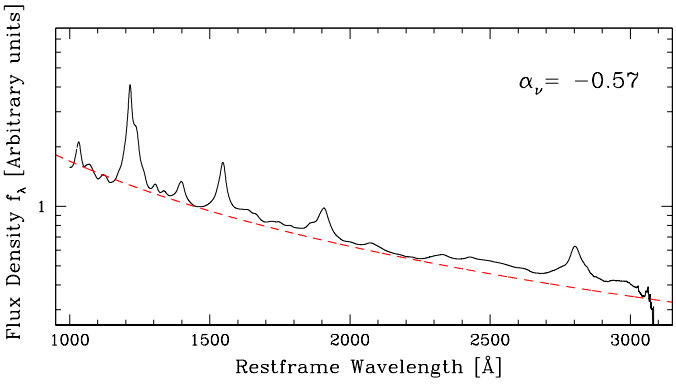

Fig. 3.5. The dashed line represents the power law fit ($f_\nu(\nu) \propto \nu^\alpha$) to the *continuum-mean* SDSS composite spectrum.

in Chapter 2. Once the simulated transmission was computed, an artificial quasar spectral energy distribution including emission lines of varying strengths and widths was generated via the principal component method described by Suzuki (2006) and in Paper I. The resolution of the spectrum was degraded using a Gaussian smoothing function with a FWHM of approximately 2Å and pixel size increased to match the SDSS specifications. Gaussian noise was added to the final quasar spectrum, in order to reproduce the S/N level of our objects.

3.4. A quasar composite spectrum

The large number of objects in our sample motivated us to compute a composite quasar spectrum. This spectrum provides important insights about the position of low and high-ionisation lines as well as global properties of the quasar spectral energy distribution. The computation of the composite spectrum required: (i) A rebinning of the spectra in rest frame wavelengths, (ii) a normalisation of the fluxes and (iii) a combining method to obtain the final composite spectrum. We computed two types of composite spectra, each of which has a different combining procedure: (1) the median spectrum employing the fluxes of the QSOs to minimise the effect of absorption lines and (2) the mean spectrum adopting the fitted continua of the QSOs. In the latter approach all quasar continua were corrected for the systematic depression in the Lyα forest as described in Sect. 3.2.2. Both results are presented in Fig. 3.4. The two composites are essentially identical until the Lyα emission where the differences between the two become visible. These differences are due to the absorption in the Ly forest which we accounted for when combining the corrected quasar continua.

The very high S/N level of our continuum composite spectrum allowed us to identify many of the well known emission lines present in the spectra of high redshift QSOs. To confirm the accuracy of the quasar redshifts provided in the Schneider et al. (2007) catalogue, we measured from the composite spectrum the location of the most prominent low and high-ionisation emission lines. For lines such as the Lyα, Si II+O I, Si IV+O IV], C IV, C III, and Mg II we fitted one or more Gaussian profiles to accurately estimate the emission wavelengths. The measured values for low-ionisation lines were in agreement with their laboratory wavelengths while the high-ionisation lines presented a systematic blueshift up to 550 km/s in the case of C IV (Gaskell 1982; Tytler & Fan 1992; Richards et al. 2006).

The computation of the two composite spectra enabled us to check the accuracy of the BAL quasars removal. If a significant fraction of such objects were misidentified, we should have detected a depression only in the flux composite, redward of the C IV emission line. The lack of such a feature ensures a correct removal of any significant contamination by BAL quasars.

The mean continuum composite spectrum is plotted in Fig. 3.5 with a single power law fit. The accuracy of this fit is compromised by the limited number of regions in a QSO spectrum free of emission lines. To perform the power law fit we adopted the three regions between 1350−1365 Å 1445−1475 Å and 2200−2250 Å. The estimated spectral slope is $\alpha_\nu = -0.57$, in agreement with previous measurements based on earlier data releases (Vanden Berk et al. 2001). This value is further supported by the distribution of spectral indices which closely follows a Gaussian distribution centred at $\alpha_\nu = -0.6$ with a dispersion of $\sigma_\alpha = 0.35$. Therefore, estimating the quasar flux at the Lyman limit via a single power law extrapolation ensures reasonable accuracy in the computation of the proximity effect.

3.5. Effective optical depth of the Lyα forest

The signature of the proximity effect is typically observed against the increase with redshift of the mean absorption in the Lyα forest. The opacity of the Lyα forest is empirically known to scale with redshift according to a power law of the form

$$\tau_{\rm eff} = \tau_0(1+z)^{\gamma+1}. \qquad (3.2)$$

for a line density evolving as $dn/dz \propto (1+z)^\gamma$. In Equation 3.2 $\tau_{\rm eff}$ is the H I effective optical depth. This quantity is related to the mean transmission as $\tau_{\rm eff} \equiv -\ln\langle T\rangle$, where the average $\langle\,\rangle$ is taken in redshift intervals.

The adopted method to estimate the parameters $(\log\tau_0, \gamma)$ consists of measuring $\tau_{\rm eff}$ in the forest of those quasars which

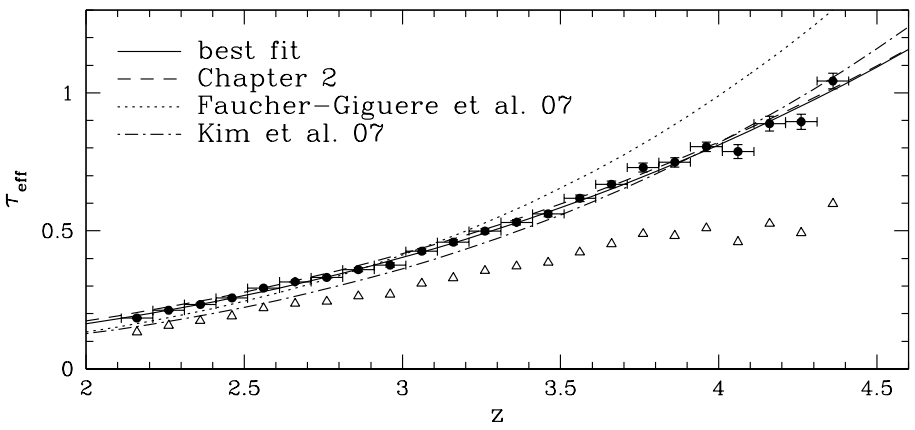

Fig. 3.6. Observed effective optical depth as a function of redshift with and without the continuum correction (dots and triangles, respectively). The solid profile shows the power law least-squares fits to the data points while the dashed, dotted and dashed-dotted curve indicates the evolution of the Lyα optical depth measured in Chapter 2 and, by Faucher-Giguère et al. (2008b) and Kim et al. (2007) respectively, using high resolution spectra. Errors on the redshift axis indicate the portion of forest used to compute the effective optical depth. The uncertainties on the effective optical depth have been estimated using our Monte Carlo simulated sight lines.

Table 3.2. Effective optical depth in the Lyα forest of our combined QSO sample, corrected for the continuum uncertainties.

$< z >$	$\tau_{\rm eff}$	$\sigma(\tau_{\rm eff})$	$< z >$	$\tau_{\rm eff}$	$\sigma(\tau_{\rm eff})$
2.16	0.183	0.002	3.36	0.531	0.009
2.26	0.211	0.003	3.46	0.561	0.010
2.36	0.233	0.003	3.56	0.617	0.011
2.46	0.256	0.003	3.66	0.668	0.012
2.56	0.291	0.004	3.76	0.729	0.016
2.66	0.315	0.004	3.86	0.748	0.016
2.76	0.331	0.004	3.96	0.804	0.017
2.86	0.359	0.008	4.06	0.787	0.025
2.96	0.376	0.008	4.16	0.888	0.026
3.06	0.426	0.008	4.26	0.895	0.027
3.16	0.459	0.008	4.36	1.043	0.028
3.26	0.499	0.008			

intersect a particular redshift slice ($\Delta z = 0.1$). We removed the influence of the quasar by considering only the rest frame wavelength range $1025 < \lambda < 1180$ Å. We performed this computation first on the transmission without continuum correction, and then applied the correction as described in Sect. 3.2.2.

The results are shown in Fig. 3.6 and listed in Table 3.2. It is evident that the continuum correction is crucial to prevent strong biases in measuring the evolution of $\tau_{\rm eff}$ at low resolution. The best fit of Eq. 3.2 to the continuum-corrected data yields values of $(\log \tau_0, \gamma) = (-2.28 \pm 0.03, 2.13 \pm 0.04)$. Despite the moderate spectral resolution, our results are in excellent agreement with the evolution of the Lyα optical depth as recently measured by us from high resolution quasar spectra in Chapter 2 and also by different authors (e.g. Schaye et al. 2003; Kim et al. 2007). We also observe that for $z \gtrsim 3.5$ our estimated $\tau_{\rm eff}(z)$ is significantly lower than recent measurements by Faucher-Giguère et al. (2008b), based on a sample of 84 QSO spectra obtained by different instruments. We have no explanation for this discrepancy. Because of the excellent agreement with other studies we proceed adopting our newly estimated fit parameters for further computations.

As a parenthetical note we remark that we do not detect any deviation from a single power law evolution at $z \simeq 3.2$. Around this redshift, Bernardi et al. (2003) detected a dip in $\tau_{\rm eff}(z)$ based on a much smaller sample of SDSS quasar spectra and speculated that this might be related to He II reionisation. While our higher resolution data do show a similar dip (cf. Chapter 2), there is no evidence for such a feature in Fig. 3.6. A more detailed analysis of the reality of that dip is probably worthwhile, but outside the scope of the present work.

3.6. Measurements of the proximity effect

3.6.1. Definitions and procedure

The ionisation state of the IGM near a quasar will be dominated by the local source rather than the UVB, leading to the observed weakening of the Lyα absorption in its vicinity. An efficient technique of detecting the proximity effect is to compare the effective optical depth measured near a quasar to its expected value in the Lyman alpha forest (e.g. Liske et al. 1998; Liske & Williger 2001). The flux statistic technique is applicable to high- and low-resolution spectra and has been used by us to detect the proximity effect on individual lines of sight (Paper I & Chapter 2).

The influence of the quasar modifies the effective optical depth to

$$\tau_{\rm eff} = \tau_0 (1+z)^{\gamma+1} (1+\omega)^{1-\beta} \tag{3.3}$$

where β is the slope in the column density distribution. The quantity ω is defined as the ratio between the quasar and background photoionisation rates:

$$\omega(z) = \frac{\Gamma_{\rm q}(z)}{\Gamma_{\rm H\,I}(z)} = \frac{1}{\Gamma_{\rm H\,I}(z)} \int_{\nu_0}^{\infty} \frac{f_\nu(\nu, z)}{h\nu}\, \sigma(\nu)\, {\rm d}\nu. \tag{3.4}$$

We assume the UVB photoionisation rate to be reasonably constant for the redshift path length probed by the Lyα forest of a given QSO. Approximating the spectral energy distribution of a quasar in the form $f_\nu(\nu) \propto \nu^{\alpha_{\rm q}}$, we can rewrite $\Gamma_{\rm q}$ as:

$$\Gamma_{\rm q}(z) = \frac{\sigma_\nu(\nu_0)\, L_\nu(\nu_0)}{4\pi h\, (3-\alpha_{\rm q})\, d_L^2(z_{\rm q}, z)} \left(\frac{1+z_{\rm q}}{1+z} \right)^{\alpha_{\rm q}+1} \tag{3.5}$$

where z is the redshift along the line of sight such that $z < z_{\rm q}$, $d_L(z_{\rm q}, z)$ is the luminosity distance of the QSO as seen from any foreground redshift along the LOS, $\alpha_{\rm q}$ is the spectral slope of the QSO and L_{ν_0} its luminosity at the Lyman limit. The hydrogen photoionisation cross section at the Lyman limit is $\sigma_\nu(\nu_0) = 6.33 \times 10^{-18}$ cm^2 and h is the Planck's constant.

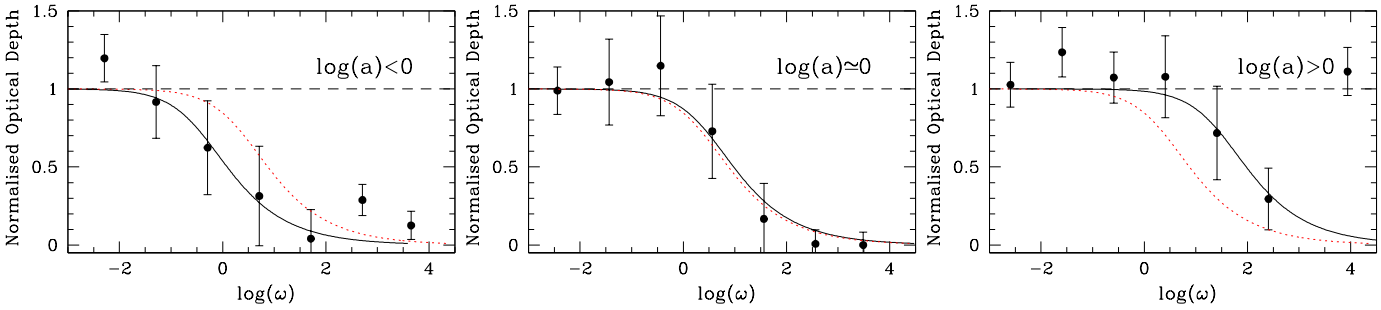

Fig. 3.7. Three examples of the proximity effect signature along individual sight lines at redshift $z \sim 3$. Each panel shows the normalised effective optical depth ξ versus ω, binned in steps of $\Delta \log \omega = 1$, with the fiducial model superimposed as the dotted line. The solid lines delineate the best fit to each individual QSO as described in the text. This subset was chosen for presentation purposes to show the variable strength of the proximity effect, going from *strong* (left panel) to *weak* (right panel).

We emphasise that all previous analyses of the proximity effect were based on a simplified determination of $\omega(z)$ as a flux ratio by assuming the same spectral energy distribution of the quasar and the cosmic UV background in Equation 3.4. With our correct definition of omega as a ratio of photoionisation rates, we do not have to assume a UVB spectral energy distribution to get poorly constrained UVB intensities. Moreover, all recent numerical studies of the UVB give the UVB photoionisation rate, facilitating comparisons between different methods.

Finally, the ratio of the observed optical depth to the one expected in the Lyα forest, or the *normalised effective optical depth* ξ, is given by

$$\xi = \frac{\tau_{\rm eff}}{\tau_0(1+z)^{\gamma+1}} = (1+\omega)^{1-\beta}. \qquad (3.6)$$

with the parameters $(\log \tau_0, \gamma)$ measured in Sect. 3.5. The slope of the column density distribution was fixed to $\beta = 1.5$ (Kim et al. 2001).

The proximity effect will manifest its signature as a departure from unity in the normalised optical depth as $\omega \to \infty$, i.e. towards the quasar systemic redshift.

3.6.2. The proximity effect along single sight lines

We now explore the application of the above method to individual objects. Our approach is as follows: We first compute, for each individual line of sight, the normalised effective optical depth as a function of ω, within bins of $\log \omega$. We then search for a systematic decrease of ξ at high values of ω.

In order to compute the ω scale (Eq. 3.4), a fiducial value for the UVB photoionisation rate had to be assumed. We fixed this value to $\Gamma^\star = 10^{-12}\,{\rm s}^{-1}$, thereby uniquely converting the redshift scale into an ω scale. Dividing the $\log \omega$ axis into an equally spaced grid, we then modelled the decrease of $\xi(\omega)$ in bins of $\Delta \log \omega$ according to the formula

$$F(\omega) = \left(1 + \frac{\omega}{a}\right)^{1-\beta} \qquad (3.7)$$

where a is the only free parameter which expresses the *observed* turnover of ξ in units of $\Gamma^\star$. In principle, each a directly provides a best-fit value of $\Gamma_{\rm HI}$, since $\Gamma_{\rm HI} = a \times \Gamma^\star$. As demonstrated in Chapter 2, however, the random scatter of a due to the finite small number of absorbers in each line of sight is so large that meaningful constraints on $\Gamma_{\rm HI}$ can only be obtained from the distribution of a values for a statistically significant sample.

For a given sight line, the value of the fitting parameter a describes how much the best-fit model disagrees with the fiducial value assumed above. We regard $\log a$ as a measure of the strength of the proximity effect, which can be classified into three principal regimes as presented in Fig. 3.7:

1. $\log a < 0$: this case describes a *strong* proximity effect. The normalised effective optical depth is already small for $\omega \ll 1$.
2. $\log a \simeq 0$: this case describes an *average* proximity effect since the ξ values follow the fiducial model profile.
3. $\log a > 0$: this case describes a *weak* proximity effect. The normalised effective optical depth will turn over only at very large $\log \omega$ values (if at all).

Of course, the boundaries between these three categories depend on the (arbitrary) choice of the fiducial UVB photoionisation rate value $\Gamma^\star$ which fixes the zero point of $\log a$.

3.6.3. The distribution of proximity effect strengths

We quantified the proximity effect in the above manner on each sight line in the sample to compute the distribution of $\log a$. Considering the UVB as a constant for each subset of Table 3.1 we plot the observed proximity effect strength distribution (PESD) of each subset in Fig. 3.8.

Each of these distributions shows a wide spread in $\log a$ values. For in total 35 objects, or 1.8 % of the sample, we obtain $\log a > 3.7$, which means that for these objects the fit hinges on a single point showing a decrease of $\xi(\omega)$ at large ω. Since the largest values of $\log a$ correspond to the weakest proximity effect signatures, we inspected these cases individually. It turned out that all of them displayed either strong associated absorption or were previously unrecognised BAL QSOs. For all other QSOs in the sample, the proximity effect signature is based on at least two and in general several points in the ξ vs. $\log \omega$ diagram; we conclude that the effect is detected in 98 % of the sample.

For all subsamples the PESD shows the two major characteristics discovered in Chapter 2: (i) A well defined peak,

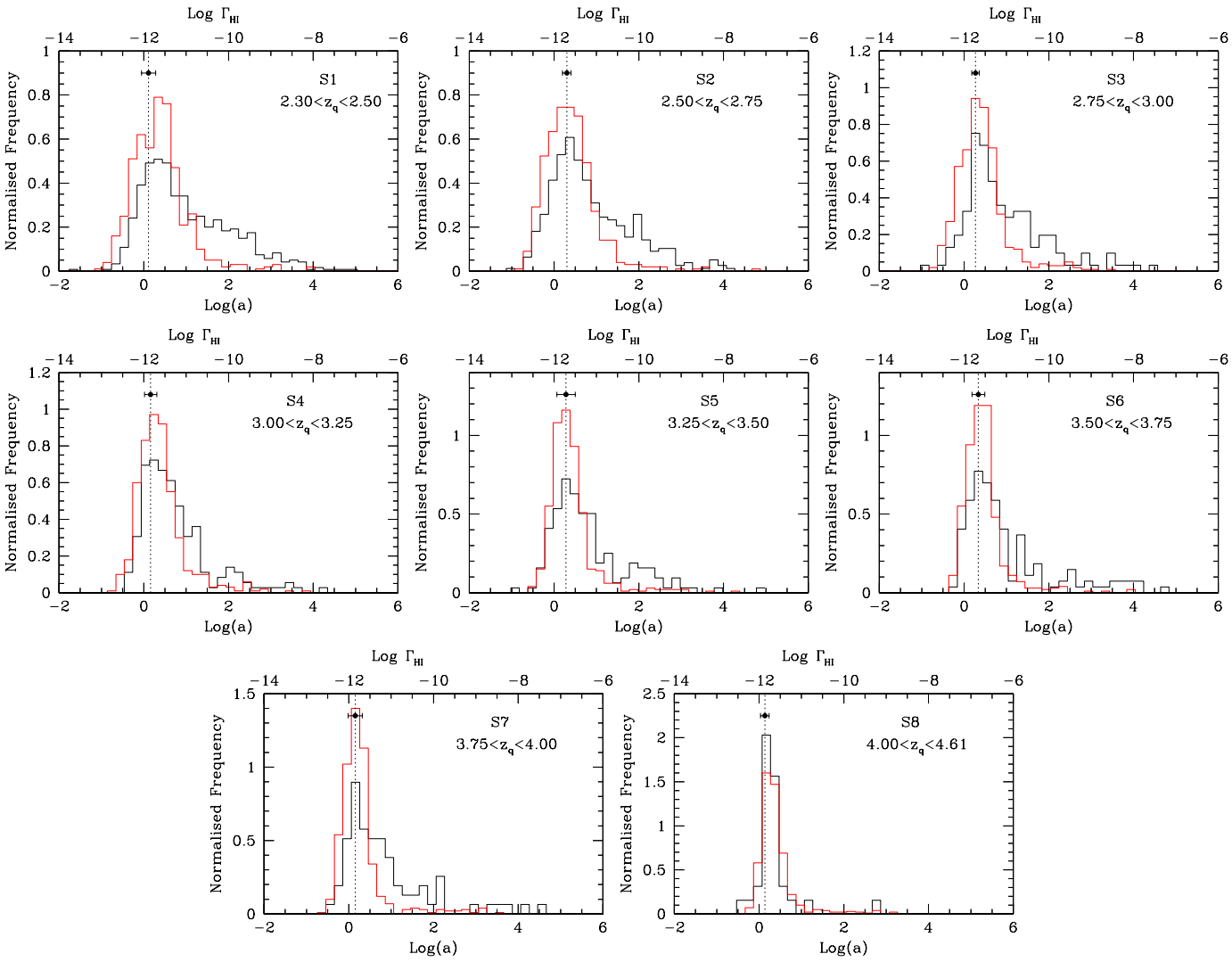

Fig. 3.8. The proximity effect strength distributions in individual subsets of our data set. Each panel shows the observed PESD for increasing redshift intervals (black histogram) along with the simulated PESD obtained from a set of simulated lines of sight (red histogram). The dotted line and the point mark the modal values of the PESD with the associated uncertainties.

and (ii) a significant asymmetry with an extended tail towards weaker proximity effects, i.e. large values of a. Additionally, the PESD becomes substantially more narrow with increasing redshift and also shows a less prominent tail towards $\log a > 0$.

The skewness in the PESD is the result of the ω definition as a function of redshift (Eq. 3.4). Approaching the quasar emission, equal $\Delta \log \omega$ bins probe progressively smaller Δz intervals, leading to a deviation in the distribution of the absorber counts from a Gaussian. This translates to a skewed distribution of ξ as $z \rightarrow z_q$ since large ξ values (and therefore a weaker observed proximity effect) become more likely. This trend becomes less prominent at high redshift because equal $\Delta \log \omega$ bins will probe progressively increasing numbers of absorbers and therefore reduce the skewness in the PESD.

The PESD asymmetry is further amplified by the presence of overdensities near some of the QSOs in each subset. In Chapter 2 we found that about 10% of our objects showed a significant excess of absorption within a few Mpc of the quasar redshift. The inferred values of a for these quasars are expected to be larger by a factor related to the amount of absorption which becomes observable in the PESD as an enhancement in the tail extension on its weak side. Since we do not have sufficiently high resolution in our spectra to estimate the excess of absorption on Mpc scales near the quasar emission, we estimated its influence by employing our Monte Carlo simulation.

We generated a set of synthetic quasar spectra as described in Sect. 3.3, matching the characteristics of each of our subsets (sample size, and redshift and luminosity distributions). For each spectrum we performed a continuum fit, also applying the appropriate correction and then we estimated the proximity effect strength. This exercise serves two purposes: (i) as an accuracy check for our automatic data analysis, and (ii) as a tool to reveal the effect of H I overdensities on the PESD. For the input photoionisation rates in the different subsets we adopted the modal value of the observed PESDs (see Sect. 3.7.1).

Each panel of Figure 3.8 shows the comparison between the observed and the simulated PESD. These distributions clearly differ with respect to the tail extension towards weaker proxim-

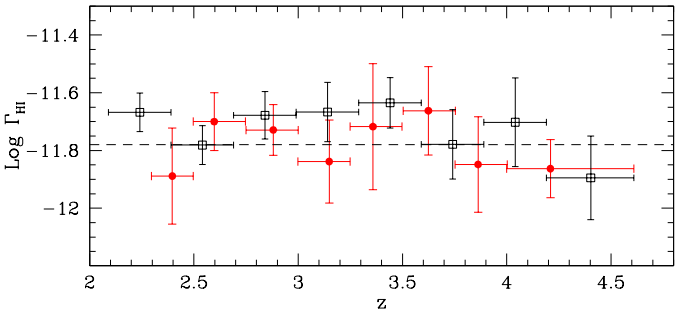

Fig. 3.9. Comparison of the two different estimates of the UVB photoionisation rate inferred from the modal value of the PESDs (solid dots) and from the combined analysis of the proximity effect after truncating the PESD as described in the text (empty squares). We also show the best-fit non-evolutionary model to our data (dashed line) yielding a photoionisation rate of $\log \Gamma_{\rm H\,I} = -11.78 \pm 0.07$ in units of $\rm s^{-1}$.

ity effect, while they are in agreement with respect to the location of the most likely value of $\log a$. The simulated PESD is narrower than the observed one, indicating that a certain fraction of QSOs may be affected by large-scale overdensities. Our approach to estimate the UV background from these distributions rests on the assumption that the peak of the PESD is unaffected by this contamination. We discuss the validity of this assumption further below (and also in Appendix C).

3.7. The evolution of the UV background photoionisation rate

3.7.1. Method

As shown in Chapter 2, the shape of the PESD depends on the cosmic photoionisation rate as well as on possible excess H I absorption on scales of several Mpc around the quasars. We now estimate the photoionisation rate $\Gamma_{\rm H\,I}$ in various redshift bins by evaluating the PESD.

The first method consists of recovering the modal value of the PESD, i.e. estimating the peak of the distribution. To achieve this goal we adopted the following bootstrap technique: Starting from the observed distribution of N_i values of $\log a$, where N_i is the total number of objects in a given subset, we randomly duplicated the strength parameter of N_i/e quasars and estimated the modal value of the new PESD. We repeated this process 500 times in each of the eight subsets, obtaining the mean and the sigma values of PESD modes.

In addition to the modal values of the PESD, we also explored another method to estimate the photoionisation rate evolution with redshift. We take advantage of the fact that overdense quasars will have statistically larger $\log a$ values and selected from our sample only those QSOs with $\log a$ below a certain threshold $\log a_0$. We fixed $\log a_0 = 1.5$ after comparing how the simulated and observed PESD change with redshift (see Fig. 3.8). This is equivalent to truncating the PESD above $\log a_0$. Such a cut does not modify the estimates of the PESD mode, but significantly reduces the biases connected to overdense quasars. We then combined the signal of all these quasars by merging them according to their redshift scale. We derived the ξ values in the same way as for measuring the proximity effect along single sight lines and then fitted Eq. 3.7 to the data, yielding a first estimate of $\Gamma_{\rm H\,I}$. We finally corrected the preliminary photoionisation rates for the systematic biases introduced by the remaining PESD asymmetry.

Figure 3.9 shows a comparison between our two estimates of $\Gamma_{\rm H\,I}$. The UVB values derived via both methods are consistent with another, yielding a roughly constant level of the H I photoionisation rate at $2 \lesssim z \lesssim 4.6$. A least-square fit to a non-evolving photoionisation rate yields $\log \Gamma_{\rm H\,I} = -11.78 \pm 0.07$ for the PESD modal values and $\log \Gamma_{\rm H\,I} = -11.75 \pm 0.05$ from the second method, both in units of $\rm s^{-1}$. While the two methods yield statistically very similar results, we adopted the modal estimates of the UVB photoionisation rate as our final estimates. This choice is mainly motivated by the conceptual simplicity of the PESD mode and its independence of *ad hoc* assumptions regarding the threshold $\log a_0$ or the PESD asymmetry correction.

3.7.2. Effect of overdensities on the proximity effect strength distribution

We now address the concern that large-scale H I overdensities around our quasars might significantly bias the UVB estimates. A fixed overdensity factor valid for *all* quasars in a sample would simply shift the PESD towards larger $\log a$ values, but preserve the shape of the distribution. Our method is completely degenerate to such a shift. We argued in Chapter 2 that a uniform overdensity factor is however rather unplausible. In the more likely case of a distribution of overdensities the width of the PESD would be significantly enhanced. Measuring the width of the distribution thus provides a useful additional diagnostic.

In Fig. 3.8 we compare the measured PESDs with simulated distributions generated by the Monte Carlo process as described above. In each panel, the simulated dataset has the same redshift distribution as the observed one, and the areas under the observed and simulated histograms are normalised to the same total number of objects.

In most of the panels of Fig. 3.8, the two histograms agree quite well in the cores, but the observed data show a significant excess of large $\log a$ values that is absent in the simulations. In terms of standard deviations, the observed distributions have dispersions typically $\sim 1.5\times$ that of the simulated ones; most of that excess is due to the objects with $\log a \gtrsim 2$. We interpret this excess as the main manifestation of H I overdensities around our quasars.

The applicability of our approach to estimate the UVB via the proximity effect now rests on the question whether or not the mode of the PESD is significantly affected by the influence of overdensities. The generally good agreement between the *cores* of the simulated and observed distributions suggests that only a minority of QSOs produce the excess; this supports our notion that the mode is approximately conserved.

Consider our highest redshift subset S8 in particular, containing 34 QSOs at $z > 4$. The PESD of this subset has a dispersion of $\sigma_{\log a} = 0.51$, while the corresponding simulated PESD has $\sigma = 0.46$. Essentially all of this difference is due to a single

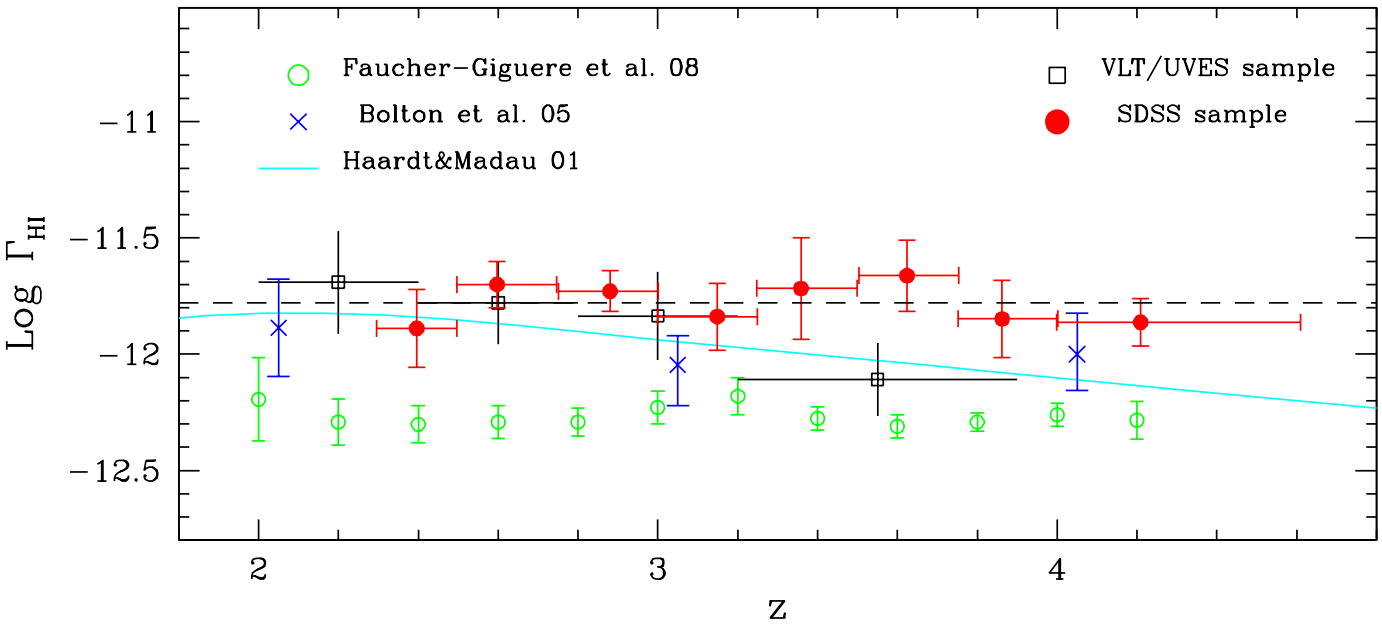

Fig. 3.10. Evolution of the UVB photoionisation rate as obtained employing the modal value of the PESDs on the SDSS data set (solid circles). The empty squares refer to the estimates from the UVES sample presented in Chapter 2. We compare our results with recent estimates from Bolton et al. (2005) and Faucher-Giguère et al. (2008a), both employing numerical simulations to infer the cosmic photoionisation rate (crosses and empty circles, respectively). The solid line represent the evolution of $\Gamma_{\rm H\,I}$ predicted by Haardt & Madau (2001).

outlier. Any excess H I absorption in the QSOs would make the PESD broader and inconsistent with the observed narrow distribution, unless the amount of such an excess absorption were nearly exactly equal for the entire sample.

We conclude that the PESD mode is quite robust against the influence of overdensities. While we cannot firmly exclude the possibility that some of our $\Gamma_{\rm H\,I}$ values at intermediate redshifts are somewhat affected, the narrowness of the $z \gtrsim 4$ PESD provides evidence against strong H I overdensities on scales of several Mpc. We consider this data point as our most significant measurement.

3.7.3. Comparison with other measurements

Figure 3.10 shows our estimated values of the hydrogen photoionisation rate $\Gamma_{\rm H\,I}$ as a function of redshift, together with recent results from the literature. In order to facilitate a direct comparison, we repeated the proximity effect analysis of our high-resolution VLT/UVES spectra (Chapter 2), but now quoting photoionisation rates rather than UVB intensities and applying a coarser binning. The redshift-averaged $\Gamma_{\rm H\,I}$ values are very similar, -11.78 ± 0.07 for SDSS vs. -11.83 ± 0.10 for UVES (in logarithmic units of $\rm s^{-1}$). While at $z \lesssim 3$ the two datasets are almost indistinguishable, the UVES measurements suggest a decrease of $\Gamma_{\rm H\,I}$ with increasing z while the SDSS data appear to favour an approximately constant photoionisation rate. The differences are not highly significant considering the error bars; we also recall that the UVES sample contains only 7 QSOs with $z > 3.3$.

The SDSS measurements are also in broad agreement with the results by Bolton et al. (2005) who inferred $\Gamma_{\rm H\,I}$ by matching hydrodynamical simulations to the observed opacity evolution in 19 QSOs (with only 4 located at $z > 3.3$). Bolton et al. discussed the main uncertainties entering in the computation such as the IGM temperature, the IGM density distribution and the evolution of the effective optical depth. Their best values of $\Gamma_{\rm H\,I}$ are slightly smaller than our SDSS estimates, but again consistent within the error bars. In particular, their results also show no downturn of the photoionisation rate towards large redshifts. On the other hand there is less agreement between our measurements and the latest estimates by by Faucher-Giguère et al. (2008a), which are globally offset by ~ 0.5 dex towards low values with respect to the SDSS results (but again show no trace of a downturn). This discrepancy is presumably (at least partly) due to the already mentioned discrepant description of the optical depth evolution $\tau_{\rm eff}(z)$ (see Sect. 3.5).

These estimates of the UVB can be compared to the semi-analytic prediction based on UV luminosity functions of quasars and star-forming galaxies (Haardt & Madau 1996; Fardal et al. 1998; Haardt & Madau 2001). As presented in Fig. 3.10, the theoretical calculations done by Haardt & Madau (2001) predict a significant decline of $\Gamma_{\rm H\,I}$ towards high redshifts, being consistent within the errors with both the results of Bolton et al. (2005) and our own from UVES. Since empirical constraints on both the quasar luminosity function and on the high-redshift stellar emissivity have been much improved in recent years, we present in the following a new calculation of the UVB (a more detailed derivation is presented in Appendix A.3.).

3.8. Origin of the metagalactic UV photons

3.8.1. Method

The intensity of the background radiation field at a given frequency and redshift is derived from the cosmological radiative transfer equation

$$\left(\frac{\partial}{\partial t} - \nu H \frac{\partial}{\partial \nu}\right) J_\nu = -3HJ_\nu - c\alpha_\nu J_\nu + \frac{c}{4\pi}\epsilon_\nu \qquad (3.8)$$

(Peebles 1993), where $H(t)$ is the Hubble parameter, c is the speed of light, and α_ν and ϵ_ν represent the absorption and emission coefficients, respectively (note that α_ν has no connection with the quasar slope estimated in Sect. 3.4). The average intensity of the radiation can be expressed, at an observed frequency ν_0 and at a given redshift z_0, as

$$J_\nu(\nu_0, z_0) = \frac{1}{4\pi}\int_{z_0}^{\infty} \frac{(1+z_0)^3}{(1+z)^3}\,\epsilon_\nu(\nu, z)\,\mathrm{e}^{-\tau_{\mathrm{Lyc}}(\nu_0, z_0, z)}\,\frac{\mathrm{d}l}{\mathrm{d}z}\,\mathrm{d}z \qquad (3.9)$$

with $\nu = \nu_0(1+z)/(1+z_0)$, $\mathrm{d}l/\mathrm{d}z$ being the proper length element and τ_{Lyc} is the Lyman continuum opacity, describing the radiation filtering due to intervening absorption.

The rapid increase of opacity along the LOS for $z \gtrsim 2$ leads to a significant reduction in the mean free path of ionising photons, which as a consequence implies that only *local* sources contribute significantly to the UV background intensity (Madau et al. 1999; Schirber & Bullock 2003). In this approximation, the solution of Eq. 3.9 is given by

$$J_\nu(\nu_0, z_0) \simeq \frac{\Delta l(\nu_0, z)\,\epsilon_\nu(\nu, z)}{4\pi}. \qquad (3.10)$$

The mean free path $\Delta l(\nu_0, z)$ is therefore related to the properties of the absorbers in the Lyα forest at redshift $z > 2$ and is given at the Lyman limit frequency by

$$\Delta l(\nu_0, z) \simeq \frac{(\beta-1)\,c}{\Gamma(2-\beta)\,N_0 \sigma_\nu(\nu_0)^{\beta-1}}\,\frac{1}{(1+z)^{\gamma+1}\,H(z)} \qquad (3.11)$$

where $\Gamma(2-\beta)$ in this case is the Gamma function and (N_0, β, γ) describe the redshift and column density distributions of the absorbers, typically well represented by

$$\frac{\partial^2 N}{\partial z\,\partial N_{\mathrm{H\,I}}} = N_0\,N_{\mathrm{H\,I}}^{-\beta}\,(1+z)^\gamma. \qquad (3.12)$$

The major contribution to the mean opacity at the Lyman limit is driven by systems with optical depths around unity, or equivalently with column densities of the order of $N_{\mathrm{H\,I}} \simeq 10^{17.2}$ cm^{-2}. In this regime the properties of the absorbers in the Lyα forest are particularly difficult to infer and only few literature measurements exist (e.g. Stengler-Larrea et al. 1995; Kirkman & Tytler 1997; Péroux et al. 2003). For simplicity and due to the non-negligible contribution of lower column density systems to the Lyman continuum opacity (Madau et al. 1999), we approximated the column density distribution to a single power law with $\beta = 1.5$. The absorber density evolution has been fixed to a power law as well with $(N_0, \gamma) = (1.4 \times 10^7, 2.45)$, following Péroux et al. (2003). Deviations from these assumptions will only have a marginal influence on both the global and relative scaling of different contributions which, as we will show, does not affect our results.

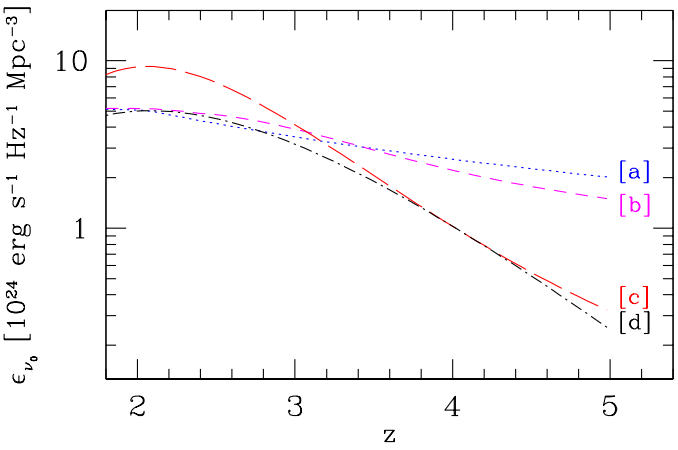

Fig. 3.11. QSO emissivity $\epsilon_\nu(z)$ at the Lyman limit obtained from four different luminosity functions as described in the text. The different lines refers to [a] the Bongiorno et al. (2007) LDDE model, [b] the modified LDDE model, [c] and [d] the Wolf et al. (2003) PLE and PDE model, respectively.

Assuming that the UV background intensity has a power law shape for wavelengths shorter than the Lyman limit ($J_\nu \propto \nu^{\alpha_\mathrm{b}}$), the UVB photoionisation rate becomes

$$\Gamma_{\mathrm{H\,I}}(z) \simeq \frac{\sigma_\nu(\nu_0)\,\Delta l(\nu_0, z)\,\epsilon_\nu(\nu_0, z)}{h\,(3-\alpha_\mathrm{b})}. \qquad (3.13)$$

The spectral index of the UV background, α_b, is a poorly known quantity which in principle could be predicted assuming a specified contribution from quasars and galaxies (Haardt & Madau 2001). In our calculation we fixed its value to $\alpha_\mathrm{b} = -1.4$ (Agafonova et al. 2005), but note that a different value would not change our conclusions as will be discussed in Sect. 3.8.4. Equation 3.13 directly converts the integrated luminosity density at the Lyman limit, $\epsilon_\nu(\nu, z)$, into a photoionisation rate and, assuming that only the quasar and star-forming galaxy populations contribute to $\Gamma_{\mathrm{H\,I}}(z)$, it can be expressed as the sum of these two different contributions, thus

$$\Gamma_{\mathrm{H\,I}}(z) \simeq \frac{\sigma_\nu(\nu_0)\,\Delta l(\nu_0, z)}{h\,(3-\alpha_\mathrm{b})}\left(\epsilon_{\nu,\mathrm{q}}(\nu_0, z) + \epsilon_{\nu,\mathrm{g}}(\nu_0, z)\right) \qquad (3.14)$$

where $\epsilon_{\nu,\mathrm{q}}(\nu_0, z)$ and $\epsilon_{\nu,\mathrm{g}}(\nu_0, z)$ represent the quasar and galaxy emissivities at the Lyman limit, respectively. In the following two sections we separately estimate and discuss these different contributors.

3.8.2. Quasar contribution

The integrated luminosity density, or emissivity, of quasars is defined as

$$\epsilon_{\nu,\mathrm{q}}(\nu, z) = \int_0^\infty \phi(L, \nu, z)\,L\,\mathrm{d}L \qquad (3.15)$$

where $\phi(L, \nu, z)$ is the quasar luminosity function (LF). In the literature, the quasar luminosity function has been estimated in a variety of rest frame bands and using different analytical descriptions. To convert from the observed passbands to the flux at the Lyman limit we approximated the quasar spectra energy distribution as a double power law ($f_\nu \propto \nu^\alpha$) with the following

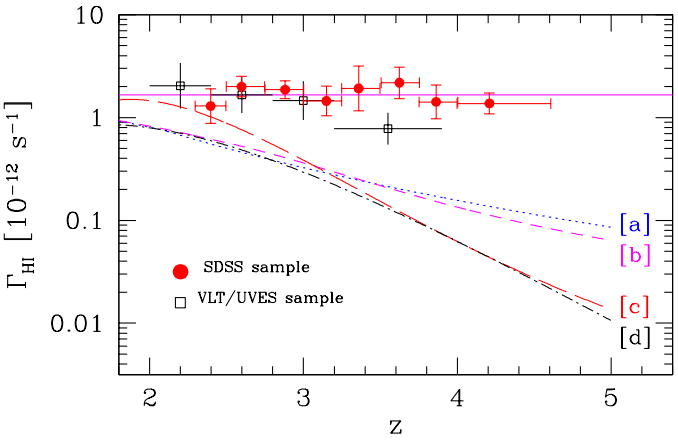

Fig. 3.12. QSO contributions to the UVB photoionisation rate (labelled lines) as obtained from the different emissivities presented in Fig. 3.11 in comparison to our estimates of the total photoionisation rate from the SDSS (solid circles) and the UVES samples (empty squares). The solid line represent the assumed level for the total photoionisation rate of $\log \Gamma_{\rm H\,I} = -11.78$. The different curves were inferred form [a] the Bongiorno et al. (2007) LDDE model, [b] the modified LDDE model, [c] and [d] the Wolf et al. (2003) PLE and PDE model, respectively, of the quasar luminosity function.

indices: $\alpha = -0.3$ at $2500 - 5000$ Å (Madau et al. 1999) and -0.57 at $228 - 2500$ Å, as estimated in Sect. 3.4.

The quasar luminosity density has to be constrained through the results of quasar surveys. However, even though the number of known quasars has probably more than tenfolded in the last decade, the relevant range in the redshift-luminosity plane is still poorly sampled, mainly due to the fact that the luminosity density is dominated by the large number of faint QSOs which are hard to identify in large numbers. Instead of relying on a single global approximation, we looked into the results of different published surveys and their implications for the quasar luminosity density.

(i) Wolf et al. (2003) presented two different analytical fits to the COMBO-17 quasar luminosity function: A pure density evolution (PDE) and a pure luminosity evolution (PLE) model, both approximated by third order polynomials. The two derived emissivity laws predict a steep decrease towards high redshift with very similar slopes, but showing different peak contributions.

(ii) Bongiorno et al. (2007) used a combined sample of quasars from the VIMOS-VLT Deep Survey (VVDS) and SDSS, probing a larger luminosity interval compared to Wolf et al. (2003). They employed a luminosity-dependent density evolution model (LDDE) with the limitation of a fixed bright end slope of the luminosity function. The resulting emissivity is considerably flatter than that of Wolf et al. (2003).

(iii) Richards et al. (2006) estimated the luminosity function from the third SDSS data release (DR3). Their DR3 quasars are so bright that they were able to probe only the bright end slope of the luminosity function and they found significant evidence for a slope variation over redshift. For our purposes their luminosity function cannot be used since their analytical fits cannot be extrapolated to magnitudes fainter than $M_i \lesssim -26$. However we included the slope information into an additional LDDE model obtained from the Bongiorno et al. (2007) model, now allowing for a variable bright-end slope. The inferred emissivity decline at high redshift is slightly steeper, but still not as pronounced as in the two models by Wolf et al. (2003).

Figure 3.11 presents a comparison of the emissivities estimated from the luminosity functions of Wolf et al. (2003); Bongiorno et al. (2007) and Richards et al. (2006). We assume that these four analytic descriptions bracket the true evolution of the emissivity. Using Equation 3.13 we converted the luminosity density into an QSO contribution to $\Gamma_{\rm H\,I}$ which we denote as $\Gamma_{\rm H\,I,q}$.

3.8.3. Contribution by star-forming galaxies

The second source population of the UV background to be considered are galaxies actively forming stars. The detection of high redshift galaxies is still extremely challenging and only a few deep surveys are available for this calculation. Among those reaching redshifts larger than $z = 3$, we consider the results by Tresse et al. (2007) using the VVDS sample and by Ouchi et al. (2004) using the Subaru Deep Field (SDF) survey.

In order to compute the galactic emissivity at the Lyman limit starting from the observed UV luminosity density we evaluated

$$\epsilon_{\nu,\rm g}(\nu, z) = f_{\rm esc}\; g(\nu)\; \epsilon_{\rm UV}(\nu, z). \qquad (3.16)$$

where $f_{\rm esc}$ is the escape fraction of UV photons from galaxies, $\epsilon_{\rm UV}(\nu, z)$ is the observed galactic UV emissivity per unit comoving volume, and $g(\nu)$ is the Lyman continuum frequency dependence of galaxies. We assumed that $g(\nu) \propto \nu^{-2}$ (e.g. Inoue et al. 2006) at all redshifts and a constant escape fraction of 10%. These quantities are highly uncertain and still controversially debated. However, we note that these assumptions affect the global scaling of the points and not their relative positions, unless one introduces a redshift-dependent escape fraction (which is possible, but adds another poorly constrained degree of freedom). We then used Eq. 3.13 to convert the observed emissivities into a stellar contribution to $\Gamma_{\rm H\,I}$ which we denote as $\Gamma_{\rm H\,I,g}$.

Notice that we refrained from attempting to construct a smooth interpolation (or even extrapolation) formula for $\epsilon_{\nu,\rm g}(\nu, z)$. We only evaluated the contribution by galaxies $\Gamma_{\rm H\,I,g}$ at the points given by the above mentioned surveys.

3.8.4. Comparison to the observed photoionisation rate

We now consider how our measurements of the overall photoionisation rate compare with the different contributions. Figure 3.12 shows the different models of the quasar contribution to $\Gamma_{\rm H\,I}$ along with the estimates based on the proximity effect. The quasar contribution shows a peak around $z \simeq 2$ and strongly declines towards higher redshifts, however with slopes varying between the different models.

A number of factors make the QSO contribution to the photoionisation rate uncertain. The analytical description of the quasar LF is by far the most prominent one, but also the assumed quasar SED, the slope of the UVB or the mean free path

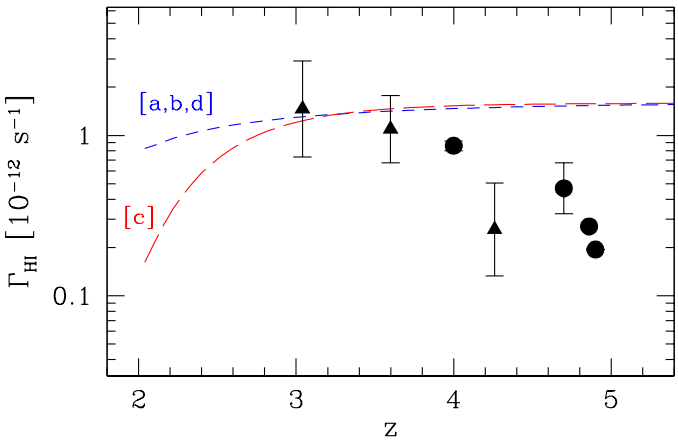

Fig. 3.13. Non-QSO contribution to the UV background photoionisation rate. The different dashed lines represent the required photoionisation rates which added to the QSO contribution lead to the observed constant photoionisation rate. The solid triangles and circles show $\Gamma_{\rm H\,I}$ estimated from the stellar emissivities of Tresse et al. (2007) and Ouchi et al. (2004) respectively and assuming a constant escape fraction of 10%.

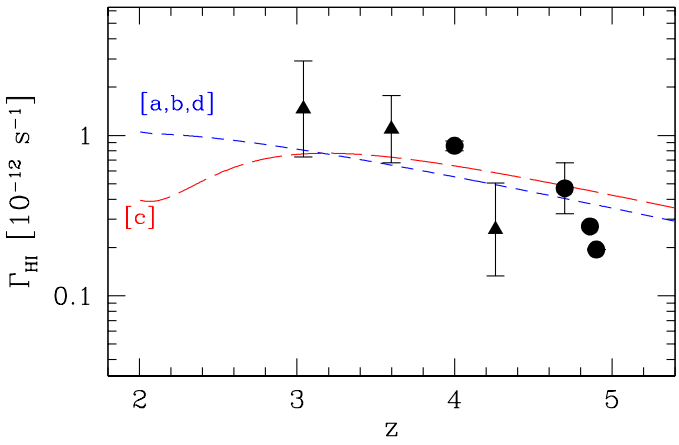

Fig. 3.14. Non-QSO contribution to the UV background photoionisation rate as in Fig. 3.13. The different dashed lines represent the required photoionisation rates which added to the QSO contribution lead to a mildly decline in $\Gamma_{\rm H\,I}$ towards high redshift. The solid triangles and circles show $\Gamma_{\rm H\,I}$ estimated from the stellar emissivities of Tresse et al. (2007) and Ouchi et al. (2004) respectively and assuming a constant escape fraction of 10%.

of ionising photons come into play especially in the global scaling of $\Gamma_{\rm H\,I}$. Despite the differences in the predicted $\Gamma_{\rm H\,I,q}(z)$, all models show a substantial decline in the quasar contribution to the global photoionisation rate, implying that galaxies must provide a substantial additional contribution in order to maintain the IGM at the observed high ionisation level.

In order to compare the UVB with the predictions from source counts, we subtracted the QSO contribution from the observed $\Gamma_{\rm H\,I}(z)$ obtained from the proximity effect analysis. For our SDSS measurements, the UVB is approximately constant at $\log\Gamma_{\rm H\,I} = -11.78$. The residuals after subtracting the different luminosity densities are show in Fig. 3.13. In all cases $\Gamma_{\rm H\,I,g}(z)$ is dominating the global photoionisation rate for redshifts larger than three, independently of the details of the assumed QSO contributions (models [a] to [d]). At smaller redshift the QSO contribution inferred from the PLE model by Wolf et al. (2003) (model [c]) is higher than that of the other models, and consequently the stellar contribution is smaller for this case.

We also considered the extreme case of a UVB completely dominated by quasars at $z \sim 2$, by rescaling all QSO emissivity models to our proximity effect measurement at $z \sim 2$. This gave us the *minimum* stellar contribution as a function of redshift. This is zero by design at $z = 2$, but increases rapidly and is in fact very similar to the model [c] in Fig. 3.13.

As the uncertainties on the global UVB photoionisation rate are still considerable, we explored the impact of this uncertainty by alternatively adopting a slowly declining UVB as favoured by our UVES results in Chapter 2. We computed a linear fit to $\Gamma_{\rm H\,I}(z)$ and simply extrapolated this towards higher redshift. We then again subtracted the predicted QSO contribution and plotted the residuals in Fig. 3.14. This has a significant impact on the predicted stellar contribution. Recall, however, that the UVES data from Chapter 2 leave the UVB at $z \gtrsim 4$ essentially unconstrained.

Fig. 3.13 and Fig. 3.14 constitute two independent assessments of the possible stellar contribution to the UVB. If $\Gamma_{\rm H\,I}$ at $z \simeq 4.2$ is as high as suggested by our highest-redshift SDSS data point, it would be fully consistent with the predictions based on the observed UV luminosity density of galaxies at $3 \lesssim z \lesssim 4$. Extrapolating our nearly flat UVB towards even higher redshifts would then result in an increasing UVB deficit based on the observed galaxy surveys. However, that extrapolation is unsupported by the coverage of our data. Furthermore, some degree of deficit is also perfectly conceivable since high-redshift surveys as the SDF sample only the luminous part (considerably above $L^\star$) of the LBG population, and the number density of smaller star forming galaxies is still very poorly known.

If on the other hand the UVB should continue to decline towards higher z as obtained by extrapolating the results from our UVES sample, the counts of star forming galaxies are in good agreement at $z > 4$, but almost too high in the better constrained range of $3 < z < 4$. We reiterate that these conclusions rest on the assumption of a constant UV escape fraction. By adjusting $f_{\rm esc}$ and allowing for a variation with z, the stellar contribution to the UVB becomes essentially unconstrained.

3.9. Conclusions

Quantifying the metagalactic H I photoionisation rate at $z \gtrsim 4$ remains a challenge. The three available methods all provide estimates that are not inconsistent with each other, but the uncertainties are still considerable. For example, the poorly constrained escape fraction of UV photons in galaxies makes a safe prediction of the UVB from population modelling virtually impossible at present. Likewise, the fundamentally very powerful method to match numerical simulations to the observed opacity evolution of the UVB has to rely on several theoretical assump-

tions that influence the outcome of the simulations. The proximity effect is arguably the most direct way to measure a quantity that can be translated into an estimate of $\Gamma_{\rm H\,I}$. The fundamental issue here is the question whether large-scale H I overdensities around quasars can weaken the proximity effect and thus bias the UVB towards high values. Our SDSS sample provides clear evidence for the presence of such overdensities, but our analysis also suggests that the fraction of QSOs heavily affected by overdensities is small. Certainly our data point at $z \simeq 4.2$ is very robust and unlikely to be affected by any significant overdensity bias.

Compared to previous analyses of the proximity effect in quasar spectra, the main improvement of the present study lies the size of the dataset. It constitutes an increase by a factor of $\sim$ 20 compared to the hitherto largest sample by Scott et al. (2000), at similar spectral resolution, and by a factor of 50 compared to our recent evaluation of 40 high-resolution spectra from VLT/UVES (Chapter 2). At redshifts $z > 4$, our new SDSS dataset contains 34 objects, whereas previous investigations of the proximity effect at such high redshifts were always based on individual objects (Williger et al. 1994; Lu et al. 1996; Savaglio et al. 1997).

We have also introduced an automated continuum determination and correction algorithm, which is of fundamental importance in quantifying the inevitable effects of continuum misplacement. The quality of this correction is impressively demonstrated by the fact that our inferred global evolution of the Lyα forest optical depth is very close to the results of most recent studies using high spectral resolution. We thus conclude that the moderate spectral resolution of the SDSS data has been well accounted for and is not an issue.

In continuation of our previous work on the proximity effect (Paper I and Chapter 2) we have searched for the proximity effect signature not only in the combined sample, but in individual quasar spectra. We detected the effect in 98 % of the objects, with the remaining 2 % all clearly affected by strong associated absorption. With a sample of this size we could construct the 'proximity effect strength distribution' (PESD) in several redshift bins, with 30–600 QSOs contributing to each bin. The observed proximity effect strengths display a considerable dispersion and a pronounced asymmetry. Both the dispersion and the skewness of the PESD decrease with increasing redshift, just as predicted from a simple model of randomly distributed absorption lines following the global line density redshift evolution. While it is clear that quasar absorption lines are not exactly randomly distributed but follow the cosmic web, the distribution of pixel optical depths can be reasonably well described as a random process. In Chapter 2 we predicted a very strong change of the PESD width with redshift, but owing to a sample size of only 40 objects we could not demonstrate the reality of the effect. The SDSS data show this trend very clearly.

The fact that the PESD at higher redshift becomes increasingly narrow has profound implications for the accuracy of measuring the UV background. While any QSO at $z \sim 2$ may show a proximity effect strength that deviates by up to 2 orders of magnitude from the expectation value, the dispersion is much lower at $z \gtrsim 4$, and relatively small samples, even individual objects can give meaningful constraints on the UVB. This is impressively confirmed by the subset of 34 QSOs at $z > 4$ in our sample.

While our measurement of the metagalactic H I photoionisation rate at $z \sim 4$ has yielded a rather high value, it is nevertheless fully consistent with most other recent estimates, certainly within 1–2σ deviations. There is thus a clear trend that the UVB is almost constant between $z \simeq 2$ and $z \simeq 4$, at best it decreases very mildly. It will be a most challenging task in the future to push the current limit of $z \simeq 4$ towards higher redshifts and see whether the UVB continues to be flat, or whether a downturn will be detected.

Acknowledgements. We would like to thank the Astrophysical Research Consortium (ARC) for making the Sloan Digital Sky Survey (SDSS) data archive publicly available. A.D. and L.W. acknowledge support by the Deutsche Forschungsgemeinschaft under Wi 1369/21-1.

References

Agafonova, I. I., Centurión, M., Levshakov, S. A., & Molaro, P. 2005, A&A, 441, 9
Bajtlik, S., Duncan, R. C., & Ostriker, J. P. 1988, ApJ, 327, 570
Bernardi, M., Sheth, R. K., SubbaRao, M., et al. 2003, AJ, 125, 32
Bolton, J. S., Haehnelt, M. G., Viel, M., & Springel, V. 2005, MNRAS, 357, 1178
Bongiorno, A., Zamorani, G., Gavignaud, I., et al. 2007, A&A, 472, 443
Carswell, R. F., Webb, J. K., Baldwin, J. A., & Atwood, B. 1987, ApJ, 319, 709
Carswell, R. F., Whelan, J. A. J., Smith, M. G., Boksenberg, A., & Tytler, D. 1982, MNRAS, 198, 91
Cooke, A. J., Espey, B., & Carswell, R. F. 1997, MNRAS, 284, 552
Cristiani, S., D'Odorico, S., Fontana, A., Giallongo, E., & Savaglio, S. 1995, MNRAS, 273, 1016
Dall'Aglio, A., Wisotzki, L., & Worseck, G. 2008, A&A, 480, 359
Davé, R., Hernquist, L., Katz, N., & Weinberg, D. H. 1999, ApJ, 511, 521
Fan, X., Narayanan, V. K., Strauss, M. A., et al. 2002, AJ, 123, 1247
Fardal, M. A., Giroux, M. L., & Shull, J. M. 1998, AJ, 115, 2206
Faucher-Giguère, C.-A., Lidz, A., Hernquist, L., & Zaldarriaga, M. 2008a, ApJ, 682, L9
Faucher-Giguère, C.-A., Prochaska, J. X., Lidz, A., Hernquist, L., & Zaldarriaga, M. 2008b, ApJ, 681, 831
Gaskell, C. M. 1982, ApJ, 263, 79
Giallongo, E., Christiani, S., D'Odorico, S., Fontana, A., & Savaglio, S. 1996, ApJ, 466, 46
Gunn, J. E. & Peterson, B. A. 1965, ApJ, 142, 1633
Haardt, F. & Madau, P. 1996, ApJ, 461, 20
Haardt, F. & Madau, P. 2001, in Clusters of Galaxies and the High Redshift Universe Observed in X-rays, ed. D. M. Neumann & J. T. V. Tran
Inoue, A. K., Iwata, I., & Deharveng, J.-M. 2006, MNRAS, 371, L1
Kim, T.-S., Bolton, J. S., Viel, M., Haehnelt, M. G., & Carswell, R. F. 2007, MNRAS, 382, 1657
Kim, T.-S., Cristiani, S., & D'Odorico, S. 2001, A&A, 373, 757
Kirkman, D. & Tytler, D. 1997, ApJ, 484, 672
Liske, J., Webb, J. K., & Carswell, R. F. 1998, MNRAS, 301, 787
Liske, J. & Williger, G. M. 2001, MNRAS, 328, 653
Lu, L., Sargent, W. L. W., Womble, D. S., & Takada-Hidai, M. 1996, ApJ, 472, 509
Madau, P., Haardt, F., & Rees, M. J. 1999, ApJ, 514, 648
Meiksin, A. & White, M. 2004, MNRAS, 350, 1107
Meiksin, A. A. 2007, ArXiv e-prints
Murdoch, H. S., Hunstead, R. W., Pettini, M., & Blades, J. C. 1986, ApJ, 309, 19
Ouchi, M., Shimasaku, K., Okamura, S., et al. 2004, ApJ, 611, 660
Peebles, P. J. E. 1993, Principles of Phisical Cosmology (Princeton Univeristy Press)
Péroux, C., McMahon, R. G., Storrie-Lombardi, L. J., & Irwin, M. J. 2003, MNRAS, 346, 1103
Rauch, M. 1998, ARA&A, 36, 267
Rauch, M., Miralda-Escude, J., Sargent, W. L. W., et al. 1997, ApJ, 489, 7

Richards, G. T., Strauss, M. A., Fan, X., et al. 2006, AJ, 131, 2766
Savaglio, S., Christiani, S., D'Odorico, S., et al. 1997, A&A, 318, 347
Schaye, J., Aguirre, A., Kim, T.-S., et al. 2003, ApJ, 596, 768
Schirber, M. & Bullock, J. S. 2003, ApJ, 584, 110
Schneider, D. P., Hall, P. B., Richards, G. T., et al. 2007, AJ, 134, 102
Scott, J., Bechtold, J., Dobrzycki, A., & Kulkarni, V. P. 2000, ApJ, 130, 67
Shen, Y., Strauss, M. A., Oguri, M., et al. 2007, AJ, 133, 2222
Stengler-Larrea, E. A., Boksenberg, A., Steidel, C. C., et al. 1995, ApJ, 444, 64
Suzuki, N. 2006, ApJS, 163, 110
Theuns, T., Leonard, A., Efstathiou, G., Pearce, F. R., & Thomas, P. A. 1998, MNRAS, 301, 478
Tresse, L., Ilbert, O., Zucca, E., et al. 2007, A&A, 472, 403
Tytler, D. & Fan, X.-M. 1992, ApJS, 79, 1
Vanden Berk, D. E., Richards, G. T., Bauer, A., et al. 2001, AJ, 122, 549
Weymann, R. J., Carswell, R. F., & Smith, M. G. 1981, ARA&A, 19, 41
Weymann, R. J., Morris, S. L., Foltz, C. B., & Hewett, P. C. 1991, ApJ, 373, 23
Williger, G. M., Baldwin, J. A., Carswell, R. F., et al. 1994, ApJ, 428, 574
Wolf, C., Wisotzki, L., Borch, A., et al. 2003, A&A, 408, 499
York, D. G., Adelman, J., Anderson, Jr., J. E., et al. 2000, AJ, 120, 1579
Young, P. J., Sargent, W. L. W., Boksenberg, A., Carswell, R. F., & Whelan, J. A. J. 1979, ApJ, 229, 891

Chapter 4

Analysis of methods for detecting the proximity effect in quasar spectra⋆

Aldo Dall'Aglio[1] and Nickolay Y. Gnedin[2,3,4]

[1] Astrophysikalisches Institut Potsdam, An der Sternwarte 16, D-14482 Potsdam, Germany
[2] Particle Astrophysics Center, Fermi National Accelerator Laboratory, Batavia, IL 60510, USA
[3] Kavli Institute for Cosmological Physics, The University of Chicago, Chicago, IL 60637, USA
[4] Department of Astronomy & Astrophysics, The University of Chicago, Chicago, IL 60637 USA

ABSTRACT

Using numerical simulations of structure formation, we investigate multiple methods of determining the strength of the proximity effect in the H I Lyα forest. We analyse three high resolution ($\sim$ 10 kpc) redshift snapshots ($\overline{z}$ = 4, 3 and 2.25) of a Hydro-Particle-Mesh simulation to obtain realistic absorption spectra of the H I Lyα forest. We model the proximity effect along the simulated sight lines with a simple analytical prescription based on the assumed quasar luminosity and the intensity of the cosmic UV background. We begin our analysis investigating the intrinsic biases thought to arise in the widely adopted *standard technique* of combining multiple lines of sight when searching for the proximity effect. We confirm the existence of this biases, albeit smaller than previously predicted with simple Monte Carlo simulations. We then concentrate on the analysis of the proximity effect along individual lines of sight. After determining its strength with a fiducial value of the UV background intensity, we construct the proximity effect strength distribution (PESD). We confirm that the PESD inferred from the *simple averaging technique* accurately recovers the input strength of the proximity effect at all redshifts. Moreover, the PESD closely follows the behaviours found in observed samples of quasar spectra. However, the PESD obtained from our new simulated sight lines presents some differences to that of simple Monte Carlo simulations. At all redshifts, we identify in the smaller dispersion of the strength parameters, the source of the corresponding smaller biases found when combining multiple lines of sight. After developing three new theoretical methods of recovering the strength of the proximity effect on individual lines of sight, we compare their accuracy to the PESD from the *simple averaging technique*. All our new approaches are based on the maximisation of the likelihood function, albeit invoking some modifications. The new techniques presented here, in spite of their complexity, fail to recover the input proximity effect in an un-biased way, presumably due to some (unknown) higher order correlations in the spectrum. Thus, employing complex 3D simulations, we provide strong evidence in favour of the proximity effect strength distribution obtained from the *simple averaging technique*, as method of estimating the UV background intensity, free of any intrinsic biases.

4.1. Introduction

The transition from a neutral to an ionised state of the baryonic matter in the Universe, known as the *epoch of reionisation*, also resulted in the appearance of the cosmic ultra-violet background radiation field (UVB). While it is still debated whether more exotic objects and processes (like mini-quasars or dark matter annihilation) had significant influence on the process of reionisation (Haiman & Loeb 1998; Ricotti & Ostriker 2004), it is widely accepted that young star-forming galaxies and quasars are the primary sources of this radiation field in the post-reionisation era ($z < 6$). Thus, after reionisation, any change in the properties of the source population is reflected in the evolution of the UV background (UVB, Haardt & Madau 1996; Fardal et al. 1998; Haardt & Madau 2001). Accurate estimates of the UVB intensity at different redshifts therefore provide important constraints on the evolution of star-forming galaxies and quasars in the Universe.

The most direct probe for the UVB is the ionisation state of the intergalactic medium (IGM). Mainly consisting of hydrogen and helium, the IGM becomes detectable as the light from high redshift ($z > 2$) quasars travels toward us through the intergalactic space. Numerous absorption lines observed at wavelength shorter than the rest frame Lyα transition, known as the Lyα forest, arise from the small fraction of neutral matter (about 1 part in 100,000) in the IGM (Sargent et al. 1980; Weymann

⋆ A version of this Chapter will be submitted to the *Astrophysical Journal*.

et al. 1981; Rauch 1998). The UVB is directly responsible for keeping the IGM ionised at this level, thus encoding its intensity (and, to a lesser extent, its spectrum) in the absorption profiles of the Lyα forest.

Observationally, the only technique known so far to *directly* infer the photoionisation rate or, equivalently, the UVB intensity over some a range of wavelengths is based on the so-called *proximity effect*. This effect is the manifestation of the IGM response to a systematic enhancement of UV radiation around bright quasars.

In the vicinity of a bright quasar, its UV radiation becomes several orders of magnitudes stronger than the cosmic UVB, leading to the decreased absorption blueward of the quasar Lyα emission line (Weymann et al. 1981; Carswell et al. 1982; Murdoch et al. 1986). If the quasar luminosity is known, and the relative enhancement in the UV flux near the quasar relative to the average Universe is measured from the Lyα absorption spectra, the strength of the cosmic UVB can be deduced from the proximity effect (Carswell et al. 1987; Bajtlik et al. 1988). While the proximity effect has been detected for more than a decade, primarily in large samples of quasars (e.g. Bajtlik et al. 1988; Lu et al. 1991; Giallongo et al. 1996; Cooke et al. 1997; Scott et al. 2000; Liske & Williger 2001), recent investigations of its signature along individual lines of sight have been employed to develop a new technique for estimating the UVB intensity (Dall'Aglio et al. 2008, Chapter 2).

This new approach is based on the analysis of the proximity effect strength distribution (PESD). Two distinct features appear in the analysis of the PESD. First, the strength distribution shows a clear peak and, second, it is significantly asymmetric. The peak of the PESD directly relates to the intensity of the UVB, whereas its asymmetry is mainly the result of low number statistics in the absorber counts near the quasar emission (Chapter 2).

This approach is nevertheless subject to a large dispersion, as it is based on the detection of the proximity effect along individual sight lines. Such a dispersion is inversely related to the change in the opacity in the Lyα forest, and it is further amplified by effects like overdensities or quasar variability which are poorly understood. We are therefore motivated to initiate a theoretical investigation on the methodological approach of estimating the strength of the proximity effect.

The plan of the Chapter is as follows. We begin with a description of the type of simulations employed in Sect. 4.2. We then describe in detail in Section 4.3 the computation and calibration of the synthetic sight lines generated through the simulation box. Section 4.4 introduces the theoretical approach adopted to include the proximity effect on the lines of sight. We report in Sect.4.5 our results for different approaches in estimating the proximity effect signature on individual objects. We then present our conclusions in Sect. 4.6.

4.2. Simulations

In order to simulate moderate volumes of the Universe at high accuracy but with limited computational resources, we use the Hydro-Particle-Mesh (HPM) code developed by Gnedin & Hui (1998). This particular class of numerical codes differs from those following only the dark matter, in its capability of modelling both the dark matter and the baryonic components of the Universe. However, an HPM simulation is not as computationally expensive as a full hydrodynamical one.

Table 4.1. Input parameters of the HPM simulation.

Parameter	Value	Parameter	Value
Ω_m	0.237	N_p	1024^3
Ω_Λ	0.763	Mesh	1024^3
Ω_b	0.041	Cell size	$0.01^\ddagger$
h	$0.735^\dagger$	Box size	$10.24^\ddagger$
σ_8	0.742	$\bar{z}$	4.0, 3.5, 3.25, 2.75, 2.5, 2.25

†: in units of 100 km s^{-1} Mpc^{-1}
‡: in units of Mpc

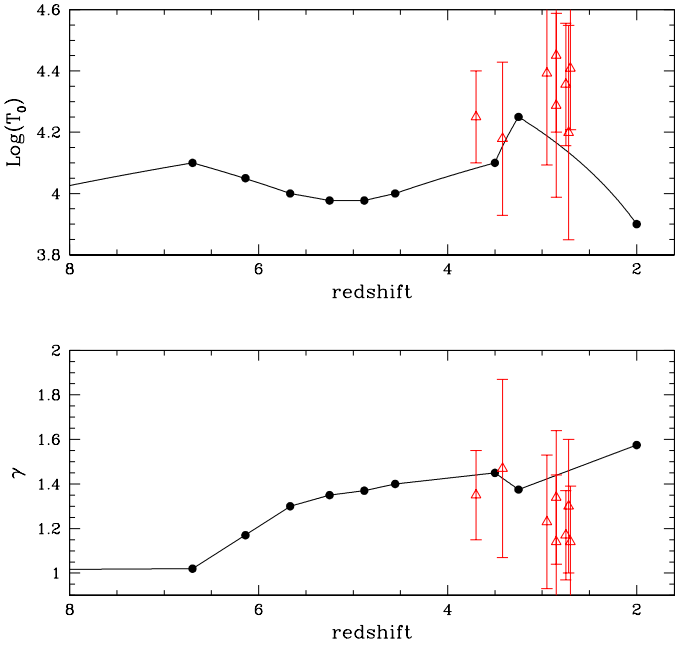

Fig. 4.1. Adopted evolution of T_0 and $\tilde{\gamma}$ with redshift, in comparison with measurements of the equation of state from Ricotti et al. (2000) (triangles).

The IGM consists of the low density cosmic gas between collapsed objects. In this low density regime there exists a tight correlation between the gas density and temperature in the form

$$T = T_0(1+\delta)^{\tilde{\gamma}-1}, \tag{4.1}$$

where δ is the baryonic density contrast, T_0 is the temperature at the mean density, which is of the order of 10^4K and $\tilde{\gamma}$ ranges between 1 and 1.6. For this reason, the thermal history of the low density component of the IGM can be described with high accuracy by the evolution of the two parameters T_0 and $\tilde{\gamma}$. Both parameters are functions of time and are sensitive to the ionisation history of the Universe. Equation 4.1, also known as the *effective equation of state*, immediately provides the thermal pressure of the gas as a function of density, thus removing the need for a full hydrodynamical solver in the code (Hui et al. 1997; Gnedin & Hui 1998).

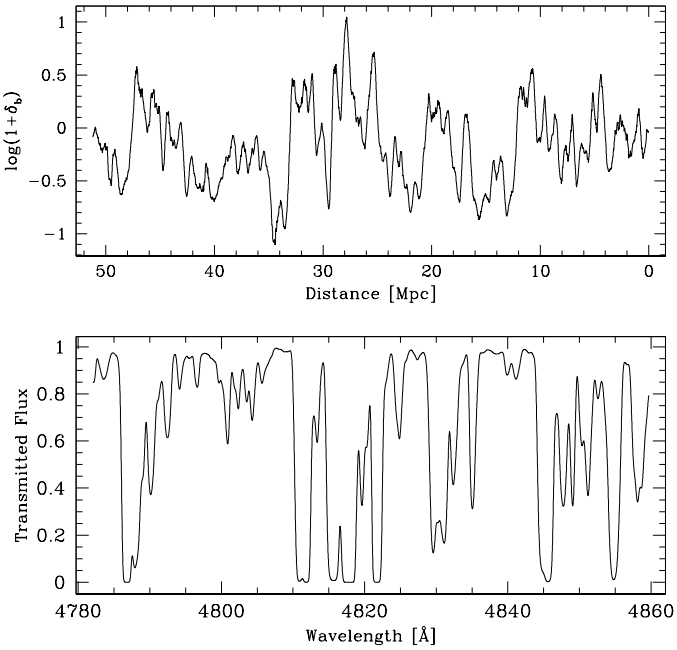

Fig. 4.2. Example of a sight line drawn through the simulation box at redshift $z = 3$. *Top panel:* baryonic overdensity as a function of position along the line of sight. The distance scale corresponds to the x coordinate of Equation 4.2 (see text for more details). *Bottom panel:* the inferred hydrogen transmitted flux as a function of wavelength.

The thermal evolution of the IGM after reionisation is mainly determined by the balance between adiabatic cooling (expansion of the Universe) and photoionisation heating of cosmic gas. Additional effects that influence the effective equation of state include Compton heating from X-ray sources (e.g. Madau & Efstathiou 1999) and radiative transfer effects during He II reionisation (e.g. Maselli & Ferrara 2005). In this work we adopt an empirical approach, and use observational constraints on the effective equation of state to ensure that the thermal state of the Lyα forest in our models is realistic.

Observational constraints on the parameters T_0 and $\tilde{\gamma}$ come from analyses of Lyα absorption lines (Ricotti et al. 2000; Schaye et al. 2000; McDonald et al. 2001a), from the Doppler parameter distribution as a function of column density. The lower cut-off of the $b - N$ distribution can be fitted by a power law $b = b_{N_0}(N/N_0)^{\beta}$, in which the proportionality constant b_{N_0} and the power law index β directly relate to T_0 and $\tilde{\gamma}$, respectively.

The effective equation of state in the simulation was set in a piece-wise manner in three different intervals. At $z < 4.5$ we used the observed evolution of T_0 and $\tilde{\gamma}$ (Ricotti et al. 2000; Schaye et al. 2000; McDonald et al. 2001a). Between $z = 6.5$ and $z = 4.5$ we used the effective equation of state from reionisation simulations of Gnedin & Fan (2006); these simulations match well the observed Lyα opacity in the spectra of high redshift quasars discovered in the Sloan Digital Sky Survey (SDSS) and smoothly merge with the observational constraints on T_0 and $\tilde{\gamma}$ at $z \approx 4.5$. Finally, during the reionisation era ($z > 6.5$) T_0 and $\tilde{\gamma}$ were assumed to increase linearly with the scale factor. This assumption is somewhat uncertain, but it is approximately consistent with high resolution numerical simulations of reionisation (Gnedin 2004; Gnedin & Fan 2006) and has a negligible effect on the thermal state of the Lyα forest at our redshifts of interest, $2 < z < 4$. Figure 4.1 shows the parameterised values of T_0 and $\tilde{\gamma}$ as a function of cosmic time up to the final redshift used in the simulation.

For the purpose of this work we are not interested in an accurate calibration of the effective equation of state with all observational constraints, simply because these parameters are poorly estimated yielding a large scatter of results (McDonald et al. 2001b; Schaye et al. 2000). The relevant fact is that Eq. 4.1 defines the underlying equation of state and that T_0 and $\tilde{\gamma}$ do evolve with redshift according to a specific ionisation history.

Following the results of the Wilkinson Microwave Anisotropy Probe three years data (WMAP3, Spergel 2006), Tab.4.1 lists the parameters adopted to generate the simulations discussed in this work. Here Ω_m is the total matter density parameter, Ω_Λ is the cosmological constant and Ω_b is the baryon density parameter. The Hubble constant is h expressed in units of 100 km s^{-1} Mpc^{-1} and σ_8 represents the rms density fluctuation on 8 h^{-1} Mpc scales at $z = 0$. We fixed the box size to 10.24 h^{-1} Mpc with $N_p = 1024^3$ particles on a 1024^3 mesh. This yields a resolution element of 10 h^{-1} kpc ensuring an accuracy on a few km s^{-1} scale in the generation of the artificial quasar spectra (see section 4.3.1). We recorded the state of the simulation of seven different redshifts denoted by $\overline{z}$.

4.3. The Lyman forest

4.3.1. Computation of the H I absorption

The final product of an HPM simulation consists of a cosmological box (one at each $\overline{z}$), containing information about the hydrogen density contrast δ_b and the relative spatial velocity (v_x, v_y, v_z). We use this information to compute a set of absorption spectra as follows. We draw a set of 500 randomly distributed sight lines through the box obtaining along each line of sight a spatial coordinate plus velocity and density information. In order to compute the absorption spectrum of the Lyα forest, we follow the methodology of Hui et al. (1997), which we briefly summarise here.

The optical depth of the Lyα forest at the observed wavelength λ_0 is given by

$$\tau(\lambda_0) = \int_{x_A}^{x_B} n_{\mathrm{H\,I}} \sigma_\alpha \frac{\mathrm{d}x}{1+z}, \tag{4.2}$$

with x being the comoving radial coordinate along the line of sight, z is the redshift and $n_{\mathrm{H\,I}}$ is the neutral hydrogen density at location x. The Lyα absorption cross section is σ_α.

If we expand the redshift scale around the mean redshift of interest $\overline{z}$ (in our case the snapshot redshift of our simulation), we can introduce a new coordinate u defined as

$$u \equiv \frac{\overline{H}}{1+\overline{z}}(x - \overline{x}) + v_{\mathrm{pec}}(x) \tag{4.3}$$

where $\overline{x}$ is the position at which the redshift due to cosmological expansion is equal to the snapshot redshift $\overline{z}$. For simplicity we assume that the line of sight starts at the snapshot redshift, thus at $\overline{x} = 0$.

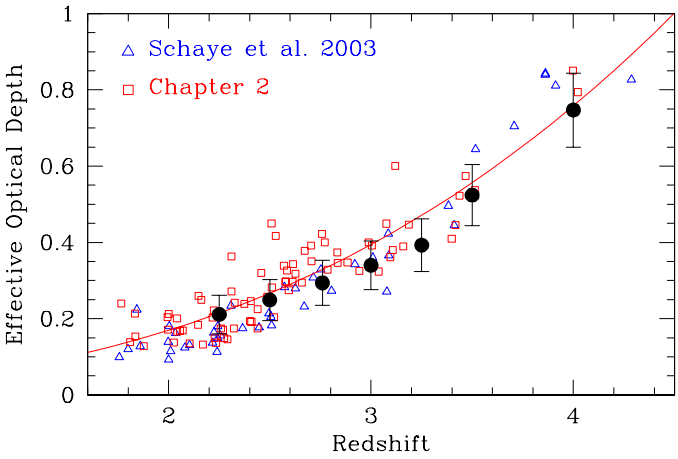

Fig. 4.3. Effective optical depth evolution in our simulated sight lines in comparison with observations. The solid circles are the average values of $\tau_{\rm eff}$ in our synthetic spectra with the relative dispersions. Triangles and squares represent the measurements performed by Schaye et al. (2003) and Chapter 2 respectively, employing different samples of high resolution quasar spectra. The solid line represents the best-fit solution of Eq. 4.7 recently estimated in Chapter 2.

It is convenient to substitute the observed wavelength λ_0 with a new velocity coordinate u_0, which is related to λ_0 by

$$\lambda_0 = \lambda_\alpha\,(1+z)\left(1-\frac{u_0}{c}\right)^{-1} \tag{4.4}$$

where $\lambda_\alpha = 1215.67$Å. In this notation the optical depth becomes

$$\tau(u_0) = \sum \int_{u_A}^{u_B} \frac{n_{\rm H\,I}}{1+z}\sigma_\alpha \left|\frac{{\rm d}u}{{\rm d}x}\right|^{-1} {\rm d}u, \tag{4.5}$$

where

$$\sigma_\alpha = \sigma_{\alpha,0}\frac{c}{b\,\sqrt{\pi}}\exp\left(-(u-u_0)^2/b^2\right). \tag{4.6}$$

The limits of integration u_A and u_B correspond to the velocity values of the positions x_A and x_B. The value of $\sigma_{\alpha,0}$ depends only on fundamental constants and is approximately 4.5×10^{-18} cm^2. The Doppler parameter b is equal to $\sqrt{2k_BT/m_p}$, where k_B is the Boltzmann constant, T is the gas temperature at the velocity u, and m_p is the proton mass. In order to compute the gas temperature at a given velocity and for a particular snapshot, we used our equation of state parameterisation $(T_0, \tilde{\gamma})_z$. The sum in the integral accounts for velocity caustics, where one value of u corresponds to more than one x.

The final step in the computation of an absorption spectrum consists of deriving the neutral hydrogen fraction $X_{\rm H\,I}$ from the baryonic overdensity δ_b estimated with our HPM code. The neutral fraction is determined by the balance between photoionisation and recombination, and it depends both on the temperature T and the intensity of the UV background $J_{\rm H\,I}$. The temperature typically is a function of the position and is determined by the effective equation of state, while the intensity of the UVB is, in our case, a free parameter. An illustrative example of the result of our procedure is shown in Fig. 4.2.

Table 4.2. The UV background intensity and the effective optical depth in the simulations.

z	$J_{\rm H\,I}/10^{-21\,\dagger}$	$\tau_{\rm eff}$
4.00	0.25	0.75 ± 0.09
3.50	0.30	0.52 ± 0.08
3.25	0.30	0.39 ± 0.07
3.00	0.35	0.34 ± 0.06
2.76	0.40	0.29 ± 0.06
2.50	0.40	0.25 ± 0.05
2.25	0.40	0.21 ± 0.05

†: in units of erg cm^{-2} s^{-1} Hz^{-1} sr^{-1}

Finally, the absorption spectrum should match two observational constraints: (i) the evolution of the effective optical depth in the Lyα forest and (ii) the flux probability distribution function. To accurately calibrate our simulation, we employed the sample of 40 high resolution ($R \sim 45\,000$), high S/N ($S/N \sim 70$) quasar spectra obtained with the UV-Visual Echelle Spectrograph (UVES), probing a redshift interval between $z \sim 1.8$ and $z \sim 4.6$ (Chapter 2). Our simulated spectra are computed with the same spectral resolution as the observed sample, and in a similar redshift range, thus the two data sets can be directly compared.

The calibration of the simulated absorption spectra has been carried out iteratively. As the main goal of this work is to test and compare different methods of estimating the proximity effect signature, we do attempt to match exactly the synthetic and observed spectra. Rather, we adjust the intensity of the UV background to obtain an acceptable (but not necessarily the best) match between the simulated sight lines and the observed flux probability distribution and the evolution of the effective optical depth from the UVES observations. The final values of the UV background are listed in Tab. 4.2.

A complete study of how well the synthetic spectra can match the observed data would require a much more careful comparison between the model and the data, including modelling the observational procedure of determining the continuum level, thorough sampling of possible temperature-density relations in the modelled forest, etc. While such effort is well worth performing, it is beyond the scope of this Chapter and we postpone it to a future work.

4.3.2. The evolution of the effective optical depth

One fundamental observed property of the Lyα forest is a steep decline in the hydrogen opacity towards low redshift. This behaviour is reflected in the so called effective optical depth, which is defined as $\tau_{\rm eff} = -\ln\langle F\rangle = -\ln\langle e^{-\tau_{\rm H\,I}}\rangle$ where F is the transmitted flux and the averaging $\langle\rangle$ is performed over a fixed redshift path length. The redshift evolution of $\tau_{\rm eff}$ is well approximated by a power law in the form

$$\tau_{\rm eff} = \tau_0(1+z)^{\gamma+1} \tag{4.7}$$

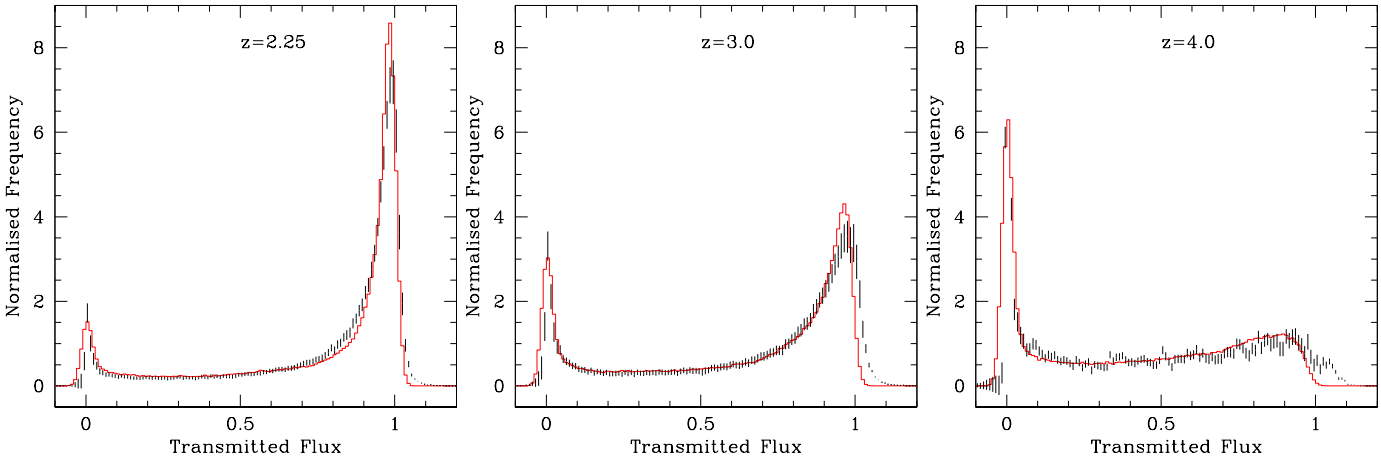

Fig. 4.4. The average flux probability distribution (FPD) estimated from 500 simulated sight lines at three different redshifts (z = 2.25, 3.0 and 4.0, solid red histogram), in comparison with the observed FPD inferred from a sample of 40 high resolution UVES/VLT quasar spectra (vertical bars). The uncertainties in the simulated FPD are negligible, while the error bars in the observed FPD account for the variance of absorption between different lines of sight and uncertainties in the continuum determination.

(Kim et al. 2002; Faucher-Giguère et al. 2008), where the slope γ has no direct connection to the slope $\tilde{\gamma}$ of the equation of state (see Eq. 4.1).

The main difference between observed spectra of the Lyα forest and our synthetic realizations is the lack of any evolution of $\tau_{\rm eff}$ with redshift along individual sight lines in the latter. This is simply because our simulated spectra are drawn through a single cosmological box at one particular redshift. Thus, for each snapshot, we can estimate the mean $\tau_{\rm eff}$ and its dispersion starting from a measure of the average transmitted flux along each of the 500 simulated lines of sight and normalising to the whole redshift interval probed by the observed spectra.

Figure 4.3 shows our results from the simulated sight lines into context while Tab. 4.2 lists the numerical values. For all snapshots at our disposal, the inferred average effective optical depth closely follows the expected enhancement at high redshift as probed by different investigations on high resolution quasar spectra (Schaye et al. 2003, Chapter 2). Note that the uncertainties on the effective optical depths represent the RMS of $\tau_{\rm eff}$ determined on each single line of sight and not the real uncertainties of the measurements.

4.3.3. The flux probability distribution

The steep evolution of the hydrogen opacity in the Lyα forest described in the previous section can be detected in quasar spectra not only by measuring the average transmitted flux, but also by analysing how the shape of the flux probability distribution (FPD) changes with redshift (Jenkins & Ostriker 1991). The FPD provides a strong observational constraint, which it is important to be satisfyingly reproduced by a realistic model of the Lyα forest.

We employ similar approaches to compute the FPD in the simulated and in the observed spectra. Both (the synthetic and simulated) distributions are sampled in bins of $\Delta F = 0.01$ and normalised by the bin size to maintain the condition that the FPD integrates to 1.

The observed FPD is estimated from the Lyα forest of those quasars intersecting a redshift slice of $\Delta z = 0.2$, centred at the redshift of the simulated snapshot ($\overline{z}$ in Tab. 4.1). The FPD for the synthetic spectra is measured by combining the signal for all 500 lines of sight at one particular $\overline{z}$. Additionally, we add Gaussian noise to the simulated line of sight in order to reproduce the average S/N level of the observed spectra.

Figure 4.4 presents the comparison between the two estimates of the flux probability distribution. The agreement between the two distributions is reasonably good even if there are some indications of a departure at high redshift, in particular for the flux around unity. This lack of agreement is explained by the differences in the continuum placement of the observed and synthetic spectra. Additionally, we note that the error bars of the observed FPD are an estimate of both continuum uncertainties and Poissonian variance between different lines of sight. For the continuum uncertainties we adopted the estimates presented in Chapter 2.

4.3.4. The column density distribution

The high resolution of our simulations allows us to further characterise the statistical properties of synthetic spectra by measuring the distribution of column densities. The differential distribution function of the hydrogen column densities $f(N_{\rm H\,I})$ is typically defined as the number n of absorption lines per unit column density and per unit absorption path length ΔX[1] (Tytler 1987). This distribution is typically very well represented by a single power law of the form $f(N_{\rm H\,I}) \propto N_{\rm H\,I}^{-\beta}$ with β ranging between 1.4 – 1.7 (Hu et al. 1995; Kim et al. 2002).

Performing a fit of an absorption spectrum is computationally expensive, therefore we proceeded as follow: (i) we ran-

[1] $\Delta X = (1+z)\,\Delta z \left[\Omega_{\rm m}(1+z) + \Omega_\Lambda (1+z)^{-2}\right]^{-1/2}$ (Misawa et al. 2002)

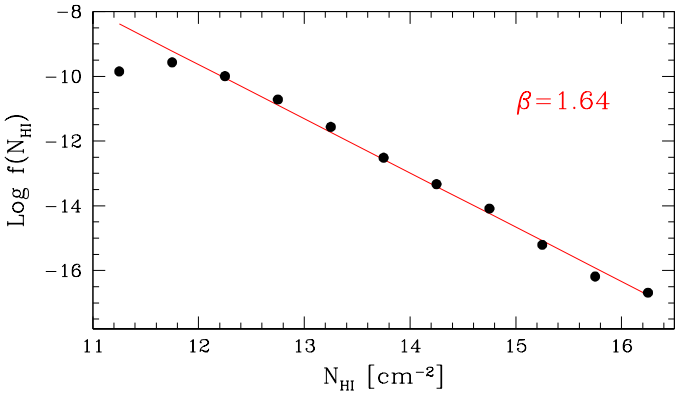

Fig. 4.5. The differential distribution function of the H I column densities estimated from a sample of 300 simulated sight lines at redshift $z = 2.25,\ 3.0$ and 4.0 (100 sight lines per redshift). The solid line represents the least square power law fit to the data points. The measured slope of the column density distribution ($\beta = 1.64$) is consistent with observations by Kim et al. (2002).

domly select 100 simulated sight lines from our full sample of 500, (ii) for each selected line of sight we performed a Doppler profile fit using the publicly available code AUTOVP[2], and then (iii) we visually inspected all the lines of sight in order to reject the few cases where the automatic fitting procedure fails. We repeat this procedure for sight lines drawn from the snapshot at $\overline{z} = 4.0,\ 3.0$ and 2.25 and then combine the results.

The estimated column density distribution is plotted in Fig. 4.5. Within the range $12 \lesssim \log N_{\rm H\,I} \lesssim 16$ cm^{-2}, the distribution accurately follows a power law with a slope of $\beta = 1.64$, close to several observational results (Tytler 1987; Hu et al. 1995; Kim et al. 2002). Our data points seem to deviate from a power law extrapolation at the low column density end. This effect, discussed in detail by Hu et al. (1995), is the result of incompleteness in the sample of lines arising primarily from line blending and further amplified by noise.

4.4. The proximity effect

The prime goal of this work is to test different techniques for detecting the proximity effect in quasar spectra. We have now a set of simulated sight lines at our disposal accurately reproducing many statistical properties of the observed Lyα forest. We now dicuss how we introduced the proximity effect in the simulated spectra.

In the vicinity of a luminous quasar, the intensity of UV radiation produced by the quasar itself is typically up to several orders of magnitudes larger than the intensity of the UV background. This enhanced ionising radiation acts on the neutral hydrogen which, after a period of only about 10^4 yr after the quasar turn-on event, reaches a new state of photoionisation equilibrium. In this regime, the neutral hydrogen density of the IGM in the absence of the quasar ionising radiation, $n_{\rm H\,I,\infty}$, relates to that with the quasar radiation, $n_{\rm H\,I}$, as

$$n_{\rm H\,I} = \frac{n_{\rm H\,I,\infty}}{1+\omega}, \tag{4.8}$$

[2] Developed by R. Davé: http://ursa.as.arizona.edu/~rad

where ω describes the excess of ionising radiation in the vicinity of the quasar in units of the average cosmic UV background (Bajtlik et al. 1988). Analytically, ω can be expressed in units of the UVB photoionisation rate $\Gamma_{\rm b}$ or in units of its intensity at the Lyman limit J_{ν_0},

$$\omega(z) = \frac{\Gamma_{\rm q}}{\Gamma_{\rm b}} \approx \frac{f_{\nu_0}}{4\pi J_{\nu_0}\,(1+z)} \left(\frac{d_L(z_{\rm q},0)}{d_L(z_{\rm q},z)}\right)^2 \tag{4.9}$$

where z is the redshift along the line of sight ($z < z_{\rm q}$), $d_L(z_{\rm q},0)$ is the luminosity distance of the quasar to the observer, and $d_L(z_{\rm q},z)$ is the luminosity distance to redshift z along the line of sight. The parameters $\Gamma_{\rm q}$ and f_{ν_0} quantify the photoionisation rate and the Lyman limit flux of the quasar, respectively. If we isolate the redshift dependence in Eq. 4.9 from the constants, we can define a new, unit-less parameter $\omega_\star$, which is independent of the quasar redshift and is given by

$$\omega_\star = \frac{L_{\nu_0}(z_{\rm q})}{(4\pi R_0)^2 J_{\nu_0}}, \tag{4.10}$$

where $R_0 = 10$ Mpc is an arbitrary distance scale introduced to make $\omega_\star$ unit-less (it also appears in Eq. 4.11). For quasars with typical Lyman limit luminosities in the range $30.5 < \log(L_{\nu_0}) < 32.5$ and a constant UVB intensity $J_{\nu_0} = 10^{-21.51}$ in units of erg cm^{-2} s^{-1} Hz^{-1} sr^{-1} (Chapter 2), we obtain $0.07 \lesssim \omega_\star \lesssim 1.5$. With our new definitions, Eq. 4.9 becomes

$$\omega(z) = \omega_\star\,\frac{1+z_{\rm q}}{1+z}\left(\frac{R_0}{d_L(z_{\rm q},z)}\right)^2. \tag{4.11}$$

From an observed quasar spectrum, any information about the neutral hydrogen density or the velocity field of the gas along the line of sight cannot be derived. Therefore, the main strategy to recover the influence of the quasar ionisation field on the Lyα forest is to translate the implications of Eq. 4.8 into observables such as the transmitted flux or the effective optical depth along the line of sight. Assuming that the optical depth follows the same type of relation as the neutral hydrogen density in Eq. 4.8, Liske & Williger (2001) included the quasar proximity effect into $\tau_{\rm eff}$,

$$\tau_{\rm eff} = \tau_0(1+z)^{\gamma+1}(1+\omega)^{1-\beta}. \tag{4.12}$$

In the case of our simulated lines of sight, the term expressing the evolution of the effective optical depth in the Lyα forest, $\tau_0(1+z)^{\gamma+1}$, will be substituted by the average $\langle\tau_{\rm eff}(\overline{z})\rangle$ at each snapshot redshift as listed in Tab. 4.2. In the rest of this Chapter, it will be convenient to use a variable ξ defined as

$$\xi = \frac{\tau_{\rm eff}}{<\tau_{\rm eff}(\overline{z})>} = (1+\omega)^{1-\beta}, \tag{4.13}$$

where β is the slope of the column density distribution.

We note that assuming the validity of Eq. 4.8 also for the optical depth along a line of sight implies that the peculiar velocity of the hydrogen in the IGM has a negligible impact on the absorption spectrum. This assumption is impossible to test observationally, but it can be justified with the simulated spectra. We have the unique possibility of estimating this effect for the first time. We thus proceed as follows: (i) we compute a set of 100 sight lines at three different redshifts ($z_{\rm q} = 2.25,\ 3$ and

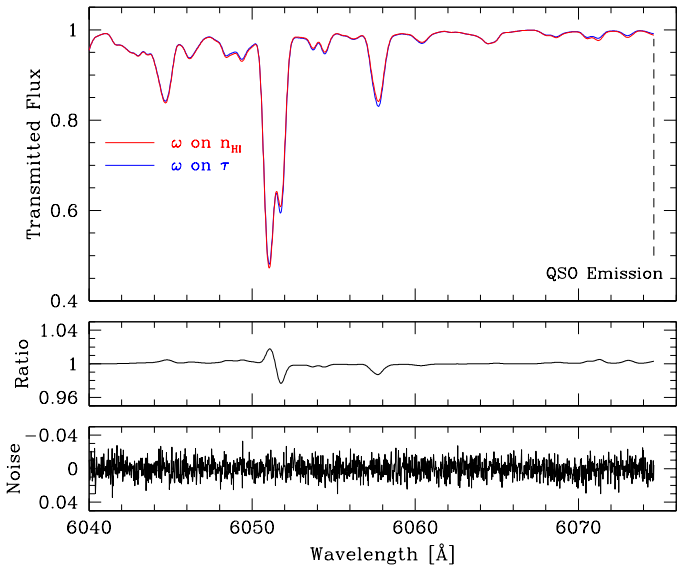

Fig. 4.6. Example of one simulated line of sight with the signature of the proximity effect introduced on the density of neutral hydrogen (red line) and on the optical depth (blue line). The difference between the two absorption patterns are due to the peculiar velocities along the sight line, which are neglected whenever the proximity effect is introduced on the optical depth. The middle panel shows the ratio between the two spectra. While the influence of peculiar velocities leads to a minor discrepancy between the two spectra, this difference is drowned in the noise even in high S/N spectra, as is shown in the bottom panel (S/N=100).

4) as described in Sect. 4.3.1 and include the proximity effect as a modification of the optical depth along the line of sight, or, alternatively, (ii) we included Eq. 4.8 into Eq. 4.5, meaning that we include the proximity effect on the hydrogen density, and then compute the same line of sight as in (i). Figure 4.6 presents the result of such a computation of the proximity effect on both the optical depth and the neutral hydrogen density. Peculiar velocities lead to a discrepancy between the two proximity effect profiles, however this difference cannot be detected, since it is dominated by noise even in high S/N quasar spectra ($S/N \sim 100$).

In the following, the proximity effect is included in the simulated spectra as a modification of the neutral hydrogen density according to Equations 4.8 and 4.11. We note that the origin of all the lines of sight is random, thus the location of the quasar (but not its emission redshift) is also random. We therefore neglect in the present analysis any effect of a biased quasar environment, i.e. overdensities. While our results do change quantitatively if we vary $\omega_\star$, the qualitative outcome of our analysis is independent of a particular choice of its numerical value. Therefore, by default we adopt $\omega_\star \equiv \omega_\star^{\rm IN} = 1$, unless stated otherwise.

4.5. Methods of estimating the proximity effect strength

4.5.1. Reference approach: the combined proximity effect

Among all the investigations of quasar spectra aimed at detecting of the proximity effect, two techniques have been employed so far: (i) the line counting statistic and (ii) the flux transmission statistic. Both adopt the common principle of estimating a certain quantity (number of lines or average transmission) within a regularly spaced grid in a sample of quasars. As we already showed in Chapter 2 the advantages of the flux transmission with respect to the line counting statistics, we will use only the flux transmission statistic as our reference technique.

For each of the simulated spectra, and given the "input" value $\omega_\star^{\rm IN}$, we construct the ω scale according to Eq. 4.11 and then define a uniform grid in $\log\omega$ space. In each of the grid elements we determine the average flux and, thus, the effective optical depth values considering all spectra simultaneously. Finally, following Eq. 4.13, we derive the corresponding values of ξ as a function of ω. The typical proximity effect signature is such that $\xi \to 0$ for $\omega \to \infty$ and it can be analytically modelled according to the formula

$$F(\omega) = \left(1 + \frac{\omega}{a}\right)^{1-\beta}, \qquad (4.14)$$

where the slope of the column density distribution was fixed to $\beta = 1.64$ at all redshifts according to our measurements (Sect. 4.3.4), and a is a single fitting parameter. The best-fit value of a can then be used to compute the "measured" value of the proximity effect strength $\omega_\star^{\rm OUT} \equiv a\,\omega_\star^{\rm IN}$. Ideally, this value should be close to the input value $\omega_\star^{\rm IN}$ (i.e. a should be close to 1).

This technique has been employed in the majority of the proximity effect investigation aiming at a constraint of the cosmic UV background intensity at the Lyman limit since $\omega_\star^{\rm OUT} \propto J_{\nu_0}^{-1}$. In Chapter 2 we first showed that this combined method is characterised by an intrinsic bias. Employing Monte Carlo simulations, we presented evidence for this bias by comparing the input and output proximity effect signal in a set of 500 synthetic spectra.

While a Monte Carlo approach may be sufficient when efficiently simulating the "randomness" in the properties of the absorbers, the new sight lines presented here are a significant step forward in terms of accurately reproducing the statistical properties of the Lyα forest. We begin our investigation comparing the results on the combined analysis of the proximity effect on both the Monte Carlo and the numerical simulated lines of sight. The Monte Carlo simulated spectra have been computed using the same procedure as in Chapter 2. In all cases we employed the signal of 500 spectra including the proximity effect in the same way as described in Sect. 4.4.

We fitted Eq. 4.14 to the values of ξ determined from a combination of all sight lines. Repeating this exercise at $\overline{z} = (2.25, 3.0, 4.0)$ we obtained for the Monte Carlo simulations an overestimation in $\omega_\star^{\rm OUT}$ equal to $\Delta\log a = (0.14, 0.1, 0.05)$ dex, respectively, while for the HPM simulations we obtained $\Delta\log a = (0.1, 0.01, 0.01)$ dex. This, on the one hand confirms the existence of the bias, but on the

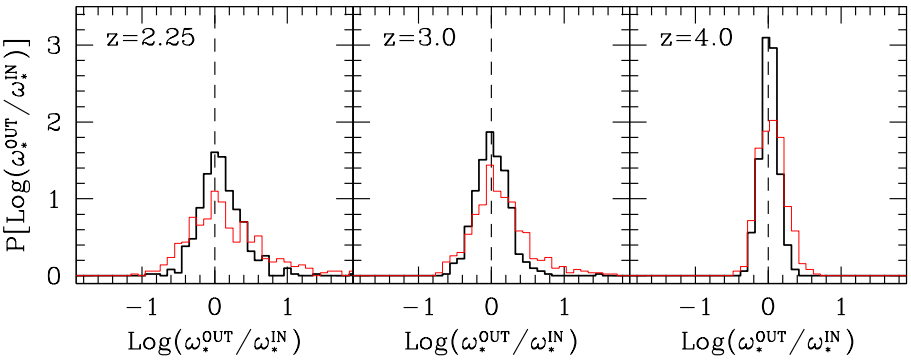

Fig. 4.8. The proximity effect strength distribution (PESD) in three different sets of 500 sight lines drawn from our HPM simulation boxes at redshift $\overline{z} = 2.25,\ 3.0$ and 4.0 (thick black histogram). The thin red histogram represents the PESD obtained from a sample of 500 Monte Carlo simulated lines of sight. For both types of simulations we determined the proximity effect strength adopting the best-fit $\log a$ value of Eq. 4.14. The vertical dashed line marks the reference model used for creating synthetic Lyα forest spectra.

other hand shows that the Monte Carlo simulations tend to overestimate it. In particular, at $\overline{z} = 3.0$ the HPM simulated sight lines predict an almost negligible overestimation. We suspect that the origin of this marginal disagreement may be primarily attribute to the procedure that generates Monte Carlo absorption spectra. The algorithm does not place a fixed number of absorption lines, instead continues to populate the spectrum with as many line as necessary to yield an evolution of $\tau_{\rm eff}$ consistent with a pre-fixed power law. This may then translate into a larger scatter of absorption very close to the emission redshift, thus enhancing the systematic bias when combining multiple sight lines. We also cannot rule out the possibility that the calibration of our new synthetic spectra against observations has an effect in reducing the bias of the combined analysis of the proximity effect.

4.5.2. The proximity effect strength distribution

A correct understanding of the biases involved in the combined analysis of the proximity effect is essential to accurately determine the cosmic UV background intensity. We proposed in Chapter 2 a new technique of measuring the UVB intensity, unaffected by the biases described in the previous section. This approach is based on the determination of the proximity effect along individual lines of sight in a quasar sample. Always adopting Monte Carlo simulated lines of sight at different redshifts, they fitted Eq. 4.14 to individual spectra and showed that

1. the distribution of $\log \omega_\star^{\rm OUT}/\omega_\star^{\rm IN} \equiv \log a$ is skewed
2. the skewness increases with decreasing redshift
3. this asymmetry is the main contributor to the overestimation of the UVB found in the literature
4. the peak of this distribution is an unbiased estimate of the UV background intensity

The skewness of the proximity effect strength distribution (PESD) originates from the definition of the uniform grid in $\log \omega$ space. In other words, as a constant $\log \omega$ range progressively probes smaller redshift intervals approaching the quasar, the absorbers tend to no longer be Gaussian distributed. This effect is further enhanced at lower emission redshifts since the line number density decreases. Therefore, the distribution not only becomes broader, but also more skewed.

To check how accurately we can recover the input value $\omega_\star^{\rm IN}$, we fit Eq. 4.14 to all 500 lines of sight at three different redshifts ($z_{\rm q} = 2.25,\ 3$ and 4). That gives us an estimate of the proximity effect strength $\omega_\star^{\rm OUT}$ along each sight line. Figure 4.7 illustrates

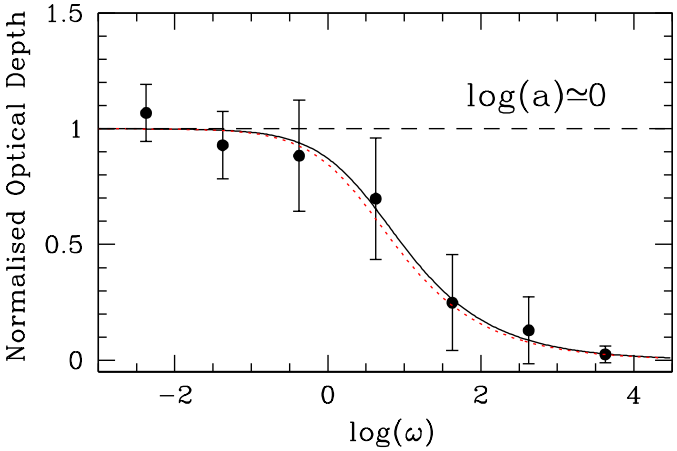

Fig. 4.7. The proximity effect signatures in one simulated line of sight. The data points show the normalised effective optical depth ξ versus ω, binned in steps of $\Delta \log \omega = 1$. The dotted line represents the reference model used to introduce the proximity effect in the synthetic spectrum. The solid line shows the best fit model as described in Sect. 4.5.1

a typical example of the proximity effect signature along one sight line in our HPM simulations. All lines of sight can then be combined to form the proximity effect strength distribution. Figure 4.8 presents our results.

We confirm, with advanced 3D numerical simulations, the recent results reported in Chapter 2: the PESD sharply peaks at the input model ($\log \omega_\star^{\rm OUT}/\omega_\star^{\rm IN} = 0$) and becomes broader towards lower redshift. Furthermore, the skewness in the PESD increases towards low redshift. However, our results on the PESD inferred from the HPM simulation quantitatively differ from the Monte Carlo simulations. While the peaks of the distributions match, the rms are significantly smaller for the HPM-based sight lines. We obtained at redshifts $\overline{z} = (2.25, 3.0, 4.0)$ a dispersion of strength parameter equal to $\sigma \log a = (0.3, 0.23, 0.1)$ dex for the HPM simulations, while in the Monte Carlo one we estimated $\sigma \log a = (0.65, 0.5, 0.2)$ dex. The larger dispersion in the latter results in the stronger bias in the combined proximity effect analysis reported in the previous section.

To precisely estimate the uncertainties related to the modal value of the PESD we adopted a bootstrap technique. Starting from a distribution of N_i values of $\log a$, where N_i represents the total number of $\log a$ estimates, we randomly duplicated N_i/e strength parameters and estimated the modal value of the

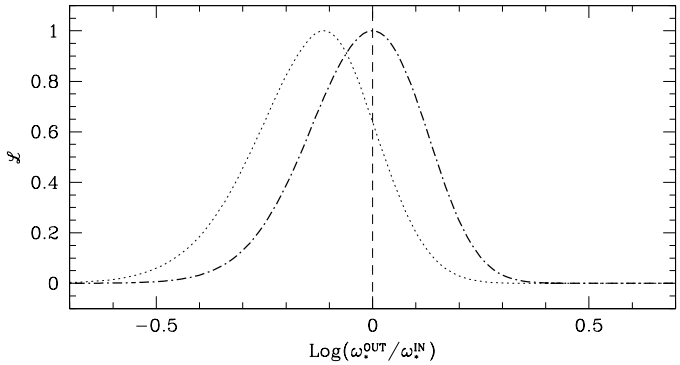

Fig. 4.9. An example of the likelihood function $\mathcal{L}$ estimated from two different sight lines in our simulations. While in one sight line (dotted dashed profile) the likelihood is maximised at the input model, the second sight line (dotted profile) has the most likely value of $\omega_\star^{\mathrm{OUT}}$ significantly below $\omega_\star^{\mathrm{IN}}$.

new PESD. We repeated this process 500 times for each redshift snapshot (as well as in the following), obtaining the mean and the sigma values of PESD modes.

Measuring the proximity effect signal along individual lines of sight, and thus determining the PESD, allows unbiased estimates of the cosmic UV background. However, this method is still based on a simple averaging process of the absorption in the Lyα forest. In other words, the advantage of dealing with very high quality data is not fully explored. Hereafter, we will refer to the PESD estimated from the normalised optical depth on individual lines of sight as the *simple averaging technique*.

4.5.3. The maximum-likelihood approach

The importance of a precise determination of the UVB intensity at different epochs motivates us to further develop and test *new* methods of determining the proximity effect strength.

A widely used, extremely flexible approach for recovering input parameters is the maximisation of the likelihood function (LF). It expresses the probability of a set of parameters in a statistical model describing certain data. In our case, we can write this function as the probability that our spectrum has been modified by the quasar radiation of a given strength $\omega_\star$.

Generally the likelihood function is defined as

$$\mathcal{L} = \prod_{i=1}^{N} P(F_i|C) \tag{4.15}$$

where the product is calculated over N data points, and $P(F_i|C)$ is the probability of occurrence of the measurement F_i given the set of parameters C. Here, all data points F_i are flux values in the observed or synthetic Lyα spectrum.

The prime limitation of Eq. 4.15 is that the product operator must be applied to uncorrelated data points. However, neighbouring pixels in the Lyα absorption spectrum are strongly correlated due to both physical correlations of cosmic large-scale structures and thermal and instrumental broadening of absorption lines. Eq. 4.15 can be generalised for the case of correlated data, but that would require knowing an $N-$ *point* correlation function for the flux, which is impossible to estimate in any reasonable way neither from the observational data nor from the simulations.

Therefore, as a first attempt, we adopt a simplified approach and re-bin the spectra over at least 40 km s^{-1} (the average width of an absorber in the velocity space) in order to significantly reduce the correlation in the Lyα forest without losing too much resolution. In the following sections we discuss more sophisticated methods of accounting for the correlations between the data points.

Let us now compare the same sight line with and without the signature of the proximity effect. These two spectra have the same original hydrogen distribution along the line of sight, thus the two hydrogen densities, or, ignoring the peculiar velocities, the two optical depths, are related by Eq. 4.8. Our aim is to express the observed flux probability density $P(F)$ in Eq. 4.15 as a function of the strength of the proximity effect and the flux probability unaffected by the quasar radiation.

The FPD affected (P_m) and unaffected (P_∞ as presented in Fig. 4.4) by the quasar radiation are related by

$$P_m(F_m)\mathrm{d}F_m = P_\infty(F_\infty)\mathrm{d}F_\infty. \tag{4.16}$$

Knowing that

$$F_m = \mathrm{e}^{-\tau_m} = \exp\left(-\frac{\tau_\infty}{1+\omega}\right) = F_\infty^{1+\omega}, \tag{4.17}$$

we can write

$$P_m(F_m) = P_\infty\left(F_m^{1+\omega}\right)(1+\omega)F_m^{\omega}. \tag{4.18}$$

The Likelihood function in Eq. 4.15 can be generalised in the presence of instrumental noise to

$$\mathcal{L} = \prod_i \int_0^1 \frac{\exp\left[-(F_{i,m}-F')^2/2\sigma_i^2\right]}{\sigma_i\sqrt{2\pi}} P_m(F')\mathrm{d}F' \tag{4.19}$$

where the additional exponential term describes the Gaussian noise with the proper normalisation. Inserting Eq. 4.18 into Eq. 4.19 we obtain

$$\mathcal{L} = \prod_i \int_0^1 \frac{\exp\left[-(F_{i,m}-F')^2/2\sigma_i^2\right]}{\sigma_i\sqrt{2\pi}} \times \\ \times\ P_\infty\left(F'^{1+\omega}\right)(1+\omega)F'^{\omega}\mathrm{d}F'. \tag{4.20}$$

This function has only one free parameter, the strength of the proximity effect $\omega_\star^{\mathrm{OUT}}$. For an infinitely high signal to noise ratio, the Gaussian becomes a delta function and the expression under the integral reduces to the flux probability distribution given by Eq. 4.18.

The methodological approach is then straightforward: (i) we introduce the proximity effect on the hydrogen neutral fraction along all the lines of sight at our disposal, (ii) we compute the likelihood function for a set of $\omega_\star^{\mathrm{OUT}}$ values within the range $-1 < \log\omega_\star^{\mathrm{OUT}} < 1$ and finally (iii) we search for the particular value of $\omega_\star^{\mathrm{OUT}}$ that maximises Eq. 4.20. For illustration purposes we present in Fig. 4.9 the likelihood function for two different lines of sight where the two maxima are located in different positions with respect to the input model. After repeating this procedure over all spectra we construct the PESDs presented in Fig. 4.10.

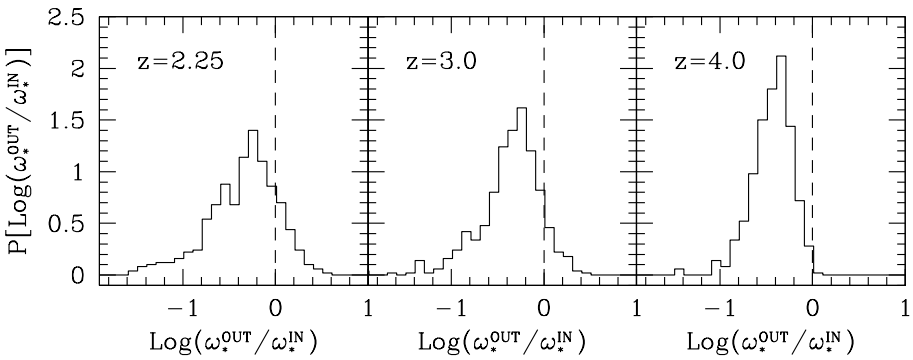

Fig. 4.10. The proximity effect strength distribution in three different sets of 500 sight lines at redshift $\overline{z}$ = 2.25, 3.0, and 4.0. The PESD has been constructed adopting the likelihood technique described in Sect. 4.5.3 to estimate the strength of the proximity effect. The extent of the biases, represented by the shift of the mode in the PESD with respect to the dashed vertical line, remains constant with redshift.

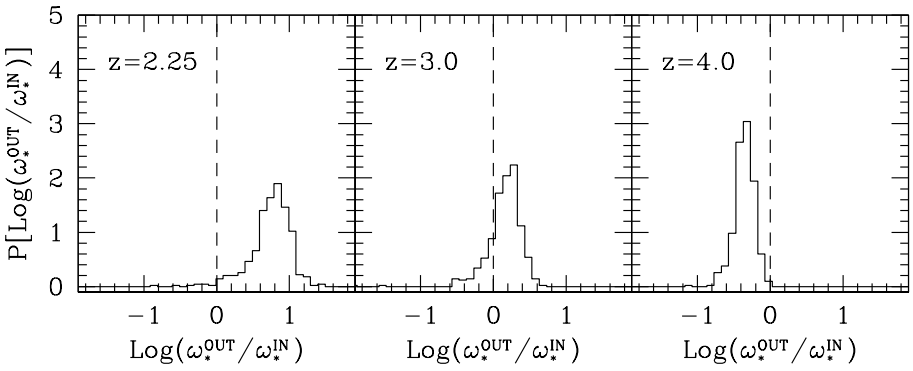

Fig. 4.12. The proximity effect strength distribution in three different sets of 500 sight lines at redshift $\overline{z}$ = 2.25, 3.0, and 4.0. The PESD has been constructed with a modified likelihood approach, which used a weighted FPD to account for the intrinsic correlations in the Lyα forest. The PESD remains biased with respect to the reference model and the amount of bias is now strongly redshift dependent.

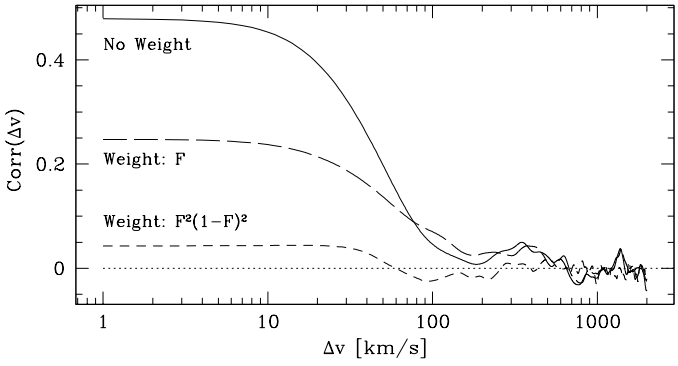

Fig. 4.11. The flux auto-correlation function in one Lyα forest spectrum (solid line) in comparison with two different non-trivial weighting schemes (long and short dashed lines). The introduction of a weighting scheme in the computation of Corr(Δv) significantly reduces the auto-correlation of the transmitted flux.

At all redshifts the inferred PESD has a clear maximum, however this maximum does not coincide with the input model, moreover the modal values of all PESDs are biased towards smaller $\omega_\star^{\rm OUT}$. Contrary to the outcome of the *simple averaging technique*, this approach fails to recover the input model and also the inferred PESD is clearly broader. Several factors may cause this bias.

(i) Our spectra might still be significantly affected by intrinsic (as opposed to thermal or instrumental broadening) correlations in the Lyα forest. Even when we re-bin the spectrum to significantly reduce the correlations between nearby pixels, the intrinsic correlations between close absorbers largely remain. For this reason we recomputed the PESD after re-binning the spectrum over several tens of km s^{-1}, up to 100 km s^{-1}. Unfortunately this had no effect neither on the modal value of the PESD nor on its shape, demonstrating that it is intrinsic correlations between absorbers and not thermal broadening that is responsible for the biased result of Fig. 4.10.

(ii) The flux probability distribution might change significantly along different lines of sight, thus concealing some uncontrolled systematic effect when assuming as common FPD the average over all sight lines. Therefore we have repeated our computation adopting the FPD estimated from the same line of sight without the influence of the quasar. Such a procedure is, of course, not feasible for real observations, but, nevertheless, it does not solve the problem of a biased PESD. We have finally tried to analytically fit the average or single FPD with different fits (Miralda-Escudé et al. 2000; Becker et al. 2007) also without success.

We conclude that the reason for the bias in the maximum likelihood analysis is caused by an intrinsic correlation in the Lyα forest not being accurately accounted for by our simple re-binning procedure. In the following, we attempt to solve this problem by estimating the correlation function in our simulated spectra.

4.5.4. The correlation function

We showed in the previous section that clustering of Lyα absorbers gives rise to correlations in the observed transmitted flux large enough to heavily bias the results of a maximum likelihood analysis, even after re-binning the simulated spectrum. We now focus on measuring how large these correlations are by means of the *correlation function*.

Given a point in redshift with transmitted flux F, the correlation function describes the probability of finding another

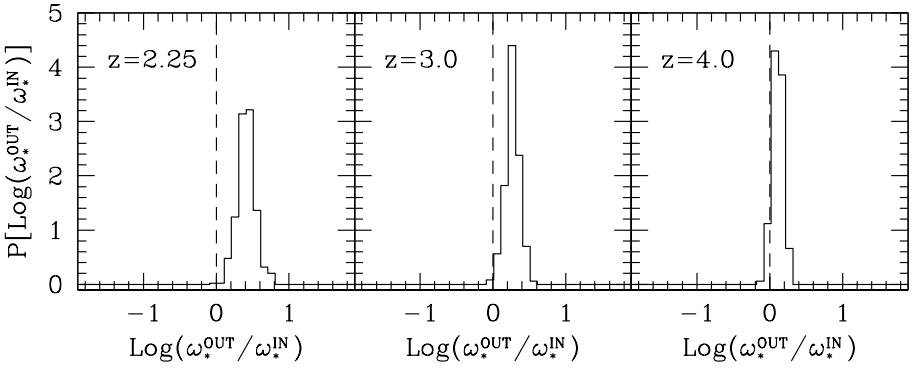

Fig. 4.13. The proximity effect strength distribution in three different sets of 500 sight lines at redshift $\overline{z} = 2.25$, 3.0, and 4.0. The PESD has been constructed employing a modified likelihood approach which adopted the unweighted FPD but samples the spectrum over 2000 km s^{-1} to account for the absorption correlations in the Lyα forest. The PESD remains biased with respect to the reference model and the amount of bias is now strongly dependent on redshift.

point, with the same F, within a given redshift interval. More precisely, if we express the interval with a velocity shift Δv we can write that

$$\mathrm{Corr}(\Delta v) = \langle \delta F(v) \delta F(v + \Delta v) \rangle / \overline{F}^2, \qquad (4.21)$$

where $\overline{F}$ represents the mean flux and $\delta F(v) \equiv F(v) - \overline{F}$. The numerical value of Corr(Δv) is obtained by directly averaging individual pixels over the spectrum, separated by a given velocity Δv.

To illustrate the properties of the correlation function, we computed Corr(Δv) for one sight line and show the result in Fig. 4.11. The amplitude of the correlation increases significantly for separations smaller than about $\Delta v \lesssim 100$ km s^{-1}, while it fluctuates around zero for separations larger than a few hundreds of km s^{-1}. This directly shows that individual pixels in the Lyα forest are not independent from an other, but strongly correlated. Such a correlation, which also changes from one sight line to another, does not vanish after a simple re-binning of the spectrum.

Motivated by the lack of success in our previous method, we explore a different approach to remove the signature of correlated pixels. We introduce a weighting scheme in the definition of the correlation function designed to give negligible weight to correlated pixels in the Lyα forest. Adopting this weight to estimate a new flux probability distribution, we would immediately remove the imprints of the correlation.

If we introduce such a weighting scheme, Eq. 4.21 becomes

$$\mathrm{Corr}(\Delta v, w) = \frac{\langle \delta F(v) \delta F(v + \Delta v) \rangle_w}{\langle F(v) \rangle_w \langle F(v + \Delta v) \rangle_w}. \qquad (4.22)$$

For this purpose, we explored two types of weighting functions: $w_1(F) = F$, which removes the correlations for strong absorbers and, $w_2(F) = F^2(1 - F)^2$, which accounts for the correlation of strong and weak absorbers. With our new definition of the correlation function, we recomputed Corr($\Delta v, w$) for the same sight line as before and place our results into context in Fig. 4.11. While already the first weight significantly reduces the correlations, the second one removes the intrinsic correlations of the the Lyα flux almost completely.

We then adopted $w_2(F)$ to recompute the FPD which will now have a different shape with respect to that of Fig. 4.4, and will show one pronounced peak for $0 < F < 1$. This new weighted probability distribution is used to infer the likelihood function following the same procedure as in Sect. 4.5.3. From the most likely values of the proximity effect strength, we reconstructed the PESDs which are now presented in Fig. 4.12. With this new approach, all the inferred distributions not only present a significant bias with respect to the input model, but this bias additionally changes from an underestimation to an overestimation as the snapshot redshift decreases. In spite of the complexity of this new method, there are still uncontrolled systematics in the analysis of the proximity effect which are not correctly accounted for, even introducing a weighting scheme.

4.5.5. Sampling the Lyα forest for the likelihood

None of the techniques presented so far performs better than the simple averaging technique in recovering the signature of the proximity effect. Our next attempt to overcome the imprints of the mentioned correlations is based on the computation of a different likelihood function.

Until now we have proceeded with the computation of $\mathcal{L}$ following Eq. 4.20, where the product is performed considering all the flux pixels in the spectrum. Due to the absorption correlations and our difficulties in removing their signature, we now try to apply a selection of the pixels from which the product will be estimated. If we consider a set of i flux pixels separated by a few thousands of km s^{-1} (Δv), these points will be uncorrelated according to Fig. 4.11. From this set of flux values we can estimate one likelihood function before considering to the next set of i flux pixels.

Depending on the resolution of our synthetic spectra (dv), we will have a set of j likelihood functions where the exact number is defined as $j = \Delta v / \mathrm{d}v$. Each likelihood function will then be maximised and yield one value of $\omega^{\mathrm{OUT}}_{\star,j}$.

The distribution of $\omega^{\mathrm{OUT}}_{\star,j}$ depends on how many points contribute to the particular set and behaves as follows: increasing the pixel separation Δv, the number of pixels from which the likelihood is estimated decreases, thus yielding a broader distribution of $\omega^{\mathrm{OUT}}_{\star,j}$. Equivalently, if the pixel separation is too small, the influence of the correlation between pixels increases, resulting is a biased result. We fix our separation to $\Delta v = 2000$ km s^{-1} and adopt the mean $\omega^{\mathrm{OUT}}_{\star,j}$ as a proxy for the most likely indicator of the proximity effect strength.

Figure 4.13 presents the results showing the PESDs at different redshifts. In our highest redshift snapshot the modal value of the PESD is, given the uncertainties, extremely close to the input model (offset by 1.4σ) with a dispersion in the strength parameter significantly smaller than that of the simple averaging technique. However, towards lower redshift, a significant

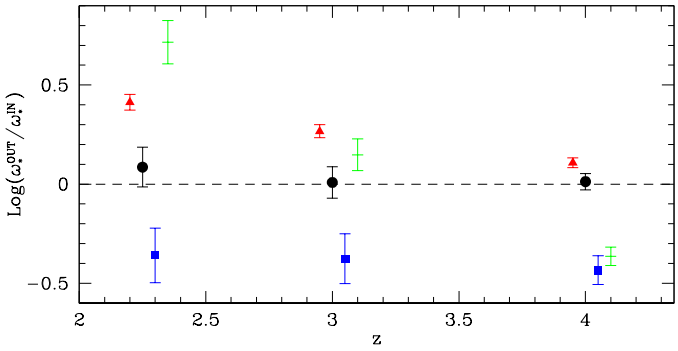

Fig. 4.14. Comparison of the best estimate of the proximity effect strength obtained with the different methods presented in this work. The black circles show the outcome of the simple averaging technique. The blue squares, the green crosses and the red triangles depict the simple likelihood, the likelihood with a weighted FPD, and the sampled likelihood, respectively. A small redshift shift has been applied to the data points to make them more easily recognisable. The modal values and associated errors have been estimated with a bootstrap technique as described in Sect. 4.5.

bias in the modal values appears again. We conclude that this approach is not superior to the simple averaging technique.

Even if we could find two new pixel separations Δv at redshifts $\overline{z} = 2.25$ and 3.0 which yield no biases in the recovery of the reference model, we are aware of the drawbacks that such approach would have on real data. The biases that are in this method due to a *wrong* choice of the sampling size are extremely difficult to control because in real spectra we typically lack of the spectral informations without the quasar impact. At best, we therefore could only guess the *appropriate* sampling size via numerical simulations, without being able to test the accuracy.

We summarise the results of all the techniques presented in this work in Fig. 4.14. None of the more maximum likelihood methods are capable of yielding tighter and unbiased constraints on the proximity effect than the simple averaging technique.

4.6. Conclusions

We have analysed a set of high-resolution, three-dimensional numerical simulations with a Hydro-Particle-Mesh code. We evolved the particle distribution in the simulated box until a redshift of $\overline{z} = 2.25$, and recorded seven snapshots within the range $2.25 < \overline{z} < 4$. For each snapshot we have drawn 500 randomly distributed sight lines through the simulated box, obtaining simulated spectra of the Lyα forest.

A sample of 40 high-resolution, high-S/N quasar spectra, with emission redshifts within the range $2.1 < \overline{z} < 4.7$, has been used to calibrate the simulated spectra. We have computed from the simulated sight lines (i) the evolution of the effective optical depth, (ii) the flux probability distribution function, and (iii) the column density distribution at different redshifts. While the computation of the synthetic line of sight depends on several free parameters, we have tuned them to be consistent (within the measured uncertainties) with the observational data in all three measurements.

Our study is focused on developing and testing new techniques of recovering the strength of the proximity effect along individual sight lines. Our analysis has begun with a comparison between the widely adopted *combined analysis* of the proximity effect signal over multiple lines of sight, with the recently developed technique of estimating its strength on individual quasar spectra. We refer to this method the *simple averaging technique*. As the strength distribution is supposed to be asymmetric, biases are expected to arise when determining the combined proximity effect signal.

We have confirmed, with a realistic set of synthetic lines of sight drawn from our numerical simulation, the existence of this biases, albeit with a different intensity as predicted with Monte Carlo simulations. We have concluded that the smaller bias is caused by the smaller scatter of the strength parameter. We have confirmed that the modal value, or peak of the proximity effect strength distribution (PESD), yields an unbiased estimate of the input parameters used to compute the proximity effect. Moreover, we have detected the expected broadening in the shape of the PESD towards low redshift, as predicted in Chapter 2 using Monte Carlo simulations.

In principle, the simple averaging technique, by combining observed pixels together, loses information. In order to avoid this loss, we have investigated several incarnations of a maximum likelihood approach. The first incarnation was a standard implementation of the likelihood function. Due to intrinsic (as opposed to thermal and instrumental broadening) autocorrelation of the transmitted flux along a single line of sight, this technique was subject of systematic bias at all redshifts and for all models of the flux probability distribution.

In the second method we have used a weighting scheme, designed to reduce the intrinsic auto-correlation in the absorption spectrum. While this weighting scheme was able to substantially reduce the two-point autocorrelation functions of the flux, the resultant PESDs were significantly biased. This failure of the weighting scheme indicates that it is not a two-point, but some (currently unknown) higher order correlation function(s) that are primarily responsible for the bias in the maximum likelihood estimate of the proximity effect.

In an attempt to reduce the bias, we have adopted a sampling approach of widely separated flux points in the spectrum to design a more complex likelihood function. While this approach yielded a substantially more accurate estimate of the best-fit value, the value itself remained biased. That bias is comparable to the statistical uncertainty of the measurement at redshift $\overline{z} = 4.0$, but becomes progressively larger towards lower redshifts.

Thus, the newly introduced *simple averaging technique*, despite of the perceived loss of information during the averaging procedure, is the only method of estimating the proximity effect signal free of biases.

Acknowledgements. We would like to thank the San Diego Supercomputer Center which allowed us to perform our simulations. A.D. acknowledge support by the Deutsche Forschungsgemeinschaft under Wi 1369/21-1.

References

Bajtlik, S., Duncan, R. C., & Ostriker, J. P. 1988, ApJ, 327, 570
Becker, G. D., Rauch, M., & Sargent, W. L. W. 2007, ApJ, 662, 72
Carswell, R. F., Webb, J. K., Baldwin, J. A., & Atwood, B. 1987, ApJ, 319, 709
Carswell, R. F., Whelan, J. A. J., Smith, M. G., Boksenberg, A., & Tytler, D. 1982, MNRAS, 198, 91
Cooke, A. J., Espey, B., & Carswell, R. F. 1997, MNRAS, 284, 552
Dall'Aglio, A., Wisotzki, L., & Worseck, G. 2008, A&A, 480, 359
Fardal, M. A., Giroux, M. L., & Shull, J. M. 1998, AJ, 115, 2206
Faucher-Giguère, C.-A., Prochaska, J. X., Lidz, A., Hernquist, L., & Zaldarriaga, M. 2008, ApJ, 681, 831
Giallongo, E., Christiani, S., D'Odorico, S., Fontana, A., & Savaglio, S. 1996, ApJ, 466, 46
Gnedin, N. Y. 2004, ApJ, 610, 9
Gnedin, N. Y. & Fan, X. 2006, ApJ, 648, 1
Gnedin, N. Y. & Hui, L. 1998, MNRAS, 296, 44
Haardt, F. & Madau, P. 1996, ApJ, 461, 20
Haardt, F. & Madau, P. 2001, in Clusters of Galaxies and the High Redshift Universe Observed in X-rays, ed. D. M. Neumann & J. T. V. Tran
Haiman, Z. & Loeb, A. 1998, ApJ, 503, 505
Hu, E. M., Kim, T.-S., Cowie, L. L., Songaila, A., & Rauch, M. 1995, AJ, 110, 1526
Hui, L., Gnedin, N. Y., & Zhang, Y. 1997, ApJ, 486, 599
Jenkins, E. B. & Ostriker, J. P. 1991, ApJ, 376, 33
Kim, T.-S., Carswell, R. F., Cristiani, S., D'Odorico, S., & Giallongo, E. 2002, MNRAS, 335, 555
Liske, J. & Williger, G. M. 2001, MNRAS, 328, 653
Lu, L., Wolfe, A. M., & Turnshek, D. A. 1991, ApJ, 367, 19
Madau, P. & Efstathiou, G. 1999, ApJ, 517, L9
Maselli, A. & Ferrara, A. 2005, MNRAS, 364, 1429
McDonald, P., Miralda-Escudé, J., Rauch, M., et al. 2001a, ApJ, 562, 52
McDonald, P., Miralda-Escudé, J., Rauch, M., et al. 2001b, ApJ, 562, 52
Miralda-Escudé, J., Haehnelt, M., & Rees, M. J. 2000, ApJ, 530, 1
Misawa, T., Tytler, D., Iye, M., et al. 2002, AJ, 123, 1847
Murdoch, H. S., Hunstead, R. W., Pettini, M., & Blades, J. C. 1986, ApJ, 309, 19
Rauch, M. 1998, ARA&A, 36, 267
Ricotti, M., Gnedin, N. Y., & Shull, J. M. 2000, ApJ, 534, 41
Ricotti, M. & Ostriker, J. P. 2004, MNRAS, 350, 539
Sargent, W. L. W., Young, P. J., Boksenberg, A., & Tytler, D. 1980, ApJS, 42, 41
Schaye, J., Aguirre, A., Kim, T.-S., et al. 2003, ApJ, 596, 768
Schaye, J., Theuns, T., Rauch, M., Efstathiou, G., & Sargent, W. L. W. 2000, MNRAS, 318, 817
Scott, J., Bechtold, J., Dobrzycki, A., & Kulkarni, V. P. 2000, ApJ, 130, 67
Spergel, D. N. 2006, The Universe at z ¿ 6, 26th meeting of the IAU, Joint Discussion 7, 17-18 August 2006, Prague, Czech Republic, JD07, #6, 7
Tytler, D. 1987, ApJ, 321, 49
Weymann, R. J., Carswell, R. F., & Smith, M. G. 1981, ARA&A, 19, 41

Chapter 5

Radiative transfer and the line-of-sight proximity effect⋆

Aldo Dall'Aglio, Adrian Partl, and Volker Müller

Astrophysikalisches Institut Potsdam, An der Sternwarte 16, D-14482 Potsdam, Germany

ABSTRACT

We solve the radiative transfer equation in the framework of high resolution numerical simulations of structure formation to search for the imprint of the proximity effect in the H I Lyα forest. We employed dark matter simulation snapshots at redshifts $z = 3,\ 4$, and 4.9 to derive the hydrogen densities and temperatures adopting an effective equation of state. After an accurate calibration of randomly selected sight lines through the box with the observational properties of the Lyα forest, we adopted the Monte Carlo code *CRASH* to solve the radiative transfer equation in the intergalactic medium. For each redshift, we considered three plausible environments to host a quasar: A massive dark matter halo, a random filament and a void. We modelled the combined contribution of the cosmic UV background (UVB) and a quasar to predict the photoionisation state of the IGM once the ionisation equilibrium has been reached. By deriving synthetic H I Lyα forest spectra from a set of randomly oriented lines of sight, we investigate the signature of the proximity effect on each of them. We quantify the strength of this effect adopting a fiducial value of the UVB intensity at the Lyman limit multiplied by a free parameter allowed to vary along different sight lines. The simulated proximity effect strength distribution (PESD) resembles closely that obtained from an equivalent analysis on *observed* quasar sight lines. The PESD shows a well defined peak, it is significantly asymmetric and it becomes narrower towards high redshift. Comparing the sight lines obtained from the radiative transfer simulation with analytical models of the proximity effect, we find weak changes in the inferred PESDs, at best only with marginal statistical significance.

5.1. Introduction

The content of this Chapter constitutes my contribution to a recent publication by Partl et al. submitted to A&A on topics closely related to the subject of this thesis. In order to place my work into context I will summarise in this and the next Sections the basic framework and tools employed by Partl et al. to include the proximity effect in numerical simulations of structure formation. Starting from Sect. 5.3 I will enter into the details of my analysis

A key characteristic in our description of the baryonic content in the Universe consists of the ionisation state of the gas in the intergalactic medium (IGM). Upon completion of the *first* reionisation of the Universe where neutral hydrogen and helium became singly ionised, the small fraction of neutral gas in the IGM is responsible for the large number of absorption lines observed in the spectra of high redshift quasars (QSO). This phenomenon, also known as the Lyα forest (Sargent et al. 1980; Rauch 1998), is mainly attributed to intervening H I clouds along the line of sight towards a QSO.

The vast majority of these intervening systems is kept at such high ionisation state by the integrated emission of ultra-violet photons originating from the overall populations of quasars and star-forming galaxies: The ultra-violet background field (UVB: Haardt & Madau 1996; Fardal et al. 1998; Haardt & Madau 2001). As such, detailed constraints on the ionisation state of the IGM, its spatial variation and redshift evolution are of fundamental importance to observational and computational cosmology. As bright quasar are capable of emitting an extreme amount of UV photons, such an enhanced UV field on Mpc scale near the QSO is responsible for the observed lack of absorption systematically detected in their vicinity: The so-called proximity effect.

Numerical simulations of structure formation have been of crucial importance in understanding the nature and evolution of the Lyα forest. However, one challenge in the current development of 3D simulations consists of the implementation of radiative transfer into the formalism of hierarchical structure formation (Gnedin & Abel 2001; Maselli et al. 2003; Razoumov & Cardall 2005; Rijkhorst et al. 2006; Pawlik & Schaye 2008). In particular the coupling of radiative transfer with the density evolution requires a large amount of computational resources and remains up to now a largely unexplored field. Therefore,

⋆ The analysis presented in this Chapter has been included in an article submitted to *Astronomy & Astrophysics*

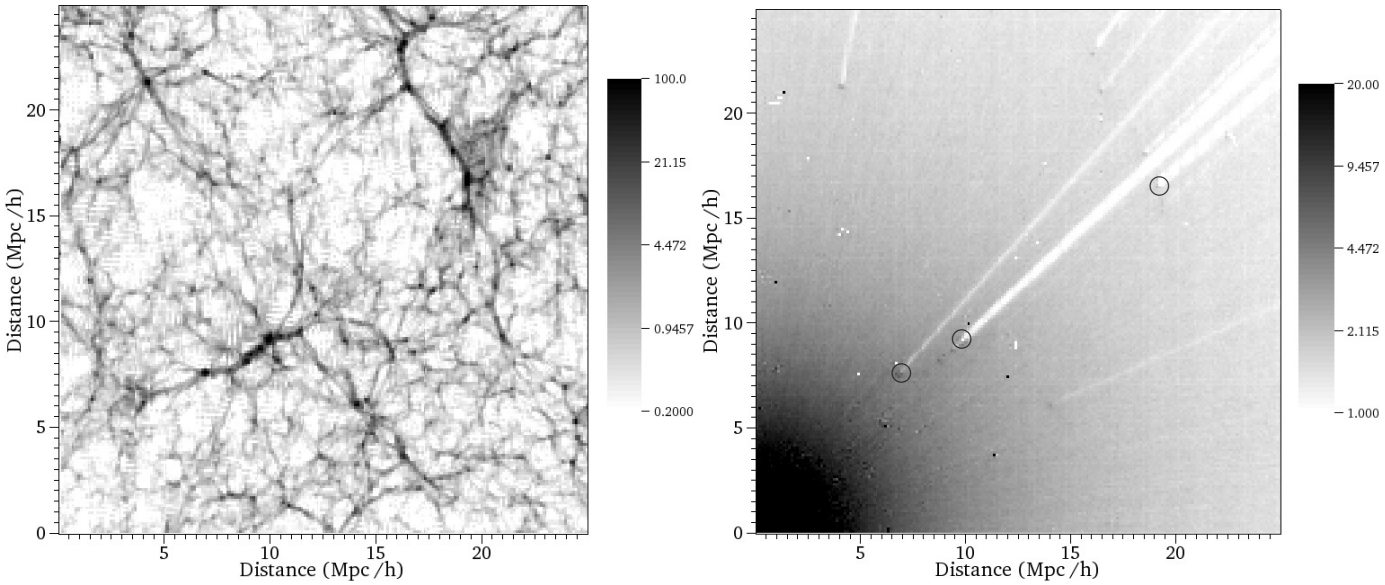

Fig. 5.1. *Left:* Snapshot of the dark matter density distribution in our simulated box at redshift $z = 4$. The gray scale represents the overdensity field of the dark matter alone before the introduction of the radiative influence of a quasar. *Right:* For the same cosmological box this panel shows the hydrogen ionised fraction constrained by the radiative transfer simulation, colour-coded in gray. The quasar is located on the bottom-left corner of this snapshot and radiates isotropically. The blank (white) regions in this panel represent portion of the cosmological box unaffected by the quasar radiation as they are shadowed by massive intervening systems (some of them marked with black circles).

most available codes apply radiative transfer as a post processing step.

Adopting such a de-coupled approach, only a limited number of studies appeared in the past decade, focusing on the Lyα forest and they primarily targeted the epoch of reionisation (e.g. Ciardi et al. 2001; Nakamoto et al. 2001; Kohler et al. 2007; Maselli et al. 2007; Trac & Cen 2007).

The aim of the present work is to investigate the proximity effect as the result of radiative transfer calculations in a numerical simulation of structure formation. This novel approach is critical in particular for the understanding of the environment in which quasars are supposed to form and evolve. Observationally only few attempts have been made towards the characterisation of quasar environments (Rollinde et al. 2005; Guimarães et al. 2007; D'Odorico et al. 2008). These authors assumed that the overestimates of the UV background obtained when combining the proximity effect on multiple lines of sight were only due to a larger density field near the quasar. This allowed them to put a constraint on the average halo mass hosting a QSO. In Chapter 2 we demonstrated that this overestimation primarely comes from the technique itself of combining more sight lines when searching for the proximity effect signal. Moreover, we presented simple arguments against a strong systematic enhancement in the matter density field near the quasar.

As the matter distribution in the vicinity of high redshift quasars is not yet known, the approach presented here enables us to compare the properties of the simulated proximity effect, varying the quasar environment, with the observations presented in the previous Chapters. Hence, this work represents the initial step towards a systematic investigation of a broad range of quasar environments, luminosities and redshifts which will provide crucial insights on the surrounding regions hosting the formation of quasars at high redshift.

This Chapter starts with an overview of the simulations and techniques exploited to implement the radiative transfer on a cosmological simulation in Sect. 5.2. We continue in Section 5.3 presenting how we extracted and modelled the signature of the proximity effect along individual sight lines. Section 5.4 concentrates on an assessment of the uncertainties involved in our analysis. Our results follow in Sec. 5.5 and the conclusions are given in Sect. 5.6.

5.2. Simulations

Our main goal is to simulate the proximity effect as the imprint of a quasar's radiation on the IGM solving the equation of radiative transfer. As a consistent implementation of a radiative transfer algorithm into a cosmological simulation of structure formation is a challenging and still open problem, we simplified our approach in several aspects.

- We started from high resolution dark matter only simulations.
- We derived the density, velocity and temperature fields of the baryons assuming that the latter are traced by the dark matter distribution neglecting all chemical spices, but hydrogen.
- We include the radiative influence of the quasar a posteriori.

The original dark matter simulations has a box-size of $50\,h^{-1}$ Mpc and has been obtained employing the PM-Tree code GADGET2 (Springel et al. 2005) with 512^3 dark matter particles. The force resolution is then $2\,h^{-1}$ kpc with a mass resolu-

tion equal to $m_p = 7.75 \times 10^7 h^{-1} M_\odot$. We adopted the cosmological parameters inferred from the WMAP 3rd year measurements (Spergel et al. 2007).

We considered three different redshift snapshots of our simulation at $z = 4.9,\ 4$ and 3 to constrain how the signature of the proximity effect changes with redshift. Furthermore, we identified three different host environments suitable for the placement of a quasar.

1. The most massive halo at $z = 3.0$ of $M_{\rm halo} = 7.9 \times 10^{12} M_\odot$, with volume averaged overdensity $\delta = 2.1$ at $z = 3.0$ in a sphere of $r = 5\ {\rm h}^{-1}$ Mpc (for the other redshift snapshots we followed its most massive progenitor).
2. A random filament with $\delta = 1.1$.
3. A random void with $\delta = 0.7$.

Due to the high computational costs of a radiative transfer simulation, we considered only a portion of the original cosmological box. The sub-box extends over 25 ${\rm h}^{-1}$ Mpc and has been placed to host in one of its corners the three environments listed above. Figure 5.1 presents one example of the dark matter distribution along with the radiative strength of a quasar as discussed below.

From the dark matter only simulation, we adopted a semi-analytical procedure to determine the hydrogen density and velocity distributions. We assumed that the baryon density is proportional to the dark matter density and we employed an effective equation of state in the form $T = T_0(1+\delta)^{\tilde{\gamma}-1}$ to obtain the hydrogen temperature (Hui et al. 1997; Gnedin & Hui 1998). Note that in our procedure the temperature at the mean density T_0, and $\tilde{\gamma}$ are free parameters.

We draw 500 randomly distributed lines of sight through the sub-box and, following the work by Hui et al. (1997) described in detail in Sect. 4.3, we computed the synthetic Lyα forest spectra. This approach comprises the cosmic UV background (UVB) intensity at the Lyman limit as a 3rd free parameter.

We calibrated our 500 sight lines to achieve an accurate match with the observed evolution of the opacity estimated by Kim et al. (2007) and the flux probability distribution determined by Becker et al. (2007). This procedure yielded an estimate of the UVB intensity at the Lyman limit $J_{\nu_0,{\rm ref}}$ which changes with redshift and is in good agreement with the theoretical predictions by Haardt & Madau (2001) at the snapshot redshifts. The values of $J_{\nu_0,{\rm ref}}$ will be used in the following as reference values for the proximity effect analysis (Sect. 5.5).

This calibration procedure ensured a reasonable description of the baryonic component for our simulation, enabling us to begin with the radiative transfer implementation process.

We adopted the CRASH Monte Carlo scheme to solve the radiative transfer equation (Ciardi et al. 2001; Maselli et al. 2003, 2009). The general idea behind this approach is to propagate photon packages containing a discrete amount of radiative energy through the computational domain. At each time step a source produces one or more discrete photon packages and emits them in random directions.

In the case of a pure hydrogen IGM, the radiative transfer equation simplifies to

$$n_{\rm H} \frac{{\rm d}x_{\rm H\,II}}{{\rm d}t} = \gamma_{\rm H\,I}(T)\, n_{\rm H\,I}\, n_e - \alpha_{\rm H\,II}(T)\, n_{\rm H\,II}\, n_e + \Gamma_{\rm H\,I,tot}\, n_{\rm H\,I} \quad (5.1)$$

where $n_{\rm H}$ is the total hydrogen density, $\gamma_{\rm H\,I}(T)$ is the collisional ionisation rate, and $\alpha_{\rm H\,II}(T)$ the recombination rate. $x_{\rm H\,II}$ denotes the ionised hydrogen fraction while $n_{\rm H\,I}$, $n_{\rm H\,II}$ and n_e represent the density of neutral hydrogen, ionised hydrogen and the electron density, respectively.

The global photoionisation rate $\Gamma_{\rm H\,I,tot}$ is the sum of the cosmic UV background and the quasar photoionisation rates. We adopted a spectral energy distribution (SED) for the UVB in the form $f \propto \nu^\alpha$ with $\alpha_{\rm b} = -1.28$ for frequencies above the Lyman limit. For the quasar we used the SED recently estimated by Trammell et al. (2007) having a spectral index of $\alpha_{\rm q} = -2.5$ for frequencies above the Lyman limit and luminosity $L_{\nu_0} = 10^{32}$ erg s^{-1} Hz^{-1} (at the Lyman limit).

5.3. Definitions and procedures

In this section, we present the different determinations of the proximity effect in our simulated lines of sight. First we consider those lines of sight where the proximity effect results from the solution of the radiative transfer in the cosmological box.

5.3.1. Sight lines drawn from the radiative transfer

As we solved the radiative transfer equation on a cosmological box, each of the sight lines drawn through the box and originating at the location of the QSO, has imprinted the signature of the proximity effect. Thus, we computed a set of 500 randomly oriented sight lines at each snapshot and for each environment accounted for the radiative transfer.

The most effective method of determining the signature of the proximity effect is based on a comparison between the simulated and expected effective optical depth in the Lyα forest (Liske & Williger 2001).

We can model the influence of the quasar radiation on the effective optical depth as

$$\tau_{\rm eff} = \tau_0 (1+z)^{\gamma+1} (1+\omega)^{1-\beta} \quad (5.2)$$

(Liske & Williger 2001) where β is the slope in the column density distribution (see Sect. 2.3). In the case of our simulated sight lines the term expressing the evolution of the effective optical depth in the Lyα forest ($\tau_0(1+z)^{\gamma+1}$) will be substituted by the average $< \tau_{\rm eff} >$ at each snapshot. The quantity ω is defined as the ratio between the quasar and background photoionisation rates which becomes

$$\omega(z) = \frac{\left(1+z'_{\rm q}\right)^{1+\alpha_{\rm q}}}{16\pi^2\, d_L^2\left(z_{\rm q}, z\right)} \left(\frac{3-\alpha_{\rm b}}{3-\alpha_{\rm q}}\right) \frac{L_{\nu_0}}{J_{\nu_0}} \quad (5.3)$$

where J_{ν_0} represents the UV background intensity at the Lyman limit, $1 + z'_{\rm q} = (1+z_{\rm q})/(1+z)$ and $d_L\left(z_{\rm q}, z\right)$ are the redshift and luminosity distance of the quasar as seen by any given absorber along the line of sight at $z < z_{\rm q}$ and L_{ν_0} is the quasar Lyman limit luminosity. Note that Eq. 5.3 accounts for the fact that the UVB and the quasar SEDs have different spectral indices (see Appendix A.1. for a detailed computation).

Finally, the ratio between the simulated optical depth and the average one in the Lyα forest without the radiative transfer,

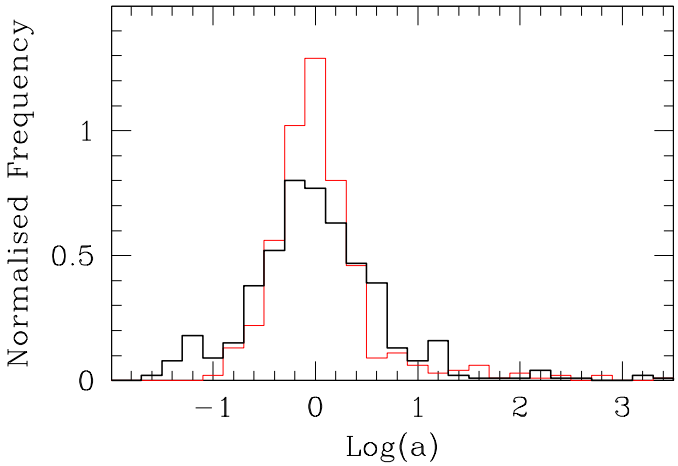

Fig. 5.2. Comparison between the PESD determined from a set of 500 Monte Carlo simulated sight lines covering (i) the whole Lyα forest (thin red histogram) and (ii) only a region of $\Delta z = 0.13$ blueward of the quasar location (thick black histogram). In both cases the modal value of the PESD is statistically recovered at the reference value, albeit with larger dispersion for short sight lines (see text for details).

or the *normalised effective optical depth* ξ, is given by

$$\xi = \frac{\tau_{\rm eff}}{<\tau_{\rm eff}>} = (1+\omega)^{1-\beta}. \quad (5.4)$$

The proximity effect will manifest itself as a departure from unity in the normalised optical depth as $\omega \rightarrow \infty$, i.e. towards the quasar systemic redshift.

5.3.2. Analytical model of the proximity effect

Next we describe how we model the proximity effect in our simulated sight lines to detect any variation originating from the radiative transfer itself. We considered the same sets of sight lines described in the previous section, *before* solving the radiative transfer on the simulations.

We adopted the definition of $\omega(z)$ introduced in Eq. 5.3 to include in these lines of sight the proximity effect as a modification of the opacity in the Lyα forest as $\tau(z) = \tau_0(z)/\,(1+\omega(z))$, where $\tau_0(z)$ indicates the optical depth in the Lyα forest without the influence of the QSO.

This procedure ignores completely the possibility that dense systems along the line of sight are capable of blocking the ionising radiation coming from the nearby quasar, i.e. acting as shields to ionising photons. An example of this shielding effect is depicted in the right-hand panel of Fig. 5.1.

5.3.3. Determining the proximity effect strength

The technique adopted to estimate the proximity effect towards single lines of sight is identical to that presented in Chapter 2 and 3, which we briefly summarise here. We started from the computation of the normalised effective optical depths for individual sight lines within a fixed $\log\omega$ interval and searched for a systematic decrease of ξ for high values of ω.

We assumed a fiducial value for the UVB intensity obtained when calibrating the sight lines with observations as described in Sect. 5.2. The $\log\omega$ axis was then regularly divided into an equally spaced grid and in each element we estimated the normalised effective optical depth ξ. To parametrise the decrease in ξ with $\log\omega$, we adopted the formula

$$F(\omega) = \left(1+\frac{\omega}{a}\right)^{1-\beta} \quad (5.5)$$

where a is the only free parameter representing the *observed* turnover of ξ in units of the fiducial value of the UVB intensity. The slope of the column density distribution was fixed to $\beta = 1.5$ (Kim et al. 2001). The free parameter $\log a$ can be used as a measure of the strength of the proximity effect. This enabled us to determine the proximity effect strength distribution (PESD).

5.4. Systematic uncertainties

Before describing our results, we want to evaluate how strong the characteristic of our simulations might affect the proximity effect signature. Our main concern is the limited wavelength coverage resulting from the cosmological box size of the simulation (only 25 h^{-1} Mpc). On average each sight line will probe only a redshift interval of about $\Delta z \simeq 0.13$ for all our snapshots, while a complete coverage of the Lyα forest would correspond to $\Delta z \simeq 0.6 - 0.9$ depending on the redshift of the snapshot.

We performed extensive Monte Carlo simulations to understand how the proximity effect strength distribution behaves when reducing significantly the redshift path length of the lines of sight. The procedure used to generate these synthetic spectra is identical to the one presented in Chapter 2 and 3 (see Sect. 2.3 for a detailed description). We included the proximity effect signature as described in Sect. 5.3.2 and then determined the PESD considering (i) the total extent of the Lyα forest or (ii) only a redshift interval of $\Delta z = 0.13$ blueward of the quasar location.

Our results are presented in Fig. 5.2. The shape of the PESD is significantly affected by the length of the sight lines. We find a smaller extend of the wings on both sides of the distribution in the case of the large redshift coverage. However, we do not detect a statistically significant bias of the *modal* value.

5.5. Results

We focus now on the results of the proximity effect analysis performed on each of the simulated spectra at our disposal. We investigated each sight line, at all the available redshifts and quasar environments, to determine the strength of the proximity effect. This enabled us to construct its strength distribution. We begin to present our results in Fig. 5.3 with an overview of the PESDs determined from the sight lines drawn from the simulations including the radiative transfer. Each panel shows the PESD of 500 spectra all of which have a common origin at the location of the QSO. These distributions display a large spread of strength parameters asymmetrically scattered around a distinct peak located at a value of $\log a \simeq 0$. This implies that the modal value of the strength distribution accurately recovers the reference UV background intensity at the Lyman limit obtained in our simulations, as $J_{\nu_0} = a\, J_{\nu_0,\rm ref}$.

Since large values of $\log a$ correspond to a weak proximity effect, the PESDs determined from our radiative transfer syn-

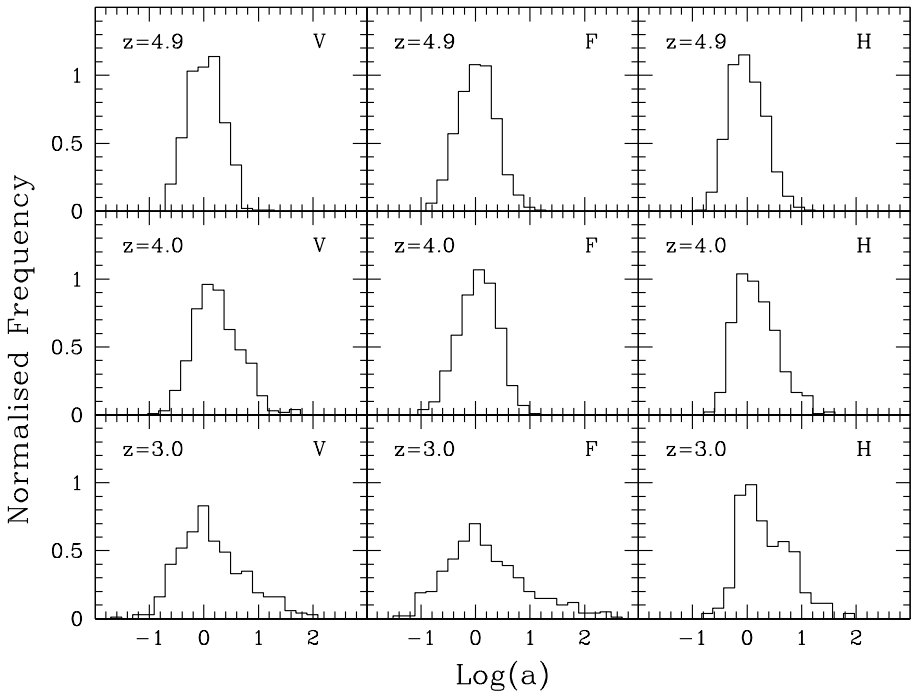

Fig. 5.3. The proximity effect strength distribution determined from randomly oriented sight lines drawn through the cosmological box *including radiative transfer*. Each panel shows the PESD of 500 synthetic spectra at the different snapshot redshifts of our simulation and for the three different environments we selected for hosting a quasar: H=halo, F=filament and V=void.

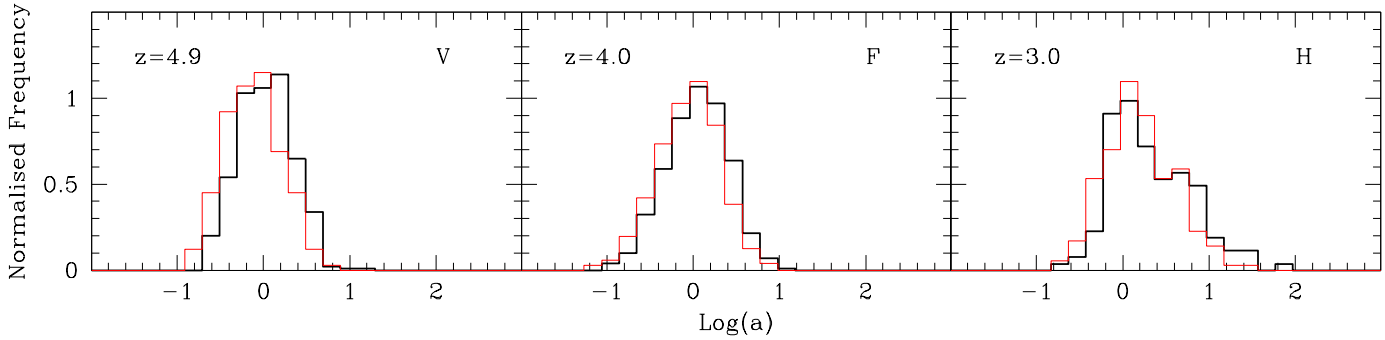

Fig. 5.4. Comparison between the PESD determined from the sight lines including the radiative transfer (black thick histogram) and the PESD when analytically modelling the proximity effect (red thin histogram). Each panel shows a different quasar environment at a different snapshot redshift of our simulation (H=halo, F=filament and V=void).

thetic spectra closely resemble the properties obtained from observed quasar sight lines. Furthermore, the degree of skewness of the PESD decreases towards high redshift as we observed in our analysis of the Sloan Digital Sky Survey quasar spectra (see Chapter 3).

This constitutes already a remarkable achievement as we consistently described the proximity effect from its radiative influence onto the IGM in cosmological simulations and found a close match to equivalent investigations of observed quasar sight lines.

We continue our analysis with a comparison between those lines of sight where the proximity effect is intrinsically imprinted in them and those where we model its signature according to the UVB intensity and the quasar luminosity. This comparison enable us to detect how realistic is the assumption that the IGM is optically thin to ionising photons, regardless of the density of the absorber, which is precisely what the sight lines in Sect. 5.3.2 represent. We therefore estimated the PESDs in the latter set of lines of sight and compare them with the PESDs shown in Fig. 5.3.

Our results are presented in Fig. 5.4 for three different redshifts, each from a different quasar environment. The PESD obtained from the radiative transfer simulation very well matches, in all cases, the corresponding one estimated when modelling the proximity effect analytically. We detect an very slightly increasing discrepancy among the two distributions towards high redshift. Under the null hypothesis that each pair of PESDs is drawn from different distributions, the KS test yields in all cases less than 3% acceptance probability which indicates a rejection at least at a 2σ level. Considering the fact that the inferred modal values of the PESDs are in agreement with each other and with the reference UVB model, this discrepancy is statistically not significant. Equivalently, we can rule out that systematic errors arise when analytically modelling the proximity effect against accurate radiative transfer calculations.

In the case of a luminous quasar ($L_{\nu_0} = 10^{32}$ erg s^{-1} Hz^{-1}) the environment hosting the quasar has no influence on the

proximity effect strength distribution, even for the most massive halo in our simulation. In Chapter 2 we predicted a significant bias towards a weaker proximity effect (i.e. towards larger $\log a$ values) in the case of a systematic overdensity within few Mpc from the quasar emission. In particular for a massive halo, we find that the strong quasar radiation is capable of removing any trace of that overdense environment, leading to no detectable effect on the PESD. However, it is important to note that the large number of assumptions necessary to perform our numerical simulations may have an additional influence on our results. In particular, we think that the size of the simulation box, the type (dark matter only) of simulation, the luminosity and spectral index of the quasar as well as the fact that we neglect all chemical elements but hydrogen may change quantitatively our results.

5.6. Conclusions

We have solved the radiative transfer equation for the transport of energy in the intergalactic medium within a numerical simulation of structure formation to study the line-of-sight proximity effect. We have demonstrated that the signature of this effect in our simulated sight lines is in good agreement with the results obtained from quasar observations at similar redshifts.

We started from a dark matter only cosmological simulation from which we computed the hydrogen density and temperature following a semi-analytic approach. We adopted the numerical code CRASH to solve the transport of energy in our cosmological box, and analysed three different snapshots at $z = 4.9,\ 4.0$ and 3.0. Three plausible quasar environments were selected within each snapshot, a massive halo, a random filament and a random void, and we have searched for a possible dependence of the proximity effect signature.

The main tool of our analysis consisted of the determination of the proximity effect strength along individual lines of sight to construct its strength distribution. The strength has been quantified assuming a fiducial value for the UV background intensity at the Lyman limit which we have estimated when calibrating our simulated lines of sight against the observed properties of the Lyα forest.

We have first determined the proximity effect strength distributions (PESDs) from the synthetic sight lines embedding the radiative transfer. The PESDs closely match the characteristics found from observed quasar spectra. At all redshift and for all quasar environments the PESD has a clear peak, is significantly skewed and its degree of asymmetry decreases towards high redshift.

Comparing those PESDs with the ones obtained when analytically modelling the proximity effect signature, we have found no statistically significant differences. As expected, we have found in our simulation that the intergalactic medium at high redshift is primarily optically thin to ionising radiation. While dense systems are capable of blocking the ionising radiation coming from the quasar, the high luminosity of the QSO is able to significantly diminish their shielding capability. As a result, we do not detect a systematic bias towards a weaker proximity effect in the PESD when our quasar is located in a very massive halo.

While our investigation yields encouraging results, it is only the beginning of a more thorough study of radiative transfer simulations on a wide range of dark matter halo masses. Such an analysis may ultimately lead to an understanding of the mass distribution within several tens of Mpc around high-redshift quasars.

Acknowledgements. We would like to thank the AstroGrid-D and the Konrad-Zuse-Zentrum für Informationstechnik in Berlin which allowed us to perform our simulations. We acknowledge support by the German Ministry for Education and Research (BMBF) under grant FKZ 05 AC7BAA and by the Deutsche Forschungsgemeinschaft under Wi 1369/21-1.

References

Becker, G. D., Rauch, M., & Sargent, W. L. W. 2007, ApJ, 662, 72
Ciardi, B., Ferrara, A., Marri, S., & Raimondo, G. 2001, MNRAS, 324, 381
D'Odorico, V., Bruscoli, M., Saitta, F., et al. 2008, MNRAS, 389, 1727
Fardal, M. A., Giroux, M. L., & Shull, J. M. 1998, AJ, 115, 2206
Gnedin, N. Y. & Abel, T. 2001, New Astronomy, 6, 437
Gnedin, N. Y. & Hui, L. 1998, MNRAS, 296, 44
Guimarães, R., Petitjean, P., Rollinde, E., et al. 2007, MNRAS, 377, 657
Haardt, F. & Madau, P. 1996, ApJ, 461, 20
Haardt, F. & Madau, P. 2001, in Clusters of Galaxies and the High Redshift Universe Observed in X-rays, ed. D. M. Neumann & J. T. V. Tran
Hui, L., Gnedin, N. Y., & Zhang, Y. 1997, ApJ, 486, 599
Kim, T.-S., Bolton, J. S., Viel, M., Haehnelt, M. G., & Carswell, R. F. 2007, MNRAS, 382, 1657
Kim, T.-S., Cristiani, S., & D'Odorico, S. 2001, A&A, 373, 757
Kohler, K., Gnedin, N. Y., & Hamilton, A. J. S. 2007, ApJ, 657, 15
Liske, J. & Williger, G. M. 2001, MNRAS, 328, 653
Maselli, A., Ciardi, B., & Kanekar, A. 2009, MNRAS, 393, 171
Maselli, A., Ferrara, A., & Ciardi, B. 2003, MNRAS, 345, 379
Maselli, A., Gallerani, S., Ferrara, A., & Choudhury, T. R. 2007, MNRAS, 376, L34
Nakamoto, T., Umemura, M., & Susa, H. 2001, MNRAS, 321, 593
Pawlik, A. H. & Schaye, J. 2008, MNRAS, 389, 651
Rauch, M. 1998, ARA&A, 36, 267
Razoumov, A. O. & Cardall, C. Y. 2005, MNRAS, 362, 1413
Rijkhorst, E.-J., Plewa, T., Dubey, A., & Mellema, G. 2006, A&A, 452, 907
Rollinde, E., Srianand, R., Theuns, T., Petitjean, P., & Chand, H. 2005, MNRAS, 361, 1015
Sargent, W. L. W., Young, P. J., Boksenberg, A., & Tytler, D. 1980, ApJS, 42, 41
Spergel, D. N., Bean, R., Doré, O., et al. 2007, ApJS, 170, 377
Springel, V., White, S. D. M., Jenkins, A., et al. 2005, Nature, 435, 629
Trac, H. & Cen, R. 2007, ApJ, 671, 1
Trammell, G. B., Vanden Berk, D. E., Schneider, D. P., et al. 2007, AJ, 133, 1780

Chapter 6

Conclusions and Outlook⋆

6.1. Summary

6.1.1. The proximity effect along individual sight lines

The greatest achievement of this thesis is the re-establishment of the proximity effect as an astrophysical tool to obtain unbiased measurements of the cosmic UV background radiation field. Employing at first an extremely high quality sample of quasars (QSOs) from the VLT/UVES spectrograph, and then one of the largest QSO data sets ever compiled (thanks to the Sloan Digital Sky Survey) we have shown that this effect is not a statistical phenomenon. Instead the proximity effect is universal and can be found in essentially every high redshift quasar.

We have performed a systematic investigation of its signature along individual lines of sight employing the flux statistic technique which allows more precise determinations of its signal than the line statistic method. Regardless of the spectral resolution at our disposal, we have significantly detected this effect along at least 98% of our quasar sight lines, i.e. finding a decreasing opacity in the H I Lyα forest approaching the quasar systemic redshift.

Based on a fiducial value of the UVB photoionisation rate (or equivalently its intensity at the Lyman limit) our model of the proximity effect has allowed us to characterise its strength along each sight line.

6.1.2. Properties of the proximity effect strength distribution

Our new systematic study of the proximity effect strength along individual object has enabled us to construct the so-called proximity effect strength distribution (PESD). The PESD is significantly asymmetric and presents a well defined mode. Supported by Monte Carlo simulations, we have explored how the PESD behaves as the redshift, the luminosity or the environment of the quasars change (Chapter 2). While the shape of the PESD can be understood by simple statistical arguments, we have shown that its modal value is tightly connected to the cosmic UVB photoionisation rate.

We have presented convincing arguments based on the PESD shape against a strong systematic influence of gravitational clustering. By constructing a simple proxy for the excess of absorption near the quasar, we have identifyied only a small ($\sim$ 10%) fraction of QSO in the UVES sample affected by significant overdensities.

In particular, we have found that the PESD asymmentry is the main source for the overestimate of the UVB arising when combining the signal of multiple sight lines. Not the systematic gravitational clustering near the quasars. Our extensive Monte Carlo simulations have allowed us to correct for the systematic biases arising in the combined proximity effect signature. This procedure yielded additional estimates on the UVB in excellent agreement with the modal value of the PESD for both our UVES and SDSS samples.

Finally, only with the PESD analysis on small redshift intervals of the SDSS data set (Chapter 3) we have observationally shown that the skewness of the PESD changes with redshift, becoming narrower towards high redshift as predicted by our Monte Carlo simulations.

6.1.3. The evolution of the UV background radiation

In this thesis we have achieved a moltitute of new determinations of the cosmic UV background intensity and photoionisation rate at different epochs. In particular, thank to our methods we have been able to estimate the evolution of the UV background in small ($\Delta z = 0.2$) redshift intervals within each of the data set at our disposal.

Adopting the modal value of the PESD in the UVES sample of quasars we have estimated the UVB intensity at the Lyman limit ($J_{\nu_0} \sim 3 \times 10^{-22}$ erg s^{-1} cm^{-2} Hz^{-1} sr^{-1}, Chapter 2). Moreover, we have achieved an estimate of the UVB evolution within the range $2 < z < 4$, in spite of the limited number of available sight lines. Both results are now the first, obtained from the proximity effect, to be in considerable agreement with theoretical predictions from model or numerical simulations.

The same analyses have been applied to the SDSS data set. The extremely large number of quasars (1733 objects at $z > 2.3$) has allowed us to investigate the PESD within small redshift intervals extending over a $\Delta z = 0.25$. Thus, we have determined the evolution of the UVB photoionisation rate and found a rather constant level at $\Gamma_{\rm H\,I} \sim 1.6 \times 10^{-12}$ s^{-1} up to a redshift of about $z \sim 4.6$. Our UVES and SDSS results, inspite the extreme differences in terms of S/N, resolution and sample size, are in considerable (statistically indistinguishable) agreement at $z \lesssim 3.3$. Unfortunately, this agreement decreases at redshift $z \gtrsim 3.3$ where the only estimate from the UVES sample

is about 2σ below the SDSS results, thus suggesting a mild decrease of $\Gamma_{\rm H\,I}$.

Considering the characteristics of the two samples of quasars, a 2σ difference in just one measurement can be expected, in particular when comparing our results to other estimates of the cosmic UVB photoionisation rate (Bolton et al. 2005; Faucher-Giguere et al. 2008; Bolton et al. 2009).

6.1.4. The stellar contribution to the UV background

Thus far, the high redshift evolution of the UVB has been poorly constrained observationally. Most measurements from the proximity effect have been focussing on the redshift range $2 < z < 3$, with only few determinations at higher redshifts (e.g. Williger et al. 1994; Lu et al. 1996; Savaglio et al. 1997). We have presented the first conclusive measurements of the UVB evolution, from the biggest sample of quasars at high redshift invoking in total almost 1800 objects.

Therefore, we have been able to investigate the source populations actively contributing to the cosmic UV background radiation field. More importantly, our estimates have been completely built on observations and not on analytical models.

Considering different quasar luminosity functions, we have estimated at first the quasar contribution $\Gamma_{\rm q}$, finding in all cases a steep decline towards high redshift. Such a decline is so steep that an additional source of UV photons is required to keep the IGM highly ionised. Thus, we have confirmed the notion that a substantial fraction of ionising photons should eventually come from stars in young star-forming galaxies at $z \gtrsim 3$.

Assuming the evolution of $\Gamma_{\rm H\,I}$ derived from both the UVES and SDSS data sets, we have inferred the stellar luminosity density and found a good agreement up to $z \sim 3.5$ with the determination from deep galaxy surveys such as the VIMOS-VLT deep survey or the Subaru deep field. Only considering the constant photoionisation rate obtained from the SDSS quasar sample the agreement decreases at higher redshifts. Our results from the UVES data set are at all redshift very close to the deep surveys estimates.

6.1.5. New theoretical methods of detecting the proximity effect

The importance of new determinations of the UV background radiation field at different epochs are critical in this era of precision Cosmology. We have initiated the search for the most accurate method of determining the UVB intensity comparing at first the two (thus far) employed techniques: The line number statistic and the flux transmission statistic. We have shown the advantages of estimating the proximity effect signature with the flux statistic in particular as this method allows accurate measurements of the mean opacity along a single line of sight. The same type of determination is impossible by fitting lines on a single quasar spectrum due to the very small number of lines available in particular close to the emission redshift.

Motivated by the broad ramifications of a precise determination of the UVB both for numerical simulations and observations, we have developed and test a number of new techniques aimed at a more accurate estimate of $\Gamma_{\rm H\,I}$ (Chapter 4). With 3D numerical simulation we have considered at first the advantages of detecting the proximity effect on single sight lines to determine the proximity effect strength distribution. We have provided strong evidences in favor of the modal value of the PESD as unbiased estimator of the UVB photoionisation rate. We then concentrate on the development of new techniques based on more complex procedure as the maximisation of the likelihood function. In spite of our efforts, the likelihood function presented high order correlations which we were unable to control.

Thus, the PESD obtained from the flux transmission statistic is up to now the only method of measuring the UVB at high accuracy, free of intrinsic biases.

6.1.6. The radiative transfer simulation of the proximity effect

In the last years, the coupling of radiative transfer with numerical simulations of structure formation has captured increasing attention (e.g. Ciardi & Madau 2003; Maselli & Ferrara 2005). We have solved for the first time the complex radiative transport of energy on a cosmological simulation aiming at the detection of the proximity effect (Chapter 5).

While the complexity of such simulations limited a few aspects of our investigation, e.g. resolution, box size or number of quasar environments, the statistical analysis of the synthetic lines of sight agreed very well with that performed on real QSOs. The proximity effect obtained from the radiative transfer simulation and from the analytical model have equivalent properties. The PESD presented its characteristic peak, with an asymmetry which changes with redshift as observed in the SDSS sample. This added further evidences in favor of the validity of our procedure to determine the proximity effect strength, and thus the cosmic UV background.

6.2. Prospects for future studies

6.2.1. The high redshift evolution of the UVB

Inspite our achievements concearning the evolution of the UVB photoionisation rate between redshift $2 \lesssim z \lesssim 5$, the uncertainties are still relatively large, in particular at the high redshift end, due to the limited number of sight lines available.

This number is likely to increase when considering the available data in the archives of various facilities (ESO, Keck, Magellan) which offers already an excellent source of additional sight lines thereby yielding tighter constraints on the UVB at these redshifts. Moreover, from the same databases we also have the possibility of extending the estimates of the UVB evolution up to $z \sim 6$ providing crucial constraints on the process of the HI reionisation. As an example, in the ESO archive, about 40 quasars have been observed with high resolution (UVES) at redshifts larger than four. This increases the sample size of objects presented in this thesis by a factor of 10 and will be exploited to robustly determine the photoionisation rate of the UV background at high redshift.

In addition to already observed quasar lines of sight, the imminent availability of new instruments like X−shooter at VLT will offer an unexplored range of possibilities. With its extreme wavelength coverage, this instrument is the only spectrograph capable of the simultaneous detection of the Lyα forest and

the [O III] emission line up to redshift of $z \sim 3.7$. This results in three immediate advantage for the analysis of the proximity effect: (i) The most accurate systemic redshift determination achieved thus far, (ii) only few percent uncertainties in the quasar continuum assessment and (iii) precise measurement of the quasar spectral energy distribution and its luminosity at the Lyman limit. The analysis of additional lines of sight at redshift $z > 3$ is of essential importance to address the question of the high redshift evolution of the UVB we posed in this thesis. An X−shooter proposal has been submitted to address all these issues.

As a complementary approach we also intend to exploit more theoretical methods to determine the UVB photoionisation rate. The high resolution quasar spectra and 3D numerical simulations at our disposal offer a unique possibility for new estimates of $\Gamma_{\rm H\,I}$. With a detailed and sophysticated match of the effective optical depth evolution and the flux probability distribution we can constrain not only the effective equation of state between $2.25 < z < 4.5$, but also the cosmic UV background (Bolton et al. 2005; Faucher-Giguere et al. 2008; Bolton et al. 2009).

6.2.2. The importance of high redshift galaxies and Lyα-emitters

There is still a substantial discrepancy between the observed luminosity density of galaxies and the outcome of the most advanced hydrodynamical simulations, in particular at high redshift where the observational detection of such galaxies is extremely challenging (Hernquist & Springel 2003). Our results for $\Gamma_{\rm H\,I}$ from SDSS support the notion of a substantial amount of missing galaxies at high redshift. The commissioning of an instrument such as the Multi Unit Spectroscopic Explorer (MUSE), with its wavelength coverage (4500 – 9500 Å) will be the best available instrument to measure the impact of stellar emissivity up to redshift $z \simeq 6.7$ and thereby helping to understand whether the current surveys are missing a large fraction of high redshift galaxies or the models are inaccurate.

In addition, the importance of Lyα-emitters at high redshift has been capturing increasing attention as they seem to play a critical role for understanding the reionisation history of the Universe since (i) they provide a significant amount of UV photons capable of maintaining a high ionisation level of the IGM and (ii) their luminosity density directly probes the ionisation history of the IGM.

Recently Rauch et al. (2008), using a simple long-slit spectroscopic search, presented a deep investigation on this subject yielding a clear connection between Lyman limit systems in QSO spectra and Lyα-emitters. While their main limitation was the resources (instrument and allocated time) available for this type of analysis, the 2nd generation instruments at VLT soon to be available will offer new room for expansion and may ensure a much deeper investigation in terms of statistics, luminosity and redshift coverage.

6.2.3. Investigation of the quasar environment

A complementary tool to interpret our observations is offered by cosmological simulations. Our latest development is focusing on the implementation of an advanced radiative transfer algorithm, crucial for the understanding of several astrophysical problems. A characterisation of the environment in which QSOs evolve is still missing. Numerical simulations with radiative transfer offer a suitable tool to study the proximity effect statistic drawn from a variety of halo masses. Comparing these results with observations will lead to a first understanding of the systematic effects involved in the proximity effect analysis and to preciser estimates of the cosmic UV background radiation. These simulations are also perfectly suitable for a statistical analysis on the transverse proximity effect, i.e. the increased IGM transmission due to a foreground quasar near the line of sight to another background quasar, and the possibility of detecting anisotropies in the QSO radiation.

References

Bolton, J. S., Haehnelt, M. G., Viel, M., & Springel, V. 2005, MNRAS, 357, 1178
Bolton, J. S., Oh, S. P., & Furlanetto, S. R. 2009, ArXiv e-prints
Ciardi, B. & Madau, P. 2003, ApJ, 596, 1
Faucher-Giguere, C.-A., Lidz, A., Zaldarriaga, M., & Hernquist, L. 2008, ApJ, 673, 39
Hernquist, L. & Springel, V. 2003, MNRAS, 341, 1253
Lu, L., Sargent, W. L. W., Womble, D. S., & Takada-Hidai, M. 1996, ApJ, 472, 509
Maselli, A. & Ferrara, A. 2005, MNRAS, 364, 1429
Rauch, M., Haehnelt, M., Bunker, A., et al. 2008, ApJ, 681, 856
Savaglio, S., Christiani, S., D'Odorico, S., et al. 1997, A&A, 318, 347
Williger, G. M., Baldwin, J. A., Carswell, R. F., et al. 1994, ApJ, 428, 574

Appendix A

Analytical derivations

ABSTRACT

We present the detailed derivation of the most important models and techniques adopted in this thesis. First we describe the ionisation state of the intergalactic medium by determining the influence of the UV background and the quasar radiation fields on hydrogen absorbers in the line of sight towards a high redshift quasar (Section A.1.). We continue in Section A.2. presenting the detailed calculation behind the flux transmission technique employed to measure the proximity effect along single sight lines. Finally we analytically derive the connection between the emitting sources contributing to the budget of ionising photons in the Universe and the intensity of the UV background radiation field (Section A.3.).

A.1. The photoionisation state of the intergalactic medium

A.1.1. The UV background radiation field

From the observation of quasars at redshift $z \lesssim 6$ we know that the intergalactic medium is highly ionised and that it is kept in such a state by the cosmic UV background (UVB) radiation field. After the epoch of reionisation the UVB is driven by the cosmological expansion and the overall population of quasars and star-forming galaxies. Their integrated contribution changes on time scales much longer than a typical photoionisation equilibrium time scale which is of the order of 10^4 yr. Thus, assuming that the IGM is in ionisation equilibrium with the UV background is, to first order, a reasonable approximation.

If we consider a pure hydrogen cloud, with particle number density n, in ionisation equilibrium with the cosmic UV background $J_{\nu,\mathrm{H\,I}}$, we can write the ionisation equilibrium as

$$n_{\mathrm{H\,II}}\alpha\,(T)\,n_e = n_{\mathrm{H\,I}}\Gamma_{\mathrm{H\,I}}, \tag{A.1}$$

where $n_{\mathrm{H\,I}}$ and $n_{\mathrm{H\,II}}$ represent the particle number densities of H I and H II, respectively, n_e is the density of free electron and, $\alpha(T)$ and $\Gamma_{\mathrm{H\,I}}$ are the recombination coefficient and the photoionisation rate of the UV background. The latter is defined as

$$\Gamma_{\mathrm{H\,I}} = \int_{\nu_0}^{\infty} \frac{4\pi J_{\nu,\mathrm{H\,I}}\,(\nu)}{h\nu}\,\sigma\,(\nu)\,\mathrm{d}\nu, \tag{A.2}$$

with ν_0 being the Lyman limit frequency and $\sigma(\nu)$ the photoionisation cross section, which is given by $\sigma(\nu) = \sigma_{\nu_0}\,(\nu/\nu_0)^{-3}$ where $\sigma_{\nu_0} = 6.33 \times 10^{-18}\ \mathrm{cm}^2$.

Assuming that such a cloud is optically thin to ionising photons, the recombination coefficient is written as $\alpha(T) \simeq 2.51 \times 10^{-13} T_{4.3}^{-0.76}\ \mathrm{cm}^{-3}\,\mathrm{s}^{-1}$ where T is given by some typical temperatures in the intergalactic medium $T_{4.3} = T/(10^{4.3}\,\mathrm{K}) \simeq 1$ (Fardal et al. 1998). The validity of Eq. (A.1) extends also to the column density $N_{\mathrm{H\,I}}$ expressing the projected particle number density along the line of sight to the quasar.

A.1.2. The additional contribution from quasars

The UV background radiation is subject to a redshift evolution, as the source populations of QSOs and galaxies change with redshift, and to inhomogeneity in the vicinity of luminous sources such as bright quasars.

A drastic increase in the ionising flux results in a: (i) Decrease of the photoionisation equilibrium timescale and (ii) change of the equilibrium conditions with respect to Eq. A.1. At the new equilibrium state we have that

$$n'_{\mathrm{H\,II}}\alpha\,(T')\,n'_e = n'_{\mathrm{H\,I}}\left(\Gamma_{\mathrm{H\,I}} + \Gamma_{\mathrm{q}}\right) \tag{A.3}$$

with Γ_{q} expressing the additional photoionisation rate due to the local sources.

Neglecting the heat induction from the quasar radiation to the IGM and the weak temperature variation in the recombination coefficient, we have that $\alpha(T') \simeq \alpha(T)$. Since we are dealing with a pure hydrogen cloud, we have that $n_e = n_{\mathrm{H\,II}}$, thus in the absorber we obtain

$$n_{\mathrm{H\,I}}\Gamma_{\mathrm{H\,I}} \simeq \left(\Gamma_{\mathrm{H\,I}} + \Gamma_{\mathrm{q}}\right)\left(1 + \frac{n'_{\mathrm{H\,I}}}{n'_{\mathrm{H\,II}}} - \frac{n_{\mathrm{H\,I}}}{n'_{\mathrm{H\,II}}}\right)^2 . \tag{A.4}$$

Because of the high ionisation state in the intergalactic medium, we have that $n'_{\mathrm{H\,I}}/n'_{\mathrm{H\,II}} \ll 1$ and $n_{\mathrm{H\,I}}/n'_{\mathrm{H\,II}} \ll 1$ and therefore the neutral hydrogen density becomes

$$n'_{\mathrm{H\,I}} \simeq n_{\mathrm{H\,I}}\frac{\Gamma_{\mathrm{H\,I}}}{\Gamma_{\mathrm{H\,I}} + \Gamma_{\mathrm{q}}} = \frac{n_{\mathrm{H\,I}}}{1+\omega} \tag{A.5}$$

where ω is defined as the ratio of the ionisation rates of the local quasar and that of the UV background

$$\omega \equiv \frac{\Gamma_{\mathrm{q}}}{\Gamma_{\mathrm{H\,I}}}. \tag{A.6}$$

As already stated, we can write a formula equivalent to Eq. A.5 for the column density, yielding

$$N_{\mathrm{H\,I}} = \frac{N_{\mathrm{H\,I},\infty}}{1+\omega} \tag{A.7}$$

with $N_{\mathrm{H\,I},\infty}$ being the column density that would be measured if the quasar was located at infinite distance from the cloud.

If we consider a constant UV background photoionisation rate over the redshift path length probed by the Lyα forest of a single quasar, ω is a scale depending on the attenuation of the quasar radiation field. In first approximation we can think of this scaling as a simple $1/r^2$ law, where r describe the distance from the QSO and thus approaching the source we have $r \to 0^+$ and $\omega \to +\infty$.

A.1.3. The ratio of photoionisation rates

Similar to Equation A.2, the photoionisation rate of a quasar can be expressed by

$$\Gamma_{\mathrm{q}}(z) = \int_{\nu_0}^{\infty} \frac{f_\nu(\nu, z)}{h\nu}\,\sigma(\nu)\,\mathrm{d}\nu \tag{A.8}$$

where $f_\nu(\nu, z)$ is the quasar flux density at redshift z at frequency ν. In the absorber rest frame, the flux density f_ν can be written in units of the quasar luminosity as

$$f_\nu(\nu, z) = \frac{L_\nu\left(\nu\left(1+z'_{\mathrm{q}}\right)\right)}{4\pi d_L^2\left(z_{\mathrm{q}}, z\right)}\left(1+z'_{\mathrm{q}}\right) \tag{A.9}$$

where $1 + z'_{\mathrm{q}} = (1+z_{\mathrm{q}})/(1+z)$ and $d_L\left(z_{\mathrm{q}}, z\right)$ are the redshift and luminosity distance of the quasar as seen by any given absorber along the line of sight such that $z < z_{\mathrm{q}}$ (the latter will be explicitly derived in Sect. A.1.4.).

The quasar luminosity can be written in units of the quasar flux density $f_\nu(\nu_{\mathrm{obs}}, 0)$ at $z = 0$ yielding

$$L_\nu\left(\nu\left(1+z'_{\mathrm{q}}\right)\right) = \frac{4\pi d_L^2\left(z_{\mathrm{q}}, 0\right)}{1+z_{\mathrm{q}}} f_\nu\left(\nu\left(\frac{1+z'_{\mathrm{q}}}{1+z_{\mathrm{q}}}\right), 0\right) \tag{A.10}$$

where the frequency $\nu_{\mathrm{obs}} = \nu\left(\frac{1+z'_{\mathrm{q}}}{1+z_{\mathrm{q}}}\right)$ is the one observed today.

The quasar flux density at wavelengths shorter than the rest frame Lyman limit is difficult to probe, mainly due to the absorption in the Lyα forest. Its numerical value is usually inferred by approximating the quasar continuum flux with a power law of the form $f_\nu \propto \nu^\alpha$. The region in the quasar spectrum redward of the Lyα emission line is typically adopted to estimate the spectral index α_{q} of the quasar since it is much less affected by absorption lines. Thus we can write that

$$f_\nu\left(\nu\left(\frac{1+z'_{\mathrm{q}}}{1+z_{\mathrm{q}}}\right), 0\right) = f_\nu\left(\frac{\nu_0}{1+z_{\mathrm{q}}}, 0\right)\left(\frac{\nu}{\nu_0}\right)^{\alpha_{\mathrm{q}}}\left(1+z'_{\mathrm{q}}\right)^{\alpha_{\mathrm{q}}}. \tag{A.11}$$

If we now integrate (A.8) with the proper substitutions we obtain

$$\Gamma_{\mathrm{q}}(z) = \frac{\sigma_{\nu_0}}{h\left(3-\alpha_{\mathrm{q}}\right)} f_\nu\left(\frac{\nu_0}{1+z_{\mathrm{q}}}, 0\right)\frac{\left(1+z'_{\mathrm{q}}\right)^{1+\alpha_{\mathrm{q}}}}{1+z_{\mathrm{q}}}\left(\frac{d_L\left(z_{\mathrm{q}}, 0\right)}{d_L\left(z_{\mathrm{q}}, z\right)}\right)^2 \tag{A.12}$$

or, equivalently, as a function of the quasar Lyman limit luminosity

$$\Gamma_{\mathrm{q}}(z) = \frac{\sigma_{\nu_0}\, L_\nu\left(\frac{\nu_0}{1+z_{\mathrm{q}}}, 0\right)\left(1+z'_{\mathrm{q}}\right)^{1+\alpha_{\mathrm{q}}}}{4\pi\, h\left(3-\alpha_{\mathrm{q}}\right)\, d_L^2\left(z_{\mathrm{q}}, z\right)}. \tag{A.13}$$

If we approximate the UV background intensity as a power law in the same form as the quasar, we have that $J_{\nu,\mathrm{H\,I}} \propto \nu^{\alpha_\mathrm{b}}$, which implies that

$$\Gamma_{\mathrm{H\,I}}(z) = \frac{4\pi\sigma_{\nu_0}}{h\,(3-\alpha_\mathrm{b})} J_\nu\left(\frac{\nu_0}{1+z_\mathrm{q}}, z\right) \tag{A.14}$$

where $J_{\nu_0}(z)$ represents the UV background intensity at the Lyman limit. We can now explicitly write ω as a function of the quasar luminosity and the UVB intensity both at the Lyman limit as

$$\omega(z) = \frac{\left(1+z'_\mathrm{q}\right)^{1+\alpha_\mathrm{q}}}{16\pi^2\, d_L^2\left(z_\mathrm{q}, z\right)} \left(\frac{3-\alpha_\mathrm{b}}{3-\alpha_\mathrm{q}}\right) \frac{L_\nu\left(\frac{\nu_0}{1+z_\mathrm{q}}, 0\right)}{J_\nu\left(\frac{\nu_0}{1+z_\mathrm{q}}, z\right)} \tag{A.15}$$

This equation has been used in Chapter 2 and Chapter 5 to measure the UV background intensity at the Lyman limit.

A.1.4. The quasar luminosity distance as seen along the sight line

The only quantity which is still missing in our calculation of ω is the quasar luminosity distance as measured by any absorber along the line of sight with redshift z smaller than the QSO redshift z_q. Such a luminosity distance $d_L\left(z_\mathrm{q}, z\right)$ is given by

$$d_L\left(z_\mathrm{q}, z\right) = \left(1+z'_\mathrm{q}\right) a(z)\, r\left(z_\mathrm{q}, z\right) \tag{A.16}$$

where $a(z) = 1/(1+z)$ is the scale factor and $r(z_\mathrm{q}, z)$ represents the distance between the quasar and the absorber in comoving units. Thus, the luminosity distance depends on the assumed cosmological model, in our case a Λ-cosmology.

For a flat Λ-Universe with matter density parameter Ω_m and a cosmological constant given by Ω_Λ we can express the redshift dependence of the Hubble parameter in the form

$$H(z) = H_0 \sqrt{\Omega_\mathrm{m}(1+z)^3 + \Omega_\Lambda} \tag{A.17}$$

and the matter density parameter by

$$\Omega_\mathrm{m}(z) = \frac{\Omega_\mathrm{m}(1+z)^3}{\Omega_\mathrm{m}(1+z)^3 + \Omega_\Lambda} \tag{A.18}$$

knowing that

$$\Omega_\Lambda(z) = 1 - \Omega_\mathrm{m}(z)\,. \tag{A.19}$$

Therefore the luminosity distance becomes

$$d_L\left(z_\mathrm{q}, z\right) = \left(1+z'_\mathrm{q}\right) \frac{c}{H(z)} \int_0^{z'_\mathrm{q}} \frac{\mathrm{d}\tilde{z}}{\sqrt{\Omega_\mathrm{m}(z)\,(1+\tilde{z})^3 + \Omega_\Lambda(z)}}. \tag{A.20}$$

The introduction of a proper cosmological model in the computation of ω has been largely disregarded leading to a significant overestimation in the measurements of the UV background intensity.

A.2. The flux transmission technique

Initially introduced by Zuo & Phinney (1993), the flux transmission statistic has been immediately adopted thanks to its wide applicability from high to low resolution spectra, to 25 Å resolution (Oke & Korycansky 1982; Zuo 1993; Press et al. 1993; Press & Rybicki 1993; Liske et al. 1998; Liske & Williger 2001; Worseck et al. 2007, and in this thesis).

This technique is based upon the assumption that the Lyα forest is represented by a large number of individual absorbers whose parameters are uncorrelated. The distribution function of those absorbers, $\eta(z, N_{\mathrm{H\,I}}, b)$, is known from observations to be a composition of the following three distributions: (i) the line number density evolution function, (ii) the differential distribution function of column densities and (iii) the Doppler parameter distribution. In the original derivation by Zuo & Lu (1993) no further assumption is made about the nature of the absorption.

Let us begin by considering a region in a quasar spectrum populated by Lyα absorption systems as presented in Fig. A.1. For each resolution element we can write that

$$F(z) = F_0(z)\, e^{-\tau(z)} \tag{A.21}$$

where F_0 is the continuum level, F is the actual value of the observed flux and $\tau(z)$ represents the optical depth along the line of sight.

The transmitted flux, or simply the transmission is defined as

$$T(z) = \frac{F(z)}{F_0(z)} = e^{-\tau(z)}. \tag{A.22}$$

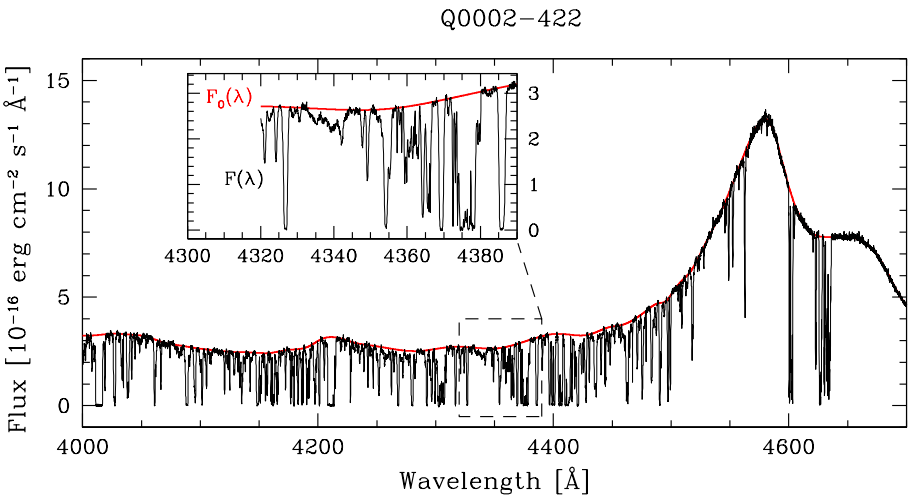

Fig. A.1. An example of a high redshift quasar spectrum (Q 0002−422 at $z_{\rm em} = 2.767$) as observed by UVES at VLT. A detailed characterisation of the absorption pattern in the Lyα forest ($F(z)$) is shown in the small panel above the quasar spectrum. The continuous thick line represent the inferred quasar flux $F_0(z)$ unaffected by the neutral hydrogen in the IGM.

If now the number of absorption lines along the sight line to a quasar follows a Poisson distribution, the average number of lines can be expressed by

$$m = \int_0^\infty \int_0^\infty \int_{z_1}^{z_1} \eta \, \mathrm{d}z \, \mathrm{d}N_{\rm H\,I} \, \mathrm{d}b \tag{A.23}$$

with $\eta(z, N_{\rm H\,I}, b)$ being the line number density per unit redshift, column density and Doppler parameter and, z_1 and z_2 are two arbitrary observed redshifts along the line of sight.

The effective optical depth is by definition

$$e^{-\tau_{\rm eff}(z)} = \left\langle e^{-\tau(z)} \right\rangle = \langle T(z) \rangle \tag{A.24}$$

and therefore, the total average transmission becomes

$$e^{-\tau_{\rm eff}(z)} = \sum_{k=0}^{\infty} p(k;m) \prod_{i=1}^{\rm k} \left\langle e^{-\tau_{\rm s}(z)} \right\rangle_i = \sum_{k=0}^{\infty} \frac{e^{-m} m^k}{k!} \cdot \overbrace{\prod_{i=1}^{\rm k} \left\langle e^{-\tau_{\rm s}(z)} \right\rangle_i}^{\left\langle e^{-\tau_{\rm s}(z)} \right\rangle^k}, \tag{A.25}$$

where $p(k;m)$ is the probability distribution of the clouds and $e^{-\tau_{\rm s}(z)}$ the optical depth of a single absorber.

With the definition of exponential we have

$$e^{-\tau_{\rm eff}(z)} = e^{-m} \underbrace{\sum_{k=0}^{\infty} \frac{m^k}{k!} \left\langle e^{-\tau_{\rm s}(z)} \right\rangle^k}_{\text{def. of Exp.}} = e^{-m} e^{m \left\langle e^{-\tau_{\rm s}(z)} \right\rangle} \tag{A.26}$$

which implies an effective optical depth equal to

$$\tau_{\rm eff}(z) = m \left(1 - \left\langle e^{-\tau_{\rm s}(z)} \right\rangle \right), \tag{A.27}$$

where the average contribution of a single absorption cloud is the average of all the absorption divided by the expected number of absorbers

$$\left\langle e^{-\tau_{\rm s}(z)} \right\rangle = m^{-1} \int_{z, N_{\rm H\,I}, b} \eta \, \exp\left[-\tau_{\rm s}(z, N_{\rm H\,I}, b) \right] \, \mathrm{d}z \, \mathrm{d}N_{\rm H\,I} \, \mathrm{d}b. \tag{A.28}$$

The effective optical depth then becomes

$$\tau_{\rm eff}(z) = m(1 - \left\langle e^{-\tau_{\rm s}(z)} \right\rangle) = \int_{N_{\rm H\,I}, b, z} \eta \left[1 - e^{-\tau_{\rm s}(z, N_{\rm H\,I}, b)} \right] \, \mathrm{d}z \, \mathrm{d}N_{\rm H\,I} \, \mathrm{d}b. \tag{A.29}$$

If we exclude from this analysis damped Lyα systems, then $e^{-\tau_{\rm s}(z, N_{\rm H\,I}, b)}$ sharply peaks at the redshift of the absorber so that

$$\tau_{\rm eff}(z) \simeq \frac{1+z}{\lambda_{{\rm Ly}_\alpha}} \int_{N_{\rm H\,I}, b} \eta \underbrace{\int_0^\infty 1 - e^{-\tau_{\rm s}(z, N_{\rm H\,I}, b)} \, \mathrm{d}z}_{W(N,b)} \, \mathrm{d}N_{\rm H\,I} \, \mathrm{d}b, \tag{A.30}$$

where $\lambda_{{\rm Ly}_\alpha} = 1215.67$ Å. The distribution function of the absorbers in the Lyα forest per unit redshift, column density and Doppler parameter can be approximated by

$$\eta(z, N_{\rm H\,I}, b) = \frac{\mathrm{d}^3 n}{\mathrm{d}z \, \mathrm{d}N_{\rm H\,I} \, \mathrm{d}b} = \eta_0 \, (1+z)^\gamma \, N_{\rm H\,I}^{-\beta} \frac{\mathrm{d}n}{\mathrm{d}b}, \tag{A.31}$$

and if we substitute Equation A.31 into Equation A.30 we obtain

$$\tau_{\rm eff}(z) = \frac{(1+z)^{\gamma+1}}{\lambda_{{\rm Ly}_\alpha}} \underbrace{\int_0^\infty W(N_{\rm H\,I}, b)\, \eta_0 N_{\rm H\,I}^{-\beta} \frac{{\rm d}n}{{\rm d}b}\, {\rm d}N_{\rm H\,I}\, {\rm d}b}_{\rm Constant} = \tau_0 (1+z)^{\gamma+1} \tag{A.32}$$

where η_0 incorporates all the proportionality constants of the different distribution functions.

Using a more accurate notation we should write that

$$\tau_{{\rm eff},\infty}(z) = \frac{(1+z)^{\gamma+1}}{\lambda_{{\rm Ly}_\alpha}} \underbrace{\int_0^\infty W(N_{{\rm H\,I},\infty}, b)\, \eta_0 N_{{\rm H\,I},\infty}^{-\beta} \frac{{\rm d}n}{{\rm d}b}\, {\rm d}N_{{\rm H\,I},\infty}\, {\rm d}b}_{\rm Constant} = \tau_{0,\infty}\, (1+z)^{\gamma+1} \tag{A.33}$$

where ∞ signifies that the given quantities are those that would be observed far away from any local source of ionising photons, i.e. a quasar.

To take into account the additional influence of ionising radiation coming from a bright quasar we need to understand how the enhanced ionising field manifests itself on the neutral gas in the vicinity of the quasar. As derived in Sect. A.1.2., the relation between the column density before and after the influence of the quasar is

$$N_{{\rm H\,I},\infty} = N^\star_{\rm H\,I}\ (1+\omega(z)) \tag{A.34}$$

where $N^\star_{\rm H\,I}$ is the column density with the proximity effect, i.e. the column density that is actually observed in the spectrum. Thus the column density distribution in Eq. A.33 becomes

$$N_{{\rm H\,I},\infty}^{-\beta}\, {\rm d}N_{{\rm H\,I},\infty} = \left(N^\star_{\rm H\,I}\right)^{-\beta}\ (1+\omega(z))^{1-\beta}\ {\rm d}N^\star_{\rm H\,I}. \tag{A.35}$$

Finally we can write the effective optical depth including the radiative influence of a quasar as

$$\tau_{\rm eff}(z) = \tau_0 (1+z)^{\gamma+1}\, (1+\omega(z))^{1-\beta}\,. \tag{A.36}$$

A.3. The cosmological radiative transfer

The equation describing the time evolution of a diffuse radiation field of specific intensity J_ν can be expressed as (e.g. Peebles 1993).

$$\left(\frac{\partial}{\partial t} - \nu H \frac{\partial}{\partial \nu}\right) J_\nu = -3HJ_\nu - c\alpha_\nu J_\nu + \frac{c}{4\pi}\epsilon_\nu \tag{A.37}$$

where $H(t)$ is the Hubble parameter, c is the speed of light and, α_ν and ϵ_ν represent the absorption and emission coefficients. The mean specific intensity at the observed frequency ν_0 and at a given redshift z_0 is

$$J_\nu\,(\nu_0, z_0) = \frac{1}{4\pi} \int_{z_0}^\infty \frac{(1+z_0)^3}{(1+z)^3}\, \epsilon_\nu(\nu, z)\, {\rm e}^{-\tau_{\rm Lyc}(\nu_0, z_0, z)}\, \frac{{\rm d}l}{{\rm d}z}\, {\rm d}z \tag{A.38}$$

with $\nu = \nu_0(1+z)/(1+z_0)$. ${\rm d}l/{\rm d}z = c/\left[H(z)(1+z)\right]$ is the proper length element and $\tau_{\rm eff}$ describes the radiation filtering due to intervening absorption.

Following the formalism introduced in (A.29), the Lyman continuum optical depth for a Poisson distribution of clouds along the line of sight is

$$\tau_{\rm Lyc}(\nu_0, z_0, z) = \int_{z_0}^z {\rm d}z' \int_0^\infty {\rm d}N_{\rm H\,I}\, \frac{{\rm d}^2 n}{{\rm d}N_{\rm H\,I}\, {\rm d}z'} (1 - e^{-\tau(z')}) \tag{A.39}$$

where ${\rm d}^2 n/{\rm d}N_{\rm H\,I}\, {\rm d}z'$ represents the redshift and column density distribution of absorbers along the line of sight and $\tau(z') = N_{\rm H\,I}\, \sigma_{\rm H\,I}(z')$ is the optical depth of a single absorber. The only difference from (A.29) is that no integral over the Doppler parameter is performed.

If we assume that the column density and redshift distribution of absorbers are well represented by a single power law (which is a good approximation for redshift $2 < z < 5$) we have that

$$\frac{{\rm d}^2 n}{{\rm d}N_{\rm H\,I}\, {\rm d}z'} = N_0\, N_{\rm H\,I}^{-\beta}\, (1+z')^\gamma. \tag{A.40}$$

The general solution to equation (A.39) is

$$\tau_{\rm Lyc}(\nu_0, z_0, z) = \frac{\Gamma(2-\beta)}{(\beta-1)(\gamma-3\beta+4)} N_0 \left(\frac{\nu}{\nu_0}\right)^{3(\beta-1)} \sigma_\nu^{\beta-1}(\nu_0)(1+z_0)^{3(\beta-1)} \left[(1+z)^{\gamma-3\beta+4} - (1+z_0)^{\gamma-3\beta+4}\right] \quad (A.41)$$

where $\Gamma(2-\beta)$ is in this case the Gamma function.

The rapid increase of opacity along the LOS for $z \gtrsim 2$ leads to a significant reduction in the mean free path of ionising photons, which as a consequence, means that only *local* sources contribute significantly to the UV background intensity (Madau et al. 1999; Schirber & Bullock 2003). This effectively means that a photon is absorbed so close to the source of emission that its redshift can be neglected. In this approximation the solution of (A.38) is given by

$$J_\nu(\nu_0, z_0) \simeq \frac{\Delta l(\nu_0, z)\, \epsilon_\nu(\nu_0, z)}{4\pi}, \quad (A.42)$$

where in general the mean free path $\Delta l(\nu_0, z)$ is expressed as

$$\Delta l(\nu_0, z) = \frac{{\rm d}l}{{\rm d}z'}(z) \left(\frac{{\rm d}\tau(\nu_0, z)}{{\rm d}z'}\right)^{-1}(z). \quad (A.43)$$

As the redshift of the photons are negligible, so are any cosmological effects on the mean free path, thus we can rewrite (A.43) adopting the Euclidean geometry yielding

$$\Delta l(\nu_0, z) = \left(\frac{{\rm d}\tau(\nu_0, z)}{{\rm d}l}\right)^{-1}(z). \quad (A.44)$$

Assuming a single power law representation for the column density distribution and the line number density evolution with slopes β and γ, respectively, at redshift $z > 2$ we obtain

$$\Delta l(\nu_0, z) \simeq \frac{(\beta-1)\, c}{\Gamma(2-\beta)\, N_0 \sigma_\nu^{\beta-1}(\nu_0)} \frac{1}{(1+z)^{\gamma+1}\, H(z)} \quad (A.45)$$

The major contribution to the mean opacity at the Lyman limit is driven by systems of optical depth near unity, or equivalently column densities of the order of $N_{\rm H\,I} \simeq 10^{17.2}$ cm^{-2}. However lower column density systems contribute non-negligibly to the Lyman continuum opacity therefore we fixed the constant values to $(N_0, \beta, \gamma) = (1.4\times10^7, 1.5, 2.45)$ following Madau et al. (1999) and Péroux et al. (2003).

Assuming that the UV background intensity has a power law shape for wavelengths shorter than the Lyman limit ($J_\nu \propto \nu^{\alpha_{\rm b}}$), the UVB photoionisation rate becomes

$$\Gamma(z) \simeq \frac{\sigma_\nu(\nu_0)\, \Delta l(\nu_0, z)\, \epsilon_\nu(\nu_0, z)}{h\,(3-\alpha_{\rm b})}. \quad (A.46)$$

This Equation A.46 directly connects the photoionisation rate with the luminosity density or emissivity at the Lyman limit of a specific population of sources in the Universe. If we assume that only quasars and star-forming galaxies are responsible for the cosmic photoionisation rate, we can decompose the emissivity term of Equation A.46 into its basic constituents as

$$\epsilon_\nu(\nu_0, z) = \epsilon_{\nu,{\rm q}}(\nu_0, z) + \epsilon_{\nu,{\rm g}}(\nu_0, z) \quad (A.47)$$

where $\epsilon_{\nu,{\rm q}}(\nu_0, z)$ and $\epsilon_{\nu,{\rm g}}(\nu_0, z)$ represent the quasar and galaxy emissivities at the Lyman limit, respectively.

References

Fardal, M. A., Giroux, M. L., & Shull, J. M. 1998, AJ, 115, 2206
Liske, J., Webb, J. K., & Carswell, R. F. 1998, MNRAS, 301, 787
Liske, J. & Williger, G. M. 2001, MNRAS, 328, 653
Madau, P., Haardt, F., & Rees, M. J. 1999, ApJ, 514, 648
Oke, J. B. & Korycansky, D. G. 1982, ApJ, 255, 11
Peebles, P. J. E. 1993, Principles of Phisical Cosmology (Princeton Univeristy Press)
Péroux, C., McMahon, R. G., Storrie-Lombardi, L. J., & Irwin, M. J. 2003, MNRAS, 346, 1103
Press, W. H. & Rybicki, G. B. 1993, ApJ, 418, 585
Press, W. H., Rybicki, G. B., & Schneider, D. P. 1993, ApJ, 414, 64
Schirber, M. & Bullock, J. S. 2003, ApJ, 584, 110
Worseck, G., Fechner, C., Wisotzki, L., & Dall'Aglio, A. 2007, A&A, 473, 805
Zuo, L. 1993, A&A, 278, 343
Zuo, L. & Lu, L. 1993, ApJ, 418, 601
Zuo, L. & Phinney, E. S. 1993, ApJ, 418, 28

Appendix B

The proximity effect on individual lines of sight in the UVES sample of quasars

ABSTRACT

We present here the signature of the proximity effect estimated along each of the 40 UVES/VLT quasar spectra presented in Chapter 2.

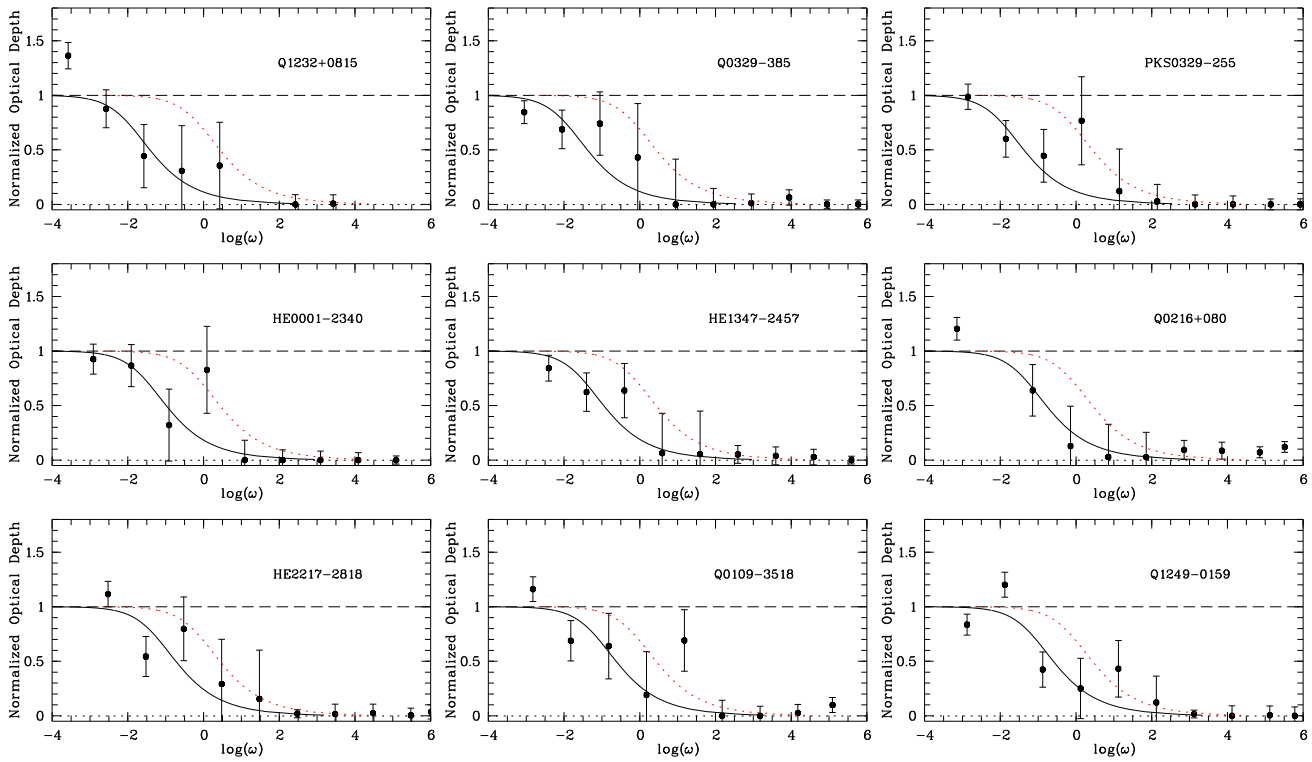

Fig. B.1. The proximity effect signatures in individual lines of sight. Each panel shows the normalised optical depth ξ versus ω, binned in steps of $\Delta \log \omega = 1$, with the best-fit model of the combined analysis superimposed as dotted red lines. The solid lines delineate the best fit to each individual QSO as described in the text.

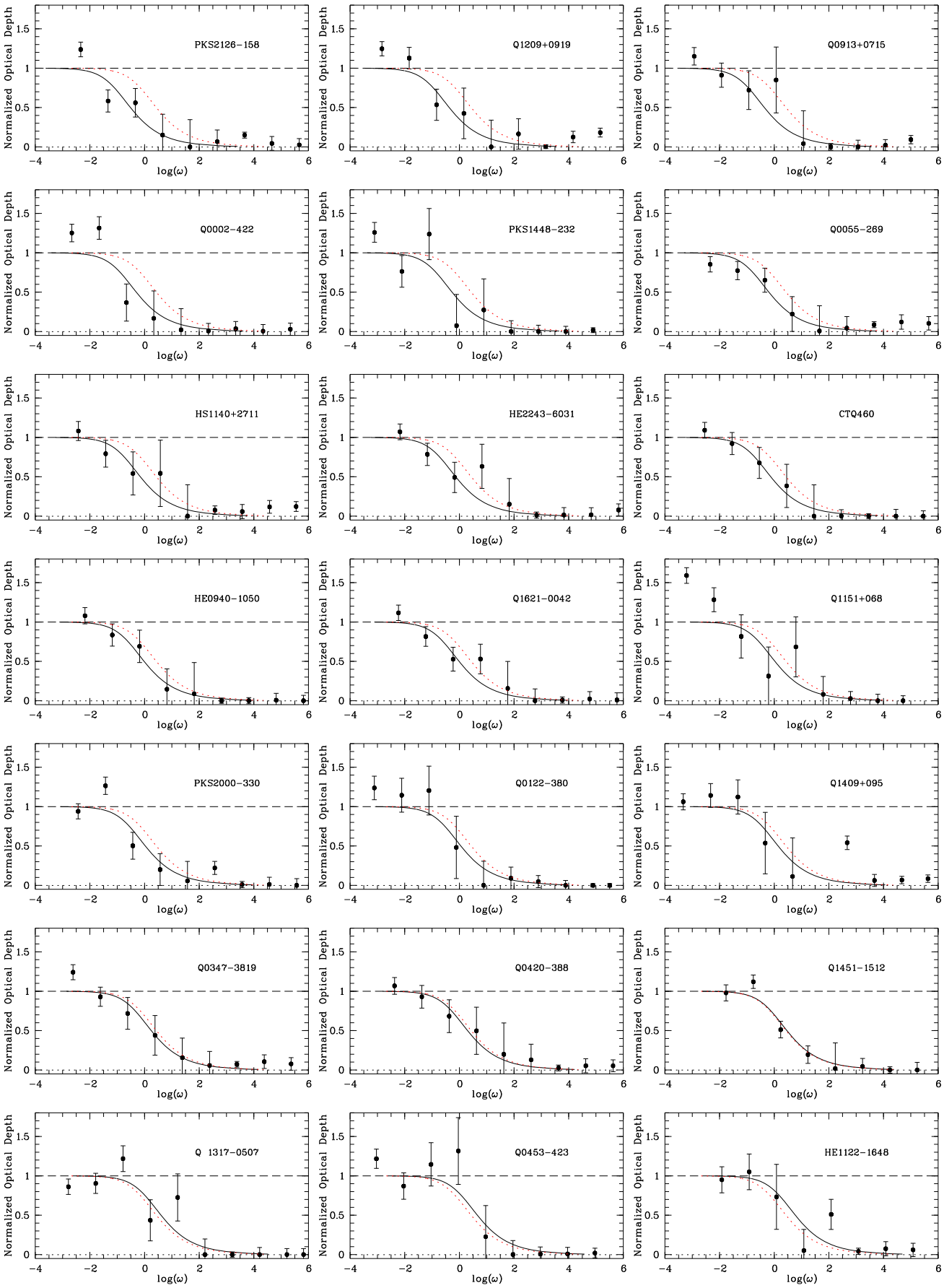

Fig. B.1. Continued

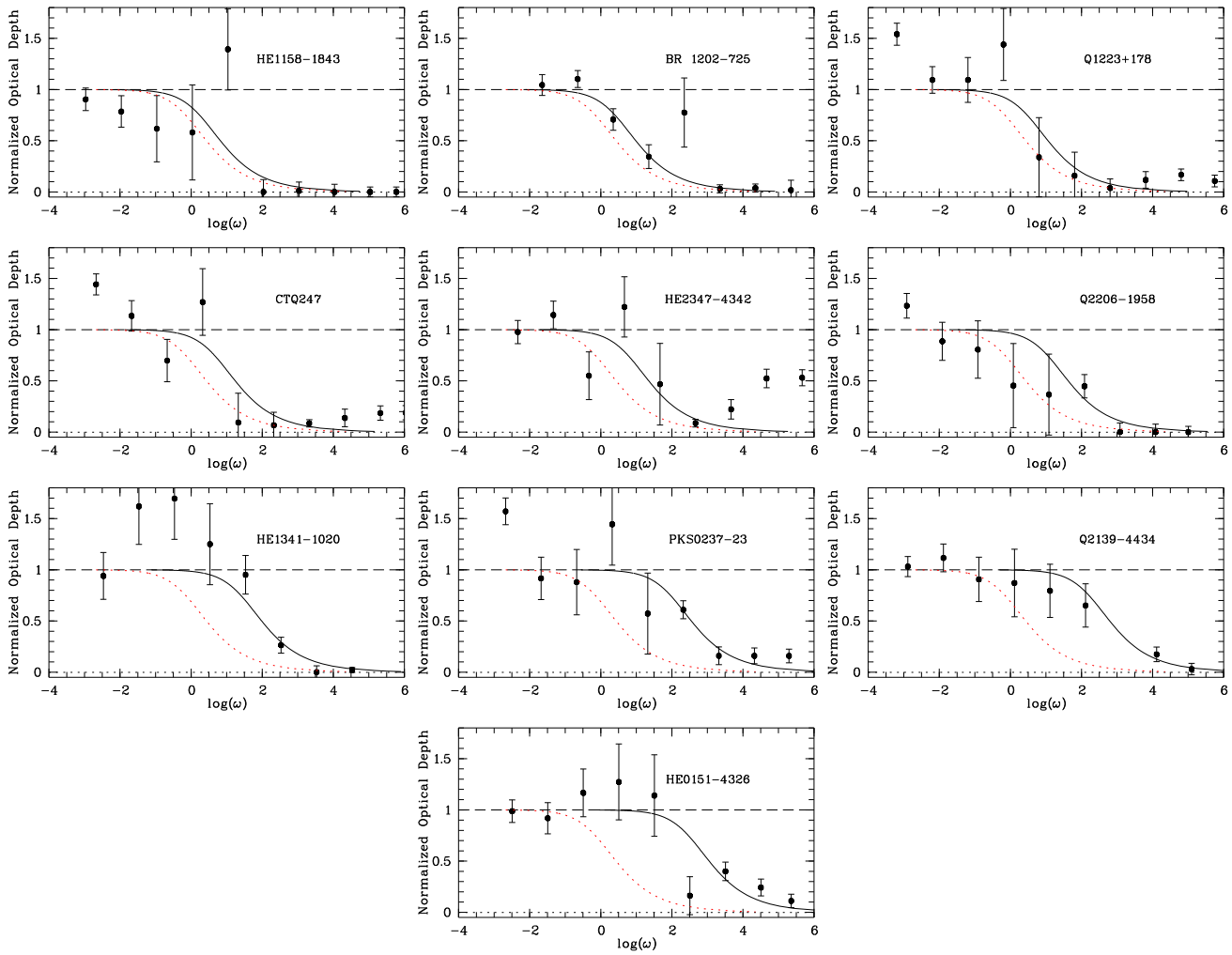

Fig. B.1. Continued

Appendix C

Error assessment of the high-z UV background derived from SDSS

ABSTRACT

The estimates of the cosmic UV background (UVB) photoionisation rate obtained from our VLT/UVES and SDSS samples of quasars are in excellent agreement at redshift $z \lesssim 3.3$. At higher redshift however, the UVES value of $\Gamma_{\rm H\,I}$ is about 2σ below the other estimates, suggesting a mild decrease of the photoionisation rate at high redshift, as already reported in Chapter 2. On the contrary, the SDSS measurements continue to show a constant UVB up to the high end of the redshift coverage. While this discrepancy has a marginal statistical significance (as only 7 QSOs in our UVES sample are at $z \gtrsim 3.3$ instead of ~ 400 in SDSS), we cannot rule out the possibility that the SDSS measurements are affected by systematic uncertainties leading them to favour a constant level of $\Gamma_{\rm H\,I}$ up to redshift $z \simeq 4.6$. We present here a detailed investigation of the principal sources of uncertainties that may have a significant influence in biasing our determination of the UVB photoionisation rate. The purpose of this Appendix is to disclose the details of our computation giving particular emphasis to explicit examples presenting the robustness of our measurements of $\Gamma_{\rm H\,I}$.

C.1. Determination of the quasar Lyman limit luminosity

The computation of the Lyman limit luminosity of each quasar is based on the estimate of the rest frame Lyman limit flux density f_{ν_0} that is inferred from a power law fit to the quasar continuum. We selected several regions redward of the Lyα emission line free of absorption or emission in order not to be biased. We adopted a fitting function of the form $f_\nu \propto \nu^\alpha$ and four rest frame wavelength intervals 1330 – 1380 Å, 1570 – 1610 Å, 1420 – 1500 Å and 2000 – 2500 Å. Unfortunately for QSOs at redshift $z \gtrsim 3.6$ the last interval falls outside the wavelength coverage and the power law fit has to rely only on the remaining three intervals.

Understanding the effect of fewer wavelength intervals when performing the fit, and therefore the determination of the Lyman limit flux, is important to reveal possible biases of the modal value of the proximity effect strength distribution (PESD) at high redshift. As we do not have at our disposal spectral information beyond a wavelength of ~ 9200 Å, the assessment of the effect of fewer intervals when computing f_{ν_0} needs to be performed in one of the lower redshift subsets. We chose the subset S2 and our

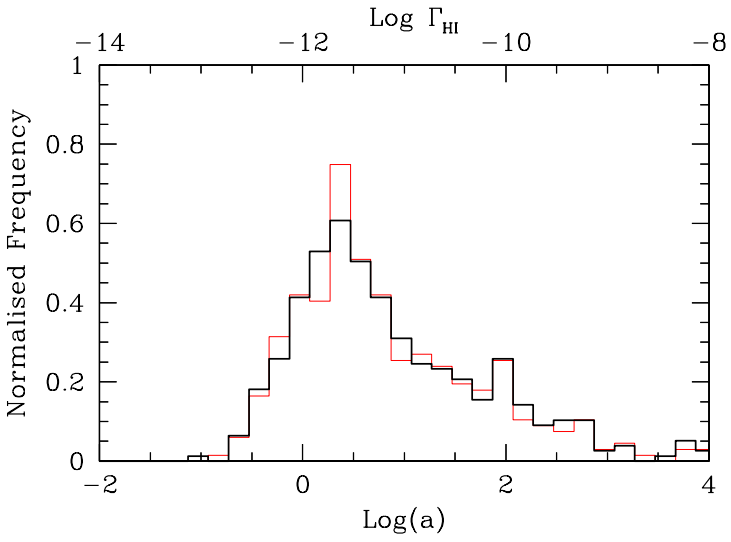

Fig. C.1. The proximity effect strength distribution determined in the subset S2, i.e. for quasars with emission redshifts between $2.5 < z_{\rm q} < 2.75$. The black thick histogram shows the PESD obtained using four wavelength intervals to estimate the quasar flux at the Lyman limit as described in the text. The PESD estimated when removing the last interval (2000 – 2500 Å) in the power law fit is plotted as the red thin histogram.

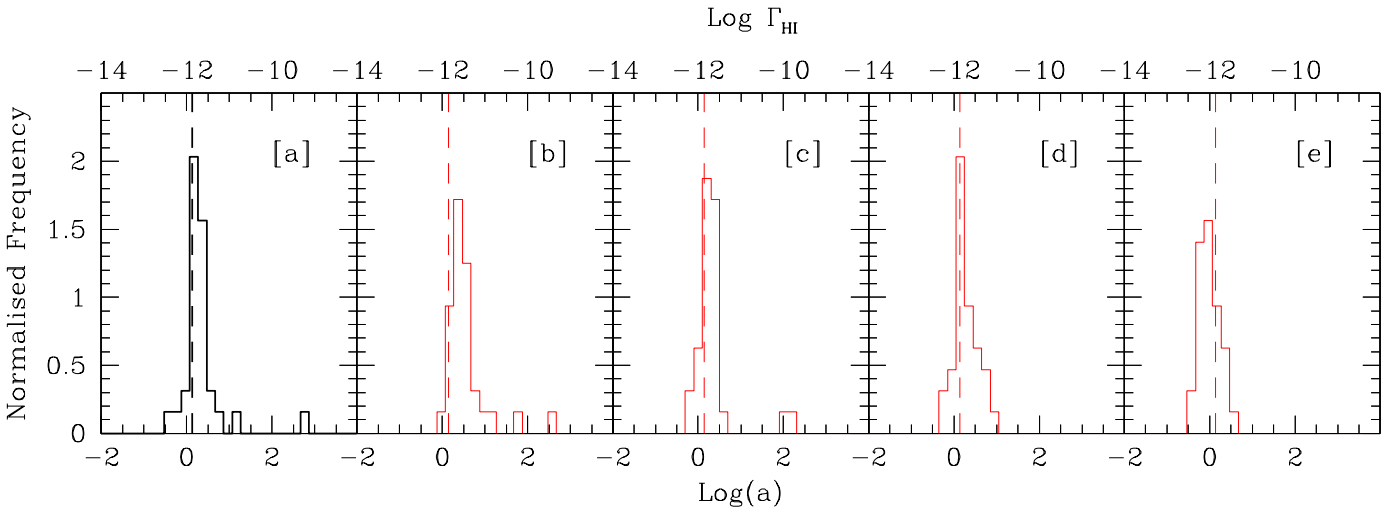

Fig. C.2. The PESD of the highest redshift subset (S8, with $4.0 < z_q < 5.0$) adopting different redshift estimates as a proxy for the quasar systemic redshift. From left to right we adopted the Schneider et al. (2007) values (panel [a], as reported in Chapter 3), the C IV emission line redshift in panel [b]. In panels [c], [d] and [e] we based the redshift determination on the C IV emission line adding 824, 1500 and 2000 km s^{-1}, respectively. In all panels the dashed vertical line marks the modal value of the PESD in the subset S8 as described in Sect. 3.7.1

results are shown in Fig. C.1. While the two PESDs present some marginal differences, there are no significant systematic biases. Thus, even if at high redshift we rely on only three intervals to estimate the best fit power law continuum, this limitation does not cause a systematic overestimation of the cosmic photoionisation rate compared to that derived at redshift smaller than $z \simeq 3$.

C.2. Redshift determination

At all redshifts considered, the proximity effect signal is determined assuming that the SDSS redshift accurately identifies the quasar systemic redshift. The SDSS redshift values adopted in our analysis were taken from the Schneider et al. (2007) quasar catalogue. They are based, for QSOs with $z_q \gtrsim 2.3$, on a few detectable broad emission lines and are further corrected for the known systematic velocity shifts present between low and high ionisation lines (Richards et al. 2002; Shen et al. 2007).

To investigate how much our results on the PESDs change as we assume a different quasar systemic redshift, we proceeded as follows. Motivated by the detection in all quasars of the C IV emission line, we considered five different redshift estimators: [a] the SDSS values, [b] the C IV emission line redshifts, [c] the C IV-based redshifts adding a velocity shift $\Delta v = 824$ km s^{-1} (Richards et al. 2002), [d] the C IV-based redshifts with $\Delta v = 1500$ km s^{-1} and [e] the C IV-based redshifts with $\Delta v = 2000$ km s^{-1}. For all these cases we re-determined the PESD in the highest redshift subset (S8). Our results are presented in Fig. C.2.

Comparing the different PESDs we note that except for some minor changes in shape, the distributions show a systematic bias only for a clear underestimation or overestimation of the emission redshift (case [b] or [e]). In particular, we note that when adopting the C IV-based redshift, the PESD is biased towards a smaller UVB photoionisation rate (weaker proximity effect strength), while it shows a bias toward larger UVB when adding the 2000 km s^{-1} shift. In the remaining cases we do not detect any significant deviation from the PESD obtained with the SDSS redshifts. In conclusion, the application of mean velocity shifts to correct the redshifts derived from the C IV or Lyα emission lines does not significantly bias our results on the cosmic photoionisation rate, unless the real (unknown) shifts are extremely large.

C.3. Definition of the quasar continuum

The detection of the proximity effect is possible only via the computation of the continuum rectified quasar flux, i.e. estimating the transmission spectrum. Unfortunately, the SDSS spectrograph ($R \sim 2000$) does not resolve individual absorbers and implies a high degree of line blending in the Lyα forest. This translates into a systematic deficit in the continuum level inferred when fitting a spline though the highest flux points of the Lyα forest as presented in Fig. 3.3 and described in detail in Sect. 3.2.2.

The systematic correction of the continuum is directly related to the amount of absorption in the forest, thus it becomes larger at higher redshift as the effective optical depth increases. However, the presence of the proximity effect, and in particular the deficit of absorption in the blue wing of the Lyα emission line, results in a smaller continuum correction approaching the quasar. Thus, along each spectrum the systematic continuum bias has a turnover point approximatively located at $\log \omega \simeq 1$, where the quasar radiation and the UVB have equal photoionisation rates.

To illustrate the effect of the continuum correction in the computation of the proximity effect and then in determining the PESD, we simulated 500 sight lines at redshift $z = 4.5$ having the same pixel size, resolution and median S/N as the SDSS observations.

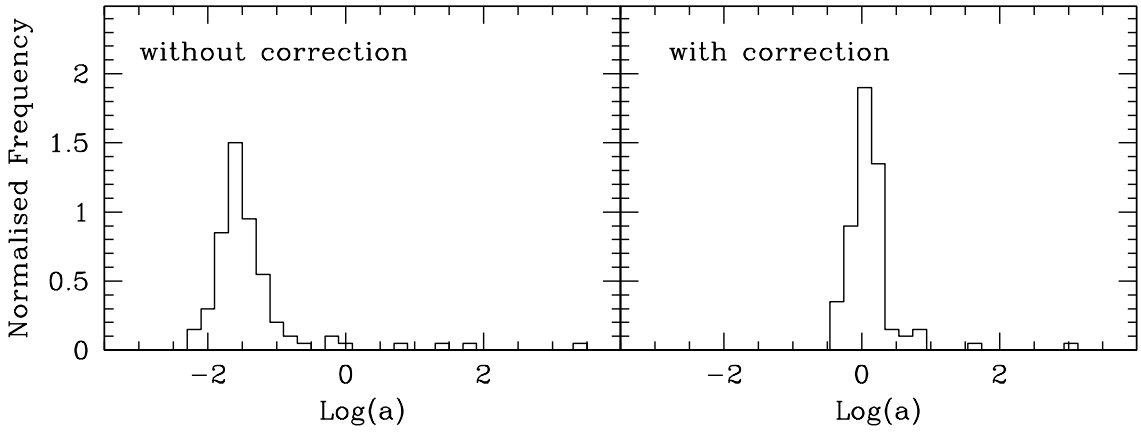

Fig. C.3. *Left:* The proximity effect strength distribution inferred from a sample of 500 simulated sight lines at $z = 4.5$. The mock spectra were not corrected for the systematic underestimation in the quasar continuum caused by the low spectral resolution. *Right:* The PESD obtained from the same simulated sight lines, this time applying the systematic continuum correction. The strength distribution in this case shows a clear peak at the reference model, i.e. its modal value is centred at $\log a = 0$.

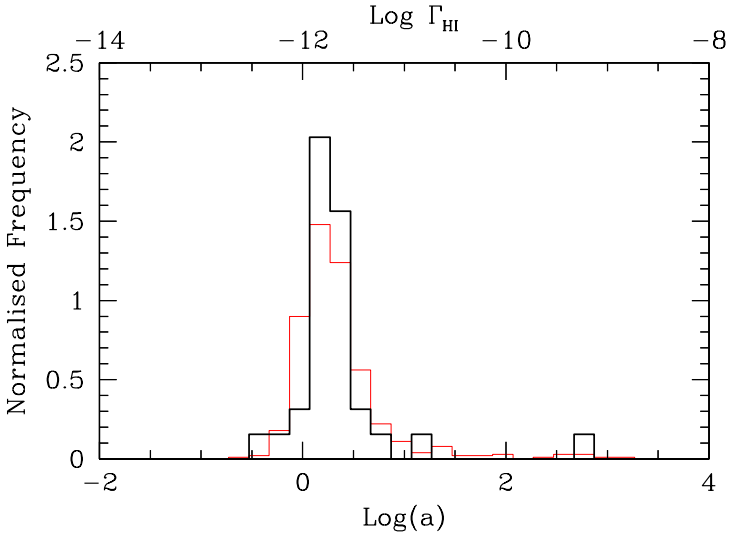

Fig. C.4. Comparison between the observed PESD in the subset S8 (black thick histogram) and the PESD estimated from 500 simulated SDSS quasar spectra having a S/N of 10 in the Lyα forest (red thin histogram). The low S/N of the mock spectra results in a broader strength distribution, but does not give rise to any systematic departure from the observed PESD.

We computed the PESD with and without the continuum correction and present our results in Fig. C.3. While the continuum corrected PESD successfully peaks at the reference value, i.e. at $\log a = 0$, the one inferred from the uncorrected continua is highly biased towards a weak effect. This example illustrate that our continuum correction accurately accounts not only for the increased line blending as the redshift increases, but also for the lack of absorption due to the proximity effect.

Unfortunately, we cannot completely rule out the possibility that our simulated spectra somehow differ from the real SDSS observations. Even though we visually inspected all quasars at redshift $z > 3.3$, a small, but systematic overestimation of the continuum correction might still occur, leading to larger values of the UVB photoionisation rate at $z > 3.3$.

C.4. Signal to noise level

In this section we searched for possible systematics connected to the low S/N of our observations. We considered a sample of 500 synthetic SDSS spectra at redshift $z = 4.5$ all having a S/N of 10 the same as the minimum value fixed in our selection criterion (Sect. 3.2.1). We introduced the proximity effect adopting as reference UVB photoionisation rate, the modal value of the observed PESD inferred from the subset S8. Figure C.4 shows the estimated PESD in these simulations compared to the observed PESD in S8. The effect of low S/N in the spectra results in a broadening of the distribution, but does not induce a systematic bias.

References

Richards, G. T., Vanden Berk, D. E., Reichard, T. A., et al. 2002, AJ, 124, 1
Schneider, D. P., Hall, P. B., Richards, G. T., et al. 2007, AJ, 134, 102
Shen, Y., Strauss, M. A., Oguri, M., et al. 2007, AJ, 133, 2222

Acknowledgements

First and foremost, I am indebted to my supervisor, Lutz Wisotzki, for his encouragement, guidance and most of all patience during the whole period of my thesis. He provided essential comments, criticism and with his language skills, improvements to my work. I am also deeply thankful to Nick Gnedin for sharing with me the challenges of science and for being present in difficult situations. It has been an honour and a privilege being able to work with both of you. I would also like to express my most sincere gratitude to Matthias Steinmetz for his constant support since my arrival at the institute.

I am also very grateful to my other collaborators, Gabor Worseck, Cora Fechner, Thorsten Tepper Garcia, Justus Vogel, Asmus Boehm, Natasha Maddox, Tae-Sun Kim for providing their advice and technical expertise on a broad range of topics. I am blessed with some of the most loving friends from whom I have received pure, selfless love and understanding. Some of those whom I want to fondly recall at this happy hour are Giuseppe Zampieri, Stefano Noventa, Antonio Nibale, Federica Marcato, Letizia d'Apolito, Domenico Tamburro, Marta Mazza but most of all Matteo Turilli, thanks for all your love and support. Additionally, I am also very grateful to all the extraordinary people I have met here in Potsdam, Adriane Liermann, Helge Todt, Malte Schramm, Pascal Hedelt and Beate Reinhold. A special thanks is reserved for Sonja and her family. I am deeply thankful for the hospitality and warm welcome you always reserve for me. In spite all the persons that inspired me thus far in my life, my mother goes beyond anyone. This work is for you and all the sacrifice we both made to be where we are. Thank you.

Finally a sincere gratitude to the financial support of the Deutsche Forschung Gemeinschaft, the Potsdam University, the Fermi National Accelerator Laboratories and the University of Chicago.